Metrology of Solar Irradiance

Dissertation
zur
Erlangung der naturwissenschaftlichen Doktorwürde
(Dr. sc. nat.)

vorgelegt der
Mathematisch-naturwissenschaftlichen Fakultät
der
Universität Zürich

von
ANDRÉ FEHLMANN
von
Staffelbach AG

Promotionskomitee
Prof. Dr. U. Straumann, (Vorsitz)
Prof. Dr. W. Schmutz
Dr. W. Finsterle, (Leitung der Dissertation)
Dr. P. Blattner

Zürich, 2011

Contents

Abstract

Determining the Total Solar Irradiance (TSI) and Spectral Solar Irradiance (SSI) reaching the top of the Earth's atmosphere is of great relevance as the solar radiation is the most important energy source to the Earth's climate system. Variations of the solar irradiance naturally contribute to climate changes. Earth observing satellites and ground based networks are used to track these natural as well as anthropogenic changes by measuring UV, visible and infrared radiation. Clearly climate change is a global problem and hence, we need a worldwide reference scale for these radiation measurements. The Physical Meteorological Observatory Davos and World Radiation Center (PMOD/WRC) has been designated to maintain the World Radiometric Reference (WRR) for TSI, the World Infrared Standard Group for integrated infrared measurements, the World Optical Depth Research and Calibration Center for atmospheric extinction measurements and the European Ultraviolet Calibration Center for integrated UV measurements.

On orbit measurements starting in the late 1970's, have revealed an 11 year cycle of the TSI. However, the results from individual experiments differ although all instrument teams claim to measure an absolute value. Especially the data from the TIM/SORCE experiment confused the community as it measures 0.3 % lower than the other instruments, e.g. VIRGO/SOHO by PMOD/WRC, which clearly exceeds the uncertainty stated for the absolute characterization of the experiments. The offsets between the instruments make it difficult to compose the different measurements to a single time series. Indeed, the three existing TSI composites show different long term trends in the solar output. This allows equivocal statements about the natural contribution of the sun to the climate change and about the fundamental processes on the sun. The PREMOS package on the PICARD platform launched in June 2010 is the latest space experiment by PMOD/WRC measuring the TSI. We have put great effort in the calibration and characterization of this instrument in order to resolve the inter-instrument differences. We performed calibrations at the National Physical Laboratory (NPL) in London and the Laboratory for Atmospheric and Space Physics (LASP) in Boulder against national SI standards for radiant power using a laser beam with a diameter being smaller than the aperture of the instrument. These measurements together with the WRR calibration in Davos allowed to compare the WRR and the SI radiant power scale. We found that the WRR lies 0.18 % above the SI radiant power scale which explains a part of the VIRGO-TIM difference. The Total solar irradiance Radiometer Facility (TRF) at the LASP also allows to generate a beam that over fills the apertures of our instruments, giving the presently best available representation of solar irradiance in a laboratory. These irradiance calibrations revealed a stray light contribution between 0.09 and 0.3 % to the measurements which had been underestimated in the characterization of our instruments. Using the irradiance calibrations, we found that the WRR lies 0.32 % above the TRF scale which in turn explains the full VIRGO-TIM difference. The first PREMOS measurements

in space confirmed our findings. If we use the WRR calibration, PREMOS yields a TSI value of 1365.5 ± 1.2 W/m^2 (k=1) which is in excellent agreement with VIRGO (1365.4 W/m^2). Else, applying the TRF calibration to PREMOS, we obtain a TSI value of 1360.9 ± 0.4 W/m^2 (k=1) which is in excellent agreement with TIM (1361.3 W/m^2).

The WRR in the framework of metrology is a conventional standard which has been defined in 1979 by the average of a group of 15 solar radiometers. Today, there are only 6 instruments of the original group still working and we face the question how to guarantee the continuity of this worldwide reference. Clearly, we could repopulate the group with new instruments but this solution would not resolve the issue of a conventional standard that is not directly traceable to a fundamental physical quantity. Metrology institutes use cryogenic radiometers to define the SI radiant power scale and key comparisons between the institutes guarantee the stability of this scale. The PMOD/WRC, the NPL and the Swiss Federal Office of Metrology (METAS) have initiated the Cryogenic Solar Absolute Radiometer (CSAR) project to adapt the advantages of cryogenic radiometry for solar measurements. The CSAR is a potential candidate to replace the WRR but it has also been designed with space flight in mind. By bringing an optical power and irradiance primary standard into orbit, we would obtain an unprecedented accuracy of Sun and Earth observations by calibrations on orbit. The preliminary CSAR results show that the cryogenic radiometer measures 0.3 % lower than the WRR.

Considering the independent results from the PREMOS/PICARD instrument and the CSAR, we have found clear evidence that the WRR scale is 0.3 % higher than a total solar irradiance scale defined by cryogenic radiometers. Hence, the observed on orbit TSI difference is solely due to the different reference scales used for the calibration. When we discuss the replacement of the WRR by the CSAR, we should also address the question whether we continue to use the WRR scale for solar irradiance measurements or if we redefine the SI solar irradiance scale by the lower CSAR value.

Zusammenfassung

Für das Klimasystem unserer Erde stellt die Sonne die bei weitem am wichtigste Energiequelle dar. Darum ist es von grosser Bedeutung zu messen, wie viel Energie in Form der Totalen Solaren Irradianz (TSI) unsere Atmosphäre erreicht und wie diese Sonnenstrahlung spektral verteilt ist. Variationen der Sonneneinstrahlung bewirken eine natürlich Form von Klimawandel. Wir benutzen erdbeobachtende Satelliten und Messnetzwerke am Boden, welche UV, sichtbare und infrarote Strahlung messen, um den natürlichen aber auch den von der Menschheit verursachten Klimawandel zu beobachten. Da der Klimawandel ein globales Problem darstellt, brauchen wir eine weltweit gültige Referenz für diese Strahlungsmessungen. Das Physikalisch Meteorologische Observatorium Davos und Weltstrahlungszentrum (PMOD/WRC) ist beauftragt, die Welt-Radiometrische-Referenz (WRR) für TSI, die Welt-Infrarot-Standard-Gruppe für integrierte Infrarotmessungen, das Welt-Forschungs- und Kalibrationszentrum für atmosphärische Trübung und Absorption und das Europäische-Ultraviolet-Kalibrationszentrum für integrierte UV Messungen, zu unterhalten.

Satellitenmessung die seit den späten siebziger Jahren durchgeführt werden, haben gezeigt, dass die TSI mit einem 11 Jahreszyklus variiert. Und obwohl alle Instrumententeams behaupten einen absoluten Wert zu messen, unterscheiden sich die Resultate individueller Experimente. Speziell der Messwert des TIM/SORCE Experiments irritierte die Wissenschaftler, da es 0.3 % weniger als alle anderen Instrumente misst, z. B. VIRGO/SOHO welches vom PMOD/WRC gebaut wurde. Dieser Unterschied zwischen den Instrumenten ist deutlich grösser als die Messunsicherheiten die angegeben werden. Des weiteren erschwert die Differenz zwischen den Resultaten die Kombination aller Daten zu einer durchgehenden Zeitreihe. Es existieren drei solcher zusammengestellter Zeitreihen, welche allerdings unterschiedliche Trends in der Sonnenintensität in den letzten dreissig Jahren aufzeigen. Dadurch können keine eindeutigen Aussagen über den natürlich Beitrag der Sonne zum Klimawandel und über die fundamentalen Prozesse auf der Sonne gemacht werden. Das PREMOS Experiment auf dem französichen PICARD Satelliten der im Juni 2010 gestartet wurde, ist das neuste PMOD/WRC Instrument, das die TSI im Weltraum misst. Wir haben uns sehr viel Mühe bei der Kalibration und Charakterisierung des Instruments gegeben um den Unterschied zwischen den Experimenten erklären zu können. Am Nationalen Physikalischen Labor (NPL) in London und am Labor für Atmosphären- und Weltraumphysik (LASP) in Boulder haben wir unsere Instrumente mit nationalen SI Standards für optische Leistung verglichen. Dabei haben wir einen Laserstrahl als Quelle verwendet, dessen Durchmesser deutlich kleiner war als die Eintrittsblende unserer Geräte. Zusammen mit den WRR Kalibrationen in Davos, haben wir diese Messungen verwendet um den vierten WRR zu SI Vergleich anzustellen. Unsere Resultate zeigen, dass die WRR 0.18 % höher liegt als die SI Skala für optische Leistung und somit nur einen Teil des VIRGO-TIM Unter-

schieds erklärt. Die Anlage für Totale solare Irradianz Radiometer (TRF) am LASP liefert auch einen Laserstrahl welcher alle Eintrittsblenden unsere Instrumente überfüllt und damit die zur Zeit bestmögliche Simulation von solarer Irradianz in einem Labor liefert. Die Irradianzkalibrationen haben gezeigt, dass je nach Instrument 0.09 - 0.3 % des Messsignals durch Streulicht verursacht werden. Dieser Beitrag ist deutlich grösser als bisher in der Charakterisierung unserer Instrumente angenommen. Wenn wir die Irradianzkalibration verwenden, so liegt die WRR 0.32 % höher als die TRF Skala, was somit den ganzen VIRGO-TIM Unterschied erklärt. Die ersten PREMOS Messungen im Weltraum bestätigen unsere Ergebnisse. Mit der WRR Kalibration liefert PREMOS einen TSI Wert von 1365.5 $\pm$ 1.2 W/m^2 (k=1), welcher sehr gut mit den Messungen von VIRGO (1365.4 W/m^2) übereinstimmt. Wenn wir die TRF Kalibration verwenden, so erhalten wir einen PREMOS TSI Wert von 1360.9 $\pm$ 0.4 W/m^2 (k=1), der sehr gut mit TIM (1361.3 W/m^2) übereinstimmt.

Im Rahmen der Metrologie stellt die WRR einen konventionellen Standard dar, welcher 1979 als Mittelwert einer Gruppe von 15 solaren Radiometern definiert wurde. Heute sind nur noch 6 Instrumente dieser Orginalgruppe funktionstüchtig und wir stehen vor der Frage, wie wir den Fortbestand dieser weltweiten Referenz garantieren wollen. Einerseits könnten wir neue Geräte in die Gruppe integrieren. Dadurch wäre die Referenz aber weiterhin ein konventioneller Standard, der nicht direkt auf eine fundamentale physikalische Grösser rückführbar wäre. Metrologische Institute verwenden kryogene Radiometer um die SI Skala für optische Leistung zu definieren. Und Vergleiche zwischen den Instituten garantieren die Stabilität dieser SI Skala. Das PMOD/WRC, das NPL und das Bundesamt für Metrologie (METAS) haben das Kryogene-Solar-Absolut-Radiometer (CSAR) Projekt ins Leben gerufen, um die Vorteile der kryogenen Radiometrie auch für Sonnenmessungen nutzbar zu machen. Einerseits ist das CSAR ein Kandidat um die WRR zu ersetzen, es wurde aber auch für eine zukünftige Weltraummission konstruiert. Wenn wir nähmlich einen Primärstandard für optische Leistung und Irradianz in den Weltraum bringen können, so würden wir durch Kalibrationen im Orbit eine noch nie dagewesene Genauigkeit der Sonnen- und Erdbeobachtungen erreichen. Die vorläufigen CSAR Resultate liegen 0.3 % tiefer als die WRR.

Die unabhängigen PREMOS/PICARD und CSAR Resultate zeigen eindeutig, dass die WRR 0.3 % höher liegt als eine totale solare Irradianzskala die durch ein kryogenes Radiometer definiert wird. Deswegen sind die im Weltraum beobachteten TSI Differenzen nur auf die unterschiedlichen Kalibrationsskalen zurück zu führen. Wenn wir über den Austausch der WRR durch das CSAR diskutieren, so sollten wir auch klären, ob wir weiterhin die WRR Skala verwenden wollen oder ob wir die solare SI Irradianzskala durch den tieferen CSAR Wert neu definieren wollen.

Acknowledgements

It is my pleasure to thank those who made this thesis possible. First of all, I would like to express my deep and sincere gratitude to my supervisor Wolfgang Finsterle. Our long discussions and his detailed and constructive comments were of great value for me and my work.

I am also deeply grateful to Werner Schmutz, the director of the PMOD/WRC, for offering me this project and supporting all the calibration campaigns.

I would like to express my sincere gratitude to Professor Straumann for accepting me as an external Ph.D student and his encouraging supervision and guidance.

I am indebted to my colleague at the NPL, Rainer Winkler, for managing and realizing the CSAR with me. The detailed discussions, the senses of achievement we shared by completing critical goals of the project and also the long hours in the lab are moments I would not want to have missed.

I would like to extend my thanks to the staff of PMOD/WRC for all their help during my project and the good time we had. Especially, my fellow Ph.D students: Stefan Wacker for his support with the MODTRAN calculations, Markus Suter for his help with the experiments and Micha Schoell for his assistance whenever there was a problem with the servers. The electronics department: Daniel Pfiffner, Silvio Koller, Diego Wasser, Etienne De Coulon and Manfred Gyo for their endless support with the measurement setups and the detailed analyses of our instruments. The technical staff: Christian Thomann for running my experiments and organizing everything in need, Ricco Soder and Marcel Spescha for their technical drawings and their enthusiasm for organizing the realization of the parts, Daniel Bühlmann for his help and the organization of the backcountry skiing training, Irene Keller for sending my stuff all around the world. Sonja Degli Esposti and Stefanie Ebert for their cordial way of solving administrative issues and organizing little celebrations. The scientists: Christoph Wehrli, Gregor Huelsen, Julian Groebner and Margit Haberreiter for the interesting and rewarding discussions.

I am heartily thankful to Nigel Fox, Peter Lovelock, Malcolm White and Irina Behnert from the NPL for their support with the CSAR project and the memorable time I had in London.

I owe special thanks to the people at the LASP for the good collaboration. Greg Kopp, Dave Harber and Karl Heuerman, I had a brilliant time in Boulder.

I am also deeply grateful to the people at METAS. Peter Blattner for his support with the CSAR project and for reviewing my thesis. Reto Schafer for measuring the transmittance of our windows. Rolf Zwahlen and his team for the great effort in producing the CSAR parts.

A few people deserve a special mention: My parents Susanne and Heinz for offering me the opportunity to follow my interests and their endless support during all these years. My brother Daniel for pushing me for success and sharing his interests. The Schmid family for welcoming me among themselves warmly.

Words fail me to express my appreciation to Sabrina whose dedication, love and persistent confidence in me, has taken the load off my shoulder. I owe her for unselfishly letting her passions and ambitions coincide with mine.

Chapter 1

Introduction

1.1 Motivation

Solar radiation is the most important external energy source for the climate system of our planet. It drives climate relevant processes like the convection in the atmosphere and evaporation on the ground and oceans. The radiative transfer of the solar radiation arriving at the Top Of the Atmosphere (TOA) through the atmosphere, includes absorption, emission and scattering processes. The interaction of these radiative transfer processes and the atmospheric chemistry determines the Earths's climate. As the radiative transfer processes and the chemical reactions are linked through many feedback processes, describing and calculating our climate poses a complex task to the climate science community.

The debate about the depletion of the ozone layer, the causes of the climate warming and ultimately the future climate of our planet have raised the awareness of the general public and the politics for this topic. Therefore the climate science community has to deliver clear and consistent statements about the current state of knowledge and implications for the future. The World Meteorological Organization (WMO) coordinates the research on this global topic and the Intergovernmental Panel on Climate Change (IPPC) assesses the current information in climate change to produce a balanced summary for decision makers.

To understand climate change, it is essential to know the global energy budget of the Earth (Figure 1.1). The incoming solar radiation of 341.3 W/m^2 at the top of the atmosphere is derived by dividing a Total Solar Irradiance (TSI) of 1365.2 W/m^2 by four. Thereby, the energy integrated over the entire solar spectrum is evenly distributed over the entire surface area. Newer experiments state a TSI of 1361.2 W/m^2 corresponding to an energy input of 340.3 W/m^2 in the global energy budget. Clouds and the earth's surface reflect some of the solar radiation directly back into space. The other fraction of the solar radiation is absorbed by the atmosphere and the ground. The heated surface emits infrared radiation that is mostly absorbed by the atmosphere. And the atmosphere reemits energy according to its temperature. The net difference between incoming solar radiation and outgoing long-wave radiation determines whether the Earth's climate is heating up or cooling down.

There exist four main processes capable of causing the observed climate warming: 1) Changes of the Earth's orbit around the Sun. 2) More energy is coming from the sun. 3) The Earth's

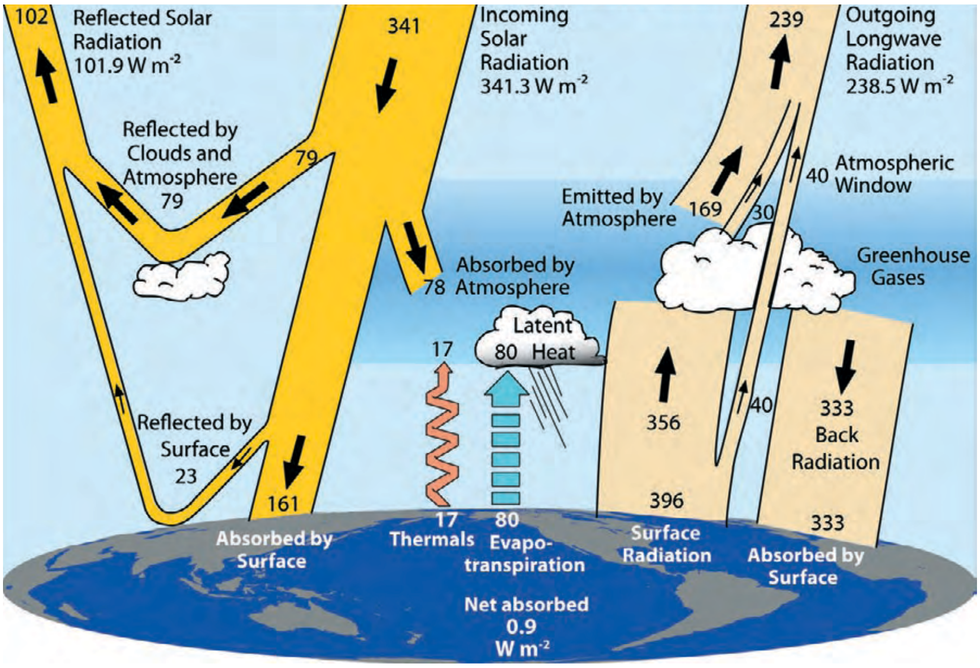

Figure 1.1: *This figure adopted from Trenberth et al. (2009), presents the individual components of the global annual mean energy budget.*

albedo has decreased, i.e. less solar radiation is directly reflected by clouds, aerosols or the surface. 4) Higher green house gases concentrations increase the absorption and the reemission towards the surface of the long-wave radiation in the atmosphere and thus reduce the infrared radiation losses of the Earth.

Changes of the Earth's orbit have long time scales, typically thousands of years, and so the other three processes are much more relevant for the current climate change. The last IPPC report (IPPC, 2007) comments the processes 2 to 4 the following:

2) *"For the period 1950 to 2005, it is exceptionally unlikely that the combined natural radiative forcing (solar irradiance plus volcanic aerosol) has had a warming influence comparable to that of the combined anthropogenic radiative forcing."* Only for the last 30 years the solar irradiance changes have been measured by space experiments. Prior to that period solar irradiance changes have to be reconstructed using proxy data. *"The low level of scientific understanding"* that we have of the influences of the changing solar irradiance on the climate, arises from the uncertainties in the relation between proxy data and solar irradiance as well as the uncertainty in the indirect effects to the climate caused by changes of the solar spectrum.

3) The direct reflection of the solar radiation by aerosols and clouds as well as the increased surface albedo caused by deforestation are considered to have *"a medium-low level of scientific understanding."* The uncertainty arises from the fact that anthropogenically and naturally induced changes are hard to separate. The decrease in surface albedo due to Black carbon aerosol deposition on snow has *"a low level of scientific understanding"* for the same reason.

4) *”Human activities result in emissions of four principal green-house gases: carbon dioxide (CO_2), methane (CH_4), nitrous oxide (N_2O) and the halocarbons (a group of gases containing fluorine, chlorine and bromine). These gases accumulate in the atmosphere, causing concentrations to increase with time. Significant increases in all of these gases have occurred in the industrial era since 1750. All of these increases are attributable to human activities and remain the largest and most important driver of climate.”* The contribution of green-house gases to climate change is assessed with *”a high level of scientific understanding.”*

The assessments in the IPPC report are based upon measurements of the individual components of the energy budget and simulations with climate models. The low level of scientific understanding in the processes 2) and 3) is partially due to the large measurement uncertainties. Hence, only equivocal conclusions can be drawn from the data which impedes a constructive international debate on climate change.

For this reason, it is essential to improve the accuracy of our measurements and to provide unambiguous long-term records of climate relevant forcings. To homogenize the international data records it is crucial to provide a primary standard to which all measurements are traceable. This thesis focuses on the problems and uncertainties in measuring the TSI on the ground and in space. And we show how our work might improve the quality of spectral radiance measurements observing the Sun or the Earth’s atmosphere.

1.2 Traceability of Total Solar Irradiance Measurements

The first pyrheliometer measuring the Total Solar Irradiance (TSI) was developed by Pouillet (1838) to investigate the influence of solar radiation on the weather and the climate. Ångström (1893) and Abbot and Fowle (1908) increased the accuracy of total solar irradiance measurements by developing the Ångström and the Smithsonian Silverdisk pyrheliometers. According to the instrument types the Ångström and the Smithsonian scale for TSI measurements were defined. Comparisons showed a difference of a few percent between the two scales. In order to investigate the difference the International Radiation Commission IRC organized in 1934 a first pyrheliometer comparison in Davos which however could not resolve the issue. To establish worldwide homogeneity of radiation measurements, the International Pyrheliometric Scale (IPS) has been introduced in 1956 and in 1959 the WMO organized the first International Pyrheliometer Comparison (IPC-I) at the Physikalisch Meteorologisches Observatorium Davos (PMOD).

1.2.1 The World Radiometric Reference (WRR)

In the late 1960s, the modern type of electrical substitution cavity radiometers, so called absolute radiometers (Kendall et al., 1965), have been developed. The accurate measurements of the new radiometers finally allowed to define a new scale for total solar irradiance measurements. The results from the fourth IPC in 1975 were used to establish the World Radiometric Reference (WRR). This conventional standard has been defined from the mean value of 15 absolute radiometers of 9 different types and its accuracy has been estimated to be 0.3 % (Fröhlich, 1978). In 1979 the executive committee of the WMO declared the WRR as the reference to be used for irradiance measurements (WMO, 1979). The PMOD was designated as the World Radiation Center (WRC) being in charge of maintaining the World Standard Group (WSG) of absolute radiometers used to define the WRR. Since then, the IPC's are held every five years in Davos in order to disseminate the WRR and to validate the stability of the WSG. More details on the history of TSI measurements and the WRR can be found in Bolle (2008) and Fröhlich (1991).

1.2.2 The Radiant Power Scale of the International System of Units (SI)

The metrology community led by the Bureau International des Poids et Mesures (BIPM) provides the International System of Units (SI). Among the SI base units m, kg, s, A, K, mol and cd there exists the derived unit Watt that is used to quantify power. National Metrology Institutes (NMI's) use cryogenic radiometers as primary standards to maintain the SI scale for radiant power. Cryogenic radiometers have been first developed at the National Physical Laboratory (NPL) by Martin et al. (1985). As the ambient temperature absolute radiometers defining the WRR, the cryogenic absolute radiometers use an electrical substitution principle to compare optical to electrically dissipated power. The advantages of operating at cryogenic temperature are twofold. 1) Larger absorbing cavities can be used guaranteeing an absorption of 99.998 % of the incident radiation. 2) The thermal conductivity of the materials are drastically enhanced. Thermal gradients within the absorbing cavity become negligible and thus the equivalence of optical and electrical heating is vigorous (Martin et al., 1985).

Cryogenic absolute radiometers are capable of determining radiant power at the milliwatt-level with an accuracy of 4 parts in 10^5 (Martin et al., 1985). And key comparisons between the radiant power primary standards operated at the NMI's guarantee the high stability of the SI radiant power scale (Goebel et al., 2000).

1.2.3 Comparisons of the World Radiometric Reference and the SI Radiant Power Scale

Romero et al. (1991, 1995) and Finsterle et al. (2008) published three comparisons of the World Radiometric Reference with the SI radiant power scale. Their findings suggest that the two scales are identical within their stated uncertainties. The third comparison also supports a trend in the ratio of the two scales matching an observed drift of the WRR between IPC-IX and IPC-X.

In 2004 the Federal Office of Metrology (METAS) has designated the PMOD/WRC as a member of the International Committee for Weights and Measures's (CIPM) Mutual Recognition Arrangement (MRA) and in 2010, the WMO also signed the MRA. Therewith the WRR has been accepted as reference scale for solar irradiance measurements within the SI system. In chapter 2 we present the outcome of a fourth, improved comparison between the two scales.

1.3 Satellite Based Measurements

Already Abbot et al. (1942) published observational evidence for the total solar irradiance arriving at the top of the atmosphere not being constant. He claimed variations of several percent on short term periodic timescales. However, he missed the correlation between enhanced value of total solar irradiance and increased number of observed sunspots and hence proclaimed the long term constancy of the solar irradiance. Reviewers of his work criticized his covariance method to estimate the standard deviation of his results and presented techniques to reduce the uncertainty to 0.17 % (Sterne and Dieter, 1958).

The modern era of satellite based measurements starting in the late 1970s, proved the variation of the total solar irradiance and its correlation with the sunspot number. The amplitude of the variation is 0.1 % during an 11 year solar cycle. Figure 1.2 shows the original data measured by satellite based radiometers during the last three solar cycles. The first experiments still yielded high values before the results of the other measurements converged towards a value around 1365 W/m^2. In 2003 the Total Irradiance Monitor (TIM), a new type of absolute solar radiometer (Lawrence et al., 2000), delivered considerably lower TSI values. The offset of 0.35 % between TIM and the other instruments raised a vivid discussion about the characterization and calibration of the radiometers among the instrument teams (Butler et al., 2008). The PMOD/WRC is responsible for the measurements of a solar absolute radiometer on the VIRGO/SOHO (Fröhlich et al., 1995) mission. Our radiometer has been calibrated against the WRR in Davos before launch. Hence the VIRGO results are representative for the WRR in space. The characterization of the VIRGO radiometers is accurate to 0.17 % (Fröhlich et al., 1997) and implies no effect explaining the difference between VIRGO and TIM. A difference that is not compatible with the stated instrument uncertainties and that is larger than the uncertainty of the WRR.

The launch of PMOD/WRC's latest space experiments PREMOS/PICARD incorporating absolute solar radiometers, offered a great opportunity to investigate the causes of the observed differences in space. In chapter 2 we present the details of the PREMOS calibration and characterization. We have calibrated the PREMOS radiometers against the WRR as well as against the TRF (Kopp et al., 2007).

For the climate science and the solar physics communities the offsets between the different TSI measurements poses another problem. Investigating the Sun's influence on the climate and understanding the physics behind the solar activity requires an unequivocal statement about the long term behavior of the total solar irradiance so that a possible influence on the terrestrial climate of TSI and SSI trends can be investigated. The temporal overlap of the individual data records allows to create a TSI composite of the entire observational period. But depending on the combination of instruments, cross calibrations and instrumental drift adjustments, the derived slope of the long term TSI trend is different. The PMOD composite (Fröhlich, 2006) and the Space Absolute Radiometric Reference (SARR; Crommelynck et al. 1995) composite (Dewitte et al., 2004) show no significant trend during the last three solar cycles. The Active Cavity Radiometer Irradiance Monitor (ACRIM, Willson 1979) composite (Willson and Mordvinov, 2003) however, shows an increase of 0.04 % over the same period. The only way to overcome this problem is to better understand the instrumental differences. This allows us to provide a consistent absolute value of the TSI that is traceable to the SI system. And in the case of having

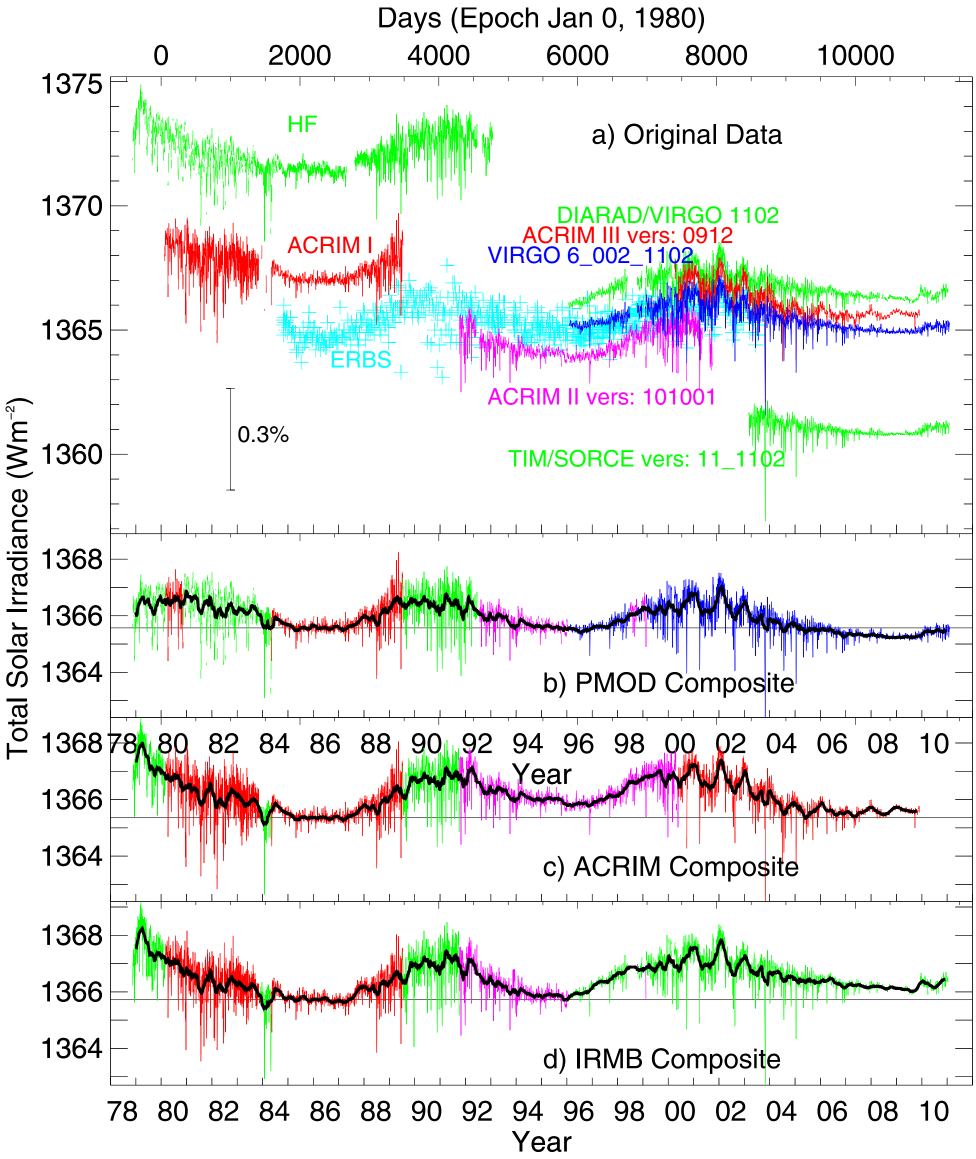

Figure 1.2: *The top panel shows the original data records of the different space experiments measuring the TSI. The 0.35 % offset between the TIM and the other radiometers is larger than the combined uncertainty stated by the individual instrument teams. The three TSI composites state different long term trend in TSI, depending on the selection of data records, cross calibrations and instrumental drift adjustments (Fröhlich, 2006; http://www.pmodwrc.ch/pmod.php?topic=tsi/composite/SolarConstant, 2011).*

no absolute radiometer operating in space, directly SI traceable instruments would ensure the smooth continuation of the TSI record after the gap.

1.4 The Cryogenic Solar Absolute Radiometer (CSAR) Project

At the moment the WSG is populated with six absolute radiometers out of the 15 instruments initially defining the WRR. These instruments are operating for more than three decades and their failure is simply a matter of time.

In 2007 the PMOD/WRC, the NPL and the METAS initiated the Cryogenic Solar Absolute Radiometer (CSAR) project. The main goal of the joint effort was to design and build a cryogenic radiometer suitable to replace the WRR as standard for solar irradiance measurements. In chapter 8 we discuss the assembling and commissioning phase of the CSAR and we present the first measurements results. The details on the design and the data evaluation can be found in Winkler (2011a). Using a cryogenic radiometer on the ground always demands an entrance window. In chapter 6 we discuss the characterization of the CSAR entrance window and in chapter 7 we present a Monitor to measure the Integral TRAnsmittance (MITRA) of such windows with high precision.

Replacing the conventional standard WRR with a cryogenic radiometer would lead to direct traceability of solar irradiance measurements to the SI radiant power scale as the CSAR could participate in future BIPM key comparisons.

The second goal of the CSAR project was to design and build the CSAR for space flight. Like cryogenic radiometers in laboratories, the CSAR could provide the SI reference for radiant power on orbit. Through this realization of the SI scale in space, solar radiometry would reach a new level of accuracy and long term stability. The CSAR has been proposed as core pay load of the Traceable Radiometry Underpinning Terrestrial- and Helio- Studies (TRUTHS) mission (Fox et al., 2003). With the CSAR on board, TRUTHS will be the first satellite mission calibrating its Earth Observation (EO) instrumentation directly to SI on orbit. Of course all EO missions could benefit from the calibration facility which would reduce the errors due to different calibration biases. This would lead to an unprecedented accuracy in solar irradiance measurements as well as in climate relevant Earth observations.

Chapter 2

Characterization of the PREMOS Absolute Solar Radiometers

The PREcision MOnitoring Sensor (PREMOS) is the latest in a long-standing series of space experiments by PMOD/WRC. The package is on board the French PICARD satellite and incorporates two absolute solar radiometers and three 4-channel filter radiometers (Thuillier et al., 2006). In this chapter we will focus on the characterization and calibration of the absolute solar radiometers. In Appendix A we present ideas to better characterize upcoming absolute solar radiometers. Brusa and Fröhlich (1986) describe the experiments needed to obtain the correction factors accounting for the deviation from the radiometer's ideal behavior. We repeated some of those experiments and developed techniques to determine novel corrections. Besides the characterization, the PREMOS radiometers have been calibrated against the WWR. The PREMOS-B radiometer has been compared with the NPL radiant power scale. PREMOS-A is traceable to the Total solar irradiance Radiometer Facility (TRF; Kopp et al. 2007) at the Laboratory for Atmospheric and Space Physics in Boulder (LASP) and to the NPL radiant power scale.

2.1 Operating Principle of a PMO6-type Radiometer

The PMO6-type instrument is an absolute Electrical Substitution Radiometer (Kendall et al. 1965) developed by Brusa and Fröhlich (1986). It determines the solar radiant power received through an aperture with known area and hence is measuring the absolute value of the total solar irradiance in units of Watts per square meter. A characterization of our radiometer's behavior is needed due to the imperfect transfer from solar irradiance to the measured electrical heating (Figure 2.2).

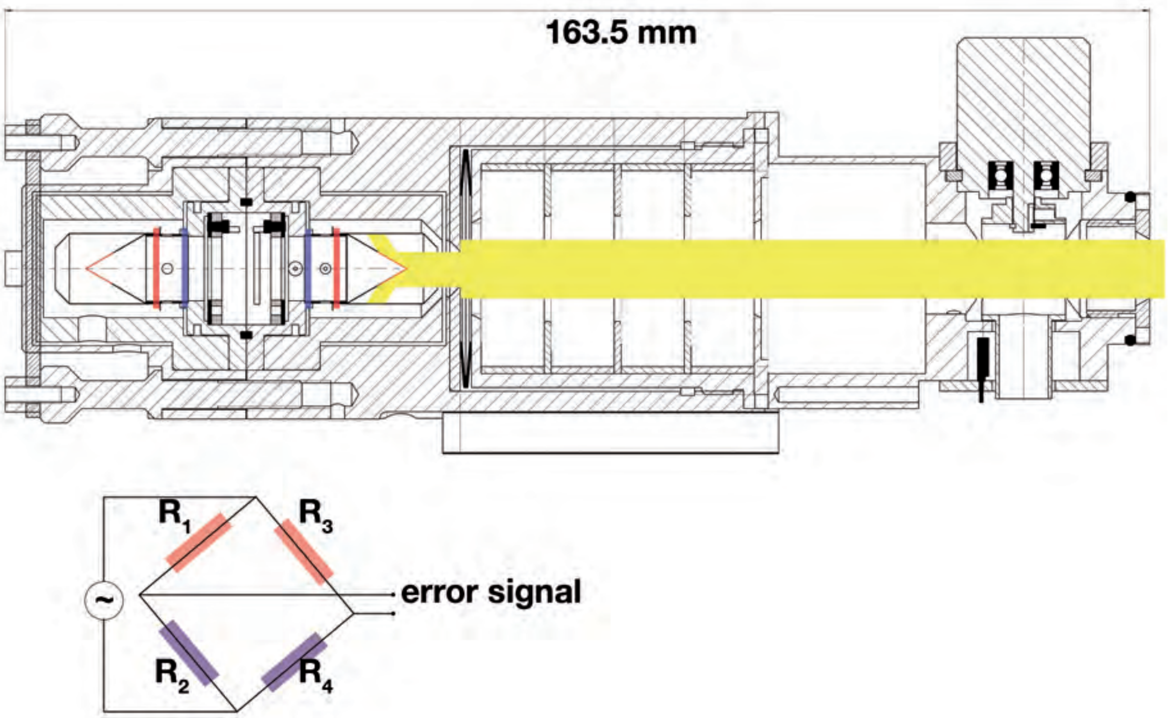

Figure 2.1: *Cross section of a PMO6-type radiometer (top) and the electrical circuit diagram (bottom). A PMO6-type radiometer has a reference and a measuring detector. Each detector has an absorbing cavity connected to a common heat sink through a thermal resistor. Copper coils R_1, R_2, R_3 and R_4 on either side of the thermal resistor serve as thermometers. The four thermometers are connected to a Wheatstone bridge measuring the heat flux imbalance from the cavities to the heat sink. Heater foils on the illuminated areas of the cavity cones dissipate electrical power. The interior of a cavity is coated with a specular black paint which absorbs 93 % of the incident light. The remaining 7 % of the solar radiation are reflected onto the cavity walls. Thus, dissipating energy on a different cavity part than the location of the electrical heater.The reference cavity is heated with a constant electrical power while the servo controller balances the bridge by adjusting the heater power in the measuring cavity. Hence the heat flux from both cavities to the heat sink is equal at all times. A closed measurement before and one after the open measurement is used to account for thermal drifts of the environment. By linearly interpolating the closed data, we obtain the reference value at the time of the open measurement. We calculate the difference between the closed and the open heater power in the measuring cavity to determine the optical power. Knowing the area of the precision aperture and the optical power, we have determined the total solar irradiance in Watts per square meter.*

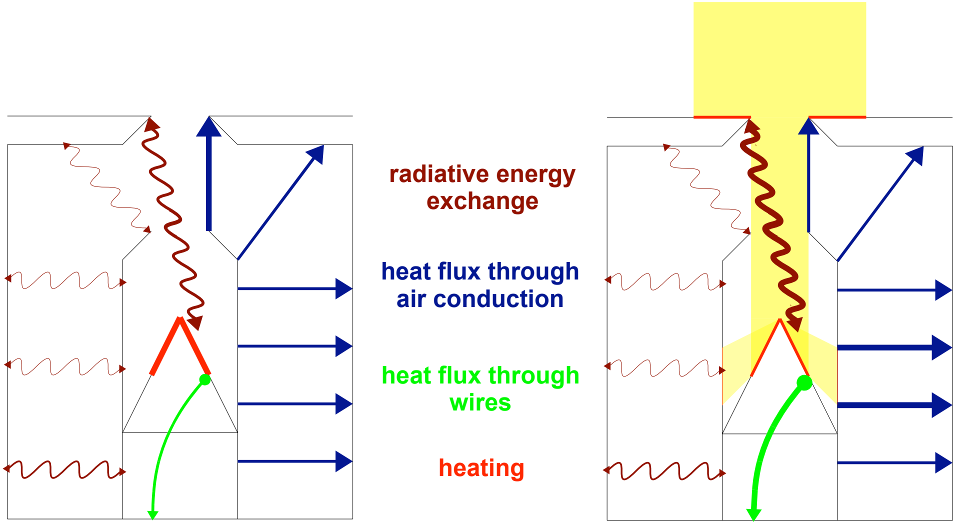

Figure 2.2: *Illustration of the heat exchange mechanisms affecting PMO6-type radiometer measurements. Differences between closed (left) respectively open (right) state of the instrument make corrections necessary. Radiative energy exchange: The precision aperture temperature rises due to the absorbed solar radiation and the enhanced thermal radiation causes the radiometer to read too high. The gold coating of the cavity minimizes the radiative energy exchange between the detector and the environment. Heat flux through the wires: The larger heater current during the closed measurement phase causes higher Joule losses in the leads which in turn suppress the cavity heat losses through the wires. Heat flux through air conduction: The cavity heat losses change according to the thermal gradients. The heat flux from the cavity to the precision aperture is highest if the aperture is not heated by the solar radiation and the losses from the cavity to the housing are enhanced by the optical heating of the cylindrical cavity walls.*

2.2 Heating of the Leads

The PREMOS PMO6-type radiometer design is shown in Figure 2.1. The sensing and the current feeding wires are thermally heat-sinked at a temperature T_0 at one side. The other ends are soldered to the heater keeping the cavity at a constant temperature $T_1 > T_0$. The power dissipated in the leads is different in the open and closed state of the radiometer. This affects the measuring cavity dissimilarly and we have to correct the measurements for the lead heating effect.

A fraction of the power dissipated inside the cavity is lost by a small heat flux through the four wires to the heat sink. The Joule losses within the current feeding leads suppress the heat flux. The difference between open and closed state of the measurement is best illustrated by Figure 2.3. When the shutter is closed, the servo controller adjusts the dissipated heater power in the measuring cavity, to keep the thermal flux through the thermal resistor the same as for the reference detector. In this state the losses through the leads are the same for both detectors. However, when the shutter is open, optical power is dissipated inside the measuring cavity. The electrical heater power has to be adjusted to keep the heat flux constant. Reducing the heater current implicates increasing losses through the leads. The servo controller compensates these additional losses by increasing the electrical heater power and we measure an open heater power that is too high. Hence, the determined difference between closed and open heater power needs to be corrected by a factor $C_{leadheating} > 1$.

We performed the experiment suggested by Brusa and Fröhlich (1986) to determine the lead heating correction factor. Prior to PREMOS, all PMO6-type radiometers in space had the control electronics directly attached to the instrument. The PREMOS controller however, is mounted in the package thermally insulated from the radiometer. Thus we characterized the PREMOS radiometers using a commercial PMO6 control electronics.

The idea of the experiment is to operate the instrument normally with the servo system balancing the sensing bridge. Then we supply an additional current through the feeding and the voltage sensing wire. The additional Joule losses affect the cavity similarly to the lead heating effect. But with the external electronics we were not able to completely separate the additional current from the control circuit.

In our experiment, we first determined the sensing bridge signal for various powers electrically dissipated inside the cavity. Then we interrupted the current feeding and the voltage sensing wires between the cavity and the electronics. Supplying a known current through the feeding-sensing wire pair on one side of the heater yielded a bridge response. From this experiment we know the cavity's reaction to heat dissipated in the connected leads. The lead heating effect, is determined by the the different response to a high respectively low current during the open

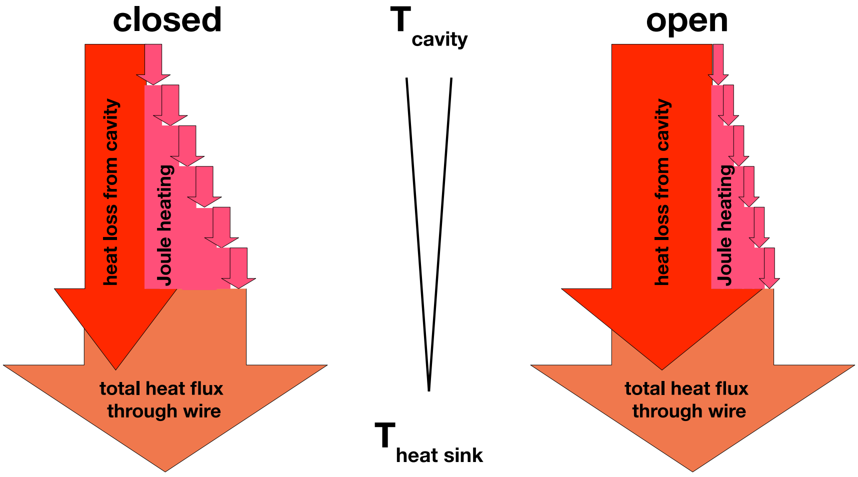

Figure 2.3: *This flow diagram explains the lead heating effect. During the closed state of the radiometer the heater current is high and the Joule losses suppress the heat losses of the cavity through the wires to the heat sink. Once the radiometer opens its shutter, the lower heater current causes less Joule losses. The control electronics will compensate the higher losses from the cavity through the wires by increasing the heater power. As a result, the difference between closed and open heater power measurements is too low and we underestimate the optical power dissipated inside the cavity.*

	lead heating vacuum	relative uncertainty	lead heating ambient	relative uncertainty	lead heating Brusa	relative uncertainty
PREMOS-1	1.000496	0.000040	1.000444	0.000040	1.000200	0.000034
PREMOS-2	1.000428	0.000040	1.000357	0.000040	1.000200	0.000034
PREMOS-3	1.000412	0.000040	1.000449	0.000040	1.000200	0.000034

Table 2.1: *Lead heating correction factors (upper limits) and standard uncertainty (k=1) for the three PREMOS radiometers measured with our technique. We also present the mean value found by Brusa and Fröhlich (1986) which we will use as final correction for the PREMOS instruments.*

and closed measurement phase of the radiometer. The initial calibration allows us to link the different lead heating response to a dissipated power change in the cavity. As the applied currents correspond to a virtual optical power, we can calculate the lead heating effect as the ratio of the measured electrical power change and the virtual optical power (Table 2.1).

However, these values represent an upper limit to the lead heating effect. This is because the cavity being at a lower temperature in our experiment than under normal working conditions. The heat produced in the leads flows in equal shares to the cavity and the heat sink. Normally, the cavity temperature is raised by 1 degree Celsius above the heat sink temperature. Thus we overestimate the heat flux from the leads into the cavity and hence the lead heating effect.

The ambient pressure does also affect the experiment. With air surrounding the detector, some of the heat generated in the leads is lost by conduction through the air. In vacuum the cavity should be less influenced and we would expect the lead heating effect to be smaller. This is true for PREMOS-1 and PREMOS-2 but not for PREMOS-3, indicating problems with the wiring of the third instrument close to the cavity. We will discuss possible implications of this problem in section 4.2.

Since our results only yield an upper limit to the lead heating effect, we use the Brusa correction factor of 1.000200 ± 0.000034 for the final correction of the PREMOS instruments.

2.3 Temperature Variations of the Heat Sink

The first indication of a changing heat sink temperature affecting PMO6-type radiometer measurements can be found in the data of the SOVA instrument on the EURECA mission (Crommelynck et al., 1993). Oscillations of the total solar irradiance values were found which correspond to the eclipse of the satellite. A laboratory experiment in 2008 gave a second hint of the importance of this effect: We were investigating the influence of wind to PMO6-type radiometer measurements by blowing air from different angles at the PMO6-11 Rocket instrument. The radiometer electronics is directly attached and the power dissipated by the components warms the heat sink to above room temperature. Therefore, we let the radiometer reach thermal equilibrium before starting the fan. As expected, blowing frontally into the instrument causes the radiometer to read too low: With the shutter closed, the instrument is not affected by the air flow. But once the shutter opens, the wind cools the cavity more effectively than still air and the controller compensates these increased losses by raising the heater power. As a result, the difference between closed and open heater power is too small. Surprisingly, the instrument also measured a spurious signal experiencing wind laterally from behind. We explain this behavior with small asymmetries in the construction of the radiometer. Hence, the heat flux from the cavities to the heat sink is not equally affected while the heat sink temperature is changing due to the wind chill and we measure a false solar irradiance.

Also in 2008, the SOlar Variable and Irradiance Monitor (SOVIM, Thuillier et al. 1999) was operating on board the International Space Station (ISS). During the 90 minutes orbit, the temperature of the SOVIM heat sink varied by more than 2 degrees Celsius. And the total solar irradiance data showed a systematic behavior when the ISS left the Earth's shadow and the instruments were heating up. This effect was more prominent for the SOVIM-1 radiometer which had one detector replaced shortly before launch. As a result, the thermal relaxation time constants of the two detectors in the radiometer no longer matched as well as they used to. And thus did not respond equally fast to a changing heat sink temperature.

2.3.1 Modeling the Heater Power as a Function of the Heat Sink Temperature

We used finite element simulations and experimental PREMOS data to develop a model allowing us to correct for the effect of the changing heat sink temperature. With this model we are able to correct the SOVIM and other PMO6-type radiometer data.

After discovering the effect with the PMO6-11 Rocket radiometer, we set up an experiment for the PREMOS instruments. To avoid any disturbance by the surrounding air, we performed the tests in vacuum. A heating coil was wrapped around the heat sink so that we could change the temperature of the instrument. The result of such a measurement is shown in Figure 2.4. We observe a changing heater power in the closed measuring cavity while the heat sink temperature is drifting. Plotting the heater power as a function of the heat sink temperature reveals a hysteresis effect: Depending on whether the heat sink temperature is increasing or decreasing, we observe different heater powers for a given temperature (Figure 2.5).

Our approach is to model the signal of the Wheatstone bridge formed by the four resitance thermometers. For the identification of the resitances R_1, R_2, R_3 and R_4 refer to Figure 2.1.

$$\text{signal} = U_0 \frac{R_1 \cdot R_4 - R_2 \cdot R_3}{(R_1 + R_2) \cdot (R_3 + R_4)} \tag{2.1}$$

where U_0 is the supply voltage of the bridge.

We assume a linear temperature dependence of the resistors

$$R_x = R_{x0}(1 + \alpha(T_x - T_0)), \tag{2.2}$$

where T_2 and T_4 are equal to the heat sink temperature T for the thermometers (R$_2$, R$_4$) on the heat sink. The thermometers on the cavities have a temperature $T_{1,3} = T + \Delta T_{1,3}$, where ΔT_1 respectively ΔT_1 represent the cavity temperature rises. The fact that signal $= 0$ at the temperature T_0 at which the bridge has been balanced, allows us to eliminate R_{40} and R_{30} in our equations.

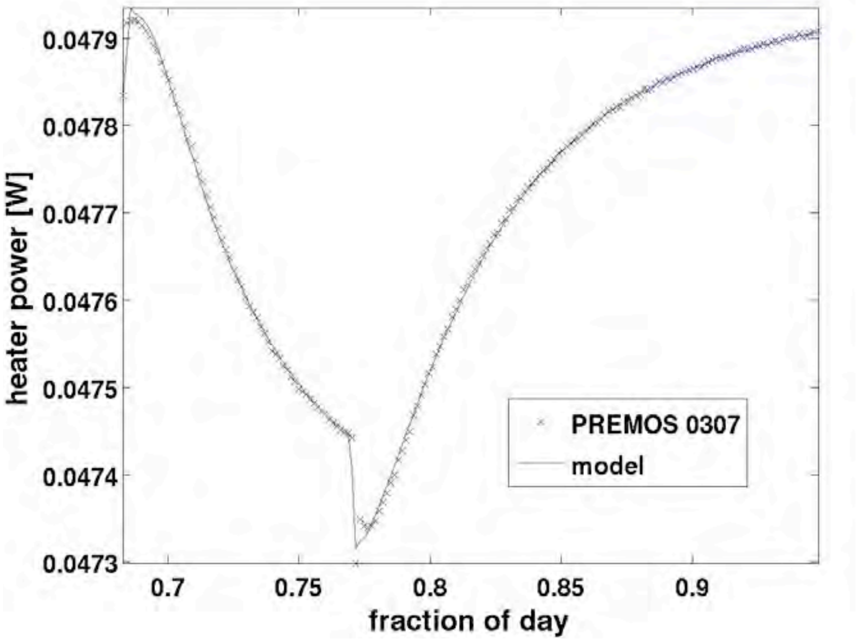

Figure 2.4: *The closed heater power in the measuring cavity changes when the temperature of the heat sink varies. Our model reproduces the variations measured with the PREMOS radiometer.*

$$signal = \frac{-(\alpha^2 R_{10} R_{20} (1+\alpha(T-T_0))(T-T_0) U_0 (\Delta T_1 - \Delta T_3))}{(((R_{10}+R_{20})(1+\alpha(T-T_0))+\alpha R_{10} \Delta T_1)(R_{20}(1+\alpha(T-T_0))(1+\alpha \Delta T_3)+R_{10}(1+\alpha \Delta T_1)(1+\alpha(T-T_0+\Delta T_3))))} \tag{2.3}$$

To complete our model, we need an expression describing the temperature rise ΔT_1 and ΔT_3 of the cavities as a function of the heat sink temperature. We used a finite element model created with the ANalysis SYStem (ANSYS) program to find an appropriate function $\Delta T_x(T)$. ANSYS gives us full control over the thermal boundary conditions allowing us to investigate several heat sink temperature forcings.

The empirical expression

$$\Delta T_1 = \Delta T_{10} + k_1 \frac{\partial T}{\partial t} + \frac{k_2}{T - k_3} \tag{2.4}$$

best describes the temperature rise of a cavity for different forcings, as can be seen in Figure 2.6. The first term in Equation 2.4 represents the temperature rise of the cavity when the heat sink temperature does not change. The second term accounts for the enhanced respectively inhibited heat flux from the cavity to the heat sink when the heat sink temperature varies. And the third term models the temperature dependent material properties, especially the one of the thermal resistor.

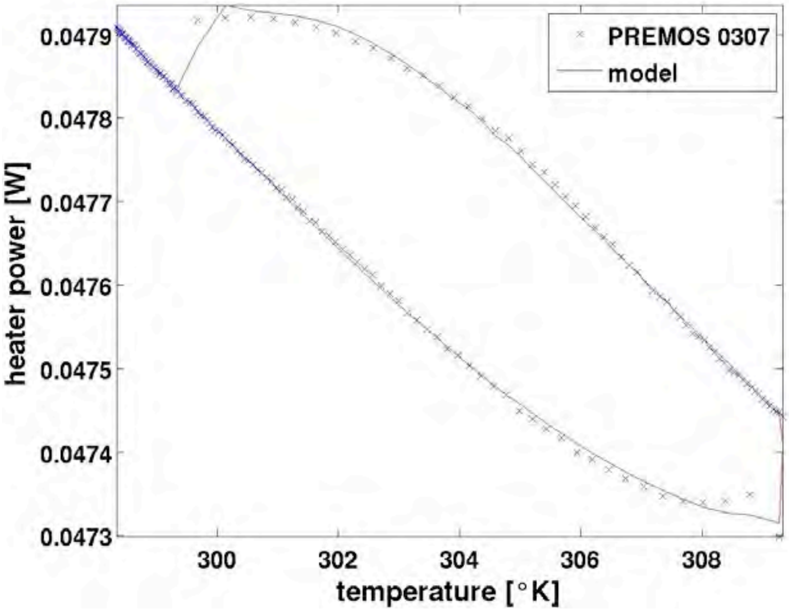

Figure 2.5: *Plotting the closed heater power in the measuring cavity as a function of the heat sink temperature reveals a hystereses effect. Therefore, our model has a term which incorporates the derivative of the heat sink temperature. Our model reproduces the hystereses measured with the PREMOS radiometer.*

We use the same fitting constants k_1, k_2 and k_3 to describe the two detectors in an instrument. But we introduce asymmetry factors a_1, a_2 and a_3 accounting for the differences between the two detectors.

$$\Delta T_3 = \Delta T_{30} + a_1 \cdot k_1 \frac{\partial T}{\partial t} + \frac{a_2 \cdot k_2}{T - a_3 \cdot k_3} \tag{2.5}$$

Substituting Equation 2.4 and Equation 2.5 into Equation 2.3 completes the heater power model of the measuring detector.

$$P(T)_{model} = P_0 + g \cdot signal, \tag{2.6}$$

where P_0 is the heater power at temperature T_0 and the bridge signal is amplified by the gain factor g.

We are able to describe the experimental PREMOS data by our model, as shown in Figure 2.4. To determine a correction for the SOVIM data, we fit our model to the closed heater power values and correct the measured open heater power accordingly. Figure 2.7 shows the successful correction of the SOVIM measurements.

To justify our model we formed a one dimensional heat equation with the boundary conditions describing our problem. But the solution includes a large number of variables making a proper fitting to the data impossible.

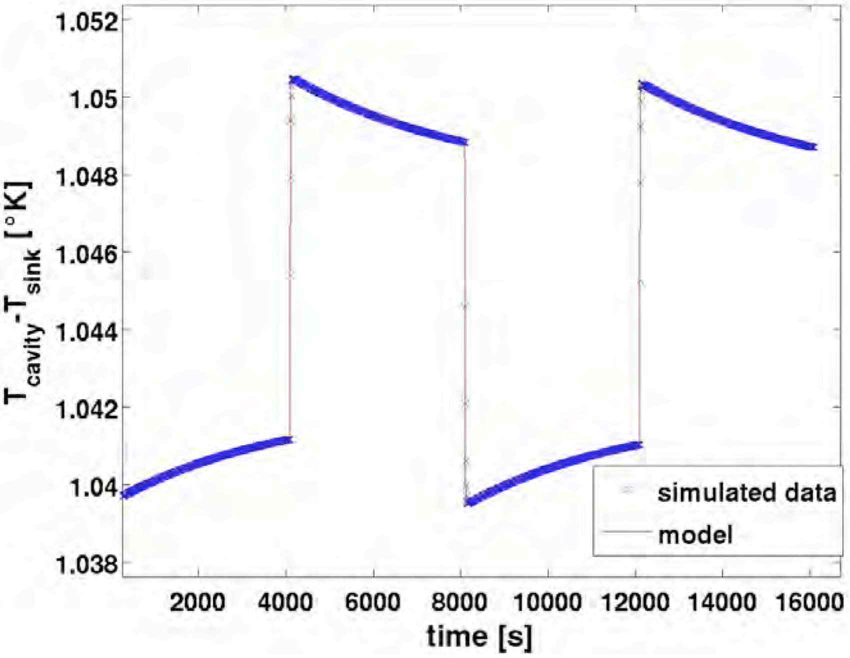

Figure 2.6: *Simulated temperature rise of a PMO6 cavity for an exponential temperature forcing of the heat sink temperature. Our model of the temperature rise reproduces the simulated data.*

We start with the one dimensional heat equation where $x = 0$ denotes the position of the heat sink and and $x = L$ is the position where the cavity heater dissipates the power P per surface area A. And we define $a = \sigma/(c \cdot \rho)$ where σ is the thermal conductivity, c is the heat capacity and ρ is the density of the material. To account for the temperature variation on the heat sink, we apply a time dependent function $f(t)$ at the boundary. With these informations we are able to formulate our mixed boundary condition problem with a known initial value:

$$\begin{aligned} &\text{PDE} \qquad \partial_t T(x,t) = a \cdot \partial_{xx} T(x,t) \\ &\text{BC} \qquad \begin{cases} T(0,t) = f(t) & t > 0 \\ \partial_x T = \frac{P}{\sigma \cdot A} & x = L \end{cases} \\ &\text{IC} \qquad T(x,0) = T_0 + \frac{P \cdot x}{\sigma \cdot A} \end{aligned}$$

We can use the definition $s(t) = \partial_t f(t)$ and the transformation

$$T(x,t) = v(x,t) + f(t) + \frac{P \cdot x}{\sigma \cdot A}.$$

to homogenize the boundary conditions.

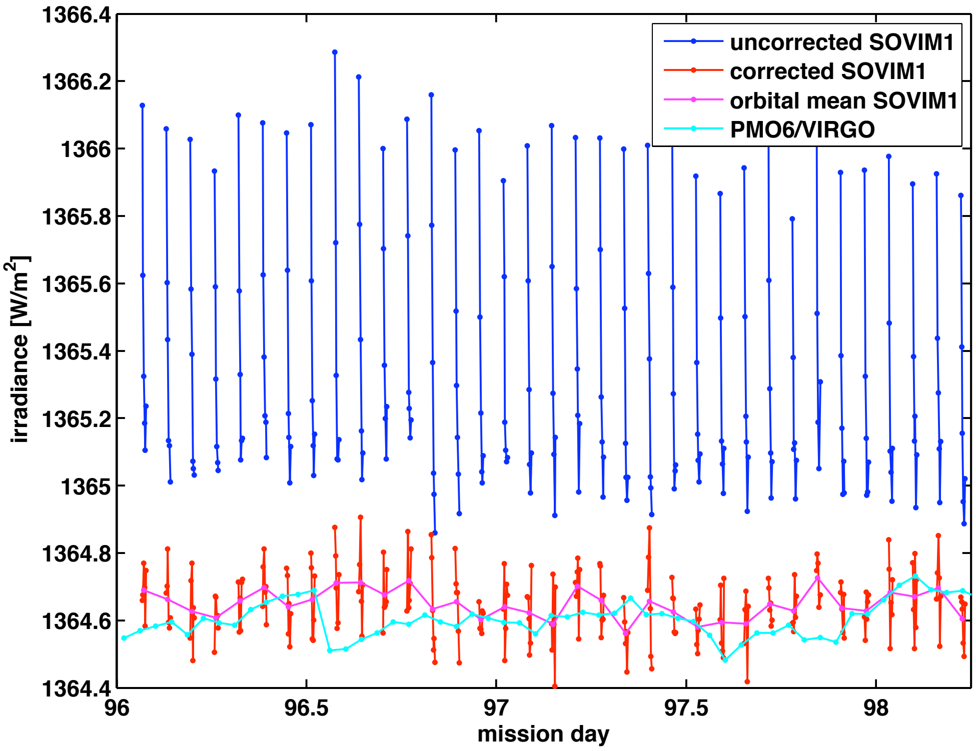

Figure 2.7: *We were able to correct the SOVIM/ISS data with our model. The orbital mean values of SOVIM-1 and PMO6V which is part of the VIRGO/SOHO experiment, agree reasonably well.*

$$
\begin{array}{ll}
\text{PDE} & \partial_t v(x,t) - a \cdot \partial_{xx} v(x,t) = -s(t) \\
\text{BC} & \begin{cases} v(0,t) = 0 & t > 0 \\ \partial_x v = 0 & x = L \end{cases} \\
\text{IC} & v(x,0) = 0
\end{array}
$$

To solve the problem we use the definition $\lambda_n = \frac{n\pi}{2L}$, the ansatz

$$v(x,t) = \sum_{n=1}^{\infty} v_n(t) \cdot \sin(\lambda_n x) \tag{2.7}$$

and

$$s(t) = \sum_{n=1}^{\infty} s_n(t) \cdot \sin(\lambda_n x) \tag{2.8}$$

where

$$s_n(t) = \frac{1}{L}\int_0^{2L} s(t)\cdot\sin\left(\lambda_n x\right)dx.$$

We substitute Equation 2.7 and Equation 2.8 into our partial differential equation and find

$$\sum_{n=1}^{\infty}\left(\partial_t v_n(t) + a\cdot\lambda_n^2\cdot v_n(t) + s_n(t)\right)\sin\left(\lambda_n x\right) = 0.$$

Now we use orthogonality. We multiply both sides of Equation 2.3.1 by $\sin\left(\lambda_j x\right)$ and integrate from 0 to $2L$. Then we obtain an ordinary initial value problem.

$$\begin{array}{rl} \text{ODE} & \partial_t v_n(t) + a\cdot\lambda_n^2\cdot v_n(t) = -s_n(t) \\ \text{IC} & v_n(0) = 0 \end{array}$$

We multiply this new differential equation by $e^{a\lambda_n^2 t}$, integrate from 0 to t and multiply again both sides by $e^{-a\lambda_n^2 t}$ and get

$$v_n(t) = v_n(0) - \int_0^t s_n(s)\cdot e^{a\lambda_n^2(s-t)}ds.$$

The first term on the right side is 0 because of the initial condition and we have solved our complex problem

$$T(x,t) = v(x,t) + f(t) + \frac{P\cdot x}{\sigma\cdot A}$$

where

$$v(x,t) = \sum_{n=1}^{\infty}\left(-\int_0^t s_n(s)\cdot e^{a\lambda_n^2(s-t)}ds\right)\cdot\sin\left(\lambda_n x\right)$$

and

$$s_n(t) = \frac{1}{L}\int_0^{2L} s(t)\cdot\sin\left(\lambda_n x\right)dx.$$

We could try to numerically solve the problem for any measured heat sink temperature variation $f(t)$. Instead, we investigate the special case of an exponential heat sink temperature variation $f(t) = T_0 + \Delta S - \Delta S\cdot e^{-\tau\cdot t}$. This behavior best represents the situation of an externally heated respectively cooled heat sink. Further, we are interested in the cavity temperature and thus we set $x = L$. For this special case we obtain

$$s_n(t) = \frac{4}{n\pi} \cdot \Delta S \cdot \tau \cdot e^{-\tau \cdot t},$$

$$v(x,t) = \sum_{n=1}^{\infty} \frac{4 \cdot \Delta S \cdot \tau}{n\pi(a\lambda_n^2 - \tau)} \left(e^{-a\lambda_n^2 t} - e^{-\tau t}\right) \cdot \sin\left(\lambda_n x\right)$$

and the final solution

$$T(L,t) = \left(\sum_{n=1}^{\infty} \frac{4 \cdot \Delta S \cdot \tau}{n\pi(a\lambda_n^2 - \tau)} \left(e^{-a\lambda_n^2 t} - e^{-\tau t}\right) \cdot \sin\left(\lambda_n L\right)\right) + T_0 + \Delta S - \Delta S \cdot e^{-\tau \cdot t} + \frac{P \cdot L}{\sigma \cdot A}.$$

In the lowest order $n = 1$, we have a sum of two exponentials with 7 independent parameters describing the temperature rise of one cavity. Using the result in our heater power model, yielded no proper fit because of the large number of free parameters. However, if we combine the constants and cancel small terms, the analytical solution resembles our model (Equation 2.4).

$$\Delta T(L,t) = \frac{P \cdot L}{\sigma \cdot A} + c_1 \tau \Delta S \cdot e^{-\tau t} + \frac{c_2}{a - c_3},$$

where the first term describes the temperature rise of the cavity for a constant heat sink temperature. The second term is the derivative of the heat sink temperature and the last term accounts for the temperature dependent material properties.

2.4 Non-Equivalence

The non-equivalence is the most complex correction factor characterizing a PMO6-type radiometer. This is because the effect is a superposition of three phenomena. 1) The heating of the precision aperture during the open state of the instrument coupling to the cavity by radiation or by conduction through the air. We discuss this effect in more detail in section 2.7. 2) Electrical and optical power is not dissipated at the same location within the cavity. The solar radiation is absorbed by the black paint and the heat flows through the paint and the heater foil into the silver cone of the cavity. The electrically generated heat however, has to pass only through the heater foil. Thus the illuminated black paint gets hotter and looses more heat to the air than the same part of the cavity cone during the shaded phase. 3) The temperature distribution inside the cavity is different in the open respectively closed state of the radiometer. During the closed reference measurement all the power is dissipated by the heater foil on the cone. Whereas in the open phase, about 7 % of the radiation is not absorbed on the cone but is reflected onto the cylindrical cavity wall. This results in a non-equal heat loss by conduction through the air for the two phases.

To obtain the correction factor for the non-equivalence, we alternately determine the sensitivity of the instrument in vacuum and at ambient pressure and calculate the air-to-vacuum ratio. We assume that all the non-equivalence phenomena are negligible in vacuum. The radiative

	NA factor	relative uncertainty	aperture material
PREMOS-1	1.008374	0.000303	carbide
PREMOS-2	1.001585	0.000281	carbide
PREMOS-3	1.006879	0.000446	steel

Table 2.2: *Non-equivalence factors and standard uncertainty (k=1) for the three PREMOS radiometers. These are the weighted mean values from the data measured on the 26th and the 28th of April behind a flat window.*

exchange of the cavity with the aperture being relevant in vacuum, is the same at ambient pressure and cancels out in the vacuum to air ratio determination. Hence, we cannot determine the radiative component of the aperture heating effect with this experiment.

We placed the radiometer under investigation in a vacuum chamber which we evacuated respectively filled with dry nitrogen in an hourly cadence. The integral transmittance of the entrance window to the chamber may vary due to the changing solar spectrum. Therefore, we determined the sensitivity of the PREMOS radiometers relative to an instrument at ambient pressure measuring the solar irradiance through an identical window.

The results for the three PREMOS radiometers revealed a discrepancy. Although all instruments are of identical construction, they showed different non-equivalence factors lying either below or above typical values measured with former PMO6-type radiometers. But as we studied the records of past experiments, we found that there have always been some problems to determine this correction factor.

Table 2.2 lists the non-equivalence factors measured for the three PREMOS radiometers. The PREMOS-1 and PREMOS-3 values were of the same order but considerably higher than a factor 1.004 measured with other radiometers. PREMOS-2 yielded a small non-equivalence factor of 1.001585. To test the repeatability of our measurements, we assigned PREMOS-2 another place in the vacuum chamber behind a different window. With this setup, the non-equivalence factor changed by 300 parts per million to 1.001893 raising our concerns about the pointing sensitivity of such an experiment. At that moment we had to integrate the PREMOS-1 and PREMOS-2 flight instruments into the PICARD satellite. And we could only use the flight spare radiometer PREMOS-3 to further investigate the pointing sensitivity.

In December 2008 we reinstalled PREMOS-3 in the vacuum chamber on the sun tracking platform. This time we determined a non-equivalence factor of 1.010630. After a slight pointing change, the correction factor (1.004565) more than halved. Next, we shortened the distance from the instrument to the window and the correction factor doubled again (1.009364). And a repointing of the instrument resulted in a smaller correction (1.005492). We interpret this pointing sensitivity as the result of inter-reflections between the precision aperture and the window being different under evacuated respectively ambient pressure conditions.

In April 2009 we replaced the original stainless steel precision aperture by a steel aperture coated with a diffuse black paint (MAP) on the frontside. The non-equivalence determination yielded a factor of 1.004434 ± 0.000387 (k=1) which remained stable despite repeated pointing

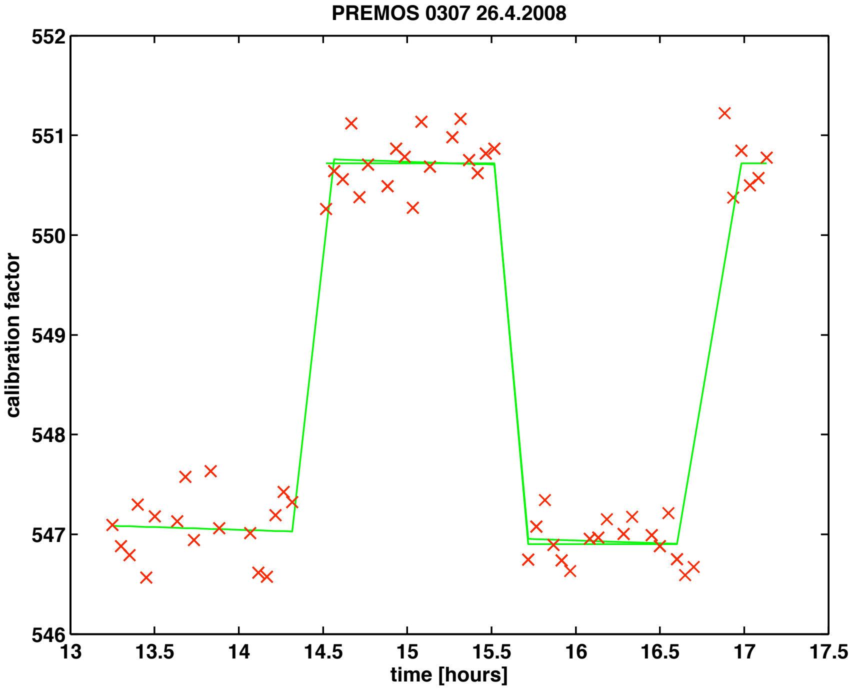

Figure 2.8: *To obtain the non-equivalnce correction factor we determine the vacuum to air calibration factor ratio relative to a reference instrument behind an identical window.*

variations. This fact supports our assumption that the pointing sensitivity is due to reflections at the precision aperture.

Figure 2.9 illustrates our explanation for the pointing sensitivity of this experiment. With the current radiometer design only one third of the radiation entering the instrument falls into the cavity. The rest hits the precision aperture where about 65 % (Karlsson and Ribbing, 1982) are reflected. The flat entrance window then partially reflects the radiation back towards the cavity. Our experiment only accounts for the relative changes between the operation in vacuum and at ambient pressure. There exist three variables influencing the measurements differently. 1) During the vacuum phase the deformed entrance window changes the back reflected radiation and also attenuates the light directly entering the cavity. 2) The inclination of the window relative to the plane of the precision aperture defines the amount of light being reflected back into the cavity. 3) A non-alignment of the center of the window relative to the precision aperture may enhance respectively attenuate the influence of the deformed window.

To verify our assumption, we wrote a MATLB simulation where we could vary the inclination α, the concentricity and the material properties of the window. The distance between the precision aperture and the window remained fixed to d=120 mm. Our calculations revealed differences of up to $\pm$ 0.3% between the vacuum and the ambient pressure state for small inclinations α. For $\alpha > 1.6°$, the back reflections do not fall into the cavity. Therefore we made a 2 degrees inclined window mounting which prevents a pointing or positioning sensitivity. In June 2009 we replaced the black stainless steel aperture of PREMOS-3 by one made of cemented carbide and repeated the experiment. Table 2.3 lists the non-equivalence factors determined with the

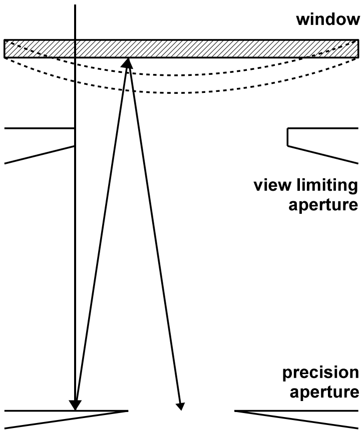

Figure 2.9: *The classical, flat window alignment does influence the vacuum to air comparisons. Two third of the solar radiation entering the radiometer are reflected or absorbed by the precision aperture and might be partially back reflected into the cavity by the window. These inter reflections should not influence the relative measurements as long as the window stays aligned during the vacuum respectively ambient pressure runs. However, the atmospheric pressure on the window causes a deformation when the chamber is evacuated. Hence, we measure different back reflections in vacuum and at ambient pressure. Inclining the window by 2 degrees solves this problem since there are no direct reflections from the window entering the cavity.*

	NA factor	relative uncertainty	aperture material
inclined window			
PREMOS-1	1.005710	0.000255	carbide
PREMOS-3	1.006709	0.000294	carbide
flat window			
PREMOS-2	1.001893	-	carbide

Table 2.3: *For PREMOS-1 and PREMOS-3 we have non-equivalence factors determined behind an inclined window (standard uncertainty k=1). But with PREMOS-2 we made only vacuum to air comparisons behind a flat window. From the pointing sensitivity tests with PREMOS-3 we know that behind a flat window, the correction might vary by up to 100 %. So the PREMOS-2 result is rather uncertain and we state no standard uncertainty.*

inclined window. For PREMOS-2 we state the mean correction factor obtained behind a flat entrance window which is our best guess for this radiometer at the moment.

2.5 Diffraction Correction

Solar irradiance illuminating a PMO6-type radiometer first passes the view limiting aperture. About one third of the light entering the instrument goes through the precision aperture and is absorbed in the cavity. We do not consider the baffles in the instrument and thus have a system of three apertures (view limiting, precision, cavity) where the solar radiation is diffracted twice. The Fresnel diffraction theory for this problem is discussed in Born and Wolf (1999, chap. 8). Lommel (1885) was the first to find a solution to the Fresnel diffraction problem on circular apertures. Brusa and Fröhlich (1986) use Lommel's solution to calculate the diffraction effect for PMO6-type radiometers. And Shirley (1998, 2004a,b) wrote numerous publications on the numerical evaluation of this problem. We use Shirley's program to determine the diffraction for the PREMOS radiometers for a monochromatic plane wave. First, we calculate the diffraction at the view limiting aperture, i.e. the system view limiting - precision aperture. Then we determine the diffraction at the precision aperture, i.e. the system precision - cavity aperture. And finally we combine the two results to the total diffraction correction of the radiometer. We repeated the calculations for distinct wavelengths and interpolated the continuos function to the entire solar wavelength range. Weighting the obtained function with the solar spectrum yields a diffraction correction for the sun.

In chapter 4 we use the diffraction calculated here for a plane wave to correct the data obtained at the TRF. This facility uses a narrow laser beam scanned over the desired area and we do not yet know how to properly calculate the diffraction for such a beam moving across the aperture. Further, the beam generated in the laboratory is collimated whereas the sun light is divergent by up to a quarter of a degree.

	Extra terrestrial precision	Extra terrestrial view limiting	Extra terrestrial combined	FA 45 precision	FA 45 view limiting	FA 45 combined	532 nm precision	532 nm view limiting	532 nm combined
PREMOS	1.000124	0.998595	0.998720	1.000124	0.998604	0.998727	1.000066	0.999205	0.999271
VIRGO	1.000182	0.998718	0.998900	1.000181	0.998725	0.998906	1.000120	0.999272	0.999392

Table 2.4: *Diffraction Correction: To obtain the appropriate correction factors, we have to consider the combined diffraction effects from the view limiting and the precision aperture. The extra terrestrial diffraction correction factor is calculated with the the Kuruzc 1997 solar spectrum. We used MODTRAN 5, a fall Davos atmospheric model and a solar elevation of 45 degrees to calculate the FA 45 solar Spectrum and the corresponding correction factors. The standard uncertainty (k=1) for all values is 0.000034.*

2.6 Stray Light

Brusa and Fröhlich (1986) used a laser beam and a silicon detector instead of the cavity to determine the amount of stray light measured with a PMO6-type radiometer. They illuminated the precision aperture with a steady 40 mW laser beam on a narrow spot and measured a 250 ppm signal as determined in the 1980's. This result transforms into a stray light correction factor of 0.999750 ± 0.000100. They repeated the stray light experiments on distinct spots on the precision aperture and at different incident angles to estimate the uncertainty.

However, we think that the measured signal strongly depends on the scattering geometry, demanding a proper weighting of the stray light when integrating over the entire precision aperture. We do not know what weighting Brusa and Fröhlich used and hence the stray light might be underestimated and a TSI workshop (Butler et al., 2008) regards stray light as the most probable explanation for the observed differences in TSI measurements.

We performed new experiments discussed in chapter 4 to quantify the amount of stray light and found factors which are considerably larger than the original PMO6 corrections.

2.7 Aperture Heating

The aperture temperature is of importance because it is different in the open respectively closed state of the instrument. Closed shutter: The precision aperture is at ambient temperature. Open shutter: Two third of the radiation entering a PMO6-type radiometer illuminate the precision aperture and cause a temperature rise. As a result, the cavity collects more thermal radiation from the aperture and the radiometer reads too high. In vacuum, the absorption properties of the aperture material and the solid angle under which the aperture is seen by the cavity determine the magnitude of the effect.

At ambient pressure, the cavity also couples to the aperture by conduction through the air. The heat flux is proportional to the temperature difference and hence the cavity looses more energy during the closed phase. The servo system reacts by increasing the closed heater power to compensate the losses. As a result, the electrical heater power difference between the open and closed phase is too large and the radiometer reads too high.

The amount of radiation absorbed by the precision aperture is not well known. It depends on the material and the surface finish of the aperture. A polished stainless steel surface has a solar absorptivity of about 35 % (Karlsson and Ribbing, 1982). This value has a large uncertainty and may increase due to a degradation of the surface when exposed to hard UV radiation in space. Two SOVA PMO6-type radiometer precision apertures were the only ones ever returning from space. Their initially polished surface degraded to a dull gray finish during the nine months of operation (Figure 2.11). This effect was used by Fröhlich (2006) to explain the observed sensitivity increase of the VIRGO radiometers in space. Suter (2007) used an electrical aperture heater to experimentally determine the aperture heating influence to PMO6-type radiometer measurements. He was able to show an aperture heating effect (Table 2.5) which is however smaller than the 600 ppm early increase observed with VIRGO.

We used the PREMOS-3 radiometer to repeat the electrical aperture heating experiment. The results are reported in Table 2.5. The designated PREMOS flight precision apertures are made of cemented carbide (85 % tungsten carbide; 15 % cobalt). The thermal conductivity of this material is three to four times higher than the one of stainless steel. We expected the higher conductivity to reduce the thermal radiation effect because of the smaller temperature rise of the aperture. However, we have not found absorptivity and emissivity values for cemented carbide in the literature and hence the theoretical considerations in subsection 4.9.5 for the flight apertures have a large uncertainty.

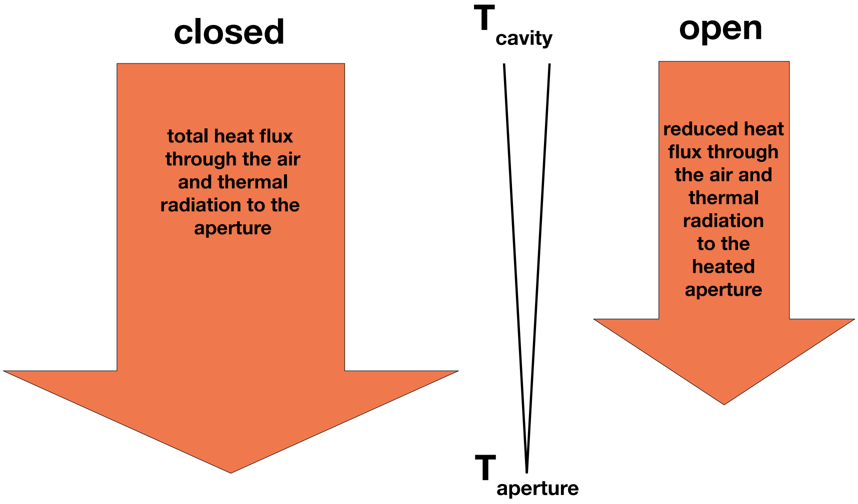

Figure 2.10: *This flow diagram illustrates the heat flux from the cavity through the air to the precision aperture. When the radiometer opens its shutter the precision aperture is heated to higher temperatures than during the closed phase. Thus the heat flux from the cavity to the aperture is smaller when the instrument is open. The control electronics compensates the higher losses in the closed phase and hence the closed heater power reads too high. Therefore, the closed/open heater power difference is overestimated and the determined solar irradiance is too high.*

For better comparability to the former experiment and to protect the flight apertures, we performed the aperture heating experiment using a stainless steel aperture (Figure 2.11). We electrically dissipated the heat which corresponds to the power of the completely absorbed solar radiation and measured a signal of 0.07 % in vacuum and 0.4 % at ambient pressure. Assuming a 33 % absorptance of steel and a good thermal contact between heater and aperture, we find an aperture heating effect of 233 in vacuum and 1333 ppm in air.

In Table 2.5 we compare our measurements with those of Suter (2007). Our higher values can be explained by: 1) The PREMOS precision apertures are closer to the cavity than those of the Rocket-11 radiometer used by Suter (2007). Hence, the cavity collects more thermal radiation from the aperture explaining the larger effect in vacuum. In air, the heat flux is inversely proportional to the distance. Hence the larger effect in air is explained by the shorter aperture/cavity distance of the PREMOS instruments. The VIRGO radiometers have the same geometry as PREMOS and we expect a similar aperture heating effect for those instruments. 2) Possibly, a better thermal contact of our heater to the aperture results in higher aperture temperatures and hence a larger heating effect.

We were able to determine correction factors for the aperture heating effect of stainless steel precision apertures. The correction in vacuum is new to the PMO6-type radiometer characterization and can be applied to the space experiments having steel apertures. The correction at ambient pressure is already included in the non-equivalence correction factor (section 2.4) and must not be applied separately. In subsection 4.9.5 we present estimations for the cemented carbide aperture heating effect.

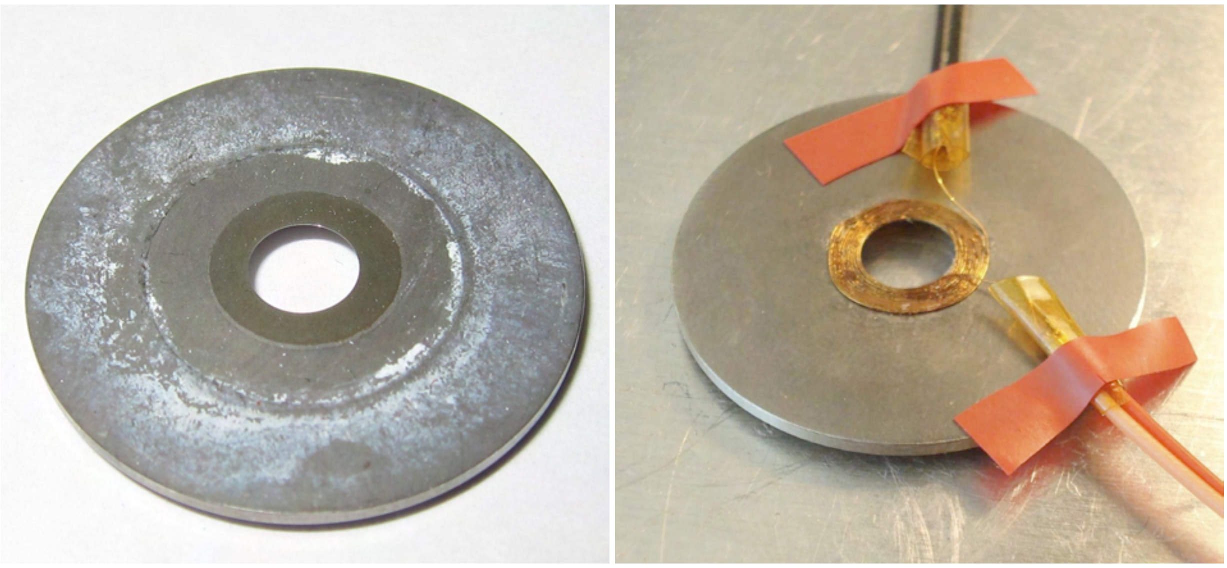

Figure 2.11: *This image shows the degraded precision aperture of the 113R SOVA radiometer (left). We can identify the innermost dark circle where solar radiation illuminated the stainless steel aperture. Right, a heater is attached to the illuminated part of the precision aperture to simulate the heating.*

Since solar absorptivity α_s and hemispherical emissivity $\epsilon(T)$ values for steel and carbide cannot be found in the literature, we plan to perform appropriate experiments. Gordon (1960) has proposed a calorimetric technique to directly determine $\epsilon(T)$ and the ratio $\alpha_s/\epsilon(T)$. The heliostat designed and being built at the PMOD/WRC will provide the perfect source for these measurements.

	ambient pressure	relative uncertainty	vacuum	relative uncertainty	aperture material
PMO6-11 (Suter 2007)	0.99984	0.000036	0.99992	0.000024	steel
PREMOS-3	0.99867	0.000300	0.99977	0.000040	steel

Table 2.5: *Measured correction factors for the steel aperture heating effect at ambient pressure and in vacuum and their standard uncertainties (k=1). The factors are smaller than one because the effect causes the instruments to read too high.*

2.8 Finite Element Model of a PMO6-type Radiometer

We are not able to fully separate the different components contributing to the non-equivalence and the aperture heating by experimentally investigating the different effects. Therefore, we developed a finite element model of a PMO6 detector with ANSYS. The model features all parts of an original PMO6 detector, an implemented PI controller to regulate the heater power inside the cavity, radiative energy exchange between the parts and the ability to include heat losses by conduction through the air. Our model is able to reproduce the non-equivalence and aperture heating measurements performed with the PREMOS radiometers.

The model allowed us to closer investigate the aperture heating effect (section 2.7). By changing the absorptance respectively emissivity properties of the materials we could determine whether a darkening of the precision aperture can explain the observed 600 ppm sensitivity increase of the VIRGO radiometers as proposed by Fröhlich (2006). We started by assuming an absorptance of 40 % (Karlsson and Ribbing, 1982) for the frontside of the steel precision aperture. The value for the emissivity of the backside is hard to estimate. Depending on the surface finish and the grade of oxidation we found values between 5 and 60 % in the literature (Rohsenow et al., 1998). We decided to set the emissivity equal to the absorptivity and found an aperture heating effect of 1.000181. Increasing the absorptance to 80 % which simulates the darkening of the aperture, yielded an increase of the aperture heating effect to 1.000409. The difference of 228 ppm between the two runs shows that the darkening of the precision aperture can only partially account for the early sensitivity increase of the PMO6 radiometers in space.

Repeating the simulation for the carbide apertures of the PREMOS instruments with an assumed absorptance and emissivity of 40 %, we determined an aperture heating effect of 1.000046. This correction is three to four times lower and has been expected as the thermal conductivity of cemented carbide is higher by this amount compared to stainless steel. Our considerations also suggest the early sensitivity increase of the PREMOS radiometers in space to be 150 ppm lower than for VIRGO.

Our experiments and simulations have shown that the early sensitivity increase can only partially be explained by a darkening of the precision aperture. Our hypothesis is that the exposure to hard UV radiation in space may cause: 1) A bleaching of the baffle coating which results in higher stray light. 2) A burning-in of the cavity paint could slightly enhance the cavity absorptance. Exposure and stray light experiments are needed to investigate this issue further.

The finite element model is an excellent tool to investigate particular effects characterizing a PMO6-type radiometer. We are going to expand the finite element model to simulate an entire radiometer. This upgrade allows the investigation of the varying heat sink temperature or the temperature dependent non-equivalence factor influencing the measurements.

2.9 Summary of the Absolute Characterization

Table 2.6 summarizes the correction factors and their standard uncertainties (k=1) needed to fully characterize the PREMOS radiometers. We distinguish between the different light sources used to illuminate the radiometers in the following sections. The non-equivalence factor is not included in the table as most experiments are performed in vacuum where the non-equivalence is assumed to vanish. Only the WRR to SI comparison (section 5.2) needs the vacuum-to-air correction stated in Table 2.3.

	PREMOS-1 (power @532 nm)	relative uncertainty (k=1)	PREMOS-1 (power @647 nm)	relative uncertainty (k=1)	PREMOS-1 (7.3 mm beam @532 nm)	relative uncertainty (k=1)	PREMOS-1 (11 mm beam @532 nm)	relative uncertainty (k=1)	PREMOS-1 terrestrial TSI	relative uncertainty (k=1)	PREMOS-1 space TSI	relative uncertainty (k=1)
lead heating	1.000200	0.000034	1.000200	0.000034	1.000200	0.000034	1.000200	0.000034	1.000200	0.000034	1.000200	0.000034
reflectivity	1.000300	0.000067	1.000200	0.000067	1.000300	0.000067	1.000300	0.000067	1.000300	0.000067	1.000300	0.000067
stray light	0.999750	0.000100	0.999750	0.000100	0.999750	0.000100	0.999750	0.000100	0.999750	0.000100	0.999750	0.000100
diffraction	1	0	1	0	1.000066	0.000034	0.999271	0.000034	0.998720	0.000034	0.998720	0.000035
aperture heating	1	0	1	0	0.999900	0.000030	0.999900	0.000030	0.999900	0.000030	0.999900	0.000030
aperture	1	0	1	0	50973.08	0.000025	50973.08	0.000025	50973.08	0.000025	50973.08	0.000025
radiometric constant	**1.000250**	**0.000125**	**1.000150**	**0.000125**	**50984.09**	**0.000135**	**50943.56**	**0.000135**	**50915.82**	**0.000132**	**50915.47**	**0.000135**

	PREMOS-2 (power @532 nm)	relative uncertainty (k=1)	PREMOS-2 (power @647 nm)	relative uncertainty (k=1)	PREMOS-2 (7.3 mm beam @532 nm)	relative uncertainty (k=1)	PREMOS-2 (11 mm beam @532 nm)	relative uncertainty (k=1)	PREMOS-2 terrestrial TSI	relative uncertainty (k=1)	PREMOS-2 space TSI	relative uncertainty (k=1)
lead heating	1.000200	0.000034	1.000200	0.000034	1.000200	0.000034	1.000200	0.000034	1.000200	0.000034	1.000200	0.000034
reflectivity	1.000300	0.000067	1.000200	0.000067	1.000300	0.000067	1.000300	0.000067	1.000300	0.000067	1.000300	0.000067
stray light	0.999750	0.000100	0.999750	0.000100	0.999750	0.000100	0.999750	0.000100	0.999750	0.000100	0.999750	0.000100
diffraction	1	0	1	0	1.000066	0.000034	0.999271	0.000034	0.998720	0.000034	0.998720	0.000035
aperture heating	1	0	1	0	0.999900	0.000030	0.999900	0.000030	0.999900	0.000030	0.999900	0.000030
aperture	1	0	1	0	50956.45	0.000025	50956.45	0.000025	50956.45	0.000025	50956.45	0.000025
radiometric constant	**1.000250**	**0.000125**	**1.000150**	**0.000125**	**50967.45**	**0.000135**	**50926.94**	**0.000135**	**50899.21**	**0.000135**	**50898.85**	**0.000135**
software implemented[a]											*50757.20*	*0.001506*

	PREMOS-3 (power @532 nm)	relative uncertainty (k=1)	PREMOS-3 (power @647 nm)	relative uncertainty (k=1)	PREMOS-3 (7.3 mm beam @532 nm)	relative uncertainty (k=1)	PREMOS-3 (11 mm beam @532 nm)	relative uncertainty (k=1)	PREMOS-3 terrestrial TSI	relative uncertainty (k=1)	PREMOS-3 space TSI	relative uncertainty (k=1)
lead heating	1.000200	0.000034	1.000200	0.000034	1.000200	0.000034	1.000200	0.000034	1.000200	0.000034	1.000200	0.000034
reflectivity	1.000300	0.000067	1.000200	0.000067	1.000300	0.000067	1.000300	0.000067	1.000300	0.000067	1.000300	0.000067
stray light	0.999750	0.000100	0.999750	0.000100	0.999750	0.000100	0.999750	0.000100	0.999750	0.000100	0.999750	0.000100
diffraction	1	0	1	0	1.000066	0.000034	0.999271	0.000034	0.998720	0.000034	0.998720	0.000035
aperture heating	1	0	1	0	0.999900	0.000030	0.999900	0.000030	0.999900	0.000030	0.999900	0.000030
aperture	1	0	1	0	50924.79	0.000076	50924.79	0.000076	50924.79	0.000076	50924.79	0.000076
radiometric constant	**1.000250**	**0.000125**	**1.000150**	**0.000125**	**50935.79**	**0.000153**	**50895.29**	**0.000153**	**50867.59**	**0.000153**	**50867.23**	**0.000153**
software implemented[a]											*50621.13*	*0.001508*

	VIRGO-2 (power @532 nm)	relative uncertainty (k=1)	VIRGO-2 (power @647 nm)	relative uncertainty (k=1)	VIRGO-2 (7.3 mm beam @532 nm)	relative uncertainty (k=1)	VIRGO-2 (11 mm beam @532 nm)	relative uncertainty (k=1)	VIRGO-2 terrestrial TSI	relative uncertainty (k=1)	VIRGO-2 space TSI	relative uncertainty (k=1)
lead heating	1.000200	0.000034	1.000200	0.000034	1.000200	0.000034	1.000200	0.000034	1.000200	0.000034	1.000200	0.000034
reflectivity	1.000300	0.000067	1.000200	0.000067	1.000300	0.000067	1.000300	0.000067	1.000300	0.000067	1.000300	0.000067
stray light	0.999750	0.000100	0.999750	0.000100	0.999750	0.000100	0.999750	0.000100	0.999750	0.000100	0.999750	0.000100
diffraction	1	0	1	0	1.000120	0.000034	0.999392	0.000034	0.998900	0.000034	0.998900	0.000035
aperture heating	1	0	1	0	0.999770	0.000040	0.999770	0.000040	0.999770	0.000040	0.999770	0.000040
aperture	1	0	1	0	50882.82	0.000204	50882.82	0.000204	50882.82	0.000204	50882.82	0.000204
radiometric constant	**1.000250**	**0.000125**	**1.000150**	**0.000125**	**50889.94.64**	**0.000245**	**50852.89**	**0.000245**	**50828.16**	**0.000245**	**50827.86**	**0.000245**

Table 2.6: *Multiplicative correction factors PREMOS-1, PREMOS-2, PREMOS-3 and VIRGO-2 and their standard uncertainties (k=1) needed to convert the measured power in Watt to the corrected power in Watts. The aperture factor (1 m^2/aperture area) transforms the measured power in Watt to the incident irradiance in units of W/m^2. All corrections are multiplicative factors and slightly depend on the light source.*

---

[a] Radiometric constants as they are implemented in the PICARD/BUSOC software to convert PREMOS counts to niveau 2 TSI products (N2A_TSI).

Chapter 3

SI Calibration of the PREMOS Absolute Solar Radiometers at the NPL in London

In the past, all PMO6-type radiometers operating on spacecrafts have been calibrated against the World Radiometric Reference. For the first time in the era of TSI measurements, the PREMOS instruments have additionally been compared with the SI radiant power scale. In April 2008 we compared the three PREMOS instruments with the primary standard at the National Physical Laboratory (NPL) in London. The experimental set up (Figure 3.1) was similar to the three previous comparisons of the WRR and the SI radiant power scale (Romero et al., 1991, 1995; Finsterle et al., 2008). However, we improved the comparison by placing the PREMOS radiometers in a vacuum chamber to avoid the non-equivalence correction (section 2.4) which used to dominate the uncertainty of the result.

3.1 Characterizing the NPL Comparison Set Up

The cryogenic radiometer acting as primary standard accepts up to 1 mW of optical power. Because the solar irradiance dissipates 20 mW in the PREMOS cavities with a 5 mm diameter aperture in place, we had to use trap detectors as transfer standards (Fox, 1991). The traps are thought to respond linearly up to a threshold of 2 mW Romero et al. (1991).

The principle of the comparison is to calibrate the beam splitter ratio using a monitor and a reference trap at a power level of 0.5 mW in the transmitted beam. Then we replace the reference trap by the radiometer under test and increase the power to a solar value of 20 mW. The expected reference power in the radiometer is calculated by multiplying the beam splitter ratio with the power measured by the monitor trap. Thereby we rely on the linear response of the monitor trap and hence the beam splitter ratio being constant at all power levels. Out of the past three WRR to SI comparisons, only Romero et al. (1991) report on experiments investigating the linearity of the beam splitter ratio. Between the second and the third comparison a new generation of NPL traps has been introduced and we decided to retest the linearity of the trap detectors.

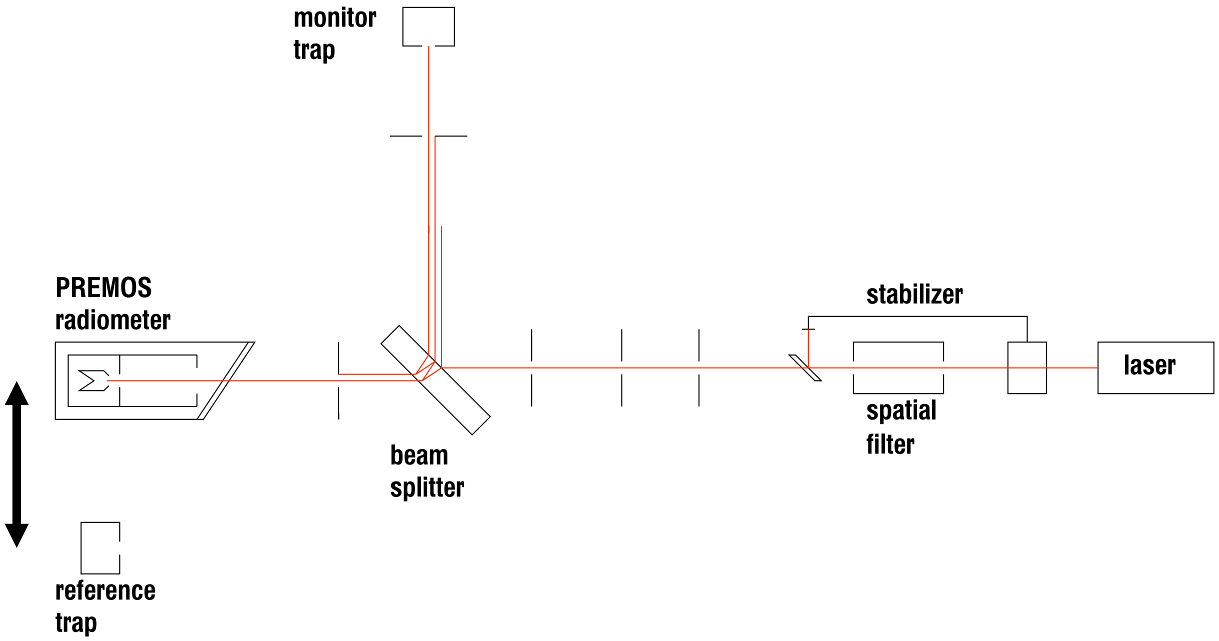

Figure 3.1: *The PREMOS to SI calibration set up at the NPL. An intensity stabilized laser beam at a wavelength of 647 nm with a diameter of 3.8 mm is used as source. Along the beam path we placed iris diaphragms to minimize the stray light. A wedged beam splitter deflects a fraction of the beam to the monitor trap detector observing the beam stability. The remaining beam passes on to either the reference trap detector or the radiometer under test. Compared to former SI calibrations at NPL, we operated the radiometers behind a brewster window in a vacuum chamber.*

As entrance window to the PREMOS vacuum chamber we used the brewster window from the NPL's primary cryogenic radiometer. The alignment of the window was optimized before each measurement run with the PREMOS radiometers and we conducted repeated tests to determine the window transmittance and the introduced stray light.

The accurate radiometer positioning relative to the laser beam was guaranteed by two techniques: 1) The back reflection off the precision aperture is used to align the radiometer perpendicular to the beam. 2) We measured the radiometer signal whilst scanning the laser beam with a micrometer stage across the precision aperture along two perpendicular axis. Analyzing the scanned profile gave us the precise and reproducible position of the aperture edge and hence the aperture center within 5 µm.

3.1.1 Non-Linearity of the Traps

To investigate the linearity of the trap response, we determined the beam splitter ratio at different power levels of the laser beam. The trap under test was placed as reference trap in the transmitted beam. The highest power level we used for this experiment was 2 mW and the lowest

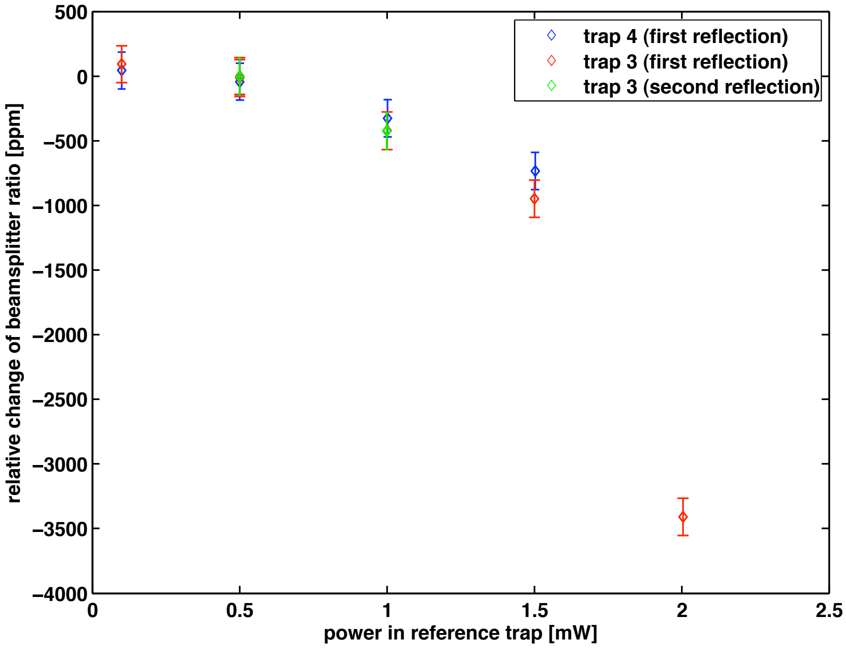

Figure 3.2: *We determined the apparent beam splitter ratio at different power levels in the transmitted beam. We assume that there is no polarization effect. We found a non linear behavior of the beamsplitter ratio starting at 0.5 mW in the transmitted beam which we attribute to the saturation of the used Hamamatsu S1337-1010 photo diodes.*

beam splitter ratio was 10:1. Hence the maximum power in the monitor trap was 0.2 mW where we assume a linear behavior of the detector.

The PREMOS calibration were performed with the NPL trap number 3 and 4 and we checked their linearity using NPL trap number 5 as monitor. In the beginning the primary reflection off the beam splitter was used to illuminate the monitor trap. We assumed the beam splitter ratio to be constant at all power levels. Figure 3.2 shows the outcome of the experiment where the beam splitter ratio apparently decreased with increasing power for both traps under test. Considering the relative changes, both detectors respond identically to the increasing powers. At 0.5 mW in the transmitted beam, we find a relative deviation of 100 ppm compared to the lowest power level. At 1 and 1.5 mW, the difference increases to 530 respectively 940 ppm. And at 2 mW, we measured a deviation of 3500 ppm. A changing polarization of the beam might explain this non linear behavior. Repeating the experiment on different days and using the second reflection off the beam splitter yielded a consistent result. But a polarization effect is expected to change as more boundary layers are involved in the reflection. Hence we conclude that the trap detectors must have a non linear response.

The NPL traps use three parallel interconnected Hamamatsu S1337-1010 silicone photodiodes (Fox, 1991) to measure the optical power. Boivin (1993) showed that the S1337 photodiodes are highly linear for low photocurrents up to 1 mA before starting to saturate rapidly. And Fischer and Fu (1993) measured the non linearity versus the radiant power of the S1337. They found at 1 mW a non linearity of 100 ppm and at 1.5 respectively 2 mW the effect was 300 and 800 ppm.

These findings are largely independent of the beam diameter as long as the 10 x 10 mm^2 active area of the photodiode remains under filled. They recommend not to use higher powers than 0.8 mW with a S1337 diode in order to avoid corrections for non linearity. Considering these findings, the non linear response of the trap detectors must be due to the saturation of the used Hamamatsu S1337 photodiodes.

We avoided the non linearity complications by using the third reflection off the beam splitter to illuminate the monitor trap. Thereby, we get a beam splitter ratio of ∼1853:1 and the power in the monitor trap is 0.0003 mW during the low power phase respectively 0.01 mW when the radiometer is calibrated at high power. At these low levels, the trap response is linear and we performed an accurate comparison.

Considering our non linearity measurements of the trap detectors, we are surprised that Romero et al. (1991) have not found any non linearity up to 2 mW. However, this might be due to the new generation of trap detectors. The second and third WRR to Si comparisons provide no evidence of trap linearity experiments and we would like to discuss possible implications of our findings for these comparisons.

Possible Implications for Previous WRR to SI Comparisons

We define the beam splitter ratio B as

$$B = \frac{reference\, power}{monitor\, power}.$$

Our measurements show that the beam splitter ratio appears lower at higher power levels

$$\frac{reference\, power^{low}}{monitor\, power^{low}} \cdot monitor\, power^{high} > reference\, power^{high}.$$

The left hand side of this inequality is the expression determining the reference power for the comparison with the radiometer and the right hand side is the actual power in the transmitted beam. So, if the trap detectors show a non linear response then the power reaching the radiometer is lower than calculated.

Moebus (2005) states a beam splitter ratio of ∼20:1 and a calculated reference power of 17 mW used in the third comparison between the SI and WRR scale at the NPL. This information allows us to calculate a power of 0.85 mW in the monitor trap during the high power level phase when the radiometer was calibrated. However, we do not know the power level at which the beam splitter ratio has been determined. Assuming the monitor trap saw less than 0.05 mW in the low power phase and the monitor trap experienced a similar non linearity as our traps, we derive from Figure 3.2 that the calculated reference power was overestimated by 400 ppm. This result accounts for half of the change observed between the second and the third comparison of the two scales. Finsterle et al. (2008) explains the difference between the second and the third comparison with the observed -100 ppm/year drift of the WRR. Given this degradation of the WRR, we would have to increase the offset between the WRR and SI scale found in all previous comparisons by 400 ppm. We plan to investigate how the three past comparisons accounted for a possible trap non linearity. Depending on our findings, we have to increase the offset between the two scales.

3.1.2 Transmission of the Brewster Window

Calibrating the PREMOS radiometers in a vacuum chamber, the laser beam had to pass through a brewster window. As the alignment of the window had to be adjusted prior to every calibration run, we repeatedly determined the window transmittance throughout the comparison campaign. To obtain the transmittance we followed a standard procedure: First, we determined an unobstructed beam splitter ratio as reference. Then we introduced and aligned the brewster window in front of the reference trap. The window transmittance is calculated as the ratio of the attenuated and the reference beam splitter ratio. In total we gathered five consistent transmittance values. Two out of the five measurements have been made with the 5 mm precision aperture in front of the reference trap being removed. However, omitting the trap precision aperture did not alter the measured window transmittance. The weighted mean transmittance of all measurements is 0.999667 ± 0.000051, where the standard uncertainty (k=1) is dominated by the reproducibility.

3.1.3 Stray Light

Iris diaphragms along the beam path were used to block the stray light around the beam. But the insertion of optical components (beam splitter, the brewster window) introduces additional stray light. Because we readjusted the components during the campaign, we repeatedly investigated the stray light in the set up. The NPL trap detectors had 5 mm diameter precision apertures mounted which could be removed revealing the native 8 mm opening of the trap. Hence, we could determine the stray light outside the precision apertures by dividing the beam splitter ratio with the 5 mm aperture by the beam splitter ratio with the 8 mm aperture. We collected five data sets measuring the stray light of the set up. Calculating the weighted mean yields a ratio of 0.999718 ± 0.000071, where the standard uncertainty (k=1) is dominated by the reproducibility. Further, we have two data sets investigating the stray light introduced by the brewster. The weighted mean ratio of these two values is 0.999635 ± 0.000044, where the standard uncertainty (k=1) is dominated by the reproducibility.

We conclude that we had a clean beam in our setup with less than 300 ppm stray light outside the precision apertures of the radiometers or the traps. Inserting the thoroughly cleaned brewster window, increased the stray light by less than 100 ppm.

The positioning of the radiometers respectively the traps is reproducible with high accuracy assuring that the detectors have seen the same portion of the beam. This fact and the low stray light level guarantee that a small off pointing or the different aperture areas of the detectors do not noticeably alter the comparison result. Hence we do not have to include a stray light correction in our comparison.

3.2 Power Comparison of the PREMOS Radiometers

We have compared all three PREMOS radiometers in vacuum with the NPL SI radiant power scale. For all measurements the 3.8 mm diameter laser beam was under filling the 5 mm precision aperture. Before and after the calibration run we determined the beam splitter ratio used to calculate the reference power. Simultaneously to the power measured by the radiometer under test, we determined the power in the monitor trap detector. After applying all necessary corrections to the radiometer measurement, the PREMOS to SI ratio is calculated by

$$\frac{\text{PREMOS}}{\text{SI}} = \frac{\text{PREMOS power}}{\text{beam splitter ratio} \cdot \text{monitor power}}.$$

For PREMOS-1 we performed two calibration runs yielding a total of 25 data points. The weighted mean of the PREMOS-1 to SI ratio is 0.999605 ± 0.000146 where the standard uncertainty (k=1) is dominated by the ratio calculation uncertainty and not the reproducibility of the measurements. PREMOS-2 delivered a total of 33 data points from four calibration runs. The weighted mean of the PREMOS-2 to SI ratio is 1.000098 ± 0.000163 where the standard uncertainty (k=1) is dominated by the calculation of the ratio and not the reproducibility of the measurements. PREMOS-3 has only a total of 5 data points out of five calibration runs. This is because the measurements revealed a large offset of the intrinsic PREMOS absolute scale which seemed unrealistic at first and we therefore concentrated on the other two instruments. The weighted mean of the PREMOS-3 to SI ratio is 1.006333 ± 0.000171 where the standard uncertainty (k=1) is dominated by the calculation of the ratio and not the reproducibility of the measurements. Table 3.1 summarizes the relative difference of the three PREMOS radiometers to the NPL radiant power scale.

	relative difference to SI power [ppm]	relative uncertainty [ppm]
PREMOS-1	- 395	146
PREMOS-2	+ 98	163
PREMOS-3	+ 6333	171

Table 3.1: *Relative differences of the PREMOS radiometers to the NPL radiant power scale and their standard uncertainties (k=1).*

Our hypotheses about the causes of the large PREMOS-3 could have only be resolved by disassembling and possibly damaging the instrument. As PREMOS-3 cannot be investigated because it is in space and we are reluctant to destroy the long calibration history of VIRGO-2 which shows a similar behavior (see section 4.2), we present below our suspicion which should be investigated as soon as we identify one more PMO6 radiometer which shows the same behavior.

3.2.1 Possible Causes of Large Offsets Observed with PMO-6 Type Radiometers

The voltage sensing as well as the current feeding wires connected to the cavity heater foil are guided through a small hole from the front to the back of the cavity. We think that the insulation of the current leading wire might be damaged forming a high ohmic short circuit via the grounded instrument body. Assuming the lost current I_{short} is proportional to the heater current I_{heater}, we can write the closed heater power as

$$\mathrm{P}_{heater}^{closed} = (1+k) \cdot \mathrm{V}_{heater}^{closed} \cdot \mathrm{I}_{heater}^{closed},$$

and the open heater power as

$$\mathrm{P}_{heater}^{open} = (1+k) \cdot \mathrm{V}_{heater}^{open} \cdot \mathrm{I}_{heater}^{open}.$$

The measured optical solar power is then

$$\mathrm{P}_{sun} = (1+k) \cdot (\mathrm{V}_{heater}^{closed} \cdot \mathrm{I}_{heater}^{closed} - \mathrm{V}_{heater}^{open} \cdot \mathrm{I}_{heater}^{open}).$$

The PREMOS-3 measurements yielded k $= 0.006$, $\mathrm{I}_{heater}^{closed} = 0.02$ A and $\mathrm{V}_{heater}^{closed} = 2$ V. Hence, the lost current is $\mathrm{I}_{short}^{closed} = 0.00012$ A and the electrical resistance of the short circuit must be $\mathrm{R}_{short} = 17$ kOhm.

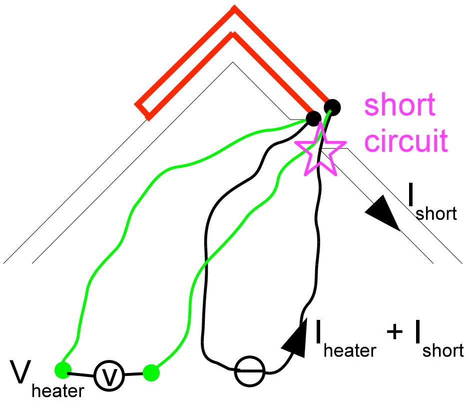

Figure 3.3: *Schematic wiring diagram of a PMO-6 type radiometer cavity. The voltage sensing (green) and the current feeding (black) wires soldered to the cavity heater (red) are guided through a hole to the backside of the cavity. A sharp edge could damage the insulation of the current feeding wire, forming a high ohmic short circuit via the grounded instrument body. Considering such a loss, we overestimate the effectively dissipated power inside the cavity and the radiometer would read too high.*

3.3 Non-Equivalence Measurements

We also performed PREMOS to SI calibrations at ambient pressure to investigate the non-equivalence effect. In air, PREMOS-1 yielded 12 data points out of three calibration runs. The weighted mean of the PREMOS-1 to SI ratio is 0.994127 ± 0.000163 where the standard uncertainty (k=1) is dominated by the calculation of the ratio and not the reproducibility of the measurements.

PREMOS-2 completed two calibration runs yielding 6 data points. The weighted mean of the PREMOS-2 to SI ratio is 0.993173 ± 0.000259 where the standard uncertainty (k=1) is dominated by the reproducibility of the measurements not the calculation of the ratio.

The third radiometer has measured only one data point yielding a PREMOS-3 to SI ratio of 0.996541 ± 0.000221 (k=1). At that time the PREMOS-3 was equipped with a stainless steel precision aperture whereas those of the other two instruments were made of cemented carbide.

Using the vacuum and ambient pressure calibrations, we are able to calculate the vacuum-to-air ratio (Table 3.2) that can be used as non-equivalence correction factor. The stated values in this thesis slightly differ from those presented in our first publication on the PREMOS calibration (Schmutz et al., 2009). This is because the NPL reconsidered and reduced the uncertainty associated with the amplifiers used for the trap detectors (Winkler, 2011b).

	vacuum to air	relative uncertainty	aperture material
PREMOS-1	1.005510	0.000136	carbide
PREMOS-2	1.006973	0.000253	carbide
PREMOS-3	1.009826	0.000264	steel

Table 3.2: *The non-equivalence factors for the PREMOS instruments and their standard uncertainties (k=1) have been determined with a 3.8 mm wide laser beam at a wavelength of 647 nm.*

3.4 Uncertainty Budget

We followed the Guide to the Expression of Uncertainty in Measurement (GUM; BIPM 2008) to estimate the standard uncertainty (k=1) of our measurements. We started by determining the individual uncertainties of the PREMOS power readings and the calculated reference powers. Then we calculated the standard uncertainty of the ratio calculation and the standard uncertainty of the reproducibility of the measurements. The resulting total standard uncertainty of the PREMOS to SI comparison is shown in Figure 3.4, where the uncertainties of the PREMOS and reference power readings equally contribute to the total uncertainty of the highly reproducible measurements. The largest uncertainty in the PREMOS power values stems from the reflectivity of the cavity and the transmission of the brewster window (Figure 3.5). The dominating part in the uncertainty of the calculated reference power is the reference trap responsivity calibration (Figure 3.6). The stated uncertainties here are lower than those given in our first publication on the PREMOS calibration (Schmutz et al., 2009). This is because the uncertainties of the trap amplifiers were overestimated by a factor of at least 10 (Winkler, 2011b).

The standard uncertainties of the vacuum to air ratios are dominated by the reproducibility of the PREMOS to SI ratios in vacuum respectively in air. As we calculate the ratio of a ratio here, all multiplicative corrections as reflectivity, responsivity or gain cancel out and the remaining uncertainty is due to the voltage readings and the reproducibility.

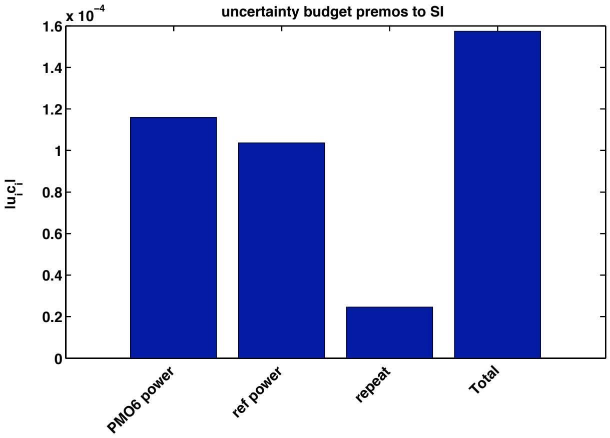

Figure 3.4: *The uncertainty budget of the PREMOS to SI comparison reveals that the radiometer measurements and the calculated reference power contribute in equal shares to the total standard uncertainty (k=1) of highly reproducible calibrations.*

3.5 Discussion of the NPL Comparison

Placing the instrument under test in a vacuum chamber allowed us to perform a calibration of PMO6-type radiometers against the SI radiant power scale with unprecedented accuracy. The PREMOS absolute solar radiometers are the first instruments in space directly traceable to the SI radiant power scale in vacuum and to the WRR.

The PREMOS-1 to SI ratio of 0.999605 ± 0.000146 and the PREMOS-2 to SI ratio of 1.000098 ± 0.000163 show that PMO6-type radiometers are able to accurately measure radiant power. PREMOS-2 agrees with the SI scale within one standard uncertainty whereas PREMOS-1 can be considered representative for the SI scale within three standard uncertainties. The 493 ppm offset between the instruments might indicate that we under- respectively overestimate individual correction factors.

The high PREMOS-3 to SI ratio of 1.006333 ± 0.000171 remains unexplained. In subsection 3.2.1 we have presented a possible explanation for the offset.

The problem of the non linear trap response at high power levels has been avoided with our set up. However, our findings could implicate that the results of previous WRR to SI comparisons have to be shifted by up to 400 ppm increasing the offset between the two scales.

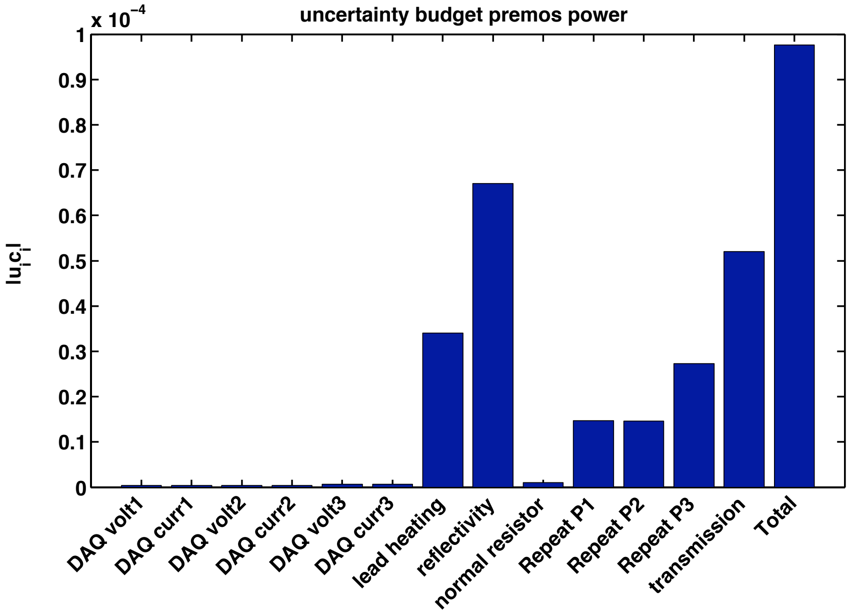

Figure 3.5: *The standard uncertainty (k=1) of the PREMOS radiometer readings is dominated by the uncertainties of the lead heating, the reflectivity of the cavity and the transmission of the brewster window.*

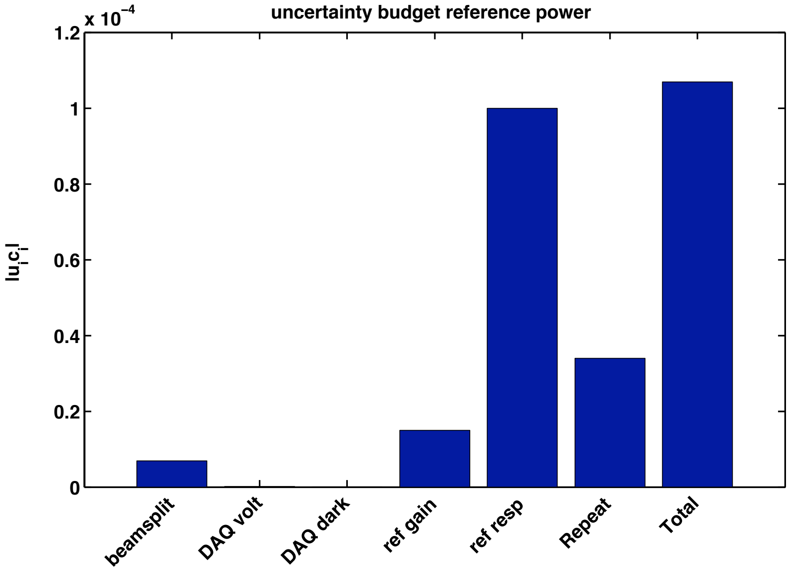

Figure 3.6: *The standard uncertainty (k=1) of the calculated reference power is completely dominated by the uncertainty of the trap responsivity calibration.*

Chapter 4

SI Calibration of the PREMOS Absolute Solar Radiometers at LASP in Boulder

After vibration tests of the PICARD satellite we noticed an increased resistance in the heater of the PREMOS-1 instrument indicating a damaged conducting path that might cause the instrument to fail in space. Therefore we replaced PREMOS-1 with the flight spare instrument PREMOS-3. Before the exchange, we got the opportunity to visit the new SI traceable Total solar irradiance Radiometer Facility (TRF) (Kopp et al., 2007) at LASP in Boulder with the PREMOS-3 instrument. In order to better understand the differing measurements of the Total Irradiance Monitor (TIM) and the Variability of Solar Irradiance and Gravity Oscillations (VIRGO) radiometers, we also brought the SOHO/VIRGO flight spare instrument (VIRGO-2) to Boulder.

4.1 The Total Solar Irradiance Radiometer Facility (TRF)

The TRF offers for the first time the possibility to calibrate solar radiometers for irradiance in a laboratory. Kopp et al. (2007) have designed and built the experiment where a solar radiometer is directly compared to a NIST calibrated cryogenic radiometer. To avoid the non-equivalence effects introduced by surrounding air, they place the instrument under test in a vacuum chamber alongside the reference as we did in our PREMOS/NPL calibration (Figure 4.1). The TRF cryogenic radiometer was equipped with a 5 mm precision aperture having an area of 19.4972 mm^2. In the following list, we discuss the characterization of the TRF.

- **Beam creation and stability -** The TRF uses a new technique to generate a flat irradiance field with a chosen diameter. A two axes fast steering mirror deflects a stabilized 1 mm wide laser beam and creates a spiral pattern (Figure 4.2). The intensity of the laser beam is stable to 0.01 % over typical comparison times of ~30 minutes. The scanning rate is 5 Hz, i.e. it takes the laser beam 0.2 s to get to the outermost position of the pattern and back to the center. The idea is that the scanning is fast enough so that the thermal receivers of the exposed radiometers will measure a constant integrated power.

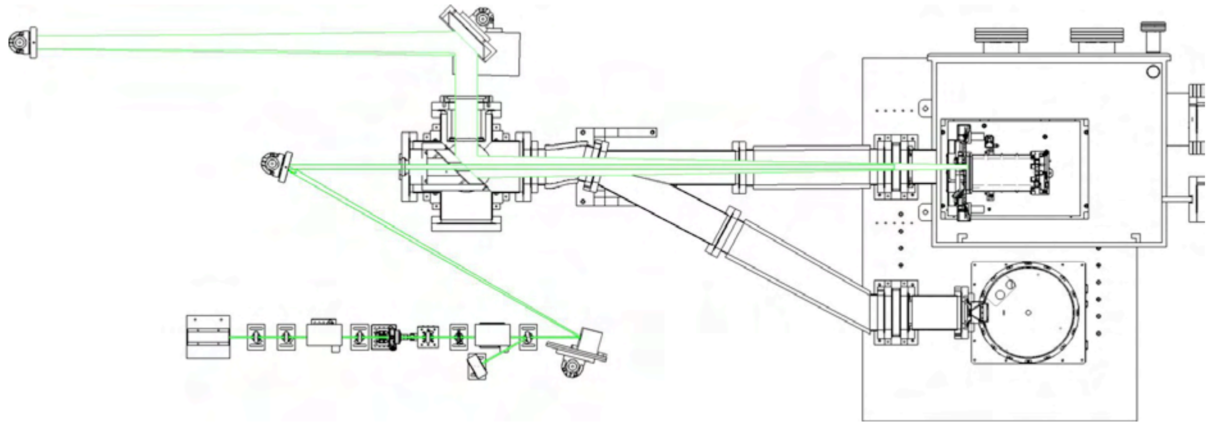

Figure 4.1: *This figure is adopted from Kopp et al. (2007) and shows the experimental set up at the TRF. The radiometer under test and the reference are mounted side by side. A translation stage moves one instrument after the other into the position where the stationary beam travels along the vacuum bellows and illuminates the radiometer.*

- **Entrance window -** Using a separate window for each instrument or sampling different sections of one window for the comparison would make corrections necessary. i) Relative transmittance changes due to different material properties or due to dissimilar stress would have to be considered. ii) Stray light is different if one changes the optical setup. Hence, the TRF uses one entrance window kept at a fixed position in the optical set up.

- **Thermal background -** The PMO6-type radiometers as well as the cryogenic reference radiometer at the TRF determined the optical power as the difference between the closed and the open measurement. The PMO6-type radiometer has an internal shutter and thus measures a different thermal background in the open respectively closed state. Once the instrument is closed, the cavity sees the gold plated shutter. Opening the shutter, the cavity exchanges thermal radiation with the laboratory environment. The correction of this effect would introduce an extra uncertainty to the comparison. We left the internal shutter open and used the TRF external shutter far up the beam path instead. In chapter 9 we discuss the implications of different radiometer aperture geometries to ground based TSI measurements. The TRF cryogenic radiometer may collect radiation from up to 5.7 degrees away from the optical axis whereas the PMO6-typ radiometers has a limiting angle of 3.9 degrees. However, thermal radiation seen by the radiometers originates from the BK7 entrance window or the vacuum bellow system. As the laboratory temperature has been stabilized, the measured thermal radiation remains constant and cancels out when we calculate the difference between illuminated and reference measurement. The stray light produced by optical components and the vacuum bellows may induce an offset between the two radiometer type measurements and we consider a 50 ppm scatter difference in the uncertainty budget.

- **Aperture size and position -** The TRF cryogenic radiometer is normally operated with a 8 mm precision entrance aperture and a view limiting aperture in front of the cavity. The PREMOS and VIRGO radiometers however, have the opposite optical design with the view limiting aperture at the front and a 5 mm precision aperture close to the cavity. Measurements (Figure 4.3) show that the TRF beam is spatially not as homogenous as the solar irradiance. Therefore both instrument types should sample the same portion of the beam to perform an accurate comparison. Kopp et al. (2007) show that the TRF comparisons are most sensitive to the beam profile right at the edge of the precision aperture. We placed the PMO6 radiometers with their precision apertures a the same distance from the source as the new 5 mm diameter precision aperture of the cryogenic radiometer. During the experiments we carefully checked the positioning of the radiometers and found a very good repeatability.

- **Scattered light -** Became the most interesting issue during the comparison and is discussed in subsection 4.9.4. The two optical geometries with interchanged view limiting and precision apertures produce differences in the scattered light. For the PMO6-type radiometers, we expect more scattered light as two thirds of the light entering the instrument are not measured but reflected by the precision aperture and illuminate the mufflers. We performed novel experiments to quantify the amount of internal stray light.

After installing the radiometer under test in the TRF, we followed a standard calibration procedure for all instruments. We started by illuminating the cryogenic radiometer and acquiring a data set. Then we moved the radiometer under test into the beam and measured with this instrument. Now we could either set up another experiment or repeat the previous two sequences. The data showed drifting PMO6-type and TRF cryogenic radiometer measurements. We use a linear fitting technique where we scale the results of one instrument, to achieve the best fit accounting for the drifts (Figure 4.5).

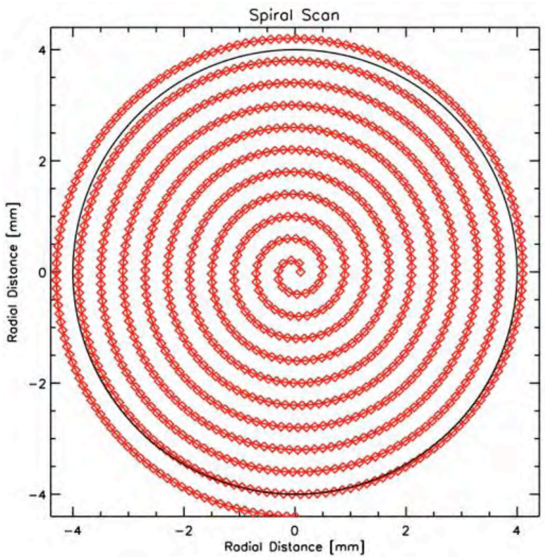

Figure 4.2: *Scanning beam technique to generate a flat irradiance field (Figure adopted from Kopp et al. (2007))*

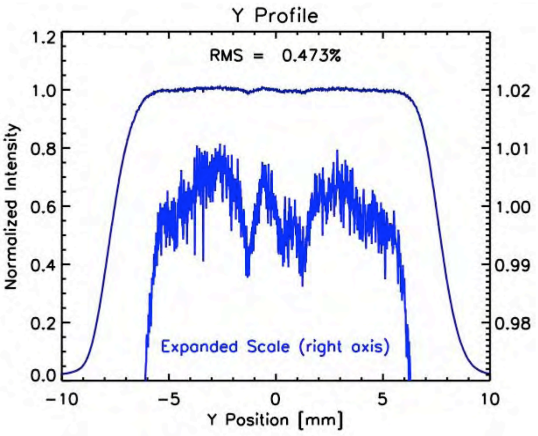

Figure 4.3: *Measured intensity profile of a typical TRF beam. The profile shows good uniformity and has non-linearities only at center of the beam (Figure adopted from Kopp et al. (2007)).*

4.2 Power Comparison of PREMOS-3 and VIRGO-2

From the 7th to the 22nd July 2009, we performed power calibrations of PREMOS-3 and VIRGO-2 at the LASP in Boulder, CO. We used the intrinsic 1 mm diameter beam widened by scanning to a 2 mm TRF beam to perform the optical power calibration. By using a beam under filling the 5 mm precision apertures of the radiometers, we essentially repeated the NPL power calibration. No uncertainties due to the aperture areas, diffraction or stray light are introduced. But the corrections for the reflectivity of the cavities have to be applied for both radiometers. The PREMOS instruments also needs a correction for the heating of the leads (section 2.9). The TRF cryogenic radiometer uses superconducting wires and hence is not susceptible to Joule losses.

The weighted mean of seven calibration runs (Figure 4.5) yields a PREMOS-3 to SI ratio of 1.006344 ± 0.000243. The standard uncertainty (k=1, Figure 4.15) is dominated by the PREMOS measurement uncertainty, the beam stability, the thermal background and the reproducibility of the measurement. This offset is in excellent agreement with the findings at NPL (section 3.2).

The two optical power calibrations with the VIRGO-2 instrument (Figure 4.4) yielded a weighted mean VIRGO-2 to SI ratio of 1.007314 ± 0.000195. The standard uncertainty (k=1, Figure 4.15) is dominated by the PREMOS measurement uncertainty, the beam stability and the thermal background.

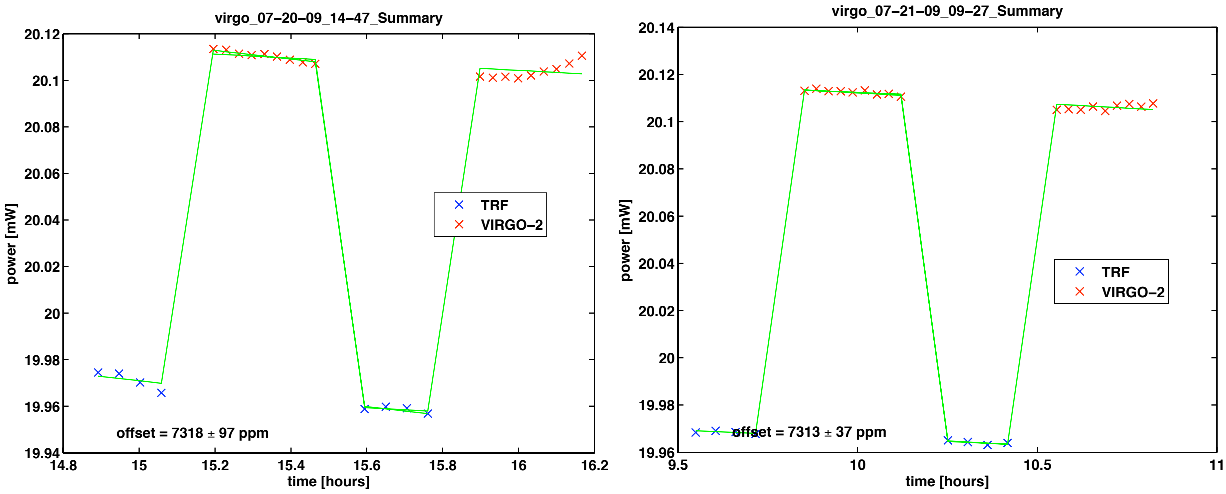

Figure 4.4: *The two VIRGO-2 power calibrations yielded a weighted mean offset of 7314 ± 195 ppm (k=1) by which the radiometer reads higher than the SI scale. The standard uncertainties (k=1) stated for the individual offsets are used to calculate the weighted mean.*

The offset fitting function which we apply assumes both radiometers to identically track drifts of the laser beam. For the fitting procedure we consider only statistical errors of the individual measurement points, i.e. only the repeatability of the power readings is used to weight the individual data points. These uncertainties are very small and we do not indicate them in the plots.

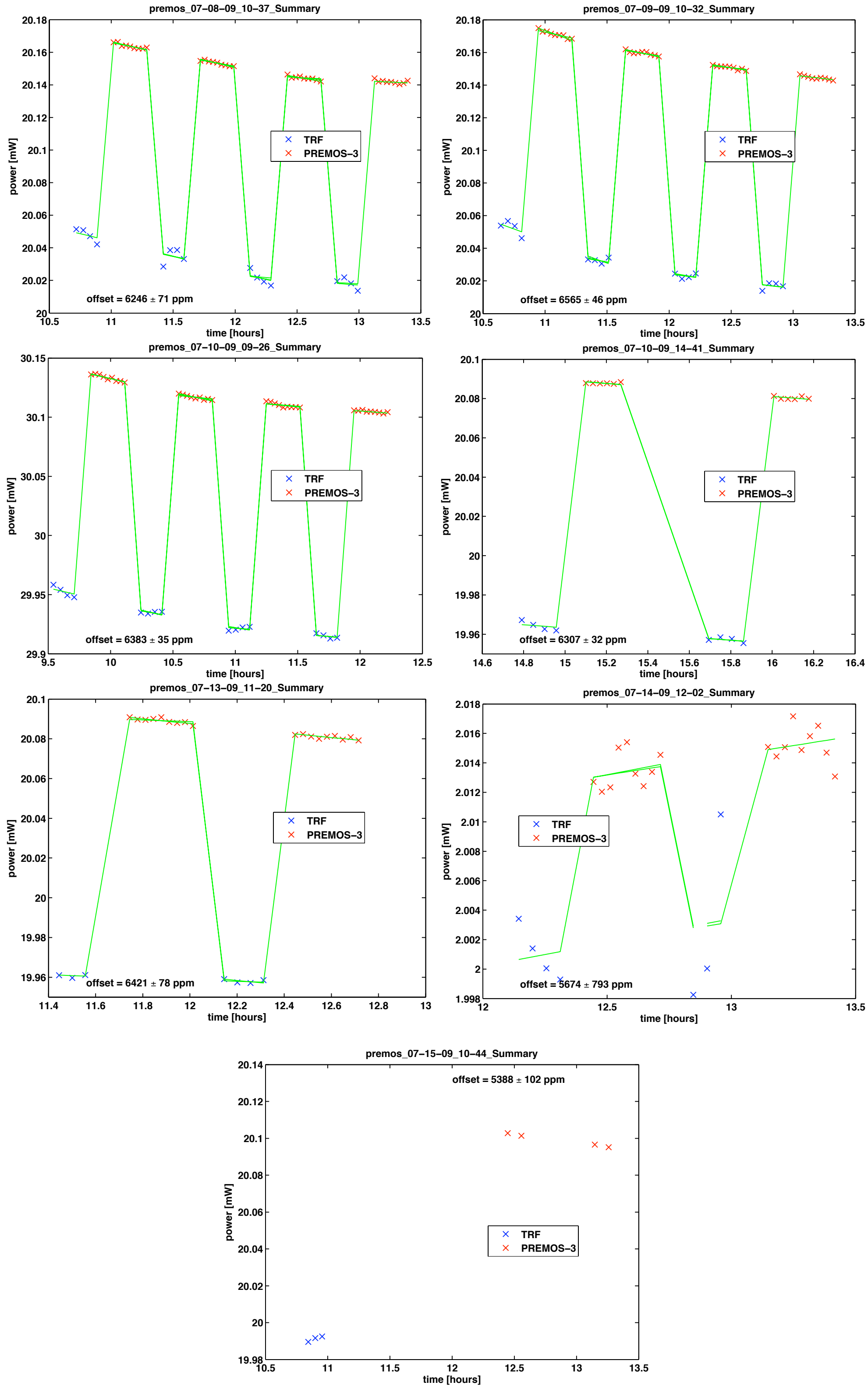

Figure 4.5: *The seven PREMOS-3 power calibrations yielded a weighted mean offset of 6344 ± 243 ppm (k=1) by which the radiometer reads higher than the SI scale. The standard uncertainties (k=1) stated for the individual offsets are used to calculate the weighted mean. The last run yielded only one data set for each instrument and we use their means to estimate the offset.*

4.3 Irradiance Comparison of PREMOS-3 and VIRGO-2

From the 7th to the 22nd July 2009, we performed irradiance calibrations of PREMOS-3 and VIRGO-2 at the LASP in Boulder, CO. We used the intrinsic 1 mm diameter beam widened by scanning to a 7.3 mm TRF beam over filling the precision aperture of the PMO6 radiometers but not the view limiting aperture. With the beam being larger than the precision aperture, we had to apply corrections for diffraction and stray light (section 2.9).

The PREMOS-3 measurement (Figure 4.6) yielded a PREMOS to SI ratio of 1.006531 ± 0.000285, where the standard uncertainty (k=1, Figure 4.16) is dominated by the PMO6 measurement uncertainty, the beam stability and the thermal background. The offset of the 7.3 mm irradiance measurement is 186 ± 325 ppm higher than the offset determined by the power comparison.

The weighted mean of two VIRGO-2 measurement runs (Figure 4.7) yielded a VIRGO-2 to SI ratio of 1.007949 ± 0.000244. where the standard uncertainty (k=1, Figure 4.16) is dominated by the PMO6 measurement uncertainty, the beam stability and the thermal background. For this instrument, the difference between the irradiance and the radiant power measurement is 630 ± 260 ppm higher. As the geometries for the PREMOS and the VIRGO instrument are similar, the diffraction correction factors are virtually identical (section 2.5). Hence, it must be the stray light correction that is underestimated in the VIRGO-2 PMO6 radiometer characterization.

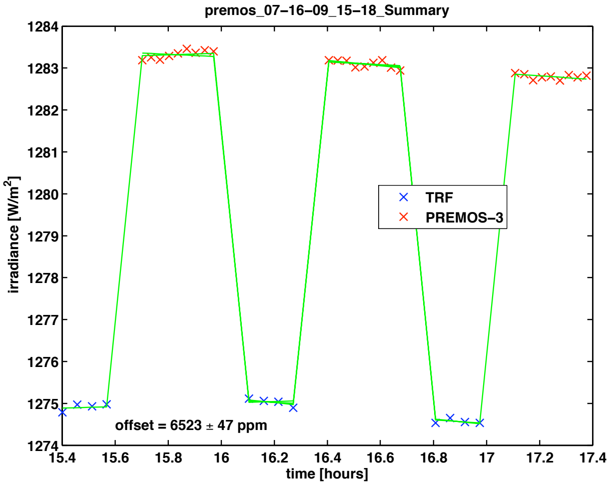

Figure 4.6: *The PREMOS-3 7.3 mm TRF beam calibration yielded a weighted mean offset of 6531 ± 285 ppm (k=1) by which the radiometer reads higher than the SI scale.*

Creating a scanned 11 mm diameter TRF beam over filling the precision and the view limiting aperture of the PMO6-type radiometers, we used the best reproduction of solar irradiance presently available in a laboratory. To correct the measurements, we applied the appropriate diffraction and stray light corrections for this irradiance mode (section 2.9).

The weighted mean of the three PREMOS-3 measurement runs (Figure 4.9) yielded a PREMOS-3 to SI ratios of 1.007768 ± 0.000623 where the large standard uncertainty (k=1, Figure 4.17) is dominated by the error of the fitting procedure and the reproducibility of the measurements.

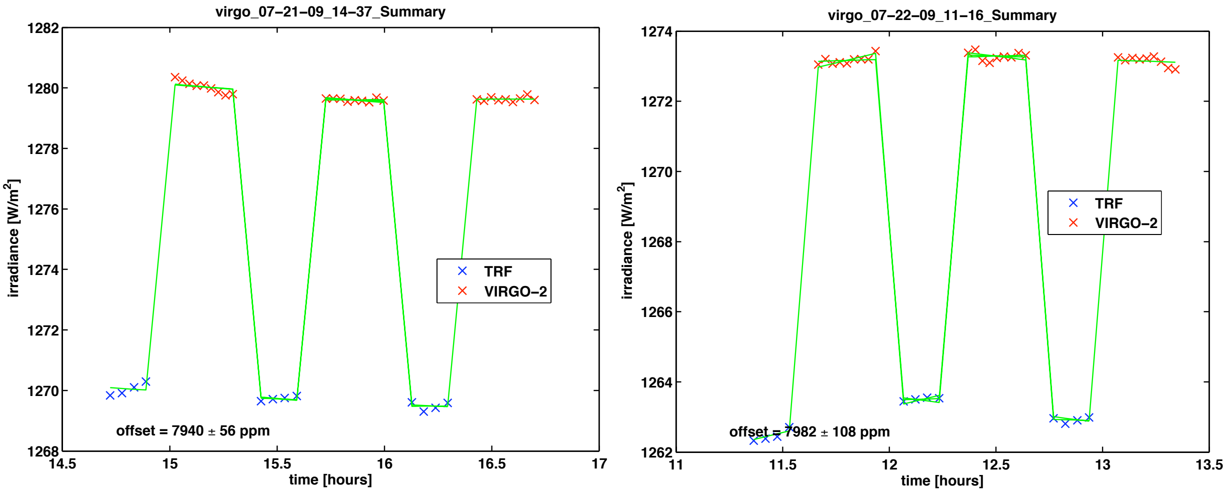

Figure 4.7: *The two VIRGO-2 7.3 mm TRF beam calibrations yielded a weighted mean offset of 7949 ± 244 ppm (k=1) by which the radiometer reads higher than the SI scale. The standard uncertainties (k=1) stated for the individual offsets are used to calculate the weighted mean.*

The VIRGO-2 measurement (Figure 4.8) yielded a VIRGO-2 to SI ratio of 1.010292 ± 0.000242 where the standard uncertainty (k=1, Figure 4.17) is dominated by the PMO6 measurement uncertainty, the fitting error and the reproducibility.

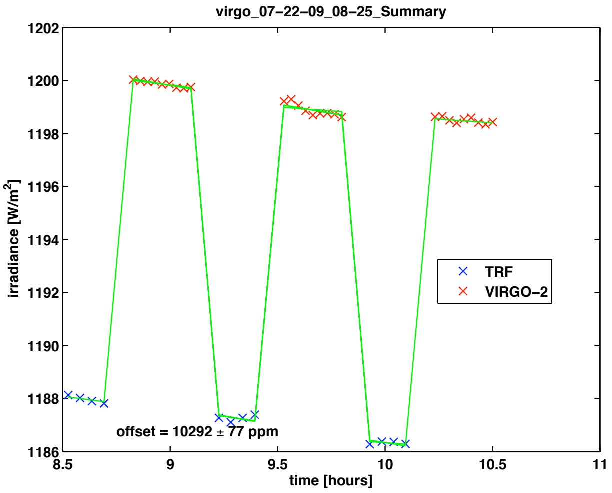

Figure 4.8: *The VIRGO-2 11 mm TRF beam calibration yielded an offset of 10292 ± 242 ppm (k=1) by which the radiometer reads higher than the SI scale.*

Comparing the offsets from the two irradiance modes gives an estimate of the additional stray light when we expand the TRF beam from 7.3 to 11 mm. The radiometer to SI ratios increase by 1229 ± 643 ppm and 2325 ± 262 ppm for PREMOS-3 respectively VIRGO-2. The standard uncertainties (k=1) of these estimations are lower than those for individual calibrations because the errors introduced by the radiometer cancel out if we calculate the ratio of two calibrations with the same instrument. We can also determine a new total stray light correction if we compare the

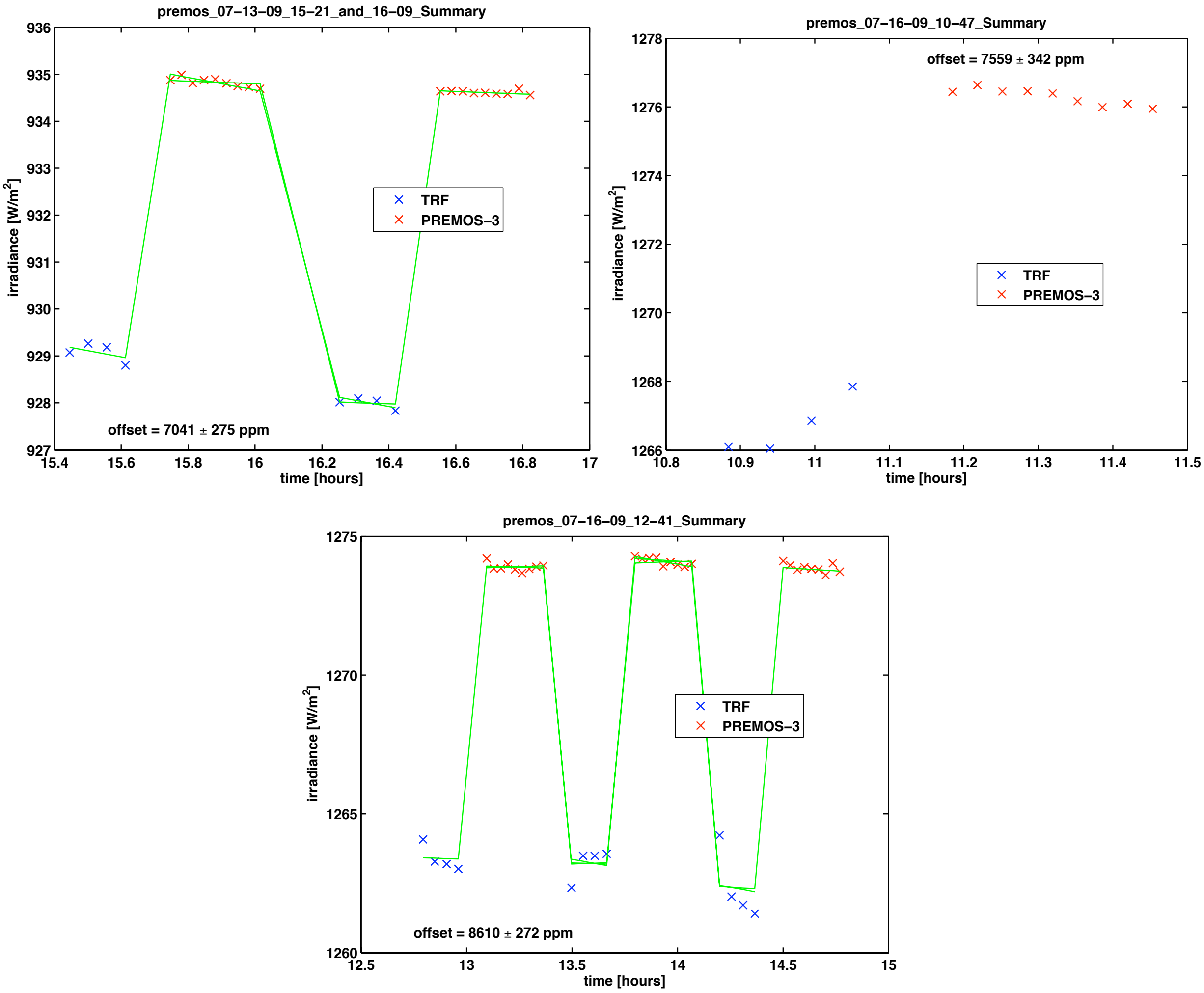

Figure 4.9: *The three PREMOS-3 11 mm TRF beam calibrations yielded a weighted mean offset of 7768 ± 623 ppm (k=1) by which the radiometer reads higher than the SI scale. The standard uncertainties (k=1) stated for the individual offsets are used to calculate the weighted mean. The second run yielded only one data set for each instrument and we use their means to estimate the offset.*

11 mm calibration to the 2 mm power calibration. As we have applied the 0.999750 Brusa and Fröhlich stray light correction factor in the calibrations, we have to add these 250 ppm correction to the newly found stray light. Hence we totally have to correct PREMOS-3 measurements by 0.998335 ± 0.000642 ppm and VIRGO-2 data by 0.996795 ± 0.000257 ppm. The standard uncertainties (k=1) of these estimations are lower than those for individual calibrations because the errors introduced by the radiometer cancel out if we calculate the ratio of two calibrations with the same instrument.

4.4 Power Comparison of PREMOS-1

After removing PREMOS-1 from the PICARD satellite, we brought the instrument to the TRF to perform a calibration and additional experiments. From the 5^{th} to the 7^{th} October 2009, we performed power calibrations of PREMOS-1 at the LASP in Boulder, CO. We used the intrinsic 1 mm diameter beam widened by scanning to a 2 mm TRF beam to perform the optical power calibration. The electrical resistance of the PREMOS-1 measuring cavity heater varied by several percent during the measurements where we illuminated the cavity with a high power densities in the laser beam. We suspect a hairline crack in the conducting path of the heater varying with the local temperature, to cause the resistance variation. We have detected no apparent influence on the irradiance readings but as long as the cause and resulting biases remain unclear, we avoid using the calibration results of PREMOS-1 in the WRR to SI comparison (section 5.2). But we consider the experimental results where the cavity has not been illuminated directly and the heater resistance remained unchanged, acceptable to characterize the radiometer.

The weighted mean of the three PREMOS-1 measurement runs (Figure 4.10) yielded a PREMOS-1 to SI ratio of 0.999374 ± 0.000229 where the standard uncertainty (k=1, Figure 4.15) stems from the PMO6 measurement uncertainty, the beam stability and the thermal background. This result is in good agreement with the NPL power calibration (section 3.2). The cavity heater resistance changed from 113.5 Ohm in the closed state to 115.5 Ohm in the illuminated state of the radiometer during the calibration.

4.5 Irradiance Comparison of PREMOS-1

The weighted mean of two 7.3 mm beam calibration runs (Figure 4.11) yielded a PREMOS-1 to SI ratio of 0.999453 ± 0.000328 where the standard uncertainty (k=1, Figure 4.16) stems from the PMO6 measurement uncertainty and the reproducibility. The offset difference between power and 7.3 mm irradiance comparison is 79 ± 359 ppm. The cavity heater resistance changed from 150 Ohm in the closed state to 170 Ohm in the illuminated state of the radiometer during these measurements.

The 11 mm beam comparison (Figure 4.12) yielded a PREMOS-1 to SI ratio of 1.001148 ± 0.000308 where the standard uncertainty (k=1, Figure 4.16) is due to the PMO6 measurement uncertainty and the fitting error. The cavity heater resistance changed from 150 Ohm in the closed state to 170 Ohm in the illuminated state of the radiometer during these measurements.

We measure 1696 ± 391 ppm additional stray light when we expand the TRF beam from 7.3 to 11 mm. The standard uncertainty (k=1) of this estimation is lower than those for individual calibrations because the errors introduced by the radiometer cancel out if we calculate the ratio of two calibrations with the same instrument. We can also determine a new total stray light correction if we compare the 11 mm calibration to the 2 mm power calibration. As we have applied the 0.999750 Brusa and Fröhlich stray light correction factor in the calibrations, we have to add these 250 ppm correction to the newly found stray light. Hence we totally have to correct PREMOS-1 measurements by 0.997975 ± 0.000341 ppm. The standard uncertainty(k=1) of

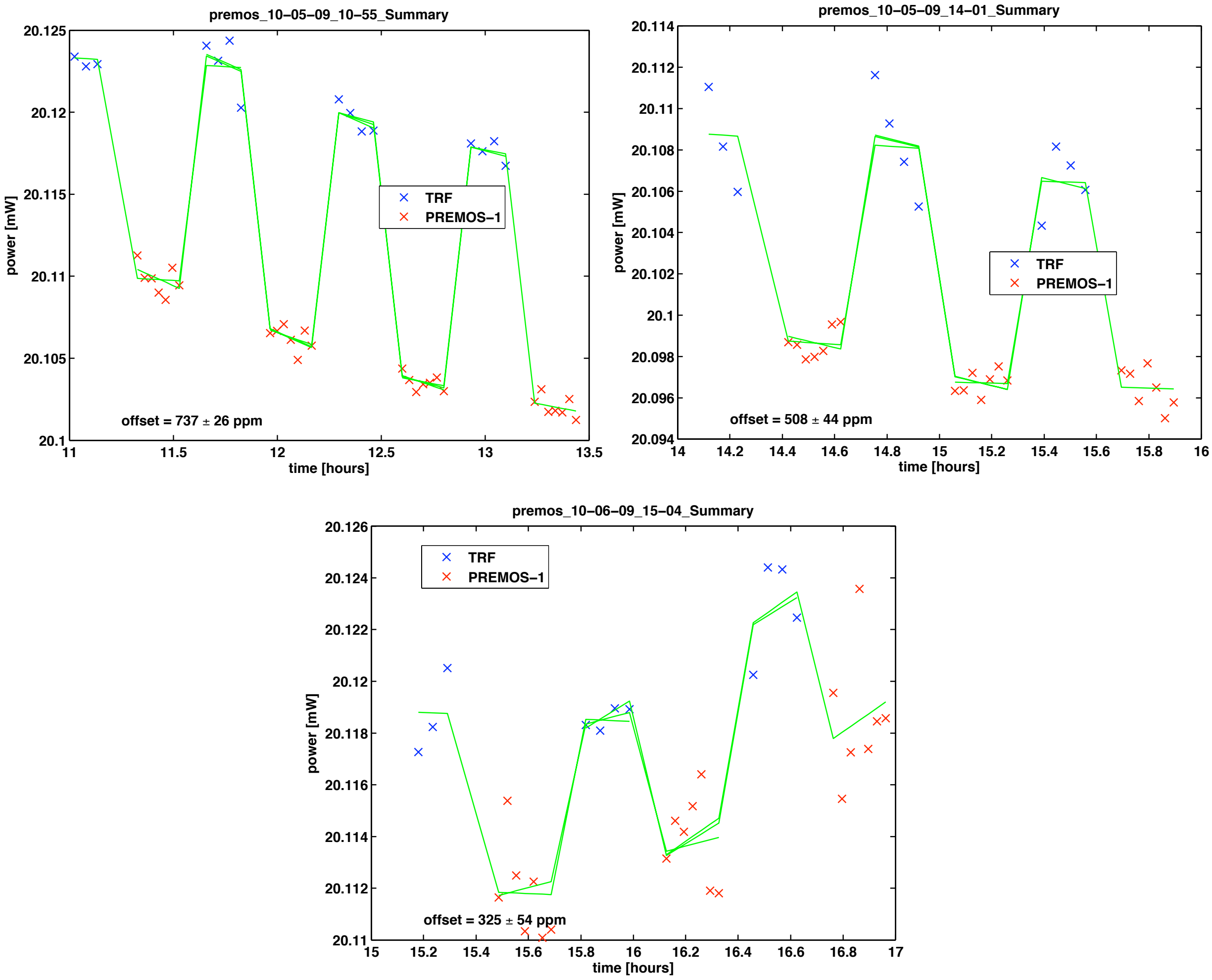

Figure 4.10: *The three PREMOS-1 power calibrations yielded a weighted mean offset of 626 ± 229 ppm (k=1) by which the radiometer reads lower than the SI scale. The standard uncertainties (k=1) stated for the individual offsets are used to calculate the weighted mean.*

this estimation is lower than those for individual calibrations because the errors introduced by the radiometer cancel out if we calculate the ratio of two calibrations with the same instrument.

4.6 Statistical Approach to Analyze the PREMOS-3 Irradiance Calibration

The large scattering of the PREMOS-3 11 mm irradiance calibration offsets (Figure 4.9) raised some concerns about our fitting technique and we applied a statistical approach to reanalyze the data. With this alternative evaluation considering all the data as one single random sample, we avoid a spurious weighting of single offset determinations. The measurements of the TRF cryogenic radiometer seems not to track identical beam stability drifts as the PREMOS-3 instru-

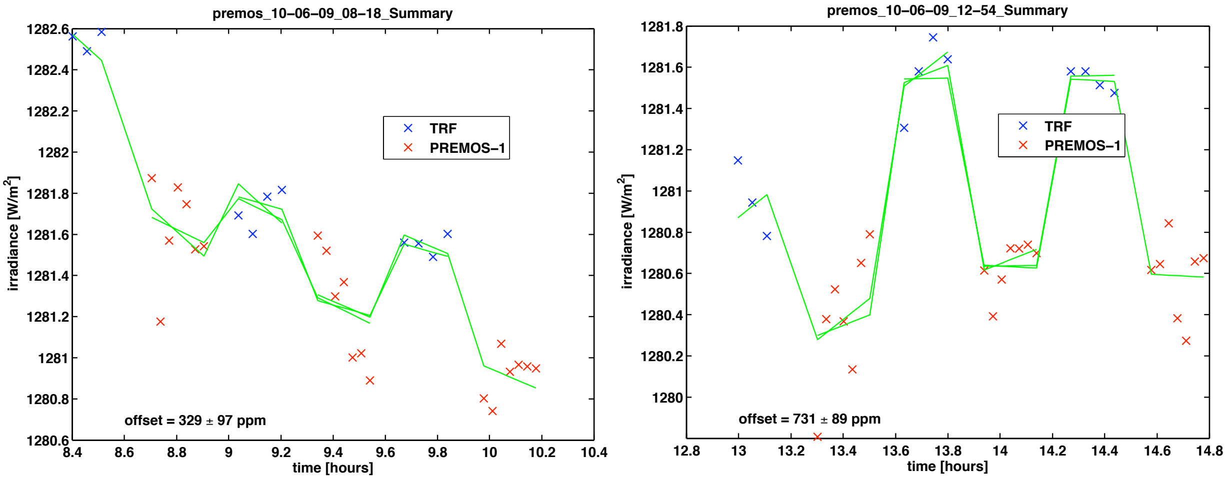

Figure 4.11: *The two PREMOS-1 7.3 mm TRF beam calibrations yielded a weighted mean offset of 547 ± 328ppm (k=1) by which the radiometer reads lower than the SI scale. The standard uncertainties (k=1) stated for the individual offsets are used to calculate the weighted mean.*

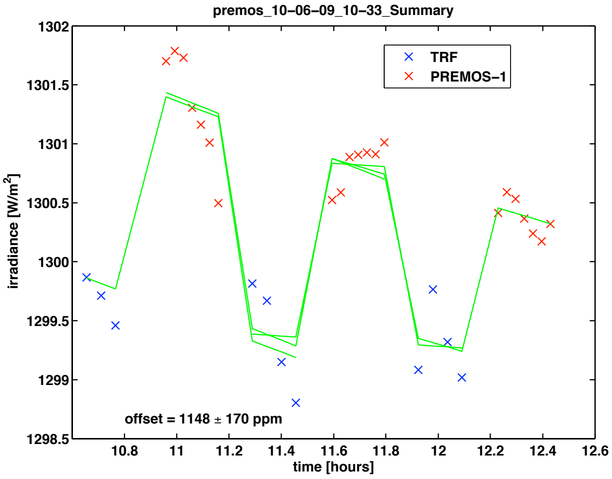

Figure 4.12: *The PREMOS-1 11 mm TRF beam calibration yielded an offset of 1148 ± 308 ppm (k=1) by which the radiometer reads higher than the SI scale.*

ment. Hence we cannot fit the same slope to the data series of both radiometers. Because the PREMOS-3 measurements are less noisier, we use these values to track the linear beam stability drift. The TRF values are then subtracted from the from the fitted PREMOS-3 trend line and normalized to the absolute irradiance level to determine a relative deviation between the two instruments. Figure 4.13 shows the distribution of all the 11 mm calibration points for the two instruments. We performed a Shapiro-Wilk test to check wether the data can be considered normally distributed. With a normal distribution of the entire population, we find a 80 % chance for PREMOS-3 and a 67 % chance for TRF cryogenic radiometer to draw the observed sample distributions. Hence, we find no contradiction to a normal distribution and we can determine a mean PREMOS-3 to TRF offset of 7904 ± 221 ppm, with PREMOS-3 measuring higher.

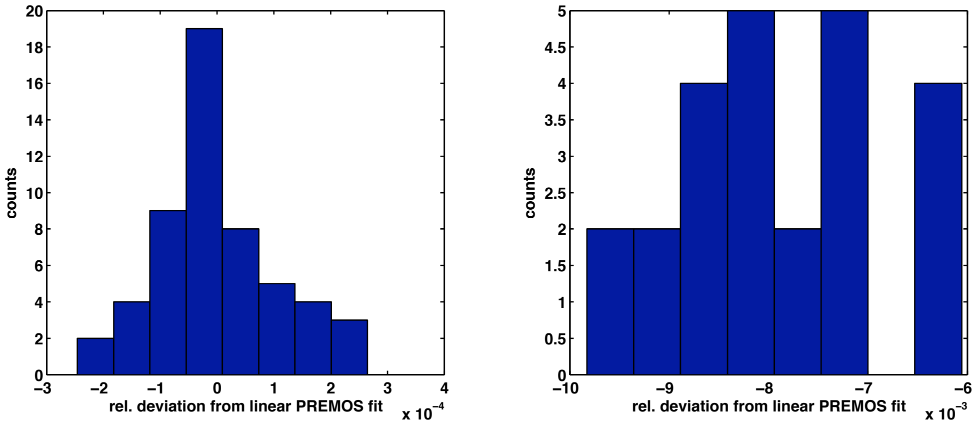

Figure 4.13: *Relative deviation from a linear trend line through the PREMOS-3 11 mm TRF beam measurements. Left: The PREMOS data are nicely distributed around the linear fit. Right: A Shapiro-Wilk test showed no contradiction to the assumption that the TRF cryogenic radiometer data are normally distributed around the PREMOS trend line shifted by 0.79 %.*

4.7 Irradiance Calibration of PREMOS-1, PREMOS-3 and VIRGO-2

In the previous sections we applied the characterization of the PMO6-type radiometers to the measurements in order to verify the correction factors. We can also follow a pure calibration approach by comparing our uncorrected radiometers to the TRF. The obtained radiometric constants have smaller standard uncertainties (k=1) as we avoid additional uncertainties due to the corrections. In Table 4.1 we present the results of these calibrations. The PREMSO-3 11 mm calibration is evaluated with the statistical approach in the previous section.

	2 mm beam	relative uncertainty	7.3 mm beam	relative uncertainty	11 mm beam	relative uncertainty
PREMOS-1	1.001126	0.000215	566.8564	0.000288	565.4467	0.000265
PREMOS-3	0.994193	0.000228	562.3373	0.000231	561.1249	0.000347
VIRGO-2	0.993235	0.000180	1010.0047	0.000187	1006.9287	0.000184

Table 4.1: *The TRF radiometric constants divided by the electronic's normal resistance (90 Ω for PREMOS; 50 Ω for VIRGO) and their standard uncertainties (k=1) were determined with monochromatic beams at a wavelength of 532 nm.*

4.8 Uncertainty Budget

We followed the GUM (BIPM, 2008) to estimate the standard uncertainties (k=1) of our measurements. Figure 4.14 shows the uncertainty budgets of the power respectively irradiance measurements with PREMOS-3. The total uncertainty for the radiant power measurements of the PMO6-type radiometers is dominated by the lead heating and the reflectivity. Expanding the

TRF beam to 7.3 respectively 11 mm, the stray light and the power readings of the instrument contribute most to the total uncertainty. The power readings uncertainty increases because of the open heater power varying with the beam scanning frequency (subsection 4.9.2).

In Figure 4.15 we present the total standard uncertainty budget for the power calibrations of the three PMO6-type radiometers. We apply the uncertainty estimates for a TRF calibration proposed by (Kopp et al., 2007) adding uncertainty components due to the offset fitting and the reproducibility of the measurements.

The uncertainty budgets for the irradiance calibrations (Figure 4.16 and Figure 4.17) show the main contributions to the total uncertainty from the PMO6-type radiometer power readings, from the offset fitting and from the reproducibility.

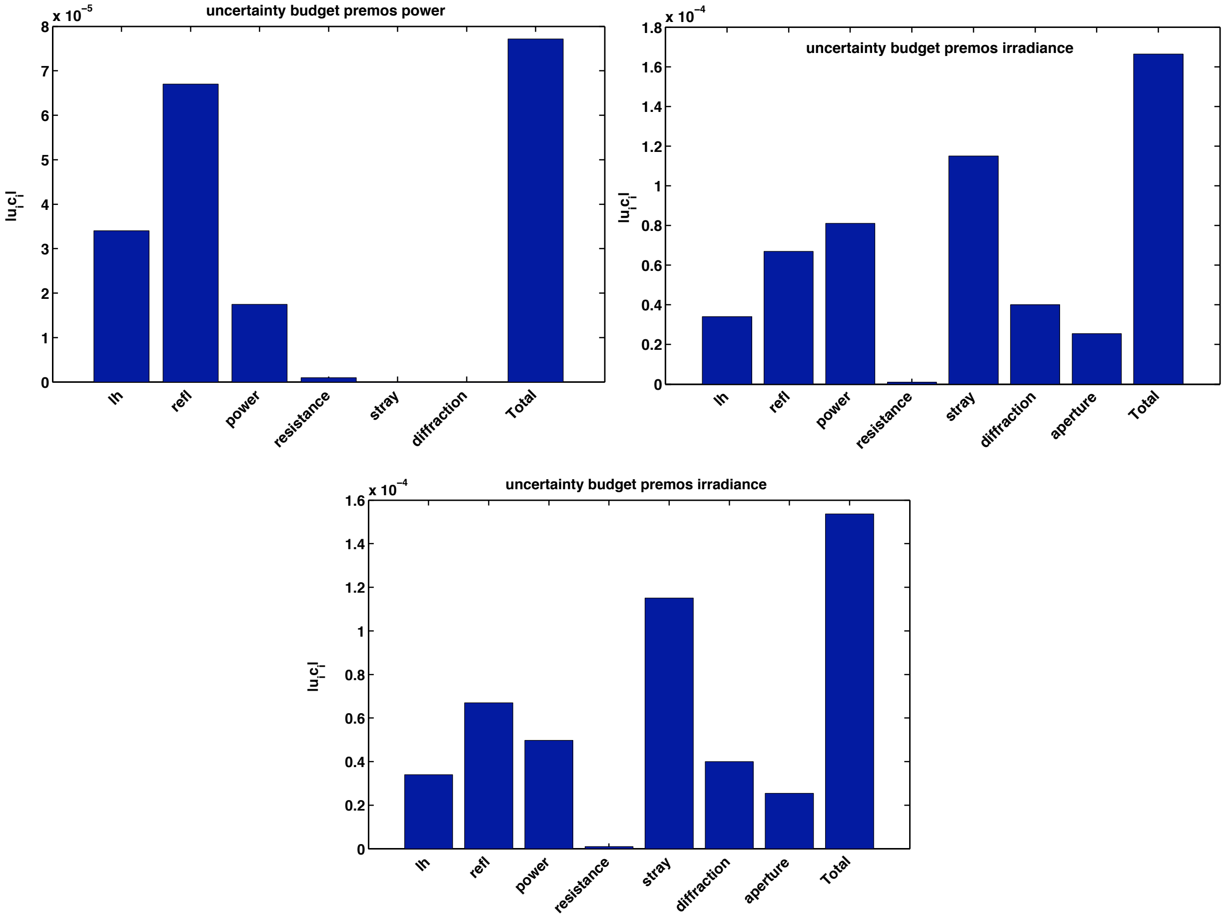

Figure 4.14: *The upper left plot shows a sample uncertainty budget for the power readings of PREMOS-3. The total standard uncertainty (k=1) is dominated by the lead heating effect and the reflectivity of the cavity. The upper right and the lower plot display sample uncertainty budgets for a 7.3 mm respectively 11 mm irradiance measurement of the same radiometer. Compared to the radiant power calibration, the stray light and the power readings add to the total standard uncertainty (k=1)*

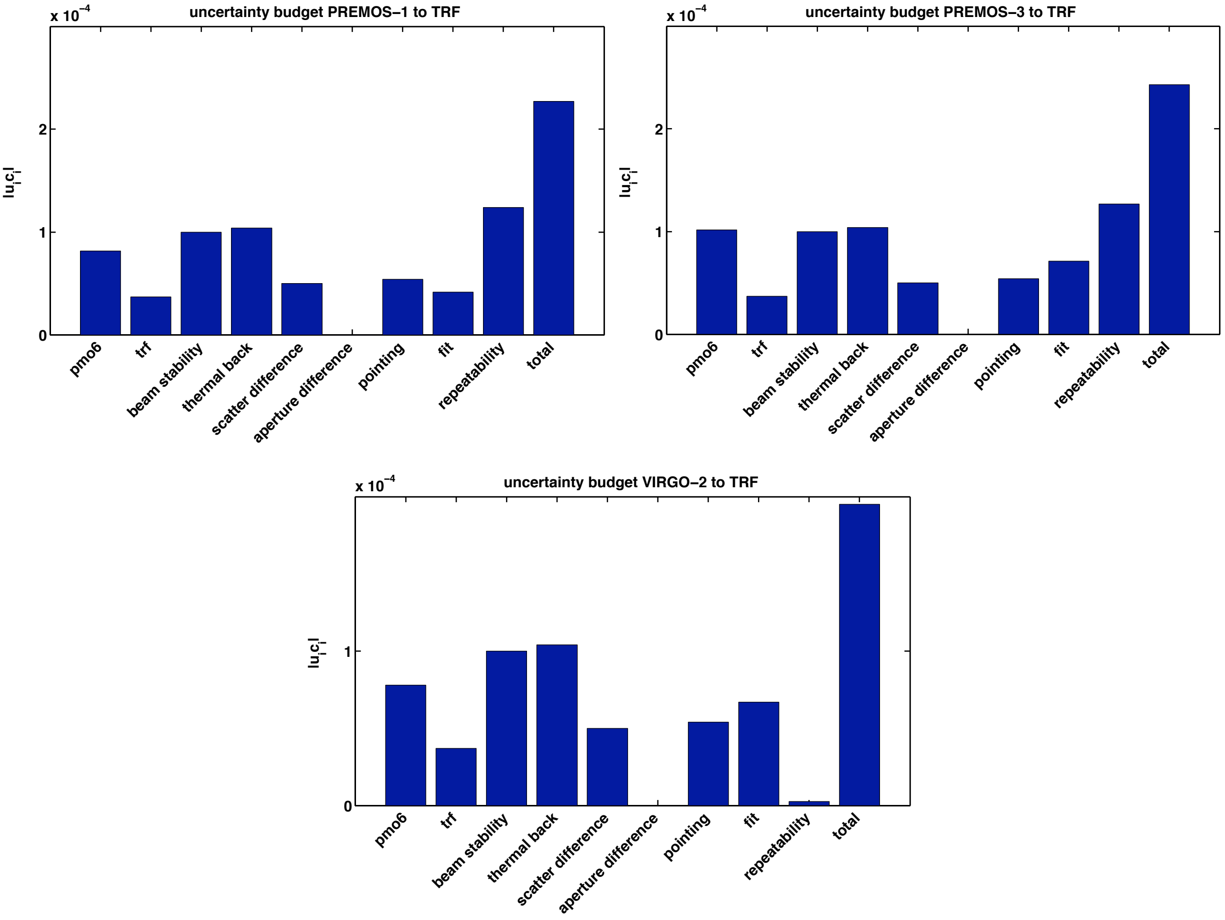

Figure 4.15: *The three plots show the uncertainty budgets for the TRF power calibrations of PREMOS-1, PREMOS-3 and VIRGO-2. The main contributions to the total standard uncertainty (k=1) stem from the PMO6 readings, the beam stability, the thermal background, the fitting procedure and the reproducibility of the measurements.*

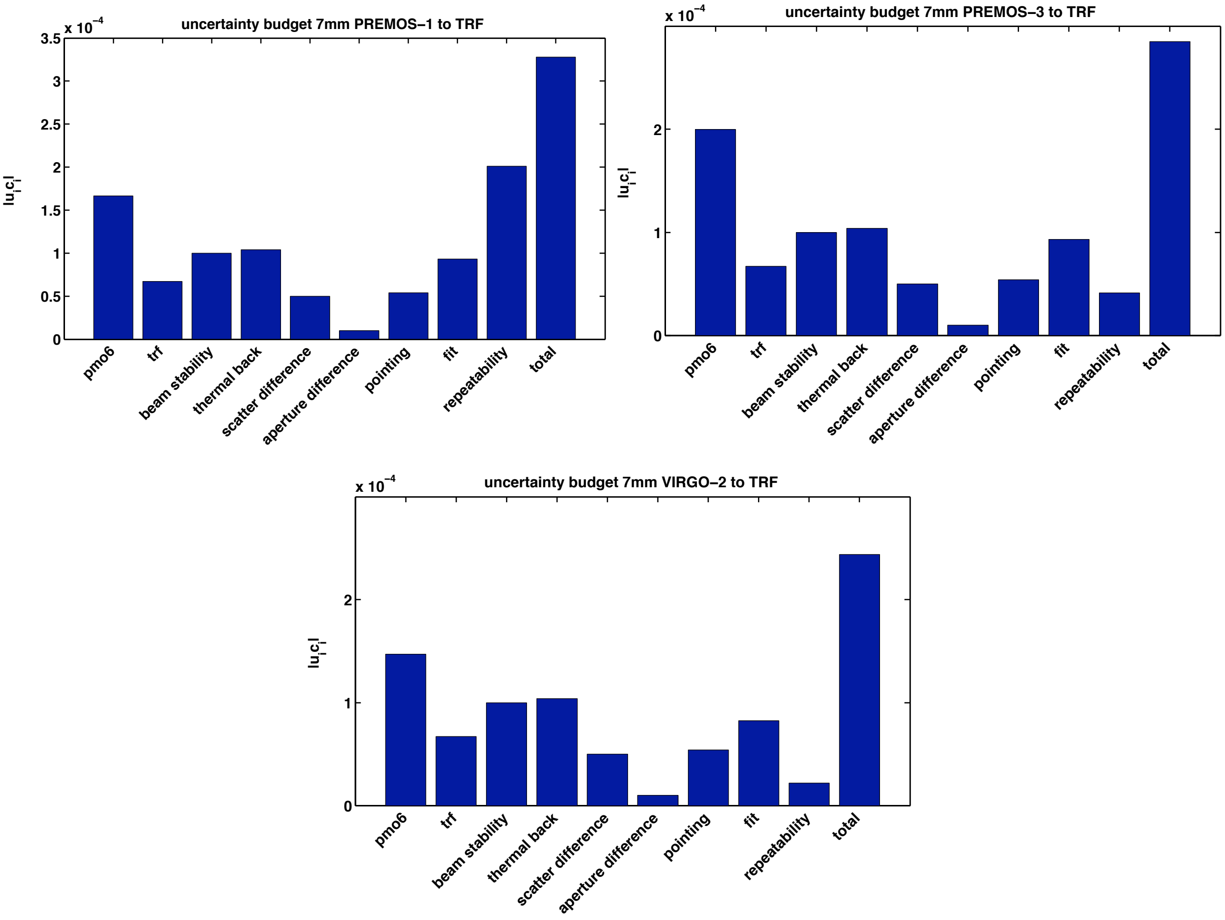

Figure 4.16: *The three plots show the uncertainty budgets for the TRF 7.3 mm calibrations of PREMOS-1, PREMOS-3 and VIRGO-2.The main contributions to the total standard uncertainty (k=1) stem from the PMO6 readings, the beam stability, the thermal background, the fitting procedure and the reproducibility of the measurements.*

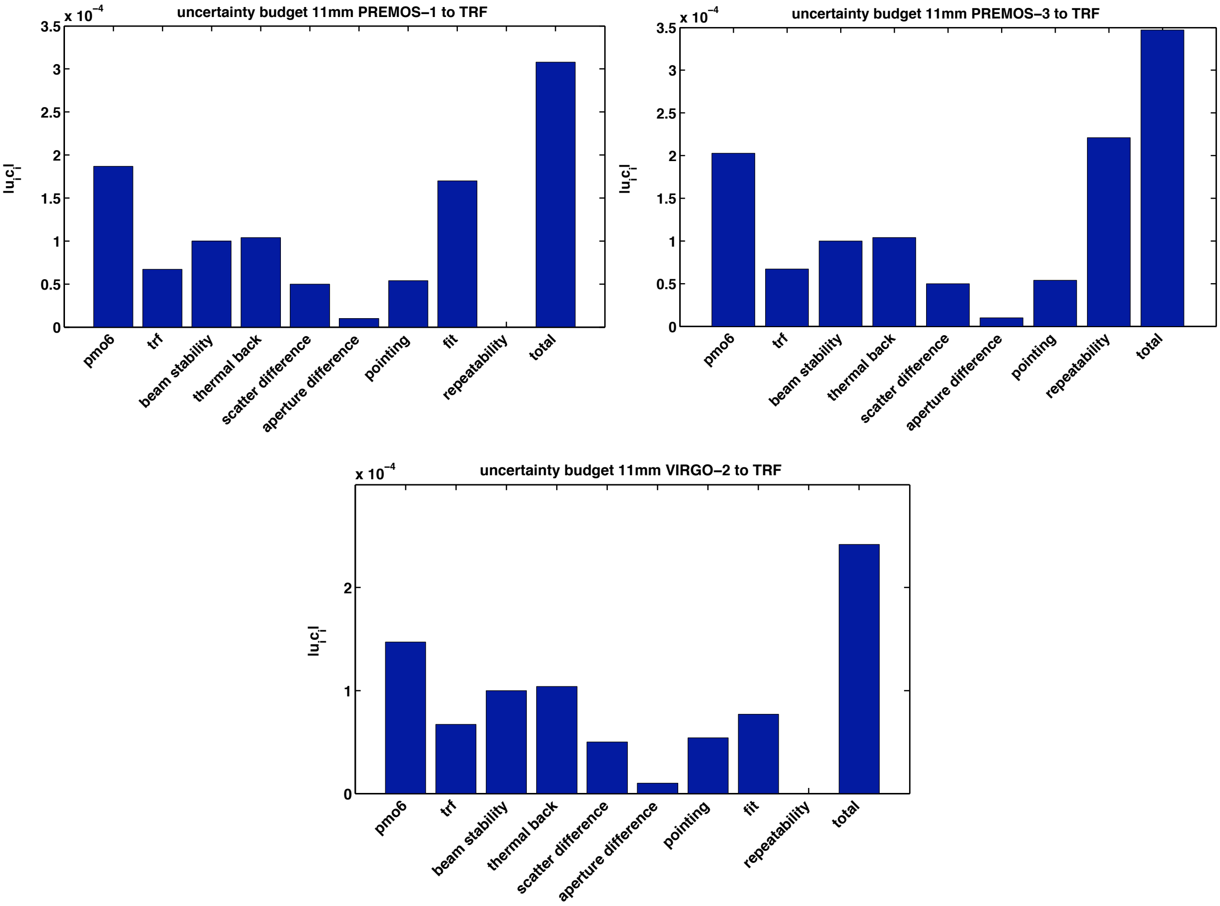

Figure 4.17: *These three plots show the uncertainty budgets for the TRF 11 mm calibrations of PREMOS-1, PREMOS-3 and VIRGO-2. The main contributions to the total standard uncertainty (k=1) stem from the PMO6 readings, the beam stability, the thermal background, the fitting procedure and the reproducibility of the measurements.*

4.9 Diagnostics

The versatile TRF beam allowed diagnostics experiments to better understand the measurements at the TRF and the facility itself. We discovered new facts about PMO6-type radiometers and identified unsolved problems possibly affecting the TRF calibrations.

4.9.1 Reflectance of the Cavities

The illuminated part of a PMO6-type radiometer cavity has a conical shape with the tip pointing towards the sun. By coating the cavity, the black paint forms a small droplet at the very tip of the cone. This droplet radius impairs the geometrical advantages of these cavities by causing diffuse reflections at the tip. We suspect this effect to contribute most to the overall reflectivity of our cavities.

The TRF has a camera capturing a 1:1 image of the reflection off the precision aperture to determine the aperture position and to monitor the pointing. Figure 4.18 shows sample reflectance images from the TRF and the PREMOS-3 aperture. The intensity apparently originating from within the cavity indicated by the red circle is an artifact of the interpolation used to create the contour plot. We used these images to look for a bright reflection off the PMO6 cavity tip. But even by enhancing the contrast and looking at the central portion of pictures (Figure 4.19), we are not able to detect the tip. We think that the cavity to camera distance is too large to capture the diffuse tip reflections but we plan to use this technique with a reduced distance to investigate the spatial reflectivity of our cavities in the future.

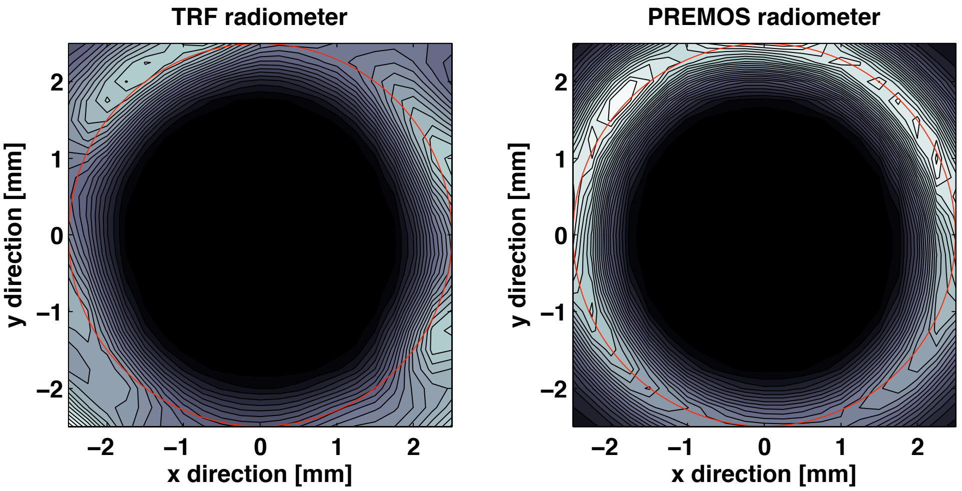

Figure 4.18: *Measured reflection off the radiometer cavities at the TRF. The red circle indicates the precision aperture edge.*

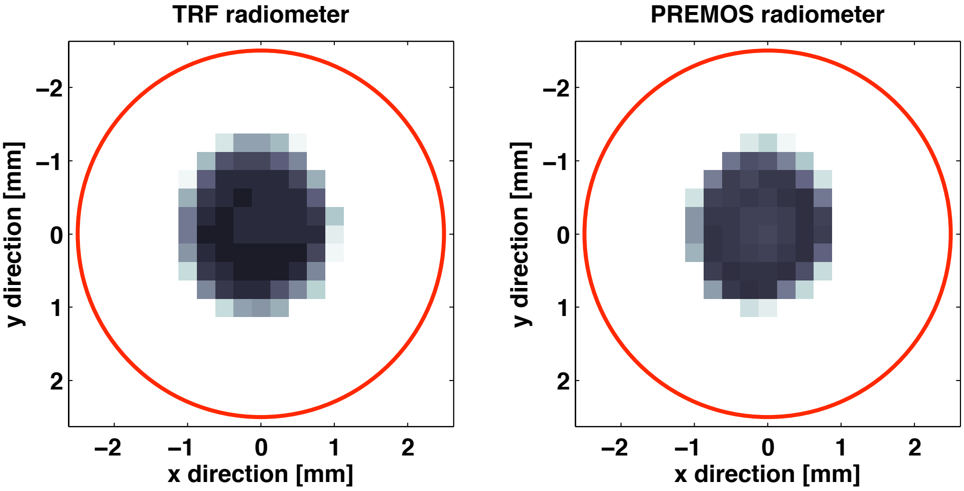

Figure 4.19: *Central part of the measured relative reflectance of the radiometer cavities at the TRF. The red circle indicates the precision aperture edge. The images look similar and we cannot detect a reflection off the PREMOS cavity tip.*

4.9.2 Sensitivity to the Beam Scanning Frequency

We used a versatile LabVIEW data acquisition program to sample the PMO6 heater power continuously allowing to monitor the response of the servo system of the electronics. The first irradiance calibrations revealed that, compared to the closed phase, the PREMOS heater power is scattering more during the open phase. To investigate this issue, we increased the sampling rate from 5 to 20 Hz and additionally acquired the error signal of the measurement bridge.

Figure 4.20 shows the heater power in the PREMOS-3 measuring cavity during an 11 mm TRF beam calibration. The closed phase heater power is stable scattering randomly around a mean value. The open heater power periodically changes with the 5 Hz frequency of the TRF beam. This indicates that the PMO6 cavities respond to the thermal change when the scanned laser beam moves in and out of the precision aperture to produce the 11 mm beam.

The error signal of the measurement bridge shows the same periodical variation with the TRF scanning frequency. The fluctuation is symmetrical with respect to the balanced state of the bridge indicating that the mean heater power represents the value we would obtain with a stationary source. Fitting a sine function to the open heater power acquired with different sampling rates confirmed this finding. Hence, we us the 10 s heater power average at the end of a measurement phase to determine the radiometer's power readings.

The sensitivity to the beam scanning frequency has not been anticipated and required further tests. We performed an experiment using the stable and stationary 0.5 mm diameter TRF laser beam at a power level of 2 mW. To simulate the effect of the laser moving in and out of the precision aperture, we used an external chopping wheel at frequencies of 43 and 5 Hz. The measurements showed that the chopping at 43 Hz is fast enough not to cause oscillations of the open heater power. At 5 Hz, we expected to see open heater power variations similar to those caused by the 11 mm scanning beam. However, the power readings remained as stable as for the closed respectively open 43 Hz measurements. The lacking response to the 5 Hz chopping

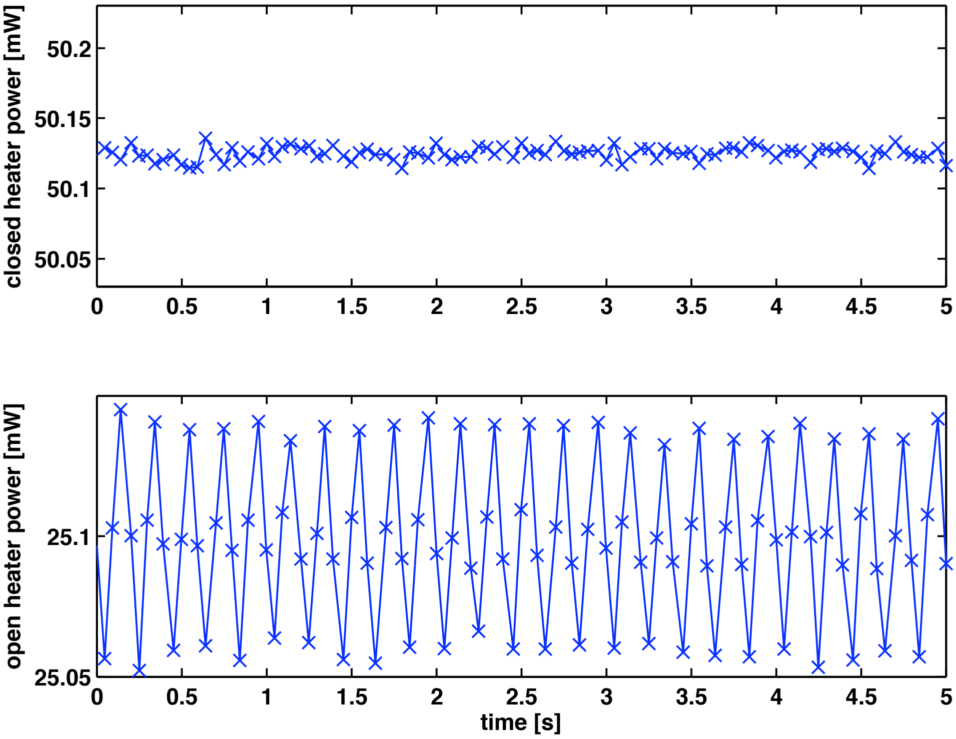

Figure 4.20: *The two graphs show the applied heater power in the measuring cavity of the PREMOS-3 radiometer. During the closed phase of the measurement (top), the applied power is stable. Illuminating the cavity with the scanned 11 mm TRF beam, the heater power periodically fluctuates with the scanning frequency of the beam (5 Hz).*

can be explained by the intrinsic power of the laser beam. The chopping experiment used a 2 mW beam dissipating a low power in the cavity. The 7.3 respectively 11 mm scanned TRF beams used 54 and 120 mW laser beams to simulate an irradiance field of 1000 W/m^2. Hence, the thermal changes in the cavities were 50 times larger than in control experiment. The servo system response is of the same magnitude being too small to be distinguished from the noise.

We should increase the power level for the chopping experiment to find oscillations of the heater power. But by illuminating our cavities at a narrow spot with a stationary 54 or 120 mW laser beam, we risk to damage them beyond repair. We could not risk to damage the radiometers with a long calibration history and hence can not conclusively resolve the PMO6-type radiometer sensitive to the TRF scanning frequency.

The TRF team has performed tests using the same chopper wheel, a 2 mW laser beam and a photo diode as reference. According to their measurements, neither the TRF cryogenic radiometer nor the TIM radiometer showed a noticeable sensitivity to the scanning frequency. Nevertheless, they ordered a new fast steering mirror allowing a faster scanning of the beam. Once this mirror is operational we will investigate the PMO6-type radiometer sensitivity to the beam scanning frequency at higher power levels.

4.9.3 Vacuum to Air Ratio

The correction factor for the measurement losses to ambient air introduces the largest uncertainty in the characterization of the PREMOS radiometers for ground based use in air (section 2.4). The TRF offered the opportunity to determine air-to-vacuum ratios using a different source. To determine the correction factor, we obtained a reference PREMOS to SI ration in vacuum ($< 10^{-5}$ mbar) before increasing the pressure. Intensity drifts of the TRF beam during the experiment were corrected using the data of the beam stability monitor. Table 4.2 presents the results of the PREMOS-3 and VIRGO-2 measurements. The PREMOS-3 data acquired at different pressure levels shows that the losses through the air are already prominent at 1.3 mbar and only marginally increase with higher pressure. This finding is consistent with the results from Ediss (2006) who found that the thermal conductivity of air saturates already at low pressures. Hence, the terrestrial PMO6-type radiometer measurements should be largely independent on the ambient pressure. However, the thermal conductivity of air depends on the temperature and hence we initiated an upgrade of the commercial PMO6 radiometers: A temperature sensor inside the heat sink is going to quantify the temperature dependence of the measurements. This experiment could explain some of the observed variations in the determination of the vacuum-to-air correction.

	2 mm beam	relative uncertainty	7.3 mm beam	relative uncertainty	11 mm beam	relative uncertainty
PREMOS-3 (1.3 mbar)	-	-	1.007282	0.000078	-	-
PREMOS-3 (133 mbar)	-	-	1.008307	0.000095	-	-
PREMOS-3 (880 mbar)	1.012039	0.000304	1.008064	0.000100	1.006482	0.000170
VIRGO-2 (880 mbar)	1.006737	0.000053	1.003500	0.000044	1.001752	0.000056

Table 4.2: *The non-equivalence factors determined at the TRF show a large beam size dependency. The 11 mm results are comparable to the vacuum-to-air ratios measured in front of the sun. All standard uncertainties are stated with a coverage factor of k=1.*

Similar to the results of Moebus (2005) our experiments revealed a beam diameter sensitivity of the vacuum-to-air ratio. Expanding the TRF beam from 2 to 11 mm reduces the vacuum to air ratio by a factor of at least 2. Comparing these results with the findings from the solar measurements in Davos, we would conclude that the 11 mm beam results best represent the situation in front of the sun. However, we should consider that the power level of the laser beam increases from 20 to 120 mW when expanding the TRF beam. The higher power density produces hotter spots in the cavity which are cooled more effectively through the air. The beam size sensitivity of the vacuum-to-air ration could not conclusively be resolved during the short comparison campaign. Hence we use the vacuum-to-air correction measured in front of the sun to correct PREMOS ambient air measurements. Neither the TRF nor the NPL calibrations are affected by this beam size dependency of the air-to-vacuum correction as these comparisons were performed in vacuum.

4.9.4 Diffraction and Stray Light

In the preceding sections we determined the amount of stray light by comparing the instrument calibration factors for different beam diameters. However, in subsection 4.9.2 we showed that the sensitivity to the beam scanning in and out of the precision aperture has not been conclusively solved. Therefore, we performed an experiment where the TRF beam never directly illuminates the cavity and the servo system remains balanced. The versatile TRF beam offers the opportunity to create an annular pattern with an inner diameter of 7.3 mm and an outer diameter of 11 mm. Assuming that we know the diffraction correction, this experiment allows to directly determine the stray light produced in the PMO6-type radiometer.

Illuminating the PMO6-type radiometer with the annular pattern yields a measurement signal from the beam wings, the scattered and the diffracted light and we have to subtract the diffraction and beam wing signals to determine the stray light. As the annular beam illuminates only the edge of the view limiting aperture, we have to consider solely the diffraction at this opening and hence use the view limiting diffraction correction factor of 0.999205 (section 2.5).

We use the 2 mm beam power measurements of the cryogenic radiometer to calibrate the beam monitoring photo diode and found a monitor current to optical power conversion factor of 1.21955 mW/µA. Applying the conversion factor to the 7.3 and 11 mm filled beam measurements, yields a total optical power of 54.3 mW respectively 125.7 mW in these beams. Dividing the expected optical power by the beam area, we calculate irradiance levels of 1297.67 and 1323.01 W/m^2. However, the cryogenic radiometer measures 1281.39 and 1299.42 W/m^2 for the same beams. The difference of up to 1.8 % can be explained by the inhomogeneity of the TRF beam on the percent level (Figure 4.3) and the fact that the monitor diode measures the entire power of the beam while the cryogenic radiometer samples only the central part. Hence, we apply an 1 % standard uncertainty (k=1) to the irradiance levels calculated from the monitor diode signal. The calculated irradiance for the 7.3 to 11 mm annular pattern is 1239 $\pm$ 12 W/m^2 which would produce a 0.98 $\pm$ 0.01 W/m^2 diffraction signal.

The TRF team determined the radial beam profile of the 7.3 to 11 mm annular pattern to estimate the radiation in the annulus wings entering the 5 mm precision aperture. They found a 0.0172 % signal corresponding to 0.012 mW for the 71 mW beam power level (Figure 4.21). This is in reasonable agreement with the TRF cryogenic radiometer measurements showing a 0.0105 mW signal for the annular pattern corresponding to an irradiance of 0.54 $\pm$ 0.05 W/m^2.

The measured, not diffraction and stray light corrected PREMOS-1 irradiance for the annular scan was 1.89 $\pm$ 0.014 W/m^2 (k=1). We subtract the signals due to the beam wing and diffraction to compute the amount of stray light. The final measured stray light signal of 0.36 $\pm$ 0.05 W/m^2 corresponds to 0.030 $\pm$ 0.004 % of the 1239 W/m^2 irradiance. This value is 5.5 times lower than the result found by expanding a filled TRF beam from 2 to 11 mm (section 4.5). However, the intensity distribution of the annular TRF beam (Figure 4.21) can explain the lower stray light results found with this experiment. From the beam intensity profile we estimate that the precision aperture is illuminated only with one third of the full irradiance. Hence, this experiment yields a total stray light effect of 0.09 $\pm$ 0.015 % (k=1) where we assumed a 30 % uncertainty on the scale factor.

Our findings also exclude stray light from the view limiting aperture edge suggested by Butler et al. (2008), as a main stray light component: Because the view limiting aperture edge is

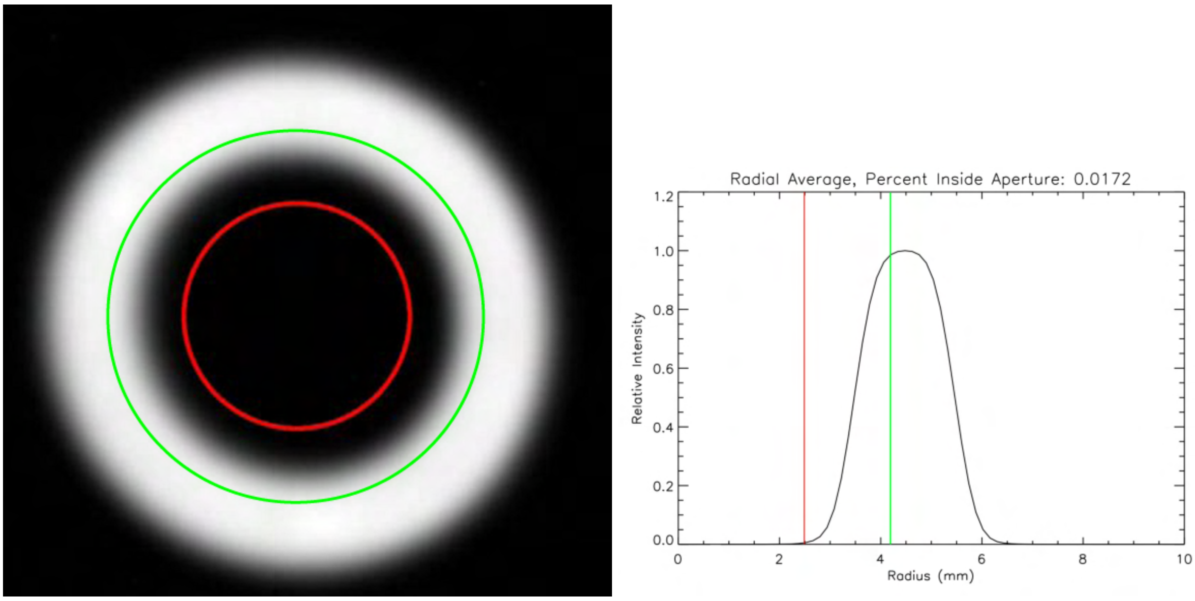

Figure 4.21: *The left picture shows a CCD image of the 7.3 to 11 mm annular TRF pattern. The red circle indicates the position of the 5 mm diameter precision aperture and the green circle shows the position of the 8.3 mm diameter view limiting aperture of the PREMOS-1 radiometer. The right graph displays the radial intensity distribution of the annular pattern. The edge of the view limiting aperture is illuminated with the full irradiance before the intensity declines across the precision aperture. The two graphics with courtesy of the TRF team.*

illuminated with the full irradiance, we would expect to find a stray light signal of the order seen with the beam expanding experiment which apparently is not the case. We prefer an explanation including two deflections: 1) The radiation impinging onto the precision aperture is reflected into the baffle system and onto the back of the view limiting aperture. 2) A fraction of the light is then reflected back into the cavity, causing the radiometer to read too high.

We also do not consider aperture heating an issue in this experiment. As the optical heating occurs where the thermal heat sinking of the aperture is good, we do not expect a large temperature rise and hence a negligible aperture heating effect.

4.9.5 Aperture Heating

Fröhlich (2006) explains the early sensitivity increase of the VIRGO radiometers with an increasing aperture heating due to darkening of the precision aperture. However, our experiments showed that the raised aperture temperature when the instrument shutter is open, can not cause the observed increase (section 2.7).

We created a 1 mm wide annular TRF pattern with a diameter of 6.3 mm to investigate the aperture heating effect with a different set up. Using the monitor current to optical power conversion from subsection 4.9.4, the applied TRF annular beam corresponds to a power of 32.21 ± 0.26 mW. As no aperture edges are illuminated in this experiment, no diffraction correction has to be applied and we can perform the calculation using optical power rather than irradiance. We use the TRF cryogenic radiometer measurements to account for the light in the beam wings entering the 5 mm precision aperture.

The PREMOS-1 radiometer measured a power of 0.48 mW. Subtracting the 0.44 mW beam wing radiation yields a 0.04 mW signal. This value corresponds to 0.1049 % of the incident power and must be due to the heating of the aperture and/or due to stray light. However, we are not able to separate the amount of stray light produced by this annular TRF beam. Hence, this experiment would only yield an upper limit of 1049 ppm for the aperture heating effect in vacuum.

However, the experiments in section 2.7 and the simulation in section 2.8 showed that the aperture heating effect changes from vacuum to ambient pressure by a factor of 5.7. We conducted the same experiment in air for PREMOS-1, using the 1 mm wide, 6.3 mm diameter annular beam and found a combined stray light and aperture heating effect of 1511 ppm. Using the two measured signals, the factor describing the increase of the aperture heating effect going from vacuum to ambient pressure and assuming that the stray light is not affected by the air to vacuum change, we can form a system of two equations with two unknowns. Table 4.3 presents the solution of the calculation and compares the results obtained in the previous sections. The measurement and the simulation agree very well for the steel aperture. The experimental results for the carbide aperture are a factor of two larger than the ANSYS simulations. This difference can be explained by the highly uncertain assumptions (e.g.absorptivity of the aperture material) made for the simulations. Hence, we use the difference between the simulation and the measurement to estimate a standard uncertainty (k=1) of 30 ppm for the 98 ppm aperture heating effect in vacuum for the carbide aperture.

	TRF 6.3 mm annular beam carbide aperture	PMOD/WRC el. heater steel aperture	ANSYS model carbide aperture	ANSYS model steel aperture
aperture heating vacuum [ppm]	98	233	46	181
aperture heating ambient [ppm]	560	1333	293	1200
stray light [ppm]	951	-	-	-

Table 4.3: *The measured and simulated aperture heating effects in parts per million for steel and carbide apertures do agree reasonably well. The uncertain absorptance properties of the aperture materials make a determination of a total uncertainty for the aperture heating correction difficult.*

4.10 Revised Stray Light Correction

The aperture heating experiment in the last section confirmed our finite element simulations and we include the correction to the PREMOS characterization (section 2.9). The stray light measurements are also affected by the aperture heating and have to be corrected accordingly.

4.10.1 Beam Expansion from 2 to 11 mm

Expanding the TRF beam from 2 to 11 mm, we determined a total stray light correction of 1800 ± 222 ppm which is 0.155 % more than the original Brusa and Fröhlich (1986) characterization for PREMOS-3. The aperture heating effect enhances the measured stray light by 98 ppm and 233 ppm for the PREMOS respectively VIRGO instruments. Hence, the final stray light correction factors for this experiment are:

	stray light correction factor	relative uncertainty (k=1)
PREMOS-1	0.998077	0.000342
PREMOS-3	0.998298	0.000222
VIRGO-2	0.997037	0.000257

Table 4.4: *Total stray light correction factor measured by expanding the TRF beam from 2 to 11 mm.*

4.10.2 Beam Expansion from 2 to 7.3 mm

Expanding the TRF beam from 2 to 7.3 mm, we determined a total stray light corrections being considerably higher than the original Brusa and Fröhlich (1986) characterization. The aperture heating effect enhances the measured stray light by 98 ppm and 233 ppm for the PREMOS respectively VIRGO instruments. Assuming a scale factor of 3 which accounts for the inhomogeneous illumination of the precision aperture, the final stray light correction factors for this experiment are:

	stray light correction factor	relative uncertainty (k=1)
PREMOS-1	0.999111	0.000360
PREMOS-3	0.998790	0.000330
VIRGO-2	0.997593	0.000260

Table 4.5: *Total stray light correction factor measured by expanding the TRF beam from 2 to 7.3 mm.*

4.10.3 Annular 7.3 to 11 mm Beam

Using a 7.3 to 11 mm annular TRF beam, we determined a 0.999100 ± 0.000150 total stray light correction factor for PREMOS-1. This result is compatible within the errors with the values from the beam expanding experiment. However, it does not account for possible stray light inhomogeneities across the precision aperture with this annular beam.

4.10.4 Annular 6.3 mm Beam (1 mm wide)

Applying a 1 mm wide, 6.3 mm diameter annular beam, yields a total stray light correction of 0.999049 for PREMOS-1. The measured stray light is enhanced by 98 ppm by the aperture heating effect. Hence, the final stray light correction factors for this experiment is 0.999147. We state no uncertainty for this value as unknown uncertainties from simulations affect the calculation. This result is in close agreement with the values found for the 7.3 to 11 mm annular beam. However, it does not account for possible stray light inhomogeneities across the precision aperture with this annular beam.

4.10.5 Conclusion

The 2 to 7.3 mm beam expansion and the two annular beam experiments yield very consistent stray light results for PREMOS-1. Expanding the TRF beam from 7.3 to 11 mm, we found a higher stray light contribution for this instrument. This difference could be due to the varying electrical heater resistance.

The flight instrument PREMOS-3 and spare VIRGO-2 radiometer were tested only with the beam expansion technique. The results from both expansions agree very well. We will use the stray light values from the 2 to 11 mm expansion for the final correction as we do not introduce uncertainties due to the beam intensity profile.

4.11 Discussion of the TRF Calibration

The TRF allowed us for the first time, to perform an SI traceable calibration of PMO6-type radiometers in irradiance and power mode. The power comparisons (section 4.2; section 4.4) confirmed the results found at the NPL (section 3.2). The irradiance calibrations (section 4.5; section 4.3) revealed that the classical PMO6-type radiometer characterization underestimates the amount of stray light. However, we still have to investigate the transformation of the stray light correction measured with a collimated, scanned and monochromatic laser beam to a correction factor for a slightly divergent broadband source. The necessary experiments can only be performed after an upgrade of the TRF providing sources with different wavelength.

Investigating the TRF data, we notice a larger scattering of the individual cryogenic radiometer measurement points compared to the PMO6-type radiometers. As a result, the uncertainty introduced by the offset fitting is larger than expected and the reproducibility of the comparison suffers. However, a statistical analyses of he 11 mm beam calibration of PREMOS-3 showed that we can assume a normal distribution of the measured offsets which allowed to reduce the estimated standard uncertainty (k=1) from 600 ppm to 221 ppm. The tight schedule did not allow more calibration runs to further reduce the uncertainties and we are collaborating with TRF team to better understand the scattering of the cryogenic radiometer measurements.

The diffraction correction calculated for a plane wave has not yet been proven to be valid for narrow gaussian beam scanned across the apertures. We need a novel theory rather than the classic diffraction approach where spheric waves from the entire aperture edge interfere with each other. Although we think that differences are marginal, the PMOD/WRC has initiated a collaboration with NIST and LASP to determine the appropriate correction factor for the TRF beam.

The TRF beam geometry introduces an extra uncertainty. The collimated TRF beam does not exactly reproduce the solar radiation which is divergent by a quarter of a degree. This beam divergency could have two implications: 1) The small incident angles of the solar radiation impinging on the precision aperture could cause different stray light than measured at the TRF. Performing stray light measurements by expanding the TRF beam from 2 to 7.3 mm and from 7.3 to 11 mm suggest that the stray light contribution from the precision aperture is not homogenous but slightly increases if the the outer most section of the aperture is illuminated. This fact supports our assumption of the stray light being caused by back reflections from the baffle system and the backside of the view limiting aperture. However, we think that the sun to TRF stray light difference is small but we are going to investigate this dependency by varying the incident angle of the TRF beam in future calibrations. 2) Reflections from the lands of the view limiting and precision aperture could cause a Sun/TRF stray light difference. But even if we assume that all radiation falling onto the aperture lands is deflected into the radiometer cavity, the resulting measurement bias is negligible.

The sensitivity of the PMO6-type radiometer measurements to the scanning frequency of the TRF beam could not be conclusively solved. As the PMO6-type radiometers showed a quick response to the laser moving in and out of the precision aperture, we were surprised that the cryogenic cavity, did not show a response to the scanning. Together with the TRF team we are investigating the damping influence of the TRF electronics to the measurements and we are planning calibration campaigns to resolve this issue.

Chapter 5

WRR Calibration at the PMOD/WRC in Davos and First Measurements in Space

5.1 WRR Calibration at the PMOD/WRC in Davos

The thigh schedule offered only a few very clear days to compare the PREMOS radiometers with the WRR in Davos. We performed measurements setting up the instruments individually in a big chamber sheltering them from environmental influences. Each instrument has been controlled by a commercial PMO6 electronics. The data was acquired using the standard WSG data acquisition system sensing the signals prior to the amplifiers of the electronic. Thereby we avoid additional corrections due to the temperature sensitivity of the electronics components.

PREMOS-1 and PREMOS-2 provided 198 respectively 179 valid data points from the 19th until the 30th of March 2008. Because of the replaced precision aperture, PREMOS-3 needed a new WRR calibration before the integration into the satellite package. We collected 127 data points on the 29th of July 2009 to calculate the WRR calibration factor presented in Table 5.1.

In addition to the WRR calibration run with the WSG data acquisition system, we performed comparisons using the flight electronics. The complete package with the radiometers installed, yielded calibrations comparable within the uncertainties to the results acquired with the WSG system. PREMOS-1 measured a total of 1458 valid points on 8 days. The 11 days of PREMOS-2 data yield 1773 valid points. And PREMOS-3 acquired 307 calibration points during 1 day of measurements. Figure 5.1 shows the distribution of the package data for the three PREMOS radiometers.

5.2 Fourth WRR to SI Comparison

We can use the NPL, the TRF and the WRR calibrations to compare the different scales. The absolute calibration of PREMOS-1 might be affected by the damaged heater and we use only the PREMOS-2 and PREMOS-3 data for the comparison. To use the VIRGO-2 data, we have to

	WSG DAQ	relative uncertainty	package DAQ	relative uncertainty	weighted mean	relative uncertainty
PREMOS-1	568.62613	0.001022	568.21743	0.001492	568.49559	0.001309
PREMOS-2	567.39082	0.001634	567.64127	0.001320	567.54233	0.001493
PREMOS-3	566.77927	0.000770	566.23882	0.000665	566.46929	0.000862

Table 5.1: *The WRR radiometric constants divided by the electronic's normal resistance (90 Ω) and their relative standard uncertainties (k=1) of the three PREMOS radiometers have been determined in Davos using two different data acquisition systems. We will use the weighted mean value of these results as the final calibration constant.*

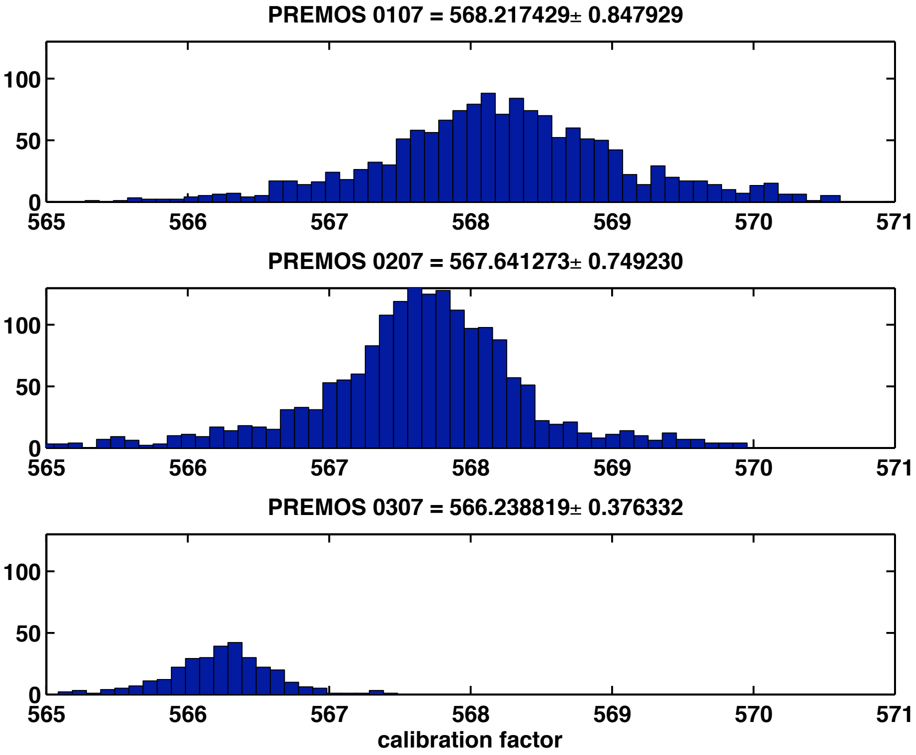

Figure 5.1: *The plots show the distribution of the radiometric constants divided by the electronic's normal resistance (90 Ω) determined with the PREMOS package data acquisition. The distributions also are representative for the calibration with the WSG DAQ system. The wide spread of the distributions contributes most to the WRR calibration uncertainty and ultimately to the standard uncertainty of the WRR calibrated TSI values measured in space.*

re-determine the WRR calibration factor for this radiometer after the ongoing construction work at the PMOD/WRC.

We use the calibration factors of the fully characterized PREMOS radiometers to repeat the three previous comparisons of the WRR and the SI radiant power scale. PREMOS-2 has a radiant power calibration at the NPL, a WRR calibration using the WSG data acquisition and a WRR calibration using the PREMOS data acquisition package. PREMOS-3 has identical calibrations and additionally has been compared with the TRF in power and irradiance mode. The weighted mean value calculated from the six WRR to SI radiant power comparisons (Table 5.2) is 1.001783 ± 0.001064, where the standard uncertainty (k=1) is dominated by the reproducibility of the WRR calibrations. Our findings are in good agreement with the first and the second comparison of the WRR and the SI radiant power scale. The third comparison however, lies 0.2 % below our result (Figure 5.2). As discussed in subsection 3.1.1 this difference could be partially explained by the non linearity of the trap detectors increasing the 2005 ratio by 0.04 %.

	WRR to SI	relative uncertainty
PREMOS-2 (WSG, NPL)	1.001370	0.001656
PREMOS-2 (package, NPL)	1.001812	0.001346
PREMOS-3 (WSG, NPL)	1.002334	0.000855
PREMOS-3 (package, NPL)	1.001379	0.000761
PREMOS-3 (WSG, TRF)	1.002345	0.000872
PREMOS-3 (package, TRF)	1.001390	0.000781
weighted mean	**1.001783**	**0.001064**

Table 5.2: *This table collects the six WRR to SI comparisons where the SI calibrations have been done in power mode, i.e. with the laser beam under filling the precision aperture. The relative standard uncertainties (k=1) are dominated by the WRR calibration uncertainty.*

Using the SI traceable irradiance TRF calibration and the WRR comparisons of PREMOS-3 (Table 5.3), we calculate a weighted mean WRR to SI irradiance scale ratio of 1.003272 ± 0.000999. The WRR calibration uncertainty and the TRF calibration uncertainty contribute in equal shares to the total standard uncertainty (k=1).

The difference between the WRR to SI radiant power scale and the WRR to SI irradiance scale comparison (Figure 5.2) is perfectly explained by the 0.15 % extra stray light found by expanding the TRF beam diameter from 2 to 11 mm.

	WRR to SI	relative uncertainty
PREMOS-3 (WSG, 11 mm TRF)	1.003798	0.000920
PREMOS-3 (package, 11 mm TRF)	1.002841	0.000833
weighted mean	**1.003272**	**0.000999**

Table 5.3: *This table collects the two WRR to SI comparisons where the SI calibrations have been done in irradiance mode, i.e. with the TRF beam over filling all apertures. The WRR calibration uncertainty and the TRF calibration uncertainty contribute in equal shares to the standard uncertainty (k=1).*

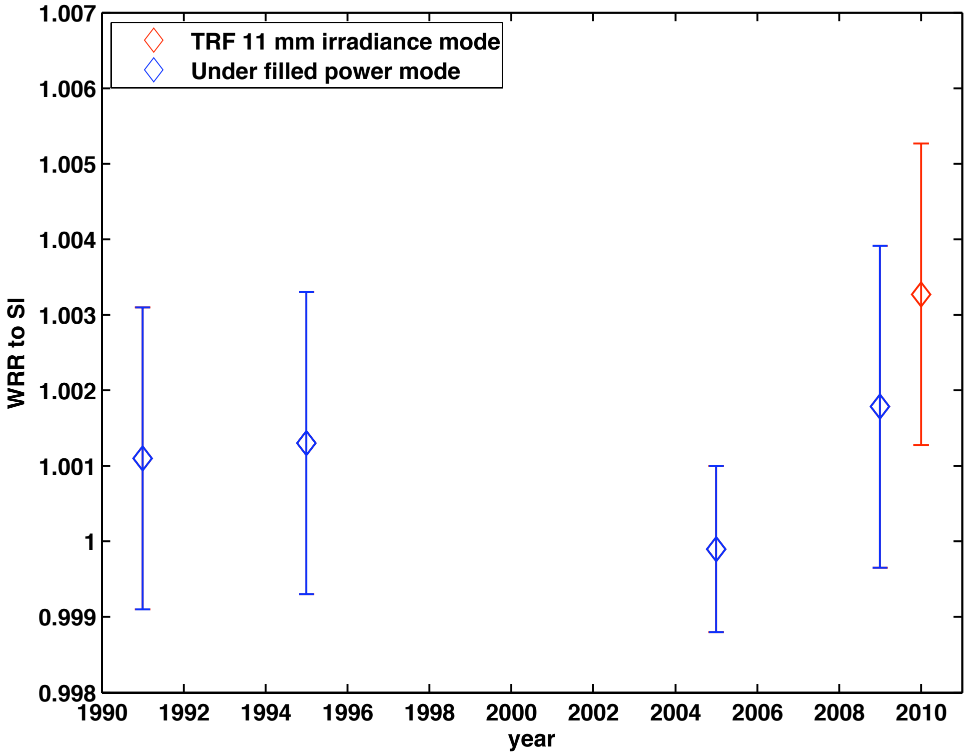

Figure 5.2: *The plot shows the four WRR to SI radiant power comparisons and their standard uncertainties (k=2). The first, second and our fourth comparisons agree whereas the third result is substantially lower. This difference could be partially explained by the non linear response of the trap detectors (subsection 3.1.1). Our experience with the fourth comparison also suggests that the uncertainty has been underestimated in 2005. Considering these two facts, the third comparison agrees with the other comparisons within the uncertainties.*

5.3 First PREMOS Measurements in Space

The PICARD satellite was launched on the 15^{th} of June 2010. After the commissioning phase, the PREMOS-A radiometer (PREMOS-3) saw its first light on the 27^{th} of July 2010. The back up instrument PREMOS-B (PREMOS-2) opened the shutter for the first time on the 6^{th} of August 2010.

Previous PMO6-type radiometers showed an early sensitivity increase with advancing exposure time (Figure 5.3). Hence, we concentrate our evaluation on the first light data of the instruments and asses the sensitivity changes at a later stage. However, to compare the two PREMOS instruments at the time of the radiometer B's first light, we have to correct the sensitivity increase of PREMOS-A. To determine the relative sensitivity increase of the PREMOS radiometers, we need the data of another space-borne instrument. We decided to use the TIM data as reference because the VIRGO level 2 data showed a temperature sensitivity at the time of the writing. During the first two days of exposure, the sensitivity of PREMOS-A increases linearly with 92 ppm per day (Figure 5.4) and we can determine a PREMOS-A sensitivity increase of 1.000176 ± 0.000003 for the time of the PREMOS-B's first light measurements.

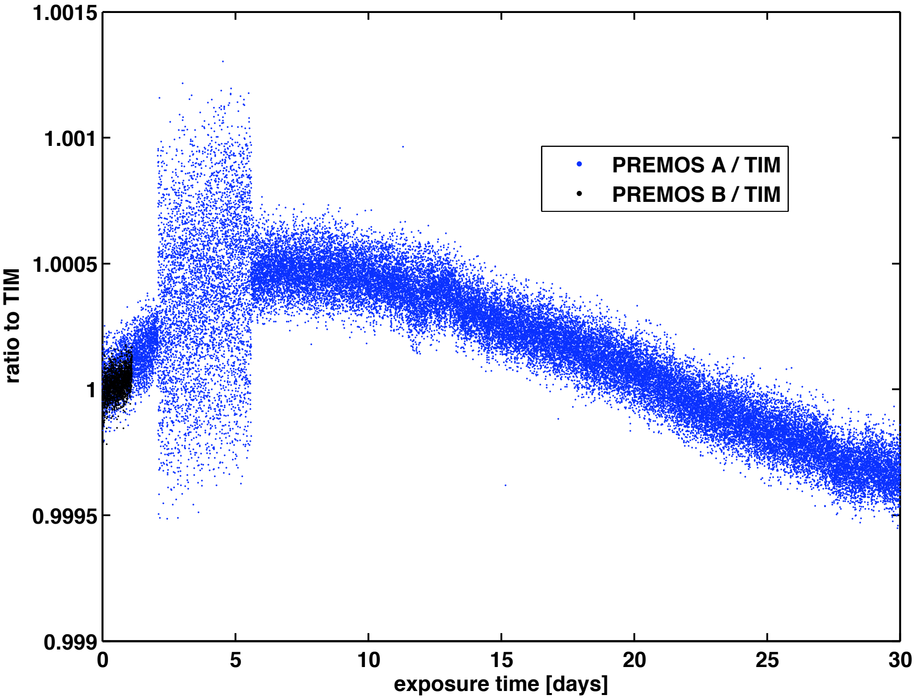

Figure 5.3: *The plot shows the sensitivity change of the PREMOS radiometers in space relative to the TIM. During the first seven days of exposure, the sensitivity of PREMOS-A increases by 500 ppm before declining. The increase is smaller than for VIRGO (600 ppm) by the amount we predicted from the aperture heating considerations (section 2.8). PREMOS-B shows an identical increase and we must consider this behavior when correcting the sensitivity degradation of PREMOS-A with the back up instrument B. The increased noise in the data from the third to the fifth day of exposure was caused by an additionally, pulse width modulated heater group being switched on.*

Transferring the WRR and the TRF calibrations into space, we have to correct the calibration constants (Table 5.4). The WRR calibration was determined at ambient pressure. In space the radiometers do not suffer from losses through air. Hence, we have to divide the WRR calibration constants by the non-equivalence factor.

The TRF calibration is valid for a monochromatic irradiance source. For the sun, the calculated diffraction correction factor decreases by 551 ppm. Hence, we have to reduce the TRF calibration factor by the same amount to use it for solar measurements.

Space-borne solar radiometer need a final correction accounting for the radiative energy exchange with the deep space surrounding the sun.

The optical power measured by the radiometers is the difference between the open and the closed heater power. During the closed phase, the cavity radiatively interacts with the muffler and marginally with the gold plated shutter. Once the instrument is open, the cavity exchanges radiation with the sun, the circumsolar region and the muffler. Brusa and Fröhlich (1986) assumed stable cavity and muffler temperatures as well as typical atmospheric conditions to find a maximal effect of 0.04 W/m^2 by which the irradiance is underestimated on the ground. In

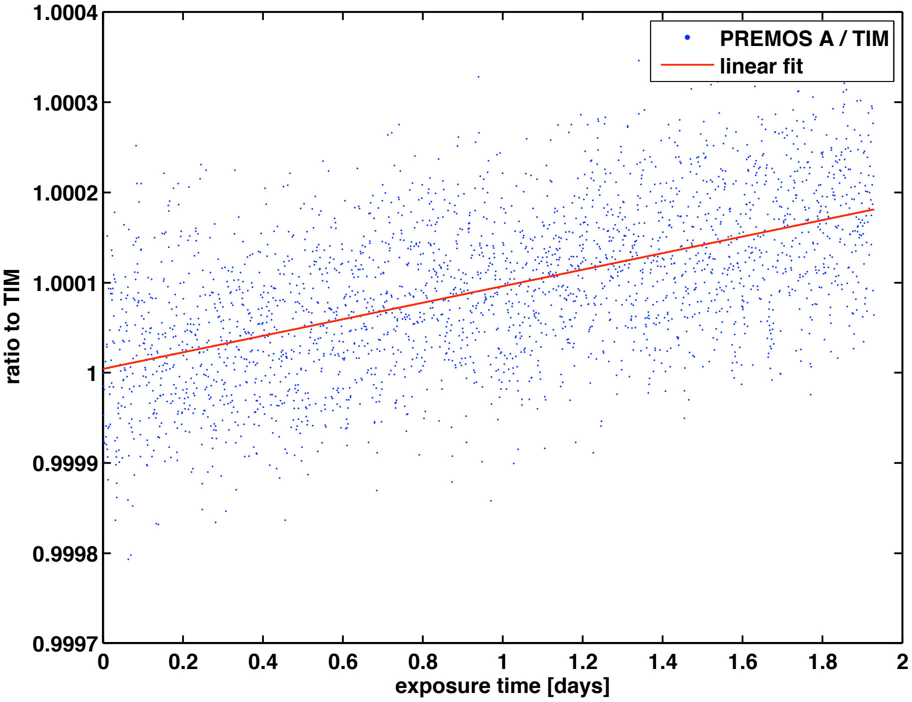

Figure 5.4: *The relative sensitivity increase of PREMOS A during the first two days of exposure is linear with a slope of 92 ± 3 ppm per day.*

	mean WRR	relative uncertainty	TRF	relative uncertainty
PREMOS-2 (B)	566.47000	0.001502	-	-
PREMOS-3 (A)	562.69417	0.000911	560.81590	0.000278

Table 5.4: *This table presents the final radiometric constants divided by the electronic's normal resistance (90 Ω) and their standard uncertainty (k=1) to be used for space measurements. The WRR calibration constant has been divided by the non-equivalence factor and the TRF constant has been reduced by the 551 ppm which accounts for the diffraction difference between solar and laser radiation.*

space however, the open radiometer loses much more energy to the 3 Kelvin cold deep space surrounding the sun.

The VIRGO instruments use a thermal radiometer model to calculate by how much we underestimate the measured irradiance. PREMOS can apply an identical thermal model but also offers the opportunity to directly measure the losses to deep space. The PICARD satellite offers a stellar operation mode aligning the optical axis with a star rather than the sun. The stellar pointing allows to characterize the SODISM telescope on the satellite. We use the stellar mode to run the PREMOS radiometers in the normal science mode measuring the losses to deep space. On the 6^{th} of October we collected the first stellar mode data and found a mean loss of -0.019 mW corresponding to to 0.95 W/m^2.

Applying the additional space corrections, we are able to determine the first results for PREMOS-A and PREMOS-B (Table 5.5).

	WRR calibration	standard uncertainty	TRF calibration	standard uncertainty
27. July 2010				
PREMOS-3 (A)	1365.5	1.2	1360.9	0.4
6. August 2010				
PREMOS-3 (A)	1365.3	1.2	1360.7	0.4
PREMOS-2 (B)	1366.4	2.1	-	-

Table 5.5: *This table presents the first light results of the PREMOS radiometers and their standard uncertainties (k=1). On the 27th of July, VIRGO states a TSI value of 1365.4 W/m^2 and the TIM measured 1361.3 W/m^2. On the 6th of August the VIRGO and TIM delivered values of 1365.1 W/m^2 respectively 1361.1 W/m^2.*

In Table 5.6 we compare the PREMOS measurements with the VIRGO and the TIM irradiance data. PREMOS-A on average measures 70 ppm higher than VIRGO and 3068 ppm more than the TIM if we use the WRR calibration. But if we apply the TRF calibration, PREMOS-A measures 281 ppm less than the TIM and 3268 ppm less than VIRGO.

PREMOS-B has only a WRR calibration which should yield the same irradiance value as for the instrument A. However, we find a PREMOS-B to PREMOS-A ratio of 1.000864. This difference can be explained by an underestimated non-equivalence factor for PREMOS-B as we could perform no vacuum-to-air measurements behind an inclined window for this radiometer. The difference between the two instruments is not affecting the absolute TSI value determined with PREMOS as we rely on the absolute calibration of the radiometer A and the measurements of the backup instrument B will solely be used to track the degradation of PREMOS-A.

	WRR calibrated to VIRGO	WRR calibrated to TIM	TRF calibrated to VIRGO	TRF calibrated to TIM
27. July 2010				
PREMOS-3 (A)	1.000047	1.003078	0.996709	0.999730
6. August 2010				
PREMOS-3 (A)	1.000093	1.003058	0.996755	0.999709
PREMOS-2 (B)	1.000957	1.003924	-	-

Table 5.6: *The WRR calibrated instruments agree with the VIRGO measurements. But if we use the TRF calibration, the PREMOS values agree with TIM. Hence, the difference between VIRGO and TIM can be explained by the usage of two different reference scales.*

5.4 Discussion

Throughout the PREMOS characterization and calibration campaign we experienced an excellent collaboration with teams at LASP and NPL involved in measuring the TSI. As a result we were able to bring the first SI traceable solar radiometers into space and to find an explanation for the differing extraterrestrial TSI measurements. The WRR respectively TRF calibrated PREMOS measurements show that the 0.3 % difference between VIRGO and the TIM (Figure 1.2) is due to two reference scales used. However, we have no confirmation of our result as PREMOS is the only experiment compared to the WRR and the TRF. The VIRGO radiometers are only traceable to the WRR. The flight TIM/SORCE instrument has not been calibrated against any scale but uses its characterization to determine an absolute TSI value. Calibrations of the TIM/SORCE witness instruments at the TRF are used to link the flight instrument to the TRF. Using this transfer, the TIM/SORCE team establishes the TRF traceability of the space-borne measurements supporting our findings (Kopp, 2010). We are awaiting the upcoming TSI experiments traceable to the WRR and/or the TRF to confirm our results.

The WRR to SI radiant power comparisons with a laser beam under filling the precision aperture, showed that the SI radiant power scale is 0.18 % lower than the WRR. However, this comparison cannot account for the stray light caused by reflections at the precision aperture. The measurements with the PMO6-type radiometers at the TRF could quantify the amount of stray light. The 0.17 % (PREMOS-3), 0.09 % (PREMOS-1) and 0.3% (VIRGO-2) corrections are much higher than suggested in the original characterization.

LASP is collaborating with other TSI instrument groups to determine the stray light in other radiometers. As all other instruments have a aperture geometry similar to our radiometers, we expect them to find similar results.

The remaining uncertainties with the TRF calibration of our radiometers are going to be resolved in upcoming comparison campaigns. 1) The transformation of the monochromatically determined stray light factor to a correction valid for the sun will be investigate at the TRF using different wavelengths. 2) We need a novel theory to describe the diffraction correction of a narrow laser beam scanned across a circular aperture. 3) We have to examine how to account for the different beam geometries provided by the sources (collimated beam at the TRF; solar radiation divergent by 0.25 degree). 4) The response of the instruments, including the TRF cryogenic radiometer, to the scanning frequency of the TRF beam should be characterized.

We expect the modifications to TRF calibration due to the above mentioned uncertainties to be small. Upcoming calibration facilities at PMOD/WRC and at the Naval Research Laboratory using broadband sources, will allow to perform valuable experiments to answer the remaining questions.

Conclusively we can say that PREMOS is the best understood and calibrated PMO6-type radiometer ever sent to space. The calibration and comparison data yield a consistent picture and solve the problem of differing TSI measurements in space that persisted for more than seven years. A collaboration has been proposed involving all TSI instrument teams, to use the new findings to create a single, unequivocal TSI composite from all the satellite based measurements.

Chapter 6

Transmission of the Direct Solar Radiation through the Atmosphere and the Entrance Window to the Cryogenic Solar Absolute Radiometer

Radiation entering the vacuum chamber of a cryogenic radiometer is attenuated by the entrance window. In laboratories, where polarized, monochromatic sources are used, we can apply Brewster or coated windows to minimize the reflection losses. For the Cryogenic Solar Absolute Radiometer (CSAR) however, we have to consider the broadband solar radiation impinging perpendicularly on our entrance window. To achieve the planned absolute accuracy in CSAR measurements, we have to determine the integral transmittance of the solar radiation through the CSAR entrance window to better than 0.01 %.

All evaluated window substrates show a wavelength dependent transmittance. And all materials cut off parts of the solar spectrum. In combination with the temporal changes of the solar spectrum, this makes the determination of the integral transmittance of solar radiation through a window a challenging objective.

6.1 The Solar Spectrum

A primary solar radiometer observes the sun and a narrow circumsolar portion of the sky. Hence, we concentrate our considerations about the solar spectrum on the radiation arriving directly from the sun at the CSAR radiometer. The solar spectrum reaching the top of the atmosphere differs from the spectrum that we observe on the ground (Figure 6.1), as the atmosphere absorbs and scatters parts of the solar radiation. It is the H_2O, the CO_2, the O_3, the N_2O, the CH_4 and the CO contributing most to the absorption. As the amount of these constituents changes, we observe variations of the solar spectrum along the line of sight. On the seasonal timescale, the water content of the atmosphere accounts for most of the variations. During a day, it is the changing air mass altering the irradiance by a maximal rate of up to 2 W/m^2 per minute in the morning and in the evening.

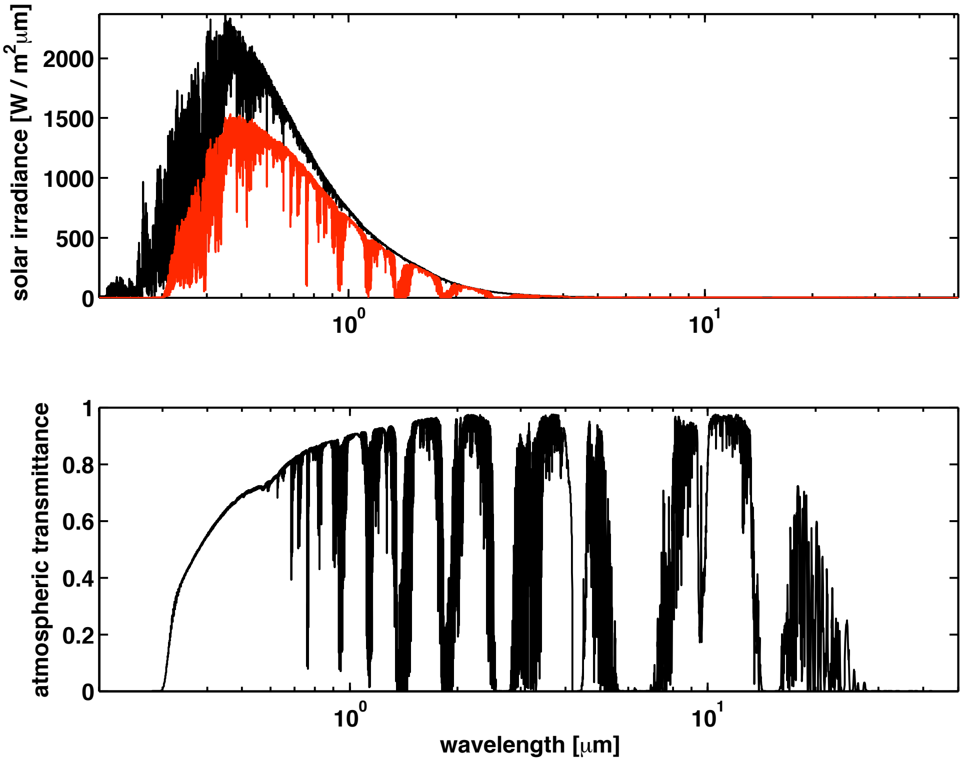

Figure 6.1: *The upper graph displays in black the Kurucz (1997) synthetic solar spectrum at the top of the atmosphere. The red curve shows the MODTRAN calculation of the transmitted solar spectrum for a standard mid-latitude Fall atmosphere. The strong absorption in the UV around 0.3 µm as well as the various absorption lines and bands become more evident in the lower plot where we show the spectral transmittance of the Earth's atmosphere.*

We use version 5.2 of the atmospheric radiative transfer code MODTRAN (Anderson et al., 1993; Berk et al., 2005, 2008) to generate synthetic solar spectra on the ground. MODTRAN has implemented standard atmospheres for Spring/Summer and Fall/Winter at a latitude of 45 degree North. The atmosphere models provide information on the vertical temperature and pressure profiles as well as the height dependent concentration of the constituents. However, these atmospheres represent a climatological mean rather than a clear sky condition and they are not in a hydrostatic equilibrium. But the standard atmospheres allow us to introduce sub-visual cirrus clouds with ice particle radii of 4 µm. Such clouds might unnoticeably influence our measurements and we need to estimate their contribution. For our considerations, we calculated mid-latitude standard (standard fa, standard wi and standard su) and mid-latitude standard cirrus (cirrus fa, cirrus wi and cirrus su) spectra for Fall, Winter and Summer.

To investigate the atmospheric influence on the solar irradiance measured in Davos under realistic conditions Fröhlich (2008) provided clear sky atmosphere models for the Alpine situation in Fall (Davos fa+0K), Winter (Davos wi+0K) and Summer (Davos su+0K). These atmosphere models incorporate temperature, humidity and pressure profiles from radiosonde measurements in Payerne. Modified versions of these atmosphere models, where the temperature has been

Model	H_20		CO_2		O_3		N_20	
	[atm cm]		[atm cm]		[atm cm]		[atm cm]	
	min	max	min	max	min	max	min	max
standard fall	522.3	2986.5	240.1	1342.2	0.3729	1.9778	0.1932	1.0853
cirrus fall	522.3	2986.3	240.1	1342.3	0.3729	1.9777	0.1932	1.0853
fall -2K	787.5	4498.9	240.8	1345.1	0.2824	1.4809	0.1961	1.1006
fall +0K	905.8	5174.4	241.1	1346.3	0.2824	1.4808	0.1961	1.1006
fall +2K	1039.0	5934.8	241.2	1346.8	0.2824	1.4807	0.1960	1.1000
standard winter	522.3	2986.5	240.1	1342.2	0.3729	1.9778	0.1932	1.0853
cirrus winter	522.3	2986.3	240.1	1342.3	0.3729	1.9777	0.1932	1.0853
winter -2K	449.2	2568.5	241.2	1348.5	0.3637	1.9193	0.1971	1.1070
winter +0K	519.7	2971.3	241.5	1349.9	0.3637	1.9192	0.1972	1.1071
winter +2K	600.1	3431.2	241.8	1351.2	0.3637	1.9191	0.1972	1.1071
standard summer	1600.8	9148.9	243.0	1356.2	0.3275	1.7215	0.1936	1.0860
cirrus summer	1601.0	9149.7	243.0	1356.3	0.3275	1.7214	0.1936	1.0861
summer -2K	693.9	3963.6	241.4	1348.4	0.3242	1.7170	0.1963	1.1020
summer +0K	799.8	4567.7	241.5	1348.7	0.3242	1.7169	0.1962	1.1012
summer +2K	919.0	5248.3	241.8	1350.5	0.3242	1.7169	0.1963	1.1016

Model	CO		CH_4		aerosols		cirrus	
	[atm cm]		[atm cm]		[550 nm	extinction]	[550 nm	extinction]
	min	max	min	max	min	max	min	max
standard fall	0.0685	0.3865	1.030	5.780	0.2207	1.2616	-	-
cirrus fall	0.0685	0.3865	1.030	5.780	0.2207	1.2616	0.0056	0.0314
fall -2K	0.0689	0.3887	1.045	5.858	0.2223	1.2708	-	-
fall +0K	0.0688	0.3881	1.045	5.859	0.2223	1.2708	-	-
fall +2K	0.0687	0.3874	1.045	5.857	0.2223	1.2708	-	-
standard winter	0.0685	0.3865	1.030	5.780	0.2207	1.2616	-	-
cirrus winter	0.0685	0.3865	1.030	5.780	0.2207	1.2616	0.0056	0.0314
winter -2K	0.0697	0.3935	1.050	5.889	0.2223	1.2709	-	-
winter +0K	0.0696	0.3928	1.050	5.891	0.2223	1.2709	-	-
winter +2K	0.0695	0.3922	1.051	5.892	0.2223	1.2709	-	-
standard summer	0.0677	0.3818	1.035	5.801	0.2444	1.3955	-	-
cirrus summer	0.0677	0.3819	1.035	5.801	0.2444	1.3955	0.0056	0.0311
summer -2K	0.0692	0.3902	1.047	5.874	0.2457	1.4032	-	-
summer +0K	0.0690	0.3893	1.047	5.871	0.2457	1.4032	-	-
summer +2K	0.0689	0.3889	1.048	5.875	0.2457	1.4032	-	-

Table 6.1: *Overview of the atmospheric constituents which contribute most to the atmospheric absorption of the solar radiation. We present a minimal value for the shortest path through the atmosphere, i.e. at a solar zenith angle of 0 degree, and a maximal value for a large air mass where the solar zenith angle is 80 degree.*

changed by ±2 Kelvin up to the height of the temperature inversion, completed the set of model atmospheres. Because of the temperature modification, the water content of the air changes and the pressure profile has to be recalculated to keep the model atmospheres in the hydrostatic equilibrium. The modified versions of the seasonal models (Davos xx+2K, Davos xx-2K) allow us to investigate the influence of the atmospheric water content and the temperature on the transmitted solar radiation.

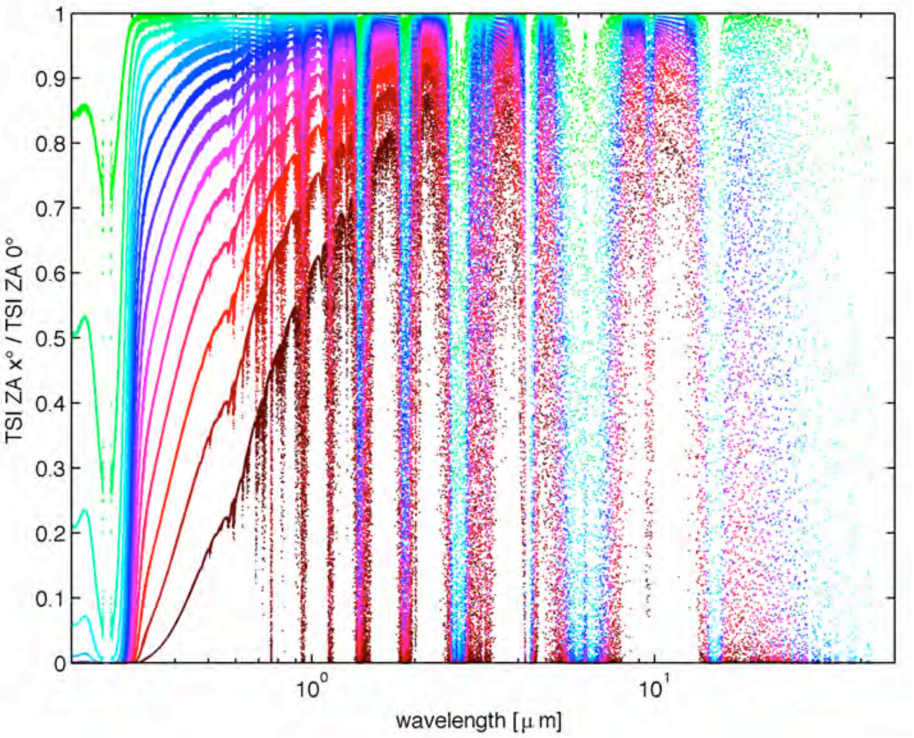

Figure 6.2: *To show the solar spectrum dependency on the solar elevation, we plot the Davos wi+0K spectra at increasing solar zenith angles relative to the zenith angle of 0 degree. The light green spectrum represents a zenith angle of 5 degrees while the dark red one is for 80 degrees. The absorption bands become wider with increasing air mass and the extinction at short wavelengths is enhanced by absorption and scattering processes.*

Table 6.1 summarizes values for the atmospheric constituents along the line of sight that contribute most to the absorption of the solar radiation in the atmosphere. Since the path length through the atmosphere changes with solar elevation, we present a minimal value at a solar zenith angle of 0 degree (path length 98.4 km) and a maximal value at a solar zenith angle of 80 degree (path length 473.1 km). Figure 6.2 shows the solar spectrum dependency on the solar elevation at ground-level. As expected, the absorption bands become wider with increasing total amount of gas in the line of sight. The decline of the short wave radiation is explained by the enhanced extinction and scattering processes for longer paths through the atmosphere (Table 6.1). As the most energy reaches the Earth at short wavelengths, the changing short wave radiation influences our measurements the most.

We also explored the spectral changes of the transmitted solar radiation depending on the season (Figure 6.3). At a solar zenith angle of 0 degree the variations in the absorption bands are as large as 100 %. And at the widest solar zenith angle, the changes are even larger. These seasonal spectral variations affect our measurements, if the window transmittance has sharp features in the same wavelength bands.

Figure 6.5 shows the total solar irradiance transmitted through the different model atmospheres. In Winter, the similar composition of the atmosphere models (Table 6.1) creates no significant

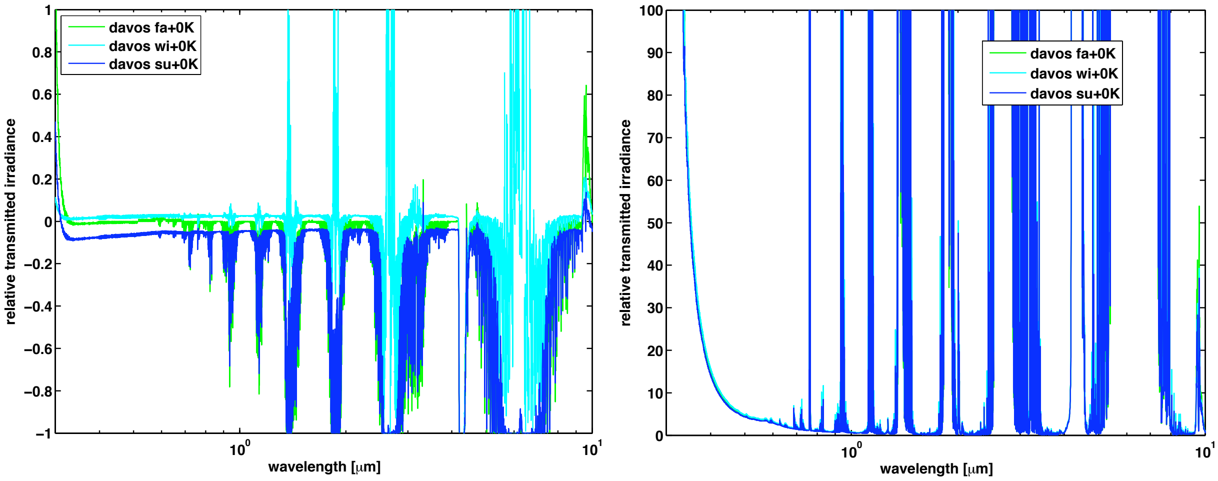

Figure 6.3: *The two graphs show the transmitted solar radiation for the Davos models relative to the standard fall model atmosphere. The left panel represents the situation at a solar zenith angle of 0 degree where the spectral variation between the seasons is as large as 100 %. The right plot shows the even larger spectral differences at a solar zenith angle of 80 degrees.*

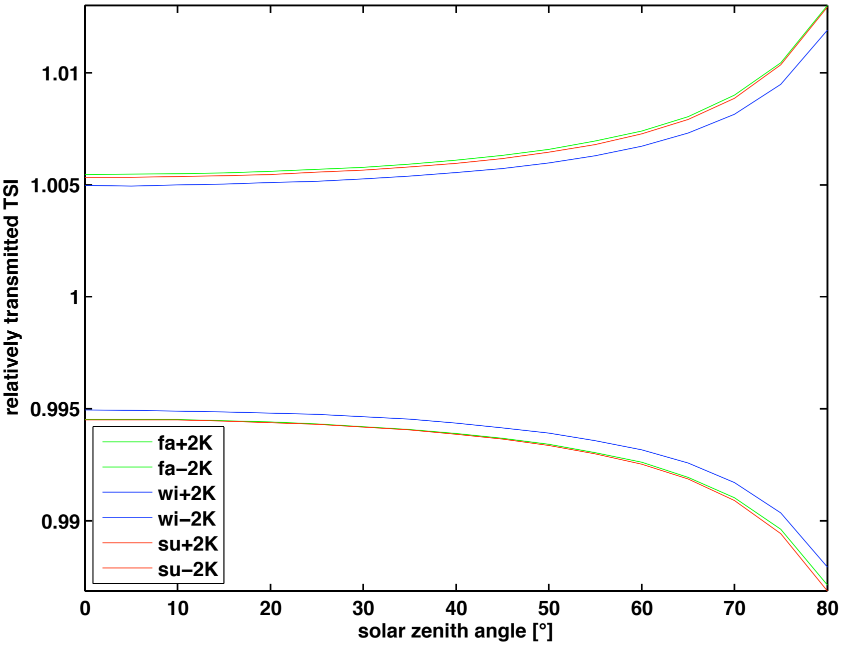

Figure 6.4: *Altering the temperature profile by ±2 Kelvin yields relative TSI changes that are larger than the intended uncertainty of the CSAR measurements.*

difference in the results. In Fall, the lower water content of the standard model atmospheres explains the higher irradiance values. And in Summer, the higher irradiance results are due to the lower water content of the Davos model atmospheres. Hence, a changing atmospheric composition can induce total solar irradiance changes larger than the intended uncertainty of the CSAR measurements.

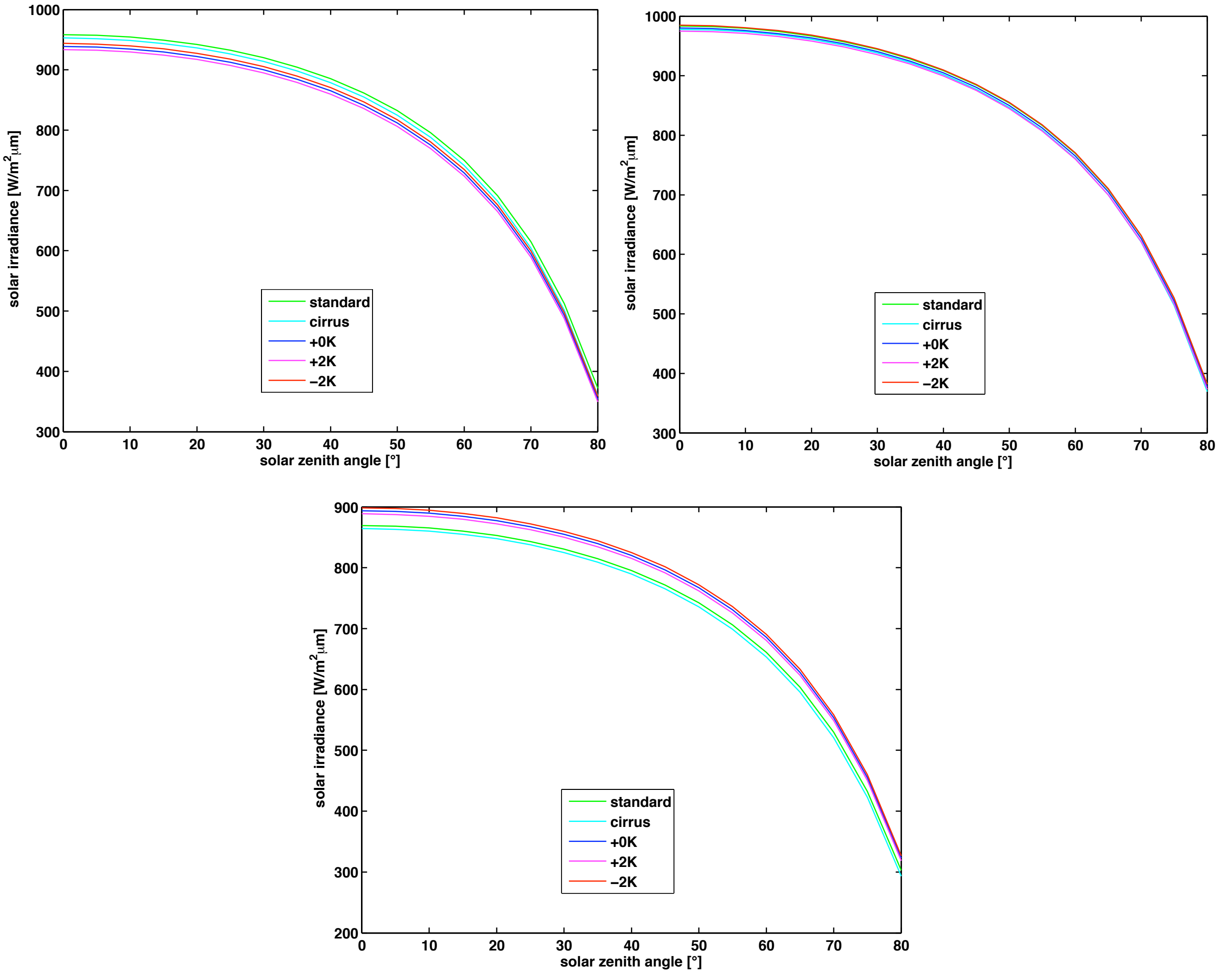

Figure 6.5: *The three graphs show the transmitted direct solar irradiance at the three seasons through the different model atmospheres. In Winter, upper right panel, we find no significant difference in the results. In Fall (upper left panel) and Summer (lower panel), the difference in the results is due to the dissimilar compositions of the model atmospheres (Table 6.1).*

The influence of the temperature and water content variations within the modified Davos atmosphere models on the transmitted solar irradiance is shown in Figure 6.4. Altering the temperature by ±2 Kelvin yields relative TSI changes of at least 0.5 % indicating that small temperature variations result in TSI changes which are larger than the intended uncertainty of the CSAR measurements.

The MODTRAN calculations show that the the TSI transmitted through the atmosphere changes on the one-tenth of a percent level due to: 1) Seasonal changes of the atmospheric composition. 2) Day to day variations of the temperature and humidity profile. 3) Diurnal changes of the solar elevation. In section 6.4 we use the calculated solar spectra to investigate the transmission through a specific entrance window and the resulting differences in the CSAR measurements.

6.2 Window Materials

The ideal window material would provide a high, constant transmittance over the entire solar spectrum. Hence, we could characterize the integral transmittance through the window by a single scale factor. Further, the window should be mechanically stable so that stress induced changes of the material properties do not noticeably alter the integral transmittance. The thermal conductivity would preferably be high in order to allow the determination and control of the window temperature and thus the radiative energy exchange between the cryogenic cavity and the window. And last, the entrance window should tolerate atmospheric moisture during the outdoor measurements without a degradation of the integral transmittance.

The transparency of most window materials is restricted to a wavelength interval. To decide on an appropriate window material, we have to know the solar spectrum reaching the Earth's surface below respectively above these cut-on/cut-off wavelengths. Table 6.2 and Table 6.3 summarize our results for the different atmosphere models and seasons. Figure 6.6 gives a graphical representation of the solar zenith angle dependency of the cut total solar irradiance.

We could select window materials which are transparent beyond the ozone absorption edge around 0.3 µm. However, in the infrared region of the solar spectrum it is much harder to chose a material. To keep the cropped total solar irradiance below the intended uncertainty of the CSAR measurement, we would need a window material which is transparent up to 20 µm.

Model	0.29 µm		0.30 µm		0.31 µm	
	sza 0° [ppm]	sza 80° [ppm]	sza 0° [ppm]	sza 80° [ppm]	sza 0° [ppm]	sza 80° [ppm]
standard fall	0	0	6	0	325	0
cirrus fall	0	0	6	0	325	0
fall -2K	0	0	18	0	468	0
fall +0K	0	0	18	0	470	0
fall +2K	0	0	18	0	472	0
standard winter	0	0	6	0	325	0
cirrus winter	0	0	6	0	325	0
winter -2K	0	0	7	0	331	0
winter +0K	0	0	7	0	332	0
winter +2K	0	0	7	0	333	0
standard summer	0	0	10	0	385	0
cirrus summer	0	0	10	0	385	0
summer -2K	0	0	10	0	380	0
summer +0K	0	0	11	0	381	0
summer +2K	0	0	11	0	383	0
extraterrestrial	7775	-	12055	-	16167	-

Table 6.2: *Fraction of the TSI below a given cut-on wavelength. Our calculations show that we do not cut a relevant portion of the total solar irradiance if we use a window material being opaque below a wavelength of 0.29 µm. We also determine the portion of the 1365 W/m^2 extraterrestrial total solar irradiance lying below a certain wavelength which represents the UV radiation being absorbed by the atmosphere.*

Model	3 µm		4 µm		5 µm		6 µm		7 µm	
	sza 0° [ppm]	sza 80° [ppm]	sza 0° [ppm]	sza 80° [ppm]	sza 0° [ppm]	sza 80° [ppm]	sza 0° [ppm]	sza 80° [ppm]	sza 0° [ppm]	sza 80° [ppm]
standard fall	15663	20818	4345	4618	1799	2230	1266	1914	1265	1914
cirrus fall	15649	20732	4340	4599	1798	2233	1266	1921	1265	1921
fall -2K	14915	19275	4130	4251	1618	1995	1214	1818	1214	1818
fall +0K	14658	18751	4057	4104	1560	1904	1193	1760	1193	1760
fall +2K	14396	18236	3986	3954	1503	1809	1172	1694	1172	1694
standard winter	15663	20816	4345	4618	1799	2229	1266	1914	1265	1914
cirrus winter	15650	20732	4339	4598	1798	2233	1266	1921	1266	1921
winter -2K	15825	21228	4368	4670	1837	2294	1277	1948	1276	1948
winter +0K	15593	20719	4298	4544	1773	2209	1257	1913	1256	1913
winter +2K	15355	20205	4227	4414	1712	2123	1236	1873	1236	1873
standard summer	13727	17535	3801	3551	1333	1466	1099	1415	1099	1415
cirrus summer	13714	17455	3797	3537	1333	1471	1099	1421	1099	1421
summer -2K	15374	20968	4241	4591	1690	2185	1240	1956	1240	1956
summer +0K	15120	20427	4169	4447	1630	2093	1220	1904	1219	1904
summer +2K	14860	19889	4097	4297	1571	2000	1199	1846	1199	1846
extraterrestrial	-	19999	-	8696	-	4594	-	2717	-	1729

Model	8 µm		9 µm		10 µm		15 µm		20 µm	
	sza 0° [ppm]	sza 80° [ppm]	sza 0° [ppm]	sza 80° [ppm]	sza 0° [ppm]	sza 80° [ppm]	sza 0° [ppm]	sza 80° [ppm]	sza 0° [ppm]	sza 80° [ppm]
standard fall	1273	1914	1266	1914	1231	1913	114	101	29	6
cirrus fall	1274	1921	1266	1921	1231	1920	114	100	29	6
fall -2K	1216	1818	1214	1818	1197	1817	94	78	18	2
fall +0K	1195	1760	1193	1760	1180	1760	89	71	15	1
fall +2K	1173	1694	1172	1694	1162	1694	84	64	13	0
standard winter	1273	1914	1265	1914	1231	1913	114	101	29	6
cirrus winter	1274	1921	1266	1921	1231	1920	114	100	29	6
winter -2K	1286	1948	1277	1948	1238	1947	116	104	31	8
winter +0K	1263	1913	1256	1913	1225	1912	110	97	28	5
winter +2K	1241	1873	1236	1873	1211	1873	104	90	24	4
standard summer	1099	1415	1099	1415	1095	1415	67	38	5	0
cirrus summer	1100	1421	1099	1421	1095	1421	67	38	5	0
summer -2K	1244	1956	1240	1956	1218	1956	102	91	22	3
summer +0K	1222	1904	1219	1904	1202	1904	96	83	19	2
summer +2K	1200	1846	1199	1846	1185	1846	90	76	16	1
extraterrestrial	-	1167	-	823	-	602	-	177	-	72

Table 6.3: *Fraction of the TSI above a given cut-off wavelength. Our calculations show that relevant portions of the total solar irradiance in the infrared extend up to a wavelength of 20 µm. We also present the portion of the 1365 W/m^2 extraterrestrial total solar irradiance lying above a certain wavelength which represents the infrared radiation being absorbed by the atmosphere.*

Chemical Vapor Deposited Diamond (CVD)

Diamond windows being produced by chemical vapor deposition (CVD) have many advantages but also a few serious drawbacks. Diamond has a wide spectral transmission range from 225 nm to the far infrared (Figure 6.7). It is mechanically stable which would allow us to use a very thin and easily to clean - since scratch resistant - window. Diamond is not hygroscopic, making the outdoor utilization possible without restrictions. And diamond has a high thermal conductivity that is about five times higher at room temperature compared to copper. Hence, we would be

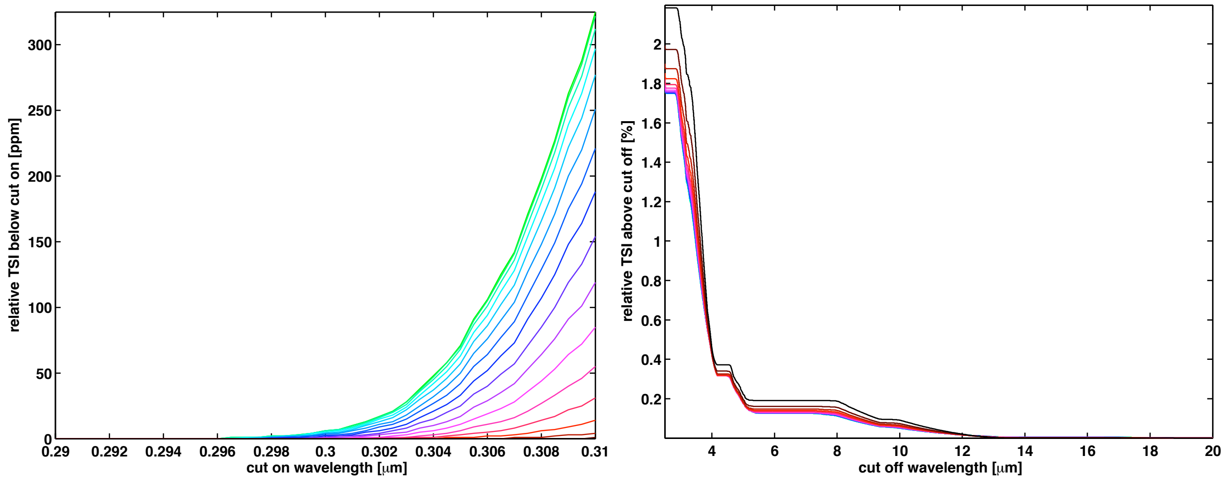

Figure 6.6: *The two graphs show the solar zenith angle dependency of the cut total solar irradiance. The light green line represents the cuts at a solar zenith angle of 0 degree whereas the dark red line shows the result at a solar zenith angle of 80 degrees.*

able to stabilize the window thermally and to accurately determine the emission of the diamond window.

However, CVD has a polycrystalline structure and carbon inclusions may produce an unpredictable amount of absorption or stray light. Further, due to the high refractive index of n =2.4, diamond suffers from severe Fresnel losses. There exist anti-reflection coatings but these are optimized for specific wavelengths - usually 10 μm for CO_2 lasers and we cannot reduce the 30 % reflection losses over the desired spectral range. Moreover, the spectral transmittance of diamond is not constant over the entire spectral range. We find absorption bands around 5 μm which are due to phonon processes. Calculating the total solar irradiance transmitted through diamond yielded a scale factor of about 1.5 that linearly scales the transmitted irradiance. We varied the spectral irradiance between 4.2 and 6 μm by ±5 %, redetermined the scale factor and found a change of about ± 50 parts per million. Hence, using a singularly determined transmittance factor for diamond and assuming a moderate variation of the spectrum yields a variation to the transmitted irradiance which is as large than the intended total CSAR uncertainty. The MODTRAN simulations showed that the variations in the spectrum are larger than in this test (Figure 6.3) making the real time monitoring of the integral transmittance of the diamond window mandatory.

Potassium Chloride

Potassium Chloride (KCl) is the most promising out of several crystals (NaCl, KBr, CaF_2) which have a high and almost flat transmittance spectrum ranging from 0.21 to 20 μm (Figure 6.7). Since KCl windows are grown as a single crystal, they have no inclusions producing stray light. Thanks to the low refractive index of n = 1.46, we would profit from a transmittance of over 90 % in the desired spectral range.

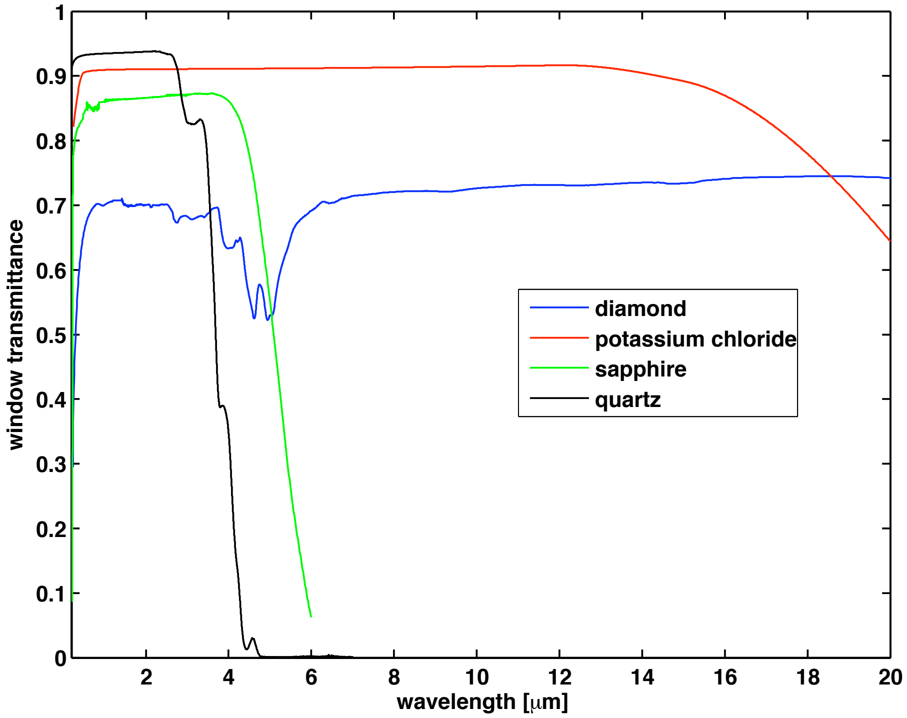

Figure 6.7: *Out of the four entrance window material candidates potassium chloride (KCl) shows the best total transmittance properties. Diamond is transparent far into the infrared but suffers from severe Fresnel losses due to the high refractive index and has some absorption bands between 4 and 6 µm. Sapphire and quartz become opaque at moderate wavelengths. The lower refractive index of quartz compared to sapphire results in a slightly higher integral transmittance of a solar spectrum through a quartz window.*

However, KCl has a low thermal conductivity of 6.53 $\mathrm{Wm^{-1}K^{-1}}$ at room temperature making the thermal stabilization of the window harder. The softness of KCl makes the material susceptible to scratching. The most crucial point of using Potassium Chloride is the degradation due to atmospheric moisture. At first, KCL appears not applicable for outdoor measurements. But a Diamond Like Carbon coating (DLC, Lu et al. 1992) having all the nice properties of diamond, could resolve this problem. The attenuation by the absorption bands does not persist because we could use a very thin coating layer. Further, these coatings have the nice feature of a tuneable refractive index.

Discussions with manufacturers of such DLC coatings revealed that their technique is not yet sophisticated enough to guarantee a satisfactory protection of a KCL window against atmospheric moisture. The main problem is the micro stress between the substrate and the coating causing hairline cracks in the coating. Through these gaps water might enter and degrade the window surface. Hence, we have to abandon the idea of using hygroscopic crystals at the moment but we will follow the development of DLC coatings and reconsider this idea when the manufactures have perfected their technique.

Quartz and Sapphire

Since we can not use potassium chloride as an entrance window material and a diamond window demands the real time monitoring of the integral transmittance, we also considered more conventional materials like sapphire and quartz. Their hardness and insolubility in water makes them ideal materials for outdoor applications. However, they become opaque at moderate wavelengths (Figure 6.7). Unlike for diamond, we cut off a relevant portion of the infrared solar spectrum. And as the solar spectrum considerably changes above the cut off wavelength, this makes a monitoring of the integral transmittance through quartz/sapphire windows inevitable. After evaluating all possible window material candidates, we realized the need to develop a Monitor to measure the Integral TRAnsmittance of windows (MITRA, chapter 7).

Calculations with the MODTRAN solar spectra showed that the low refractive index of quartz compared to sapphire and diamond results in the highest integral transmittance. Hence, we bought three windows for the CSAR project made from the high quality quartz Suprasil 3002. And for testing purposes we ordered two quartz windows made from Suprasil 300 and two single crystal spahhire windows. Table 6.4 summarizes the physical properties of the three window materials.

	Suprasil 3002	Suprasil 300	Sapphire single crystal
orientation	random	random	C oriented[1]
diameter	12 cm	2.54 cm	2.54 cm
thickness	1 cm	0.6 cm	0.3 cm
inclusions (DIN 58927)	no	no	no
bubbles (ISO 10110-3)	1/ 1·0.10	1/ 1·0.16	no
striae class (ISO 10110-4)	2 / -;5	N/A	no
Δn (peak to peak)	$\leq 5 \cdot 10^{-6}$	N/A	N/A
residual strain (center)	$\leq$6 nm/cm	$\leq$5 nm/cm	N/A
surface form (ISO 10110-5)	3 / 0.5	3 / 0.5	3 / 0.5
surface quality	10-5 (MIL-0-13830A)	10-5 (MIL-0-13830A)	10-5 (MIL-0-13830A)
surface parallelism	$\leq$1 arcmin	$\leq$10 arcsec	$\leq$10 arcsec
density	2.20 g/cm^3	2.20 g/cm^3	3.98 g/cm^3
Young modulus	70 GPa	70 GPa	345 GPa
specific heat capacity (293 K)	772 J/(kg K)	772 J/(kg K)	765 J/(kg K)
thermal conductivity (293 K)	1.38 W/(m K)	1.38 W/(m K)	42 W/(m K)
thermal expansion (293 K)	$5.1 \cdot 10^{-7}$ K^{-1}	$5.1 \cdot 10^{-7}$ K^{-1}	$7 \cdot 10^{-6}$ K^{-1}

Table 6.4: *Physical properties of the chosen entrance window materials. Heraeus provided the data for Suprasil and Boston Piezo-Optics the information about single crystal sapphire.*

---

[1] The C oriented single crystal sapphire window is free of birefringence for a light ray impinging perpendicularly on the surface.

6.3 Spectral Transmittance Measurements

The chosen quartz and sapphire windows make the real time monitoring of integral transmittance of the solar spectrum through the windows mandatory. But once the cryogenic radiometer is running, we can not remove the entrance window and we have to use an identical window in front of the monitor. The equivalence of the two windows is crucial for the total uncertainty of the CSAR measurements. To compare the entrance windows, we have to know their spectral transmittance. The NPL measured the transmittance of the three CSAR suprasil 3002 windows Ax, Ay and Az from 0.2 up to 3 µm with the monochromator based facility Cary 5E. Because the CSAR radiometer has six entrance apertures, the measurements were repeated for the six positions P1 to P6 on the windows where solar radiation will enter the instrument. METAS used a monochromator based system to measure the transmittance of the two suprasil 300 and the two sapphire test windows from 0.3 to 1 µm. At the PMOD/WRC we determined the transmittance of the two suprasil 300 test windows from 1 to 7 µm with a Bentham monochromator system. And Boston Piezo-Optics, the manufacturer of the sapphire test windows, provided a mean transmittance measurement of the two sapphire windows. Figure 6.10 and Figure 6.9 show the results of the measurements together with the calculated theoretical limit to the transmittance. The theoretical value considers the Fresnel losses due to multiple reflections but not the internal absorption of the window material.

The measured spectral sapphire transmittance agrees well with the theoretical value and the relative difference between the two windows (Figure 6.8) shows that they can be considered identical within the measurement uncertainty of 0.5 % .

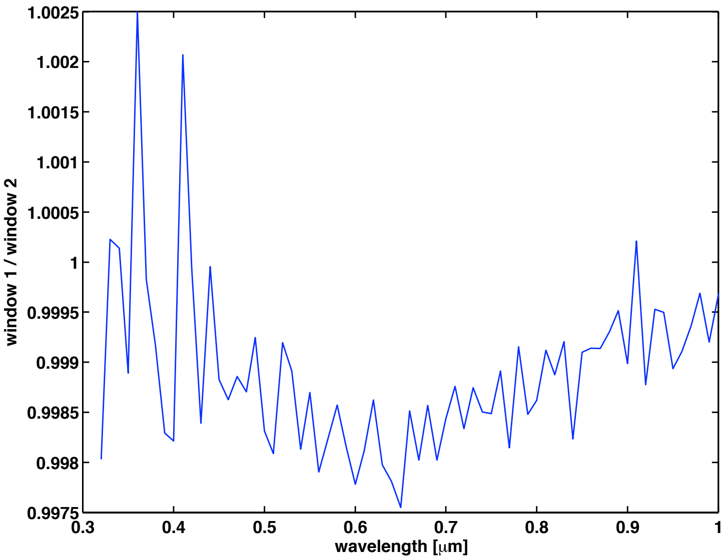

Figure 6.8: *The graph shows the spectral transmittance ratio of the two sapphire windows measured by METAS. Boston Piezo-Optics only provided a mean transmittance measurement of the two windows. So we cannot compare the windows above 1 µm. But for the METAS measurements we can consider the windows identical within the stated standard uncertainty (k=1) of 0.5 %*

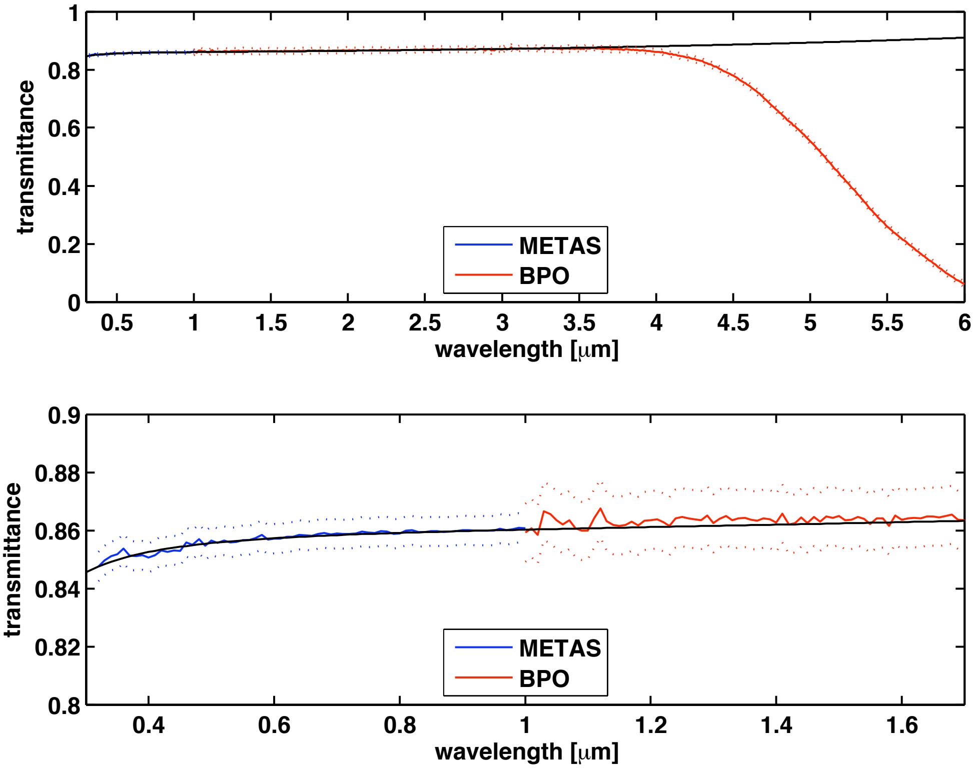

Figure 6.9: *The two graphs show the measured spectral transmittance of the sapphire windows and the calculated theoretical Fresnel losses due to multiple reflections. The detail in the lower plot displays the excellent agreement between measured and theoretical data within the stated standard uncertainty (k=1; dashed lines).*

The suprasil transmittance measurements at the METAS, the NPL and the PMOD/WRC agree within two standard uncertainties with the theoretical value. However, our measurements at the PMOD/WRC lie above the calculated upper limit. We think this is due to a divergent monochromator beam over filling the detector. The window introduced to the beam causes a lens effect which increases the power density in the beam compared to the reference beam without a window. As a result, the transmittance measurement calculated as the ratio of the obstructed and the reference beam, is too high. However, this is a geometric effect that should be largely independent of the wavelength and we can scale the PMOD/WRC spectral transmittance measurements to the theoretical or the other measured values. Figure 6.11 shows the relative difference of the CSAR windows Ay and Az at the position P1 to the CSAR window Ax at the position P1. The measured spectral transmittance of window Ax and Az excellently agree within the stated standard measurement uncertainty (k=1) of 0.1 %. The spectral transmittance of the window Az can be considered equal to the other two windows within two standard uncertainties. The discontinuity around 0.8 µm occurs where the detector of the NPL system changed. The offset is smaller than the stated uncertainty (k=2) and thus does not significantly alter the window comparison. For wavelengths larger than 3 µm, we are going to use the scaled mean spectral transmittance of the two windows measured at the PMOD/WRC and thus we cannot compare the windows above 3 µm.

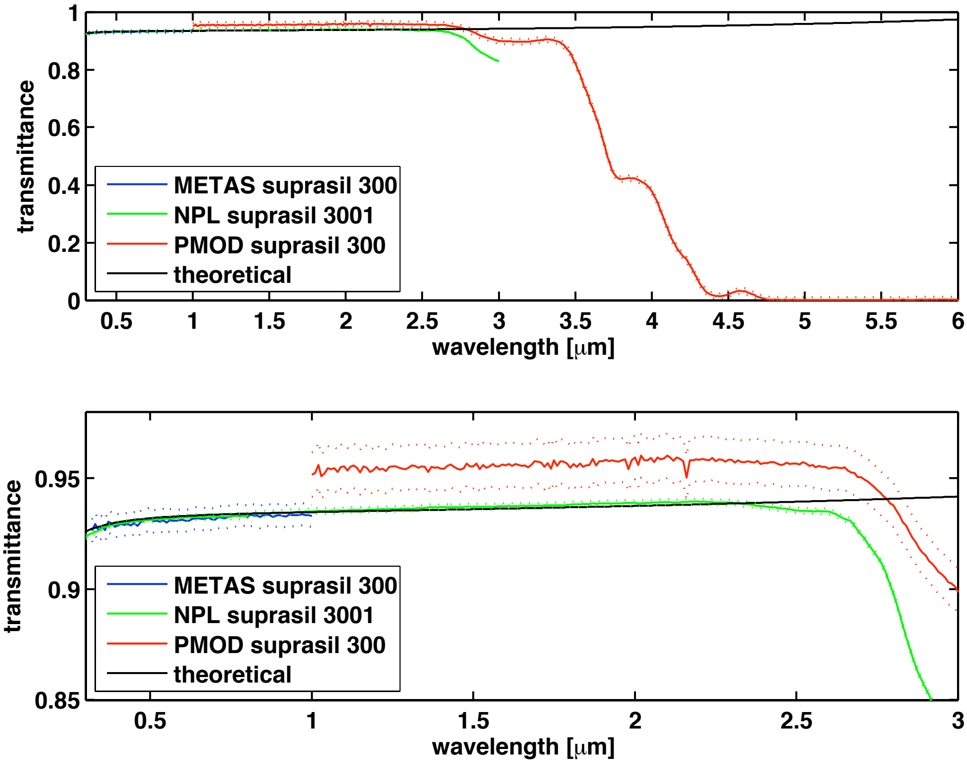

Figure 6.10: *These graphs show the measured spectral transmittance of the suprasil windows and the calculated theoretical Fresnel losses due to multiple reflections. The detail in the lower plot displays the agreement between the METAS measured and the theoretical data within the stated standard uncertainty (k=1; dashed lines). The NPL values are consistent with the calculated losses within two standard uncertainties until the internal absorption of the material increases. The PMOD/WRC measurements also agree within two standard uncertainties with the theoretical result. However the stated standard uncertainty (k=1; dashed lines) of 1 % is large and we think that the divergent beam of the monochromator can explain the offset in the measured transmittance.*

In order to use the spectral window transmittance measurements to calculate the solar radiation transmitted through the windows, we create a transmittance spectrum composite for each window and position. The transmittance properties of suprasil 3002 and suprasil 300 are virtually identical within the uncertainties and we can use these measurements to create a single transmittance spectrum composite. We created two composites from the measured data: 1) We used the measured data with the lowest uncertainty and scale the other data to fit the end points resulting in a purely measured transmittance spectrum composite. This approach does not remove systematic errors in the measurements such as the discontinuity at 0.8 µm in the NPL spectral data (Figure 6.12). 2) We create a hybrid transmittance composite considering the calculated theoretical transmittance spectrum from 0.2 µm up to 2.1 µm for Suprasil respectively 3.1 µm for sapphire where no internal absorption of the material is present. Then we scaled the measured infrared transmittance to match the end point of the theoretical curve.

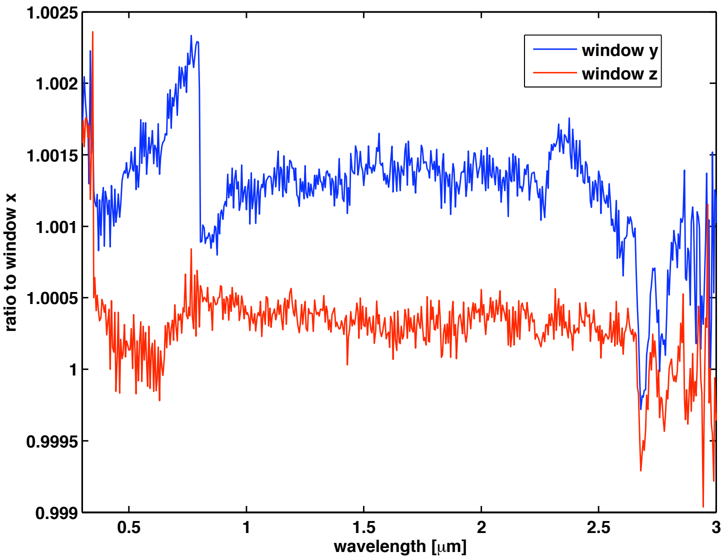

Figure 6.11: *This graph shows the spectral transmittance measurement of the CSAR Ay and Az windows at the position P1 relative to the CSAR window Ax at the position P1. Window Ax and Az excellently agree within the stated standard measurement uncertainty (k=1) of 0.1 %. The window Az can be considered equal to the other two windows within two standard uncertainties. The discontinuity of window Ay at 0.8 μm occurs where the the NPL system switches detectors.*

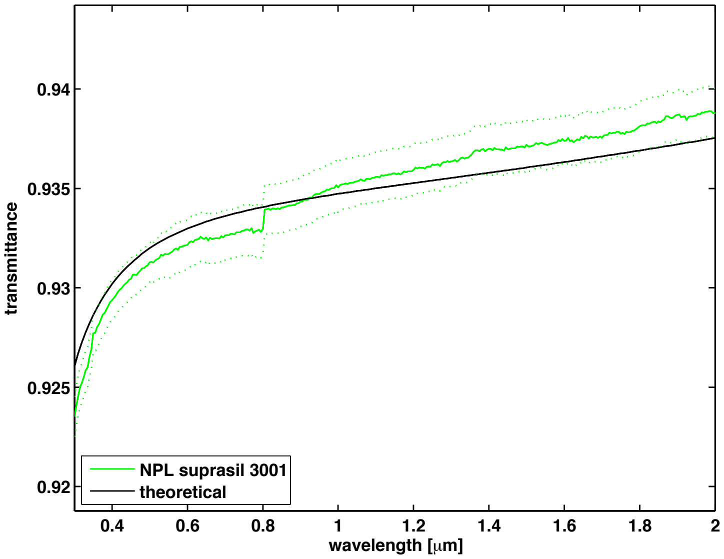

Figure 6.12: *The measured NPL transmittance values agree with the calculated theoretical value within two standard uncertainties. The dashed lines indicate one standard uncertainy (k=1). The discontinuity at 0.8 μm occurs where the detector of the NPL monochromator system changed.*

6.4 Integral Transmittance Calculations

We use the solar spectra transmitted through the model atmospheres and the spectral window transmittance composites to calculate the fraction of the total solar irradiance passing through the CSAR entrance window or the sapphire test windows. We will refer to this fraction as the integral transmittance.

The different atmosphere models allow us to investigate the influence of temperature, humidity and solar elevation changes on the integral window transmittance. To guarantee the best possible equivalence of two windows, we selected high quality substrates from a single batch with a fine optical surface finish. The hybrid window transmittance composites rely on the losses in the visible being only due to multiple reflections. This is a reasonable assumption for such optical flats since the internal absorption in the visible is less than one part in a million. Differences in the hybrid composite are due to small differences in the infrared NPL measurements. However, the influence of these differences is extremely small and we find no significant difference between two windows or individual window positions. Using the measured window transmittance composite, we find small differences between two windows or individual window positions, which are however not significant within the stated measurement uncertainties. As the measurements may also include systematic errors, we consider the hybrid window transmittance composite more reliable and hence we expect no significant difference in the integral transmittance of two entrance windows or individual window positions.

6.4.1 Integral Transmittance through the Suprasil Windows

Figure 6.13, Figure 6.14 and Figure 6.15 show the calculated integral transmittance of the CSAR Ax window at the position P1 for the different atmosphere models and the two methods of creating a spectral window transmittance composite. Common to all results is the within 0.01 % stable plateau for each model and method up to a solar zenith angle of 60 degrees. With increasing air mass the infrared part of the solar spectrum contributes more to the total irradiance. As the quartz window cuts off some of the infrared radiation, the integral transmittance through the window decreases. In Fall and Winter the decline is 0.1 % for the measured window transmittance composite respectively 0.14 % for the hybrid window transmittance composite. In Summer, the decrease beyond a solar zenith angle of 60 degrees seems to depend rather on the model atmosphere than on the window transmittance composite. The integral transmittance drops by 0.14 % for the Davos models but only by 0.05 % for the standard atmosphere models.

The results presented in Figure 6.13, Figure 6.14 and Figure 6.15 show that ± 2 Kelvin temperature variations can cause 0.02 % integral transmittance changes. This difference is larger than the targeted total uncertainty of the CSAR measurement. As we cannot predict the atmospheric changes in reality, we need to monitor the integral transmittance.

In Figure 6.16 we investigate the difference between the measured and the hybrid spectral window transmittance composite. The difference between the two composed window transmittance spectra at a solar zenith angle of 0 degree lies between 0.090 and 0.105 % for all model atmospheres except for the standard summer and the standard cirrus summer models. At increasing solar zenith angles, the difference between the two composed window transmittance spectra gradually increases up to 0.135 - 0.155 %.

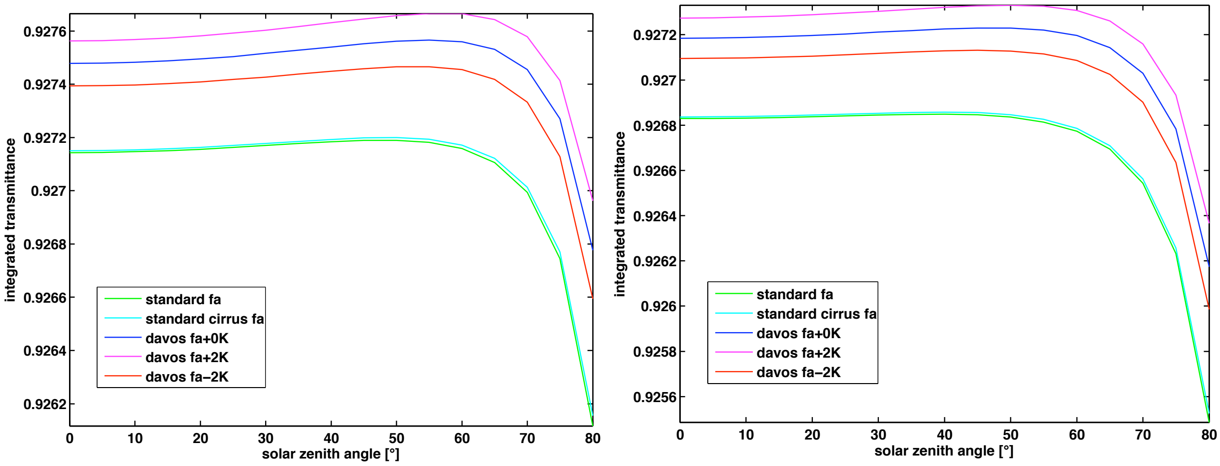

Figure 6.13: *In Fall, the calculated integral transmittance through the CSAR window Ax at position P1 varies with the solar zenith angle. The left graph shows the result for the measured spectral window transmittance composite whereas the right graph shows the result for the hybrid spectral window transmittance composite.*

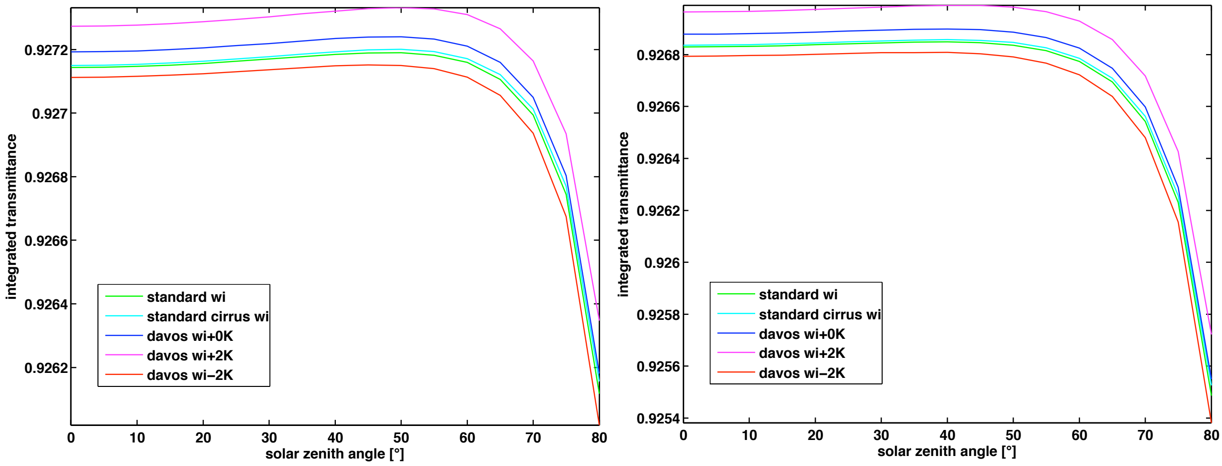

Figure 6.14: *In Winter, the calculated integral transmittance through the CSAR window Ax at position P1 varies with the solar zenith angle. The left graph shows the result for the measured spectral window transmittance composite whereas the right graph shows the result for the hybrid spectral window transmittance composite.*

Depending on the air mass lying between the sun and the radiometer, the integral transmittance varies up to 15 times more than the targeted total uncertainty of the CSAR measurements. And the absolute value of the integral transmittance through the window depends on the chosen window transmittance composite. Our calculations yield an estimate of the variation in the integral transmittance we have to expect. Because of the apparent systematic errors in the spectral transmittance measurements, we prefer the calculated integral transmittance value determined with the hybrid window transmittance spectrum composite to estimate the TSI measured with the CSAR.

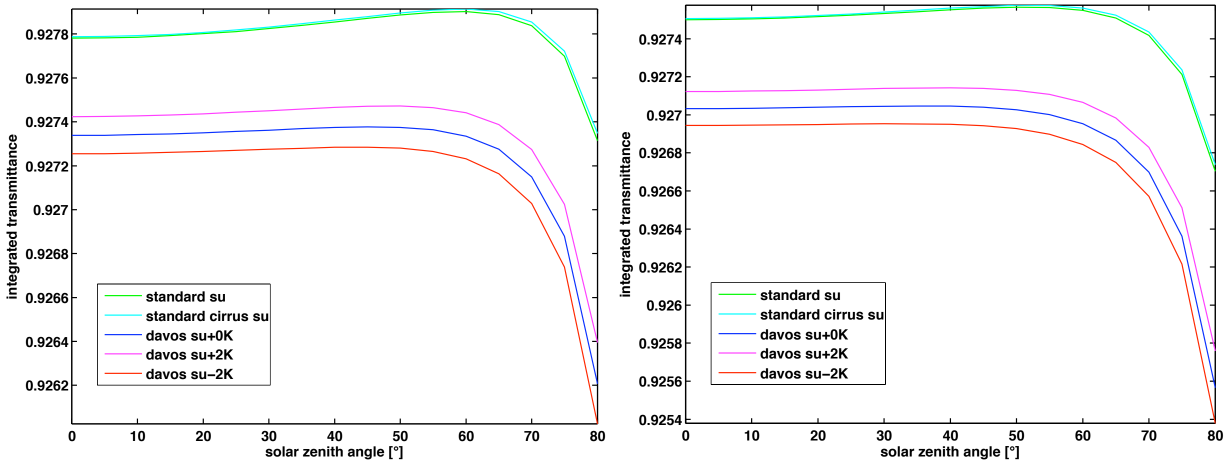

Figure 6.15: *In Summer, the calculated integral transmittance through the CSAR window Ax at position P1 varies with the solar zenith angle. The left graph shows the result for the measured spectral window transmittance composite whereas the right graph shows the result for the hybrid spectral window transmittance composite.*

Seasonal Variations

The seasonal integral transmittance dependency is shown in Figure 6.17. At a solar zenith angle of 0 degree, the results vary between 0.9268 % in Summer and 0.9275 % in Winter. And with the largest air mass in our calculation the results decrease to 0.9254 % in Summer respectively 0.9268 % in Winter.

Homogeneity of the Windows

We use our models and measurements to investigate the variations in the integral transmittance through the different positions of the windows. Applying the measured spectral window transmittance composite and comparing the integral transmittance through the six positions of the CSAR window Ax, we find a maximal difference of 0.038 %. This offset is independent of the solar zenith angle and not significant within the stated spectral transmittance measurements uncertainty. The hybrid spectral window transmittance composite yields no significant variation between the six window positions (Figure 6.18, Figure 6.19).

Difference between Windows

Comparing the two CSAR windows Ax and Az at position the P1, the calculations with the measured spectral window transmittance composite yield a difference of 0.0307 to 0.0325 % depending on the solar zenith angle. This difference is not significant within the stated spectral transmittance measurements uncertainty. The results obtained with the hybrid spectral window transmittance composite yield an insignificant difference between the two windows. As we consider the hybrid spectral window transmittance composite more reliable, we expect no significant difference between the windows or between the positions of a particular window.

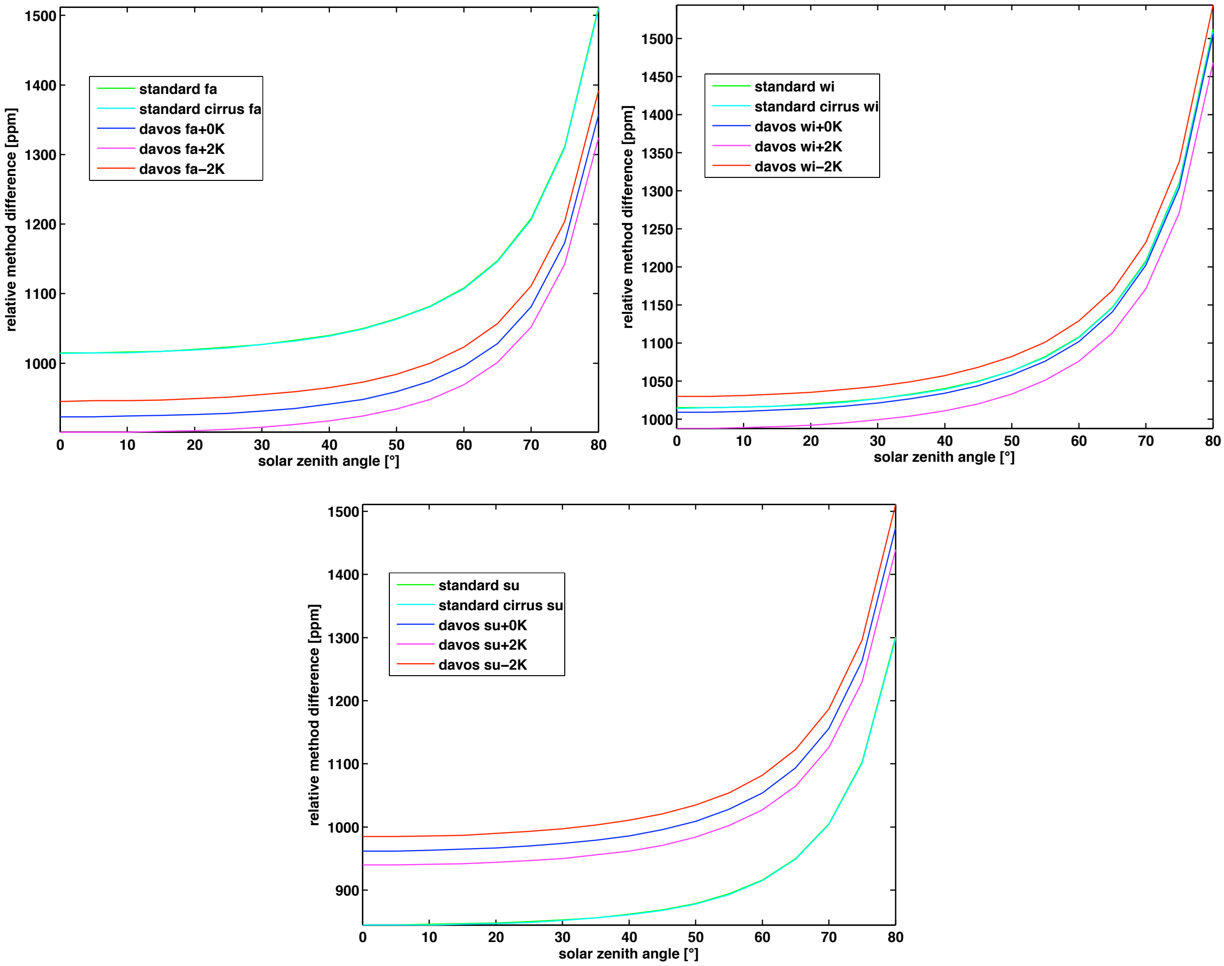

Figure 6.16: *Displaying the relative difference between the integral transmittance calculated with the two different window transmittance composite reveals an increasing difference between the two methods with wider solar zenith angles. However, the differences seem largely independent of the seasons and the atmospheric models used in the calculation. The results for the standard (green) and the standard cirrus (cyan) models are virtually identical.*

Comparing the two CSAR windows Ax and Ay at position the P1, the calculations with the measured spectral window transmittance composite yield a difference of 0.1426 %. This difference is not significant within the stated spectral transmittance measurements uncertainty. The results obtained with the hybrid spectral window transmittance composite yield an insignificant difference between the two windows. As we consider the hybrid spectral window transmittance composite more reliable, we expect no significant difference between the windows or between the positions of a particular window.

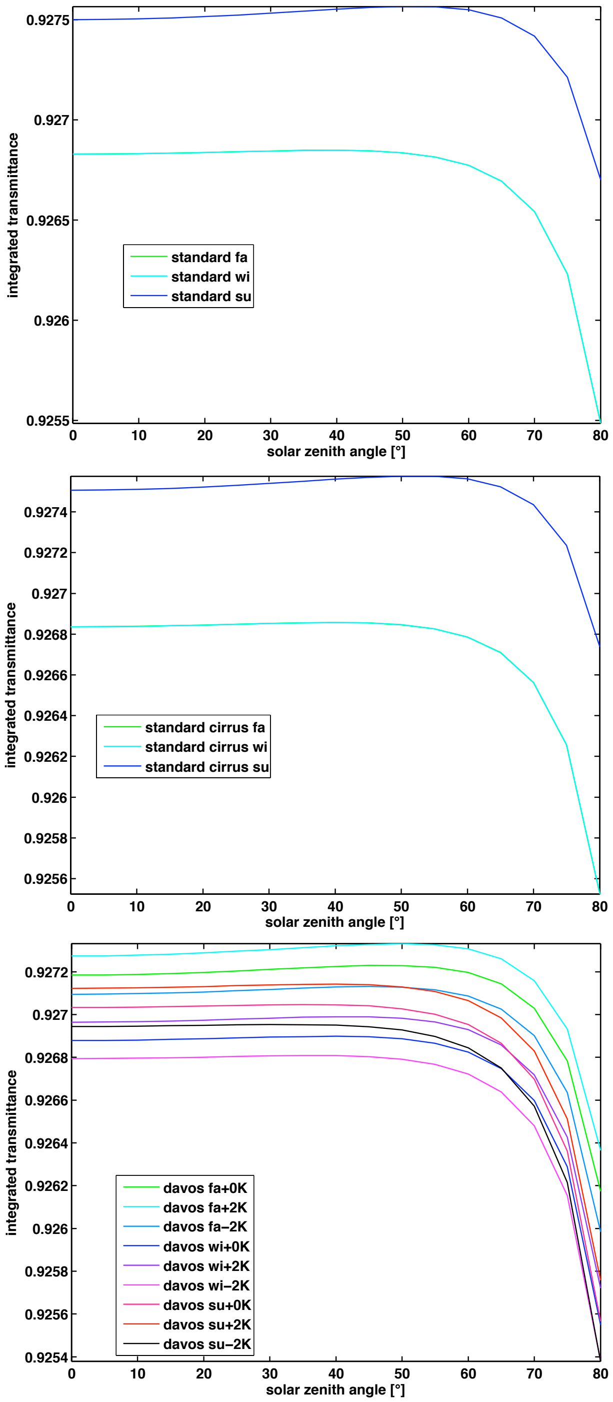

Figure 6.17: *Plotting the integral transmittance clustered according to the atmospheric model used for the calculation, we find a 0.07 % seasonal variation. The results for the standard Winter and the standard Fall models are virtually identical.*

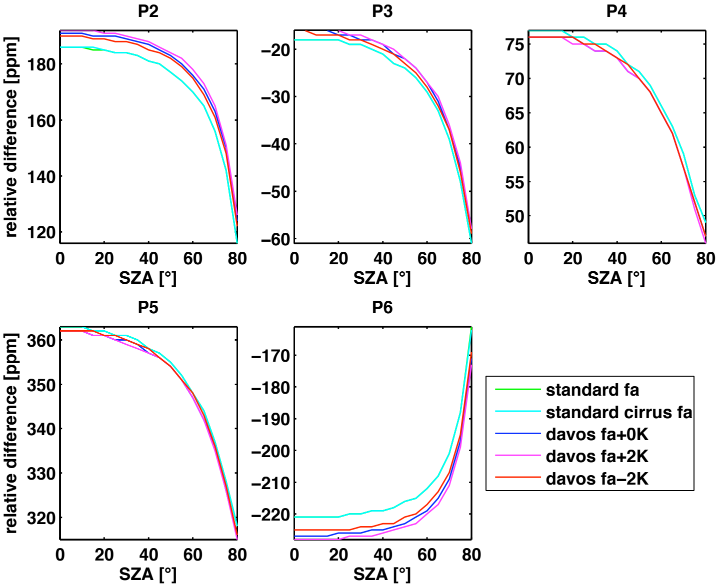

Figure 6.18: *The graphs show the integral transmittance through the five positions P2 to P6 of the CSAR window Ax relative to the value at the position P1. Using the measured spectral window transmittance composite to compare the integral transmittance through the six positions, we find a maximal difference of 0.038 %.*

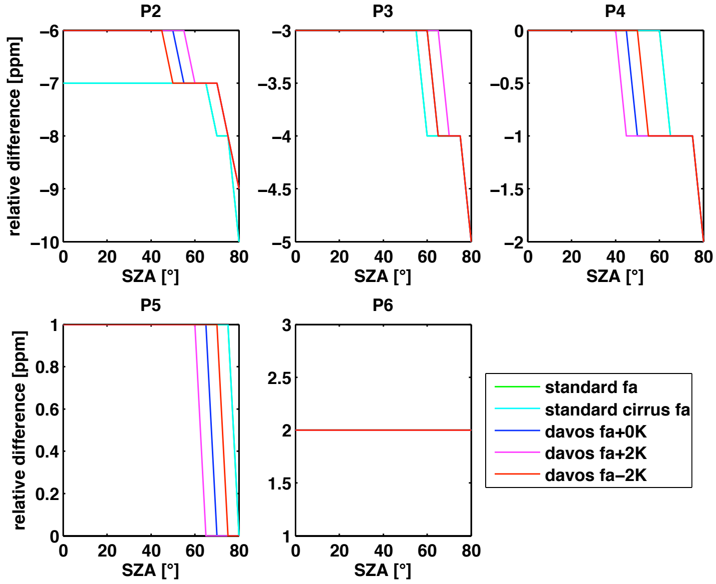

Figure 6.19: *The graphs show the integral transmittance through the five positions P2 to P6 of the CSAR window Ax relative to the value at the position P1. Using the hybrid spectral window transmittance composite, yields an insignificant difference between the six window positions.*

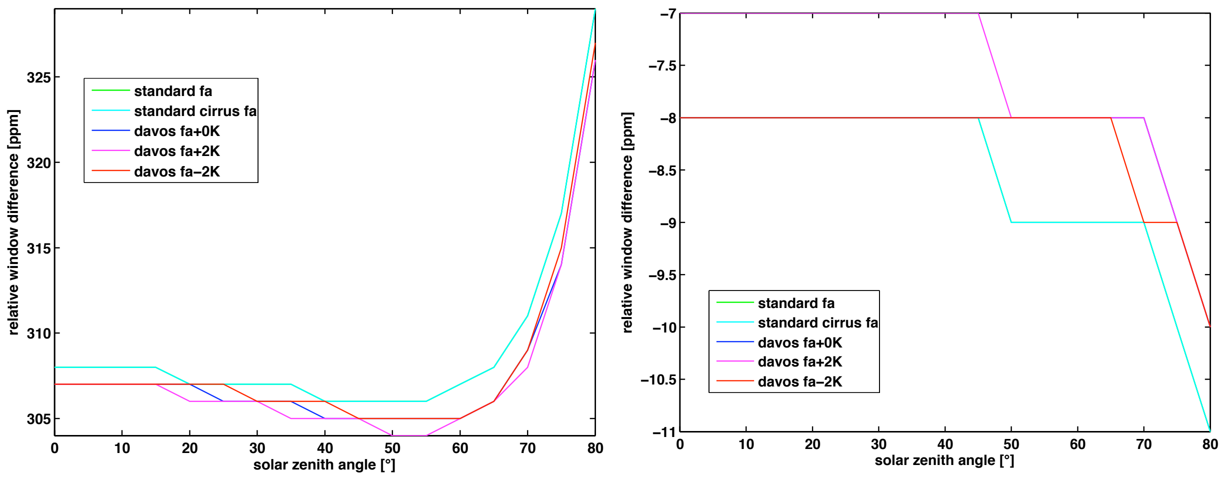

Figure 6.20: *Here we compare the two CSAR windows Ax and Az at the position P1. Using the measured spectral window transmittance composite to compare the integral transmittance through the two windows, we find that the window Ax transmits 0.0307 % more for a low air mass. The difference increases to 0.0325 % for the widest solar zenith angle. Using the hybrid spectral window transmittance composite yields an insignificant variation between the two windows.*

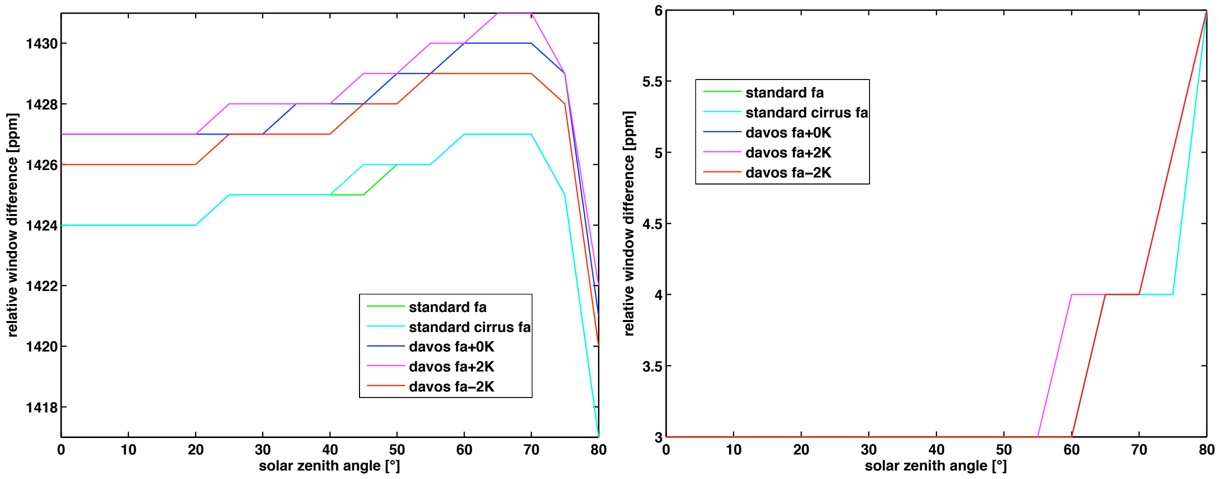

Figure 6.21: *Here, we compare the two CSAR windows Ax and Ay at the position P1. Using the measured spectral window transmittance composite to compare the integral transmittance through the two windows, we find that the window Ax transmits 0.1426 % more. Using the hybrid spectral window transmittance composite yields an insignificant variation between the two windows.*

6.4.2 Integral Transmittance through the Sapphire Windows

Figure 6.22, Figure 6.23 and Figure 6.24 show the calculated integral transmittance of the test sapphire window 1 and 2 for the different atmosphere models and the two methods of creating a spectral window transmittance composite. Common to all results is the steadily increasing integral transmittance with wider solar zenith angles. As opposed to the quartz windows, the integral transmittance through the sapphire windows neither decreases with wider solar zenith angles nor shows a plateau up to 60 degrees. The reason for this behavior is the sapphire transmittance in the UV which starts to decreases rapidly before the ozone absorption edged at 0.3 μm. With increasing air mass less short wave radiation passes through the atmosphere and the losses in the UV less and less diminish the integral transmittance. In Fall and Winter the increase is 0.12 to 0.14 % for the two window transmittance composites. In Summer, the Davos models show the same behavior as in Fall and Winter but for the standard atmosphere models the increase in the integral transmittance is slightly larger.

The results presented in Figure 6.22, Figure 6.23 and Figure 6.24 show that ± 2 Kelvin temperature variations can cause 0.03 % integral transmittance changes. This difference is larger than the intended total uncertainty of the CSAR measurement.

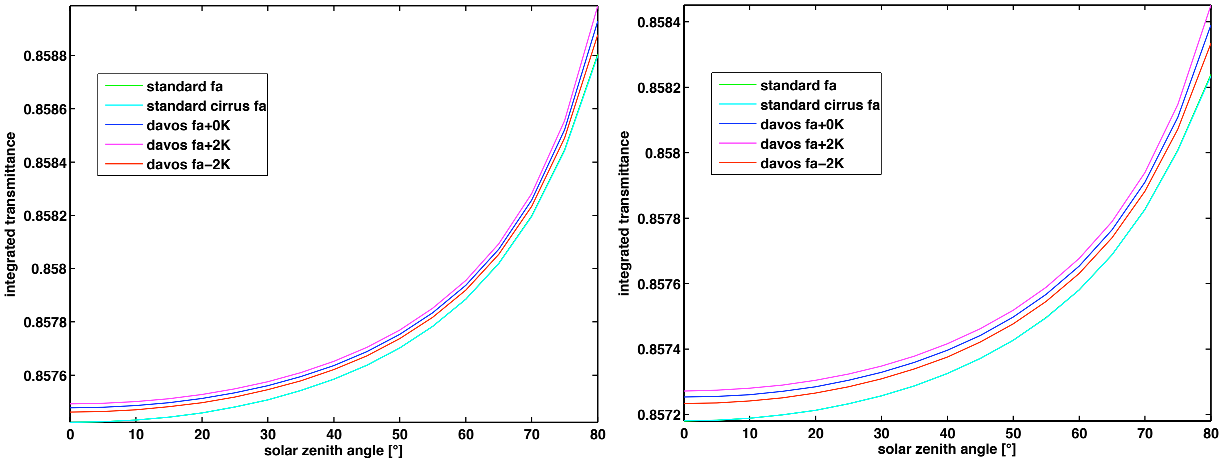

Figure 6.22: *In Fall, the calculated integral transmittance through the sapphire window 1 varies with the solar zenith angle. The left graph shows the result for the measured spectral window transmittance composite whereas the right graph shows the result for the hybrid spectral window transmittance composite. The results for the standard (green) and the standard cirrus (cyan) models are virtually identical.*

In Figure 6.26 we investigate the difference between the measured and the hybrid spectral window transmittance composite. The difference between the two composed window transmittance spectra at a solar zenith angle of 0 degree is 0.0325 % for all model atmospheres except for the standard summer and the standard cirrus summer models. At increasing solar zenith angles, the difference between the two composed window transmittance spectra gradually increases up to 0.065 %.

Depending on the air mass, the integral transmittance varies up to 7 times more than the targeted total uncertainty of the CSAR measurements. The absolute value of the integral trans-

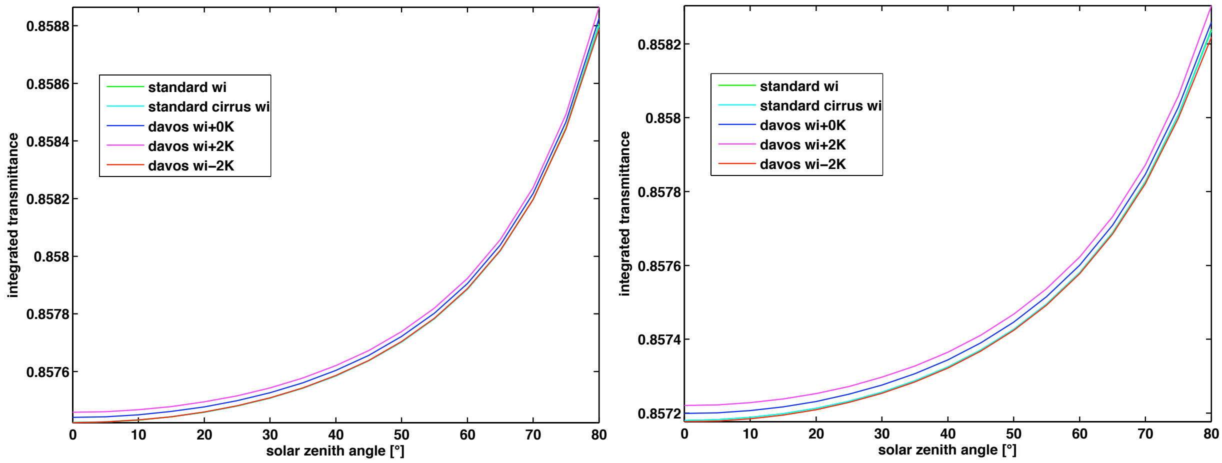

Figure 6.23: *In Winter, the calculated integral transmittance through the sapphire window 1 varies with the solar zenith angle. The left graph shows the result for the measured spectral window transmittance composite whereas the right graph shows the result for the hybrid spectral window transmittance composite. The results for the standard (green) and the standard cirrus (cyan) models are virtually identical.*

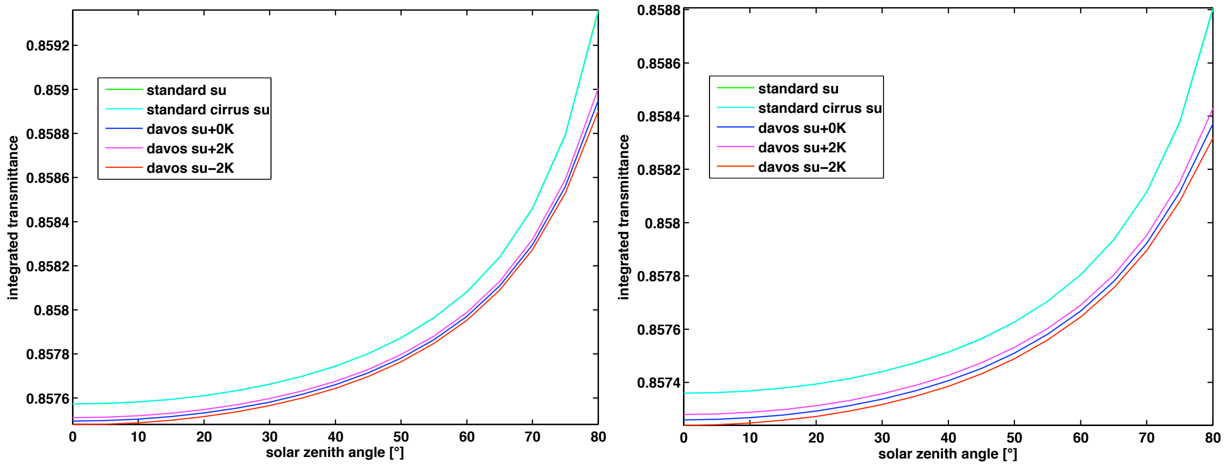

Figure 6.24: *In Summer the calculated integral transmittance through the sapphire window 1 varies with the solar zenith angle. The left graph shows the result for the measured spectral window transmittance composite whereas the right graph shows the result for the hybrid spectral window transmittance composite. The results for the standard (green) and the standard cirrus (cyan) models are virtually identical.*

mittance through the window depends on the chosen window transmittance composite. Our calculations yield an estimate of the variation in the integral transmittance we have to expec. Because of the apparent systematic errors in the spectral transmittance measurements, we prefer the calculated integral transmittance value determined with the hybrid window transmittance spectrum composite to estimate the TSI measured with the CSAR.

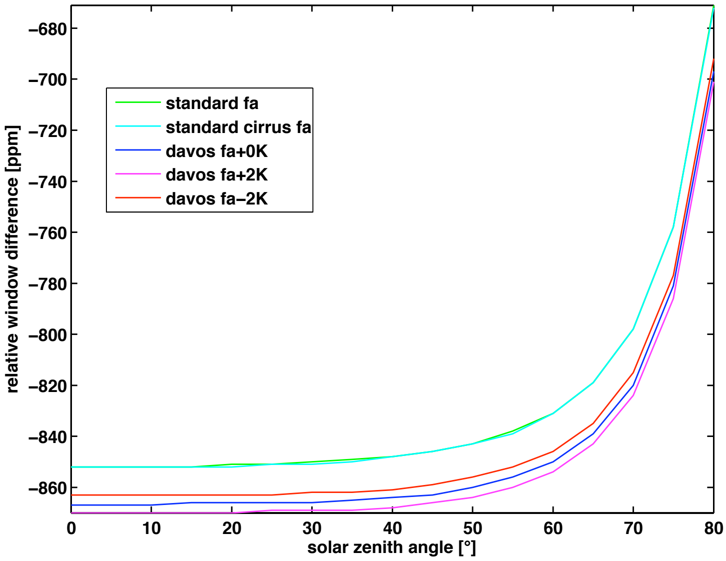

Figure 6.25: *Here, we compare the two sapphire windows. Using the measured spectral window transmittance composite to compare the integral transmittance through the two windows, we find a difference of 0.086 % between the windows for a low air mass. The difference decreases to 0.068 % for the widest solar zenith angle. The results for the standard (green) and the standard cirrus (cyan) models are virtually identical.*

Seasonal Variations

The last reason to monitor the integral transmittance of our windows, may be derived from the seasonal dependency shown in Figure 6.27. At a solar zenith angle of 0 degree, the results vary between 0.8572 % in Summer and 0.8574 % in Winter. And with the largest air mass in our calculation the results increase to 0.8582 % in Summer respectively 0.8588 % in Winter.

Difference between Windows

If we compare the two sapphire test windows 1 and 2, the calculations with the measured spectral window transmittance composite yield a difference of 0.086 to 0.068 % depending on the solar zenith angle. This difference is not significant within the stated spectral transmittance measurements uncertainty. We cannot compare the two windows using the hybrid spectral window transmittance composite because we apply the mean transmittance of the two windows in the infrared for the theoretical calculations. As we consider the hybrid spectral window transmittance composite more reliable, there is no difference between the windows.

6.4.3 Discussion

Our calculations show integral window transmittance variations due to atmospheric and solar elevation changes which are larger than the targeted CSAR uncertainty and hence have to be

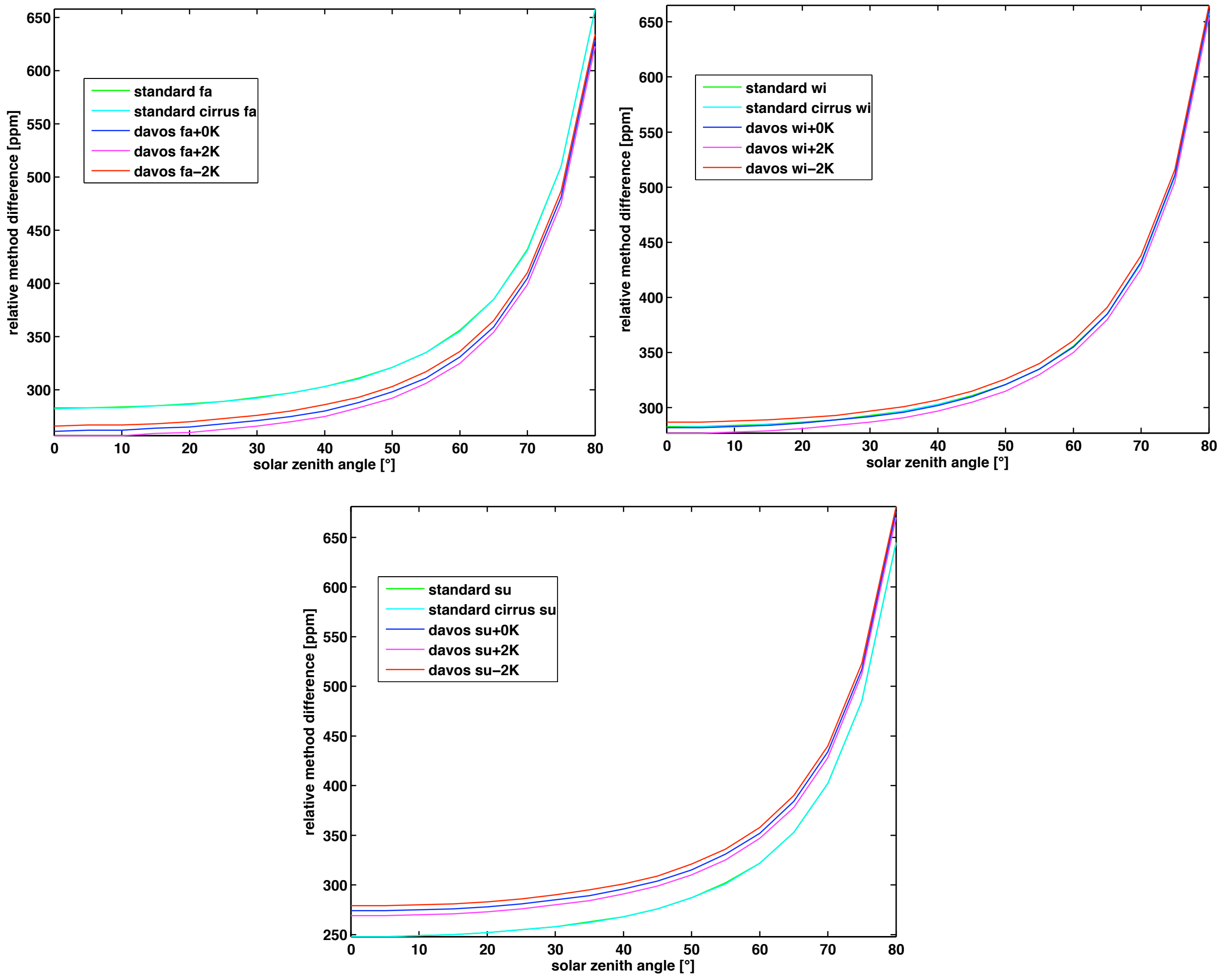

Figure 6.26: *Displaying the relative difference between the integral transmittance calculated with the two different window transmittance composite reveals an increasing difference between the two methods with wider solar zenith angles. However, the differences seem largely independent of the seasons and the atmospheric models used in the calculation. The results for the standard (green) and the standard cirrus (cyan) models are virtually identical.*

monitored. The calculated absolute integral transmittance value depends on the atmospheric model and the window transmittance composite we use.

The Suprasil windows have the nice property of a nearly constant integral transmittance up to a solar zenith angle of 60 degrees and hence we expect no daily variations caused by the solar elevation when measuring in this plateau. However, due to low cut-off wavelength in the infrared, measuring TSI through Suprasil windows is sensitive to daily or seasonal changes of the atmosphere.

The sapphire window results show no plateau when investigating the integral transmittance dependency on the solar zenith angle. Hence, using sapphire entrance windows, we expect to see a clear diurnal variation of the measurements. The high infrared cut-off wavelength of sapphire allows to detect more thermal radiation of the solar spectrum. As a result, TSI measurements

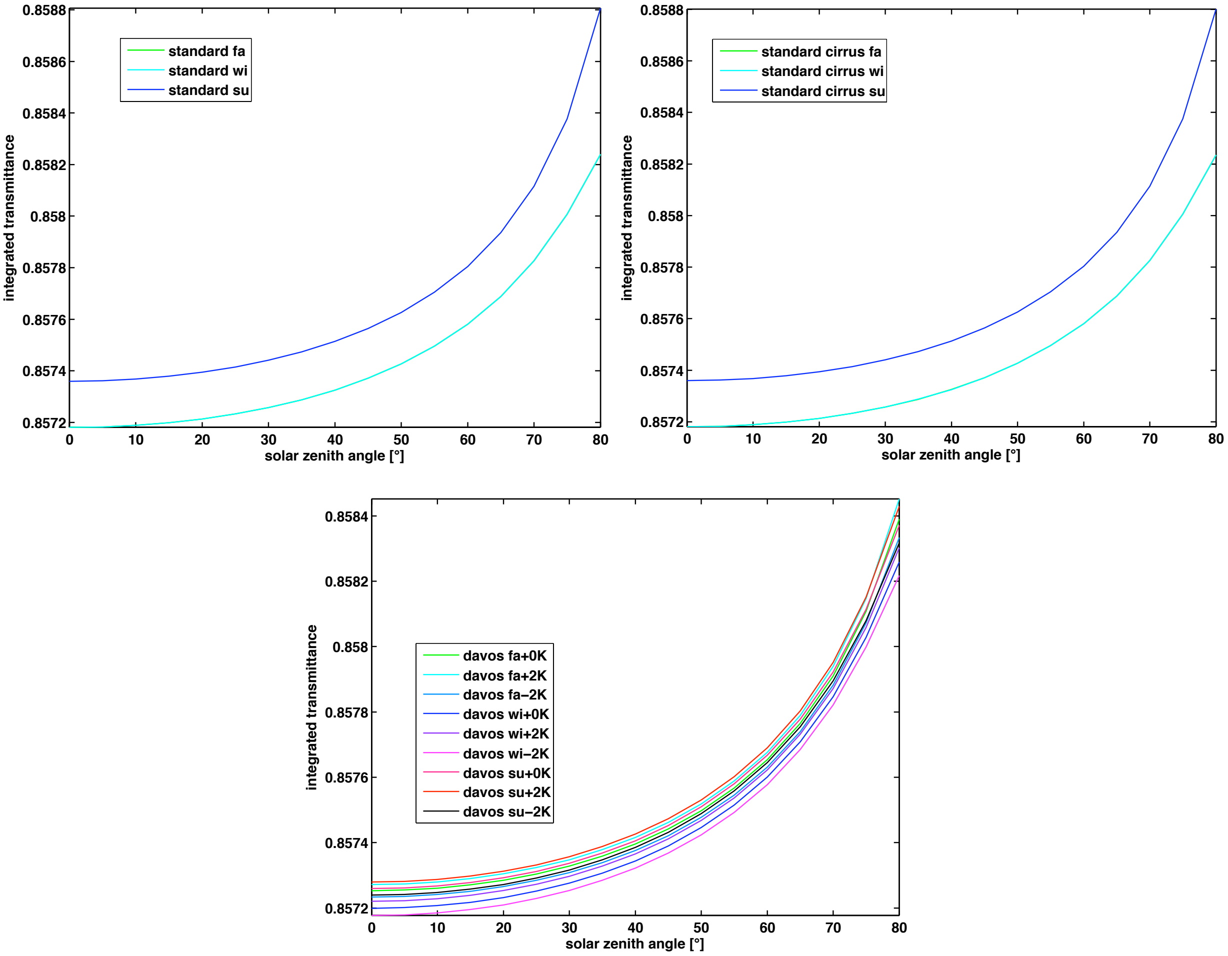

Figure 6.27: *Plotting the absolute integral transmittance clustered according to the atmospheric model used for the calculation, we find a maximal 0.04 % seasonal variation. The results for the Fall (green) and the Winter (cyan) models are virtually identical.*

through sapphire are less sensitive to daily and seasonal changes of the atmosphere. This fact makes sapphire the preferred window material under difficult atmospheric conditions and encourages us to look for humidity-resitant substrates being transparent further into the infrared.

The window equivalence and homogeneity investigations showed that the integral transmittance is most sensitive to differences in the visible range. Calculations using the hybrid window transmittance composites where we use theoretical Fresnel losses from 0.2 to 2.1 µm for Suprasil respectively 0.2 to 3.1 µm for sapphire, show no significant integral transmittance differences. Using the measured window transmittance composites, we find small differences between the windows and individual window positions which are however not significant within the stated uncertainties. Hence, we have found no indication that the windows are not equivalent. To avoid systematic measurement errors we use the hybrid transmittance composite for further calculations.

6.5 Modified PMO6 Integral Transmittance Measurements

The previous section has shown that the integral window transmittance needs to be monitored. In chapter 7 we will discuss the design and testing of such a novel monitor. Since the window transmittance monitoring is so crucial to the CSAR project, we decided to modify a conventional PMO6-type radiometer (Figure 6.28) to obtain alternative/backup integral transmittance measurements. The modified instrument should feature a similar optical design as the CSAR. We created a window holder having the same dimensions as the window insert of the CSAR and placing the aperture at the same radial position. We rebuilt the commercial PMO6-0801 radiometer according to the dimensions presented in Table 9.1. Unlike for standard PMO6 radiometers, we used an inverted geometry with the precision aperture as entrance to the instrument. We mounted the measured CSAR 01 precision aperture which is from the same batch as the apertures on the CSAR. These apertures have a volcano like shape in order to guide inter reflections between the aperture front surface and the window away from the opening. We shortened the distance between the front aperture and the cavity and widened cavity opening serving as the view limiting aperture in the modified radiometer. The aperture geometry does not completely fulfill the CIMO recommendations (see chapter 9). However, the modified PMO6 determines the integral transmission as the ratio of the obstructed and the unobstructed calibration factor, canceling out the contribution of the circumsolar radiation. Hence, the deviation does not affect the transfer of the measured integral transmittance from the modified PMO6 to the CSAR.

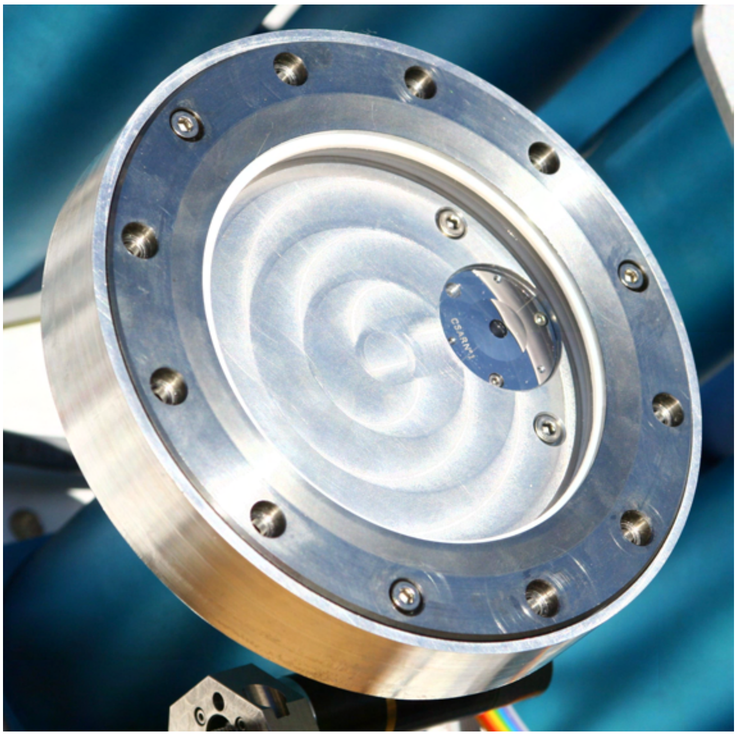

Figure 6.28: *Front view of the modified PMO6-type radiometer with the CSAR 01 precision aperture and the CSAR Ay suprasil 3002 entrance window.*

Suprasil Windows

Figure 6.29 shows the measurements with the CSAR window Ay on the modified PMO6. The ratio to the PMO2 radiometer varied within 0.4 % during the observation period which is of the order predicted by the theoretical integral transmittance calculations. Hence, the modified PMO6 is able to track day to day changes introduce by atmospheric variations. The 0.1 % scattering of the individual data points during a day represents the intrinsic variation of PMO6-type radiometer measurements which disguises the diurnal variations due to the solar elevation.

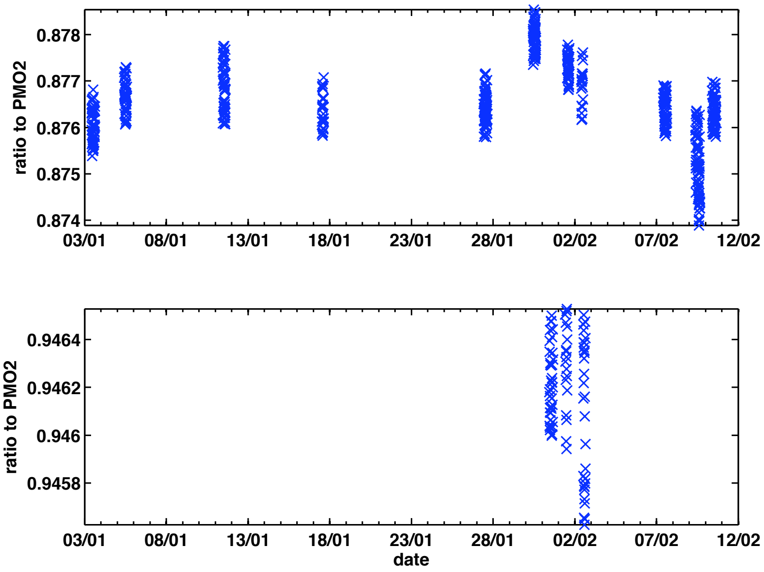

Figure 6.29: *Calibration factors determined with the modified PMO6-0801 radiometer. With the window mounted in front of the PMO6-0801 instrument, the ratio to the PMO2 reference instrument varies by up to 0.4 % during the observation period (upper graph). Changes of the atmosphere must be responsible for the calibration variations and ultimately cause variations in the integral transmittance. On the 31st January, the 1st and the 2nd February 2011 we performed reference calibrations without a window (lower graph).*

Figure 6.30 presents the measured integrate transmittance and the calculated theoretical boundaries. The scattering of the modified PMO6 measurements and the day to day variation disguise the solar elevation dependency. Averaging the measurements reduces the uncertainty of the integral transmittance caused by the scattering of the instrument and hence we calculated daily mean values. However, we loose the information of the integral transmittance variations caused by the air mass changes by using an average. The influence of the solar elevation is expected to be small for the solar zenith angles between 61 and 80 degrees during the observation period and hence we do not introduce a large extra uncertainty.

The CSAR provides TSI measurements with the CSAR Ax window on the 27th January, the 2nd and the 7th February 2011. In Figure 6.31 we present the daily mean integral transmittance values for the CSAR Ay window at the position P1 on these days. And Table 6.5 summarizes the numerical values and the estimated standard uncertainties (k=1). To determine the uncertainty, we combine the small contribution from the standard deviation with a theoretical uncertainty

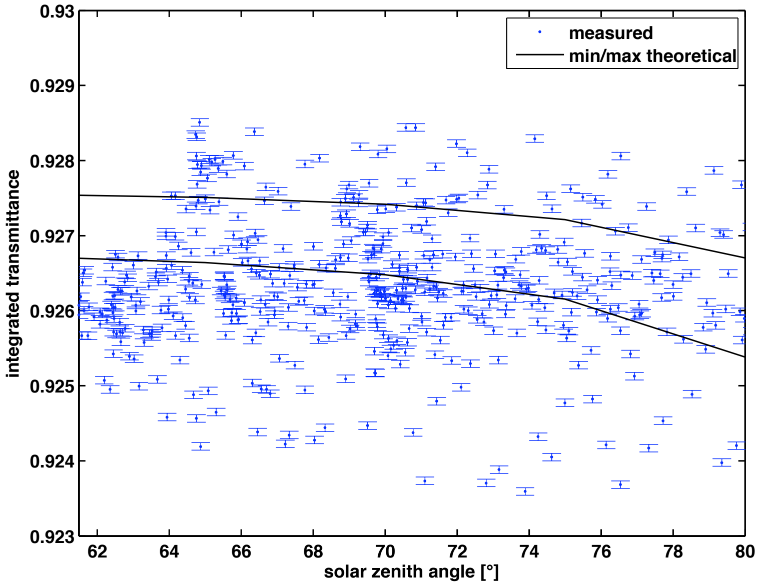

Figure 6.30: *Integral transmittance of the CSAR Ay window measured with the PMO6-0801 radiometer as a function of the solar zenith angle. We have also plotted the calculated theoretical upper and lower boundaries for this window expected for a standard summer respectively Davos Winter -2K atmosphere. The indicated standard uncertainties (k=1) are dominated by the measurement uncertainty of the modified PMO6 signals.*

which accounts for the diurnal variations. The theoretical uncertainty consideration assumes a rectangular distribution of the calculated integral transmittance. The measured integral transmittance tends to lie below the calculated boundaries. This absolute difference can be explained by dust on the window attenuating the measurements. However, this behavior does not influence the absolute value of the cryogenic radiometer as the CSAR window is identically affected by the dust (section 6.6.1).

	integral transmittance	standard uncertainty (k=1)
27. Jan 2011	0.926274	0.000296
2. Feb 2011	0.926803	0.000312
7. Feb 2011	0.926235	0.000297

Table 6.5: *The daily mean integral transmittance values of the CSAR Ay window at the position P1. The standard uncertainties (k=1) are dominated by the theoretical uncertainty accounting for the diurnal variations which are not considered when averaging the data.*

We use the daily mean integral transmittance values to determine the absolute TSI value measured with the CSAR (section 8.3). Using an average, we are able to correct the day to day variations of the integral transmittance. However, to track the diurnal variations and to achieve the intended uncertainty of individual CSAR measurements, we need a transmission monitor whose values scatter an order of a magnitude less.

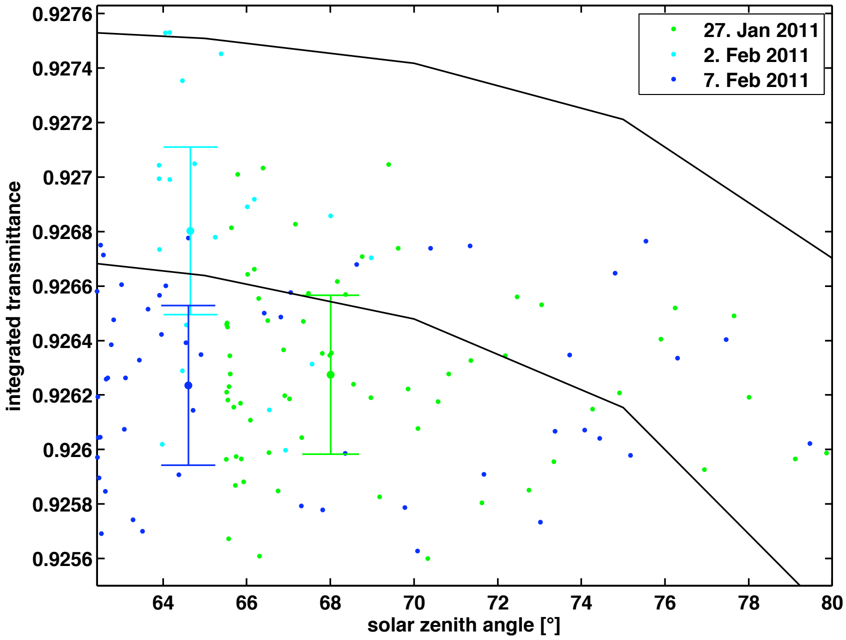

Figure 6.31: *Integral transmittance of the CSAR Ay window measured with the PMO6-0801 radiometer as a function of the solar zenith angle. We have also plotted the calculated theoretical upper and lower boundaries for this window expected for a standard summer respectively standard Davos Winter -2K atmosphere. The indicated standard uncertainties (k=1) of the daily mean values are dominated by the theoretical uncertainty accounting for the diurnal variations which are not considered when averaging the data.*

Sapphire Windows

The CSAR provides TSI measurements with the sapphire window 1 on the 7^{th} and the 8^{th} March 2011. In Figure 6.32 we present the daily mean integral transmittance values for the sapphire 2 window on these days. And Table 6.6 summarizes the numerical values and the estimated standard uncertainties (k=1). The measured integral transmittance tends to lie below the calculated boundaries. This absolute difference can be explained by dust on the window attenuating the measurements. However, this behavior does not influence the absolute value of the cryogenic radiometer as the CSAR window is identically affected by the dust (section 6.6.1).

	integral transmittance	standard uncertainty (k=1)
7. Mar 2011	0.857921	0.000297
8. Mar 2011	0.857513	0.000298

Table 6.6: *The daily mean integral transmittance values of the sapphire 2 window. The standard uncertainties (k=1) are dominated by the theoretical uncertainty accounting for the diurnal variations which are not considered when averaging the data.*

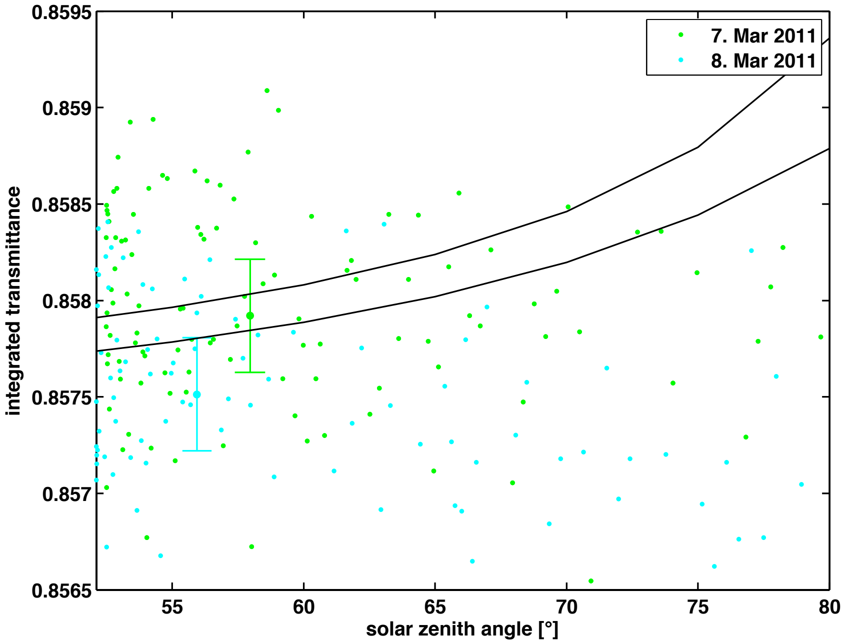

Figure 6.32: *Integral transmittance of the sapphire 2 window measured with the PMO6-0801 radiometer as a function of the solar zenith angle. We have also plotted the calculated theoretical upper and lower boundaries for this window expected for a standard summer respectively standard Davos Winter -2K atmosphere. The indicated standard uncertainties (k=1) of the daily mean values are dominated by the theoretical uncertainty accounting for the diurnal variations which are not considered when averaging the data.*

We use the daily mean integral transmittance values to determine the absolute TSI value measured with the CSAR (section 8.3). Using an average, we are able to correct the day to day variations of the integral transmittance. However, to track the diurnal variations and to achieve the intended uncertainty of individual CSAR measurements, we need a transmission monitor whose values scatter an order of a magnitude less.

6.6 Integral Transmittance Corrections and Uncertainty Budget

To transfer the measured integral transmittance from the modified PMO6-0801 window to the CSAR window, we need to apply a correction for the window equivalence. Alternatively, we could calculate the integral transmittance of the CSAR window, making corrections for dust and temperature induced transmittance changes mandatory. All corrections and possible stray light effects introduce an uncertainty to the integral transmittance value applied to the CSAR measurements.

Construction works at the PMOD/WRC and insufficient measurement days, did not yet allow to acquire data for the CSAR Az entrance window. For the CSAR windows Ax and Ay and the sapphire windows 1 and 2, we present two uncertainty budgets for each material using either a calculated or a measured integral transmittance.

Suprasil Windows

	correction calculated	standard uncertainty (k=1) in ppm	correction measured	standard uncertainty (k=1) in ppm
stray light (micro-roughness)	-	50	-	50
stray light (dust)	-	50	-	50
transmittance change due to dust	114 ppm per day	21	-	-
temperature dependent refractive index	15 ppm per K	87	-	87
window equivalence (Ax to Ay)	-	-	1.000312[1]	370
transmittance	-	225	-	302
monitor cavity reflectance	1.000012	7	1.000012[2]	7
total RSS	-	252	-	490

Table 6.7: *Using the calculated integral transmittance, the uncertainty budget for the integral transmittance through the suprasil windows is dominated by the standard uncertainty (k=1) of the calculated integral window transmittance. If we apply the measured integral transmittance to the CSAR measurements, the main uncertainty contribution comes from the window non-equivalence.*

Sapphire Windows

	correction calculated	standard uncertainty (k=1) in ppm	correction measured	standard uncertainty (k=1) in ppm
stray light (micro-roughness)	-	50	-	50
stray light (dust)	-	50	-	50
transmittance change due to dust	114 ppm per day	21	-	-
temperature dependent refractive index	15 ppm per K	87	-	87
window equivalence (1 to 2)	-	-	1.000257[3]	161
transmittance	-	100	-	298
monitor cavity reflectance	1.000023	13	1.000023[4]	13
total RSS	-	152	-	357

Table 6.8: *Using the calculated integral transmittance, the uncertainty budget for the integral transmittance through the sapphire windows is dominated by the standard uncertainty (k=1) of the calculated integral window transmittance. If we apply the measured integral transmittance to the CSAR measurements, the main uncertainty contribution comes from the window non-equivalence.*

---

[1] Window Ay is transmitting more than window Ax, hence we have to reduce the measured integral transmittance through window Ay by this correction to obtain the integral transmittance of the CSAR window Ax.

[2] The measured integral transmittance through window Ay has to be enhanced by this correction to obtain the integral transmittance of the CSAR window Ax.

[3] Window 1 is transmitting more than window 2, hence we have to increase the measured integral transmittance through window 2 by this correction to obtain the integral transmittance of the CSAR window 1.

[4] The measured integral transmittance through window 2 has to be enhanced by this correction to obtain the integral transmittance of the CSAR window 1.

6.6.1 Stray Light

Micro-Roughness of the Window Surface

Although we bought high quality optical polished entrance windows, the remaining window surface micro-roughness causes stray light. The two window surfaces are expected to scatter 100 ppm of the solar irradiance and hence the radiometer cannot detect a fraction of the radiation that would enter the precision aperture in absence of the window. We use the scattering phase function found by Nelson (2007) to estimate the stray light missing the radiometer cavity. The phase function shown in Figure 6.33 is valid for a wavelength of 1047 nm and shows a strong peak in the forward direction. Our calculations show that maximally 50 % of the stray light are not detected by the radiometer. Due to the more prominent scattering in the forward direction at shorter wavelengths, less radiation is scattered away from the detector and our calculations yield an upper boundary of 50 ppm stray light losses which we use as estimated standard uncertainty (k=1). The stray light produced by the illuminated window surfaces outside the radiometer's view limit has no significant contribution to the measurements. Hence, the differing aperture geometries of the CSAR and the MITRA do not cause a difference in stray light.

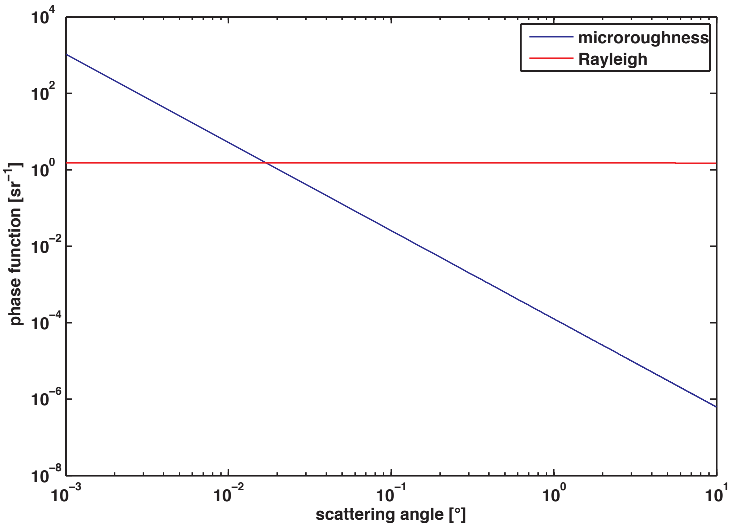

Figure 6.33: *Scattering at the window surface due to the micro-roughness for a wavelength of 1047 nm, has a strong peak in the forward direction before decreasing below the level of Rayleigh scattering.*

Inclusions and Dust

The stray light produced by inclusions in the window material and the dust aggregating on the front surface is harder to assess. Striae are convective currents inside the melt that are frozen in the window material during the cooling. These phase distortions would produce stray light but our suprasil as well as the sapphire windows are free of striae according to the specification

(Table 6.4). There are also no impurity inclusions like metals from the melting tank and only very few trapped air bubbles. Hence, we do not consider scattering at inclusions an issue.

To assess the stray light produced by the dust on the window front surface, we have to make assumptions about the coverage factor and the size distribution of the dust particles. Nelson (2007) investigated the effect of dust on a coronagraph objective and found that after thoroughly cleaning the optics, the contribution of stray light is negligible. Dust aggregation causes a stray light increase to 25 ppm. However, the coronagraph is located at the Mauna Loa Solar Observatory where the dust contamination is considerably smaller than in Davos. And as our instrument has twice the field of view, we estimate the standard uncertainty (k=1) introduced by the dust on the window surface to 50 ppm.

We performed a dust experiment with the sapphire windows in front of the modified PMO6-0801 on the 21st of March 2011. At that moment the sapphire windows had been mounted for two weeks. After cleaning the windows and repeating the measurements, we found an increase of the integral transmittance by 0.16 %. This result indicates an integral transmittance decrease rate of 114 ppm per day due to dust. The two sapphire windows are identically affected by the dust and we estimate a 21 ppm standard uncertainty (k=1) of the dust correction rate. However, the current situation with the ongoing construction works is not representative for the normal dust contamination in Davos.

In the future, when more than one CSAR cavity is simultaneously observing TSI through the entrance window, we are able to track the dust induced stray light by comparing the measurements of a regularly exposed cavity to the results of a rarely exposed and dust protected detector.

6.6.2 Variations of the Refractive Index

Temperature

The temperature coefficient of the suprasil refractive index is lower than $1.5 \cdot 10^{-5}$ per Kelvin causing an integral transmittance change of 15 ppm per Kelvin for a suprasil window. The designs of the CSAR (Winkler, 2011a), the MITRA (chapter 7) and the modified PMO6-0801 are such that the temperature rise of the illuminated portion of the window is smaller than 2 Kelvin. Hence, after opening the shutter, while the window is heating up, the integral transmittance changes by less than 30 ppm. However, this heating effect is small and has only to be considered using the CSAR measurements shortly after opening the shutter.

The ambient temperature might change by up to 20 Kelvin during a day resulting in a 300 ppm change of the integral transmittance. As we currently only are able to measure the ambient temperature, the window temperature is only defined to $\pm$ 5 Kelvin and hence the window temperature correction has a standard uncertainty (k=1) of 87 ppm.

The temperature coefficient of the sapphire refractive index is identical to that of suprasil at room temperature. Hence, we use the same correction and uncertainty estimation. Once we are able to measure the window temperature, the standard uncertainty of the temperature correction becomes smaller for sapphire as the thermal conductivity is higher and we know the temperature of the illuminated portion of the window more accurately.

Stress

The pressure differential across the CSAR entrance window causes stress. The design of the CSAR window insert (Winkler, 2011a) is such that the stress in the material is minimized where the solar radiation passes through the window. Shelton (1992) showed that window transmittance variations due to stress induced refractive index changes are negligible in our case. He also demonstrates that the minimally bent window acting as a lens has not to be considered and that the small stress asymmetry perpendicular to the line of sight causes a negligible amount of stress induced birefringence.

6.6.3 Equivalence of the Windows

Transferring the integral transmittance measurement from the monitor window to the window on the CSAR, we have to know the equivalence of the two windows. The theoretical calculations of the integral transmittance show no difference between the windows if we use the hybrid spectral transmittance composite. Using the measured spectral transmittance composite, we expect the CSAR suprasil window Ay to transmit 0.14 % less than the window Ax and the window Az to transmit 0.03 % less than the window Ax (subsection 6.4.1). The difference of the two sapphire windows applying the measured spectral transmittance composite is 0.08 % with the window 1 transmitting more (subsection 6.4.2).

We performed equivalence experiments by installing two windows of the same material in front of the modified PMO6-0801 on the same day. On the 11^{th} of March 2011, we compared the CSAR suprasil windows Ax and Ay and found an integral transmittance ratio of 1.000312 $\pm$ 0.000370 with the window Ay transmitting more. This result shows no significant difference between the two windows. Further, plotting the measured integral transmittances of the CSAR window Ay and the calculated mean of all atmosphere models (Figure 6.34) and considering a dust contamination of the window, the measured values agree with the result calculated using the hybrid spectral transmittance composite. Hence, the experimental finding supports our assumption that the windows are equivalent and supports our decision to use the hybrid spectral transmittance composite for calculations.

To estimate the standard uncertainty (k=1) of the calculated integral transmittance, we determine half the difference between the highest and the lowest theoretical transmittance curve and divide the obtained value by the square root of three assuming a rectangular distribution. The resulting standard uncertainty of 225 ppm for suprasil includes all seasonal variations due to the changing atmosphere.

On the 21^{st} of March 2011, we compared the sapphire windows 1 and 2 and found an integral transmittance ratio of 0.999757 $\pm$ 0.000164 with the window 1 transmitting more. After cleaning the sapphire windows and redetermining the integral transmittance ratio, the absolute integral transmittance value was 0.16 % higher for both windows but the ratio remained virtually unchanged at 0.999730 $\pm$ 0.000157. This outcome confirms that both windows are identically affected by the dust aggregating on the front surface and that our dust stray light uncertainty of 50 ppm covers the difference between two windows. Plotting the measured integral transmittance of the sapphire window 2 and the mean of all calculated values (Figure 6.35), we are

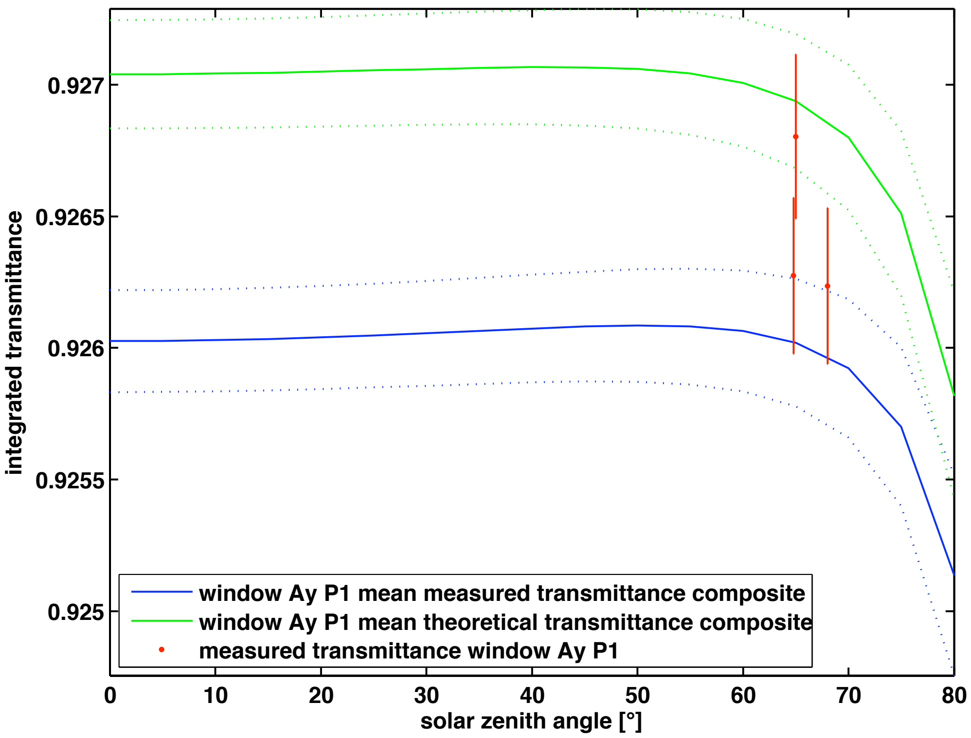

Figure 6.34: *The measured Suprasil daily mean integral transmittances agree with the mean result for all atmosphere models, calculated using the hybrid spectral transmittance composite if we consider an additional dust attenuation. The dashed lines and the error bars indicate the one standard uncertainty (k=1) intervals.*

not able to identify a significant difference. However, we use the hybrid spectral transmittance composite for calculations.

To estimate the standard uncertainty (k=1) of the calculated integral transmittance, we determine half the difference between the highest and the lowest theoretical transmittance curve and divide the obtained value by the square root of three assuming a rectangular distribution. The resulting standard uncertainty of 100 ppm for sapphire includes all seasonal variations due to the changing atmosphere.

6.6.4 Reflectance of the Cavities

The CSAR and the modified PMO6-0801 cavity are coated with the Aerolgaze Z302 specular black paint. Assuming the a constant reflectance of the paint up to 20 µm, the spectral distribution of the radiation being reflected by the cavities is the same for both instruments. However, the absolute amount of the absorbed radiation differs by 0.03 % (CSAR cavity 99.998 %; PMO6-0801 cavity 99.97 %). The reflected radiation is partially deflected by the window back into the cavity, yielding an integral transmittance value that is too small. The correction for the CSAR is 3 ppm assuming that all the radiation reflected by a sapphire window is detected. Using a quartz window, the correction is even smaller. Hence, we can neglect this correction in the

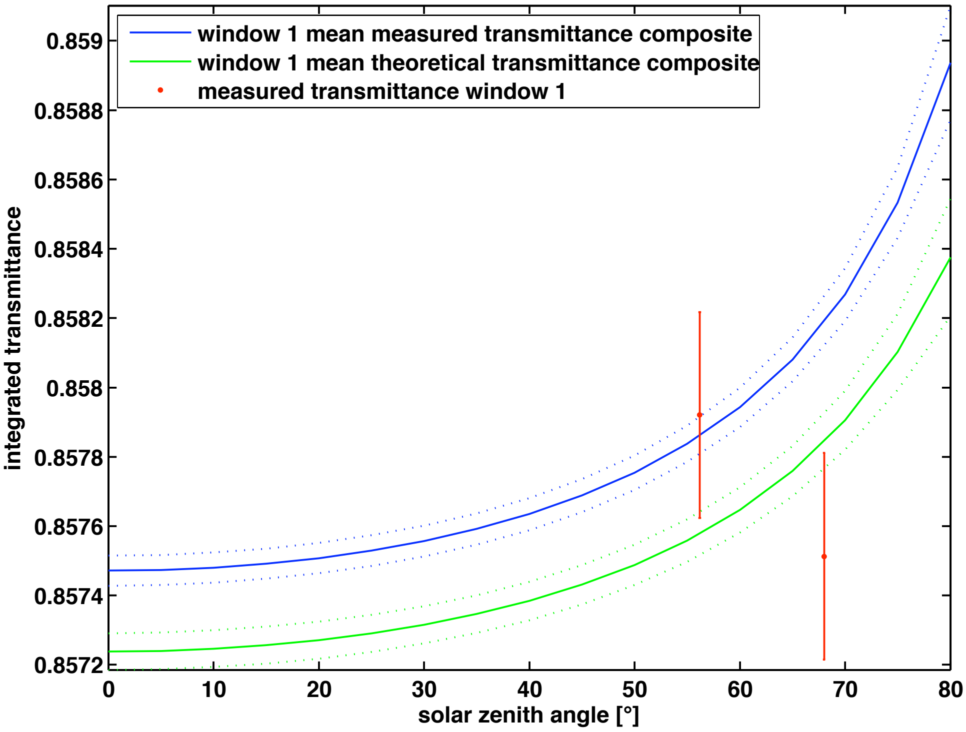

Figure 6.35: *The measured sapphire daily mean integral transmittances show no significant difference to the calculated mean results for all atmosphere models. The dashed lines and the error bars indicate the one standard uncertainty (k=1) interval.*

determination of the absolute CSAR measurements. The higher reflectance of the PMO-0801 cavity creates a larger systematic effect which is harder to asses. To exactly calculate the correction, we would need to determine the angular dependency of the reflected radiation. Since this dependency is unknown, we assume that 50 % of the radiation reflected by the window are detected. The determined correction by which the integral transmittance has to be enhanced is 1.000012 ± 0.000007 for suprasil and 1.000023 ± 0.000013 for sapphire. The standard uncertainties (k=1) are estimated by dividing half of the difference between the maximal and the minimal correction by the square root of three.

6.7 Discussion

Our calculations and measurements show that suprasil and sapphire were the right choice of entrance window materials. The stability and the high over all transmittance avoid further complications besides the determination of the integral transmittance. However, both materials cut off some of the solar spectrum expected on the ground. As the spectrum shows diurnal variations due to the changing air mass along the line of sight and seasonal variations because of the changing atmospheric composition, the integral transmittance through the CSAR entrance window changes and has to be monitored (section 6.4).

The simulated solar spectra expected in Davos allow to calculate a theoretical mean integral transmittance through the CSAR entrance window (Figure 6.34, Figure 6.35) and the associated standard uncertainty of 225 ppm for suprasil respectively 100 ppm for sapphire. These uncertainties include the seasonal variations due to the changing atmospheric composition and partially the day to day variations caused by changing atmospheric temperature and water content profiles. The calculated mean integral transmittance values can be used to estimate the CSAR measured TSI values whenever monitored integral transmittance data are not available. However, the calculations cannot track the day to day variations of the integral transmittance. Hence, an accurate monitor is needed to guarantee stable absolute CSAR TSI results.

The measurements performed with the modified PMO6-0801 radiometer can be used to track the day to day variations of the integral transmittance (section 6.5). However, the 0.1 % scattering of the PMO6-0801 measurements does not allow to correct individual CSAR data points and we use a daily mean integral transmittance value instead. Using the average, we can reduce the uncertainty but we also loose the information about the solar elevation induced transmittance changes which are however expected to be small in the observed solar zenith angle interval (60 to 80 degrees).

The uncertainty budgets (section 6.6; section 6.6) reveal that using a sapphire entrance window yields the smallest integral transmittance uncertainty. This advantage is explained by the higher cut-off wavelength of sapphire. Once we finish the commissioning phase of the CSAR, we will test $CaFe_2$ and KCl entrance windows to expand the transmittance farther into the infrared. The equivalence of the window on the CSAR and the monitor currently heavily contributes to the total uncertainty of the measured integral transmittance. Longer comparisons after the construction works at the PMOD/WRC, will be used to reduce this contribution.

The outcome of our entrance window considerations and measurements is that we need a monitor to measure the integral transmittance whose values scatter at least a factor of ten less than the PMO6-0801 data, to achieve the targeted CSAR measurement uncertainty.

Chapter 7

Monitor to Measure the Integral Transmittance (MITRA) of Windows

The integral transmittance measurements with a modified PMO6-type radiometer have shown that the intrinsic scattering of such an instrument is too large to track diurnal variations of the integral transmittance through the CSAR windows with the intended accuracy. The newly developed Monitor to measure the Integral Transmittance (MITRA) is capable of achieving this goal with the necessary accuracy.

7.1 Principle

The principle of the MITRA is to operate two passive cavity detectors at ambient temperature side by side. One monitor detector observes the total solar irradiance through an identical window as used on the CSAR. Hence, the monitor can determine the attenuation caused by the window relative to the unobstructed monitor detector. Because the MITRA performs relative rather than absolute measurements, the normal drawbacks of ambient temperature radiometry are irrelevant. The multiplicative correction factors such as the reflectivity of the cavities or the area of the precision aperture, cancel out in these relative measurements. The passive operation mode of the monitor uses no electrical substitution and hence the corrections for the non-equivalence, lead heating and the temperature dependency of the control electronics vanish.

The MITRA can be operated in the two modes visualized in Figure 7.1. 1) The left-open mode first calibrates the ratio of the two detector signals without a window. Introducing the window into the light path of the left detector and redetermining the ratio of the two detector signals, directly gives the integral transmittance as the change of the obstructed ratio relative to the unobstructed reference ratio. 2) The left-right operation switches the window from one detector to the other. Each detector works as an autonomous entity and generates its own reference signal when no window attenuates the measurement. By using this technique, we avoid spurious signals originating from detector differences. However, we obtain no reference measurement that tracks the solar irradiance change, during the actual transmittance measurement. And we have to determine the reference signal by interpolation between the unobstructed detector signals before and after the transmittance measurement to calculate the integral transmittance as the ratio of the attenuated and the interpolated reference detector signal.

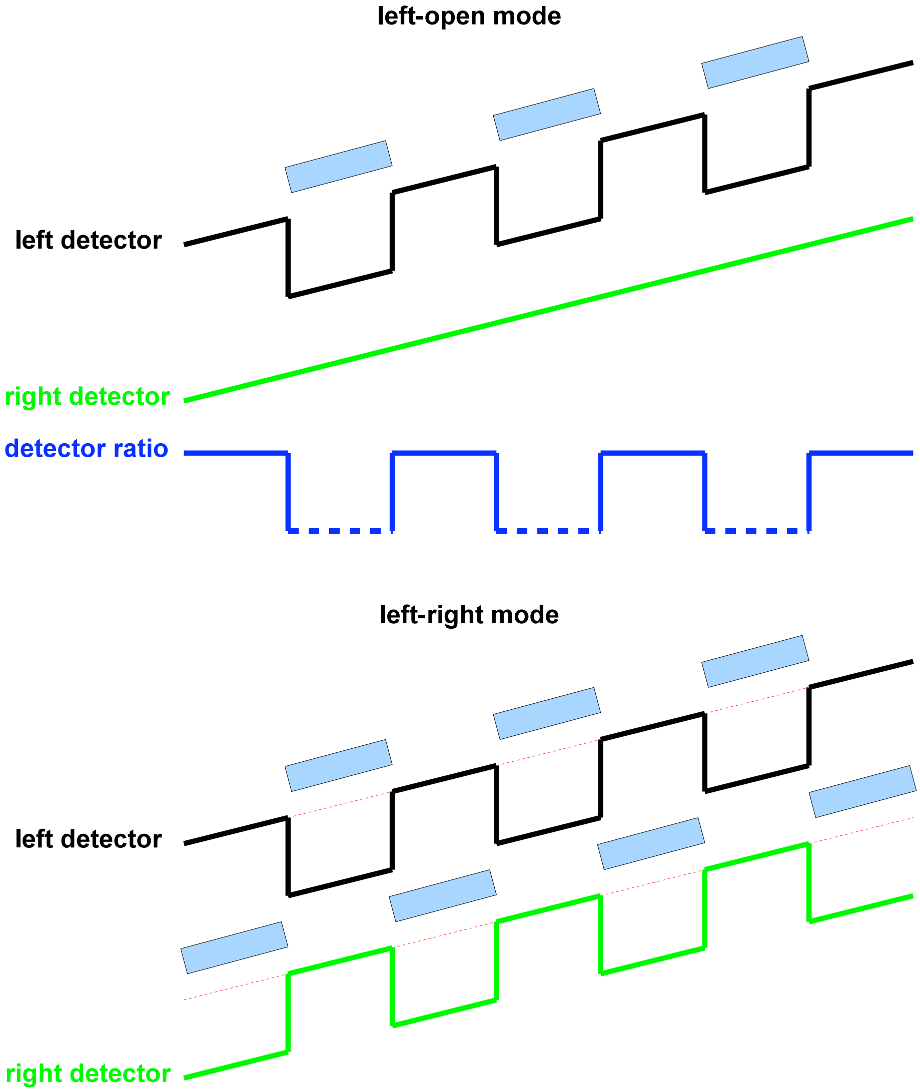

Figure 7.1: *Operation modes of the MITRA instrument. The left-open evaluation technique uses the detector ratio to eliminate the drifts in the individual detector signals. The integral transmittance is calculated as the ratio oft the obstructed and the unobstructed detector ratio. The analysis of the MITRA measurements with left-right method treats each detector as an autonomous entity. The reference detector signal has to be determined by interpolation (red) between the two unobstructed detector signals before and after the window attenuates the detector signal. The integral transmittance is then calculated as the ratio oft the obstructed and the interpolated reference detector signal.*

To determine the detector signals, we measure the temperature differences across the thermal resistors of a detectors. These differences are proportional to the heat flux through the resistor and thus proportional to the heat dissipated inside the cavity by the absorbed solar irradiance: $\Delta\mathrm{T} \propto \mathrm{P}_{sun} \propto \mathrm{I}_{sun}$. For the left-open operation mode the transmittance is determined by

$$\text{transmittance} = \frac{\text{detector ratio}_{left\ obstructed}}{\text{detector ratio}_{unobstructed}} = \frac{\frac{I^{left}_{sun\ window}}{I^{right}_{sun\ no\ window}}}{\frac{I^{left}_{sun\ no\ window}}{I^{right}_{sun\ no\ window}}} = \frac{\frac{\Delta T^{left}_{window}}{\Delta T^{right}_{no\ window}}}{\frac{\Delta T^{left}_{no\ window}}{\Delta T^{right}_{no\ window}}}, \tag{7.1}$$

where the unobstructed detector ratio would ideally be constant. Operating the MITRA in the left-right mode, we use

$$\text{transmittance} = \frac{I^{i}_{x\ window}}{\frac{I^{i-1}_{x\ no\ window} + I^{i+1}_{x\ no\ window}}{2}} = \frac{\Delta T^{i}_{x\ window}}{\frac{\Delta T^{i-1}_{x\ no\ window} + \Delta T^{i+1}_{x\ no\ window}}{2}}, \tag{7.2}$$

where x can be either the left or the right detector and i is the index of the measurement sequence.

7.2 Prototype

A prototype has been built to test the working principle of a dual-detector window transmittance monitor and to identify the critical issues of such a design. Each half of the monitor features an absorbing cavity mounted to a thermopile which is fixed on a heat sink (Figure 7.4). The thermopile acts as thermal resistor allowing the cavity temperature to rise one Kelvin above the ambient temperature if 20 mW are dissipated inside the cavity. Additionally the thermopile senses the temperature difference between the cavity and the heat sink generating a signal proportional to the absorbed solar irradiance. Placing both detector units on a common heat sink, carefully aligning the optical axes and fabricating a protective housing completed the prototype assembly (Figure 7.2).

7.2.1 Thermal Relaxation Time Constant Tuning

Not only heat dissipated in the cavity creates a measurable temperature signal but also the heat flux from the heat sink to the cavity. Some actively controlled radiometers use compensating detectors to account correctly for changes of the ambient temperature: The measuring detector is regularly exposed to the sun, the reference detector is shaded all the time and is used to track the influence of external heat fluxes to the cavities. To apply a compensating cavity technique, we need a symmetric response of the cavity temperature rise to ambient changes. This response is defined by the thermal relaxation time constant of the detectors which involves the thermal capacity of the detector as well as the resistance of the thermal resistor and all contacts.

MITRA also uses two detectors that should respond identically to ambient temperature changes. Solving the one dimensional heat equation derived in subsection 2.3.1, allowed to estimate the influence of the thermal relaxation time constant asymmetry to the detector ratio stability. We chose a Cosine function to describe the diurnal heat sink temperature variation (Figure 7.3)

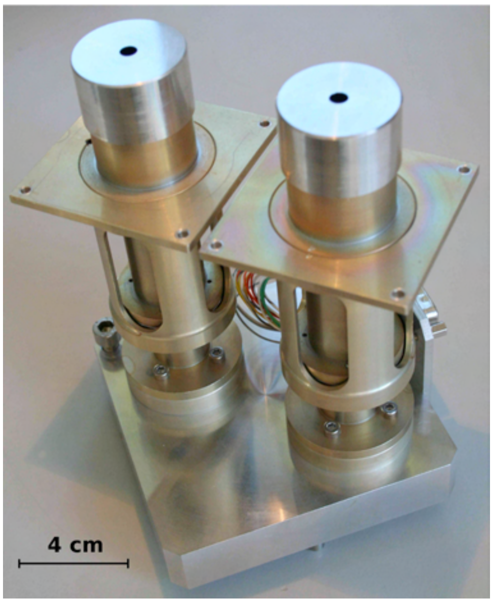

Figure 7.2: *MITRA prototype without the housing protecting the monitor from environmental influences.*

which allows to analytically solve the problem and to calculate the temperature rise of a cavity as a function of the heat sink temperature. The temperature rise of the cavity and the thermal relaxation time constant of the detector are mainly defined by the thermal resistor and hence, we use its properties to describe the reduced one dimensional situation. Because we were not able to asses the thermal properties of the the thermopiles, we use the stainless steel thermal resistor values from a standard PMO6-type detector: the thermal conductivity $\sigma = 15$ W m^{-1}K^{-1}, the density $\rho = 7800$ kg m^3, the heat capacity c $= 480$ J kg^{-1}K^{-1}, the length $L = 0.012$ m and the cross sectional area A $= 1.75 \cdot 10^{-5}$ m^2. The dissipated power P is described by a hyperbolic cosine with the maximum of 20 mW (1000 W/m^2) at noon and values of approximately 16 mW (800 W/m^2) in the morning and the evening. We identified the quantities $(a\lambda_n^2)^{-1} = (\frac{\sigma}{\rho \cdot c} \cdot (\frac{n\pi}{2L})^2)^{-1}$ as time constants τ_n. The first order $n = 1$, $\tau_1 = 14.567$ s is the thermal relaxation time constant describing the temporal behavior of our detectors. To simplify our calculations, we use only the first order $n = 1$ and hence can model the detector asymmetry by varying τ_1. Figure 7.3 shows the calculated cavity temperature and the ratio of the two cavity temperature rises for varying asymmetries. According to our calculations, a 0.5 % difference in the thermal relaxation time constants of the two detectors induces an offset of up to 600 ppm (morning and evening). Assuming a small asymmetry of 0.01 %, the offsets are very small (10^{-5}).

To minimize the influence of the thermal relaxation time constant asymmetry, we have to balance the temporal response of the two detectors to thermal changes. We applied additional thermal mass and copper wires to adjust the thermal capacity of the cavities and the conductivity of the thermal resistors (Figure 7.4). Thus, we were able to reduce the difference between the thermal relaxation time constants to 0.07 % where the balancing was limited by the reproducibility of the time constant measurements.

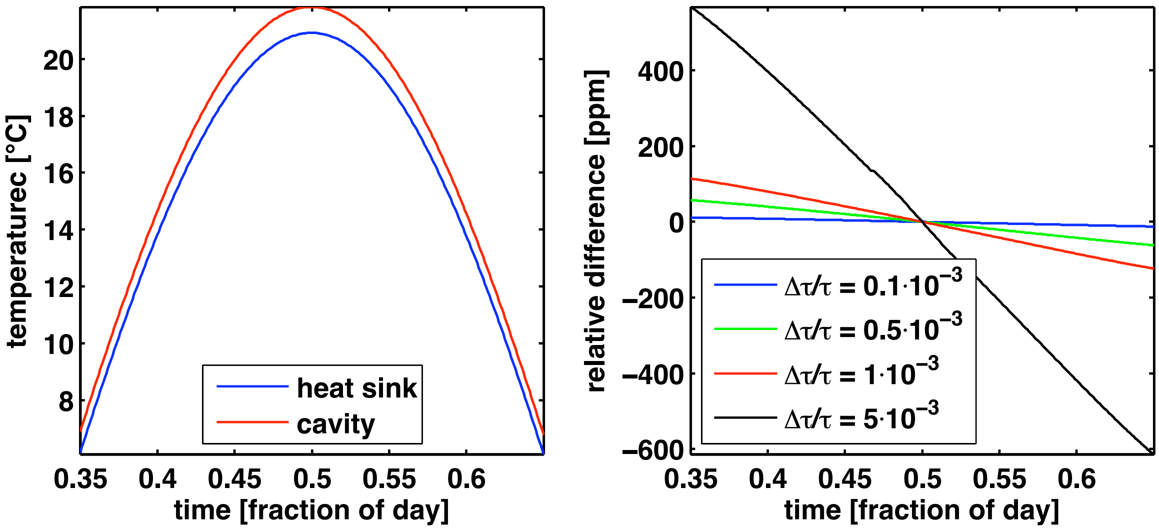

Figure 7.3: *The left figure shows the calculated cavity temperature for a given temperature profile of the heat sink. In the right graph, we introduce an asymmetry in the thermal relaxation time constant and present the determined ratio of the two cavity temperature rises. An asymmetry of 0.5 %, causes offsets of up to 600 ppm.*

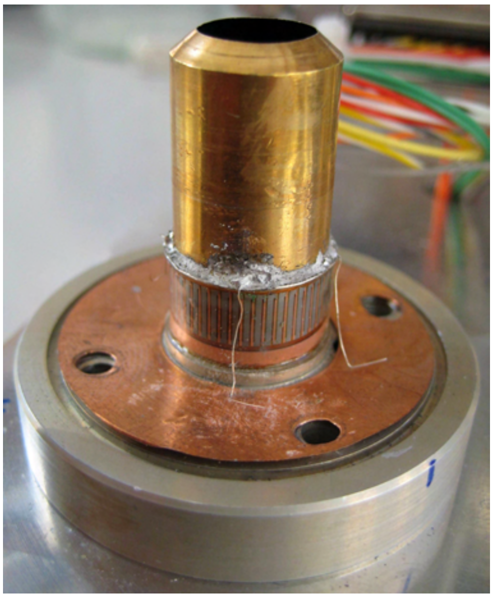

Figure 7.4: *The MITRA prototype detector features an absorbing cavity coated with black paint on the inside respectively with gold on the outside. A thermopile acts as a thermal resistor and senses the temperature difference between the cavity and the heat sink. We used solder to adjust the thermal capacity of the cavity and copper wires to control the temperature rise of the cavity.*

7.2.2 Measurements in Front of the Sun

We performed the first measurements on the sun tracking platform with no window in front of the detectors to investigate the stability of the detector ratio. The results revealed detector ratio changes of several percents at short time scales and of more than 15 % during the day (Figure 7.5). While the long term drifts could be compensated by re-calibrating the ratio once every two minutes without the window, the short time variations are unacceptable with either operation mode of MITRA.

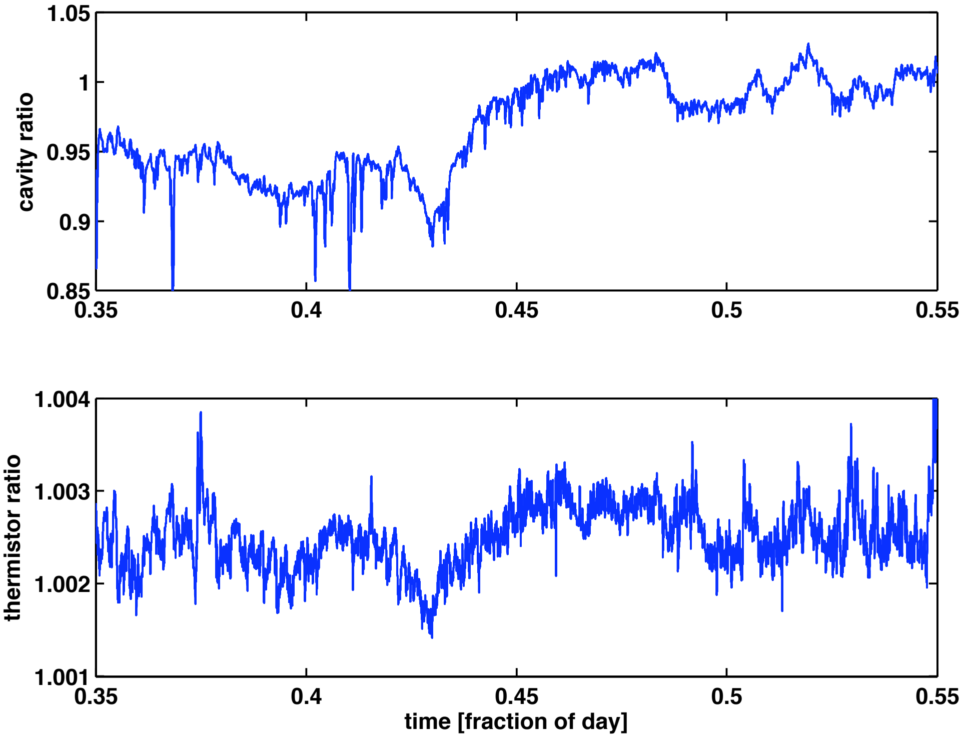

Figure 7.5: *The upper figure shows the detector ratio during a measuring day on the solar tracking platform. We find short term as well as long term variations in the detector ratio of several percent. Determining the temperature ratio inside the common heat sink at the positions where the detectors are mounted (lower figure), reveals horizontal temperature gradients inside the heat sink. These gradients affect the temperature rises of the cavities dissimilarly. Hence, the temperature variations in the heat sink are reflected slightly delayed in the long term variations of the detector ratio.*

To investigate the causes of the cavity ratio variation, we installed thermistors inside the common heat sink at the positions where the detectors are attached. Examining the thermistor signals revealed that the long term changes in the detector ratio are preceded by changes of the thermistor signal ratio by about 5 minutes. The asymmetric response of the heat sink to changes of the ambient temperature explains the long term variations in the detector signal ratio.

The short term variations of the detector ratio can not completely be attributed to the changes of the heat sink temperature. However, the heat conduction through the air from the detector to the housing might cause additional short term variations. The housing and the detector of the MITRA prototype are separated by a 1.5 mm gap. Hence, if the housing temperature is asymmetrically affected by wind or other influences, the detector losses through the air change accordingly and we measure short term variations in the detector ratio. This effect might be enhanced by mechanical asymmetries in the detector to housing distance.

7.3 Final MITRA Instrument

The MITRA prototype measurements revealed two important issues for the final design of the monitor. 1) Both detectors have to be identical in terms of thermal capacity and conductivity to the common heat sink so that temperature changes of the common heat sink affect both detectors identically. 2) The detector losses through the air to the housing have to be minimized so that externally induced changes of the housing temperature do not affect the measured detector ratio.

7.3.1 Design

Novel Cavity Design

The classical PMO6-type detectors (Figure 7.6) have two drawbacks. 1) About 7 % of the solar radiation illuminating the conical part of the cavity are reflected to the cylindrical wall of the cavity. Asymmetries in the coating and the cavity geometry will produce differences in the heat distribution of two cavities resulting in dissimilar losses through the air. 2) Building the detector from the heat sink towards the entrance aperture of the radiometer makes the proximity of the cavity to the housing and apertures inevitable. The losses by conduction through the air might be different for two detectors if there are asymmetries in the small air gaps.

To overcome these drawbacks, we decided to us a conical cavity geometry with the tip pointing away from the sun (Figure 7.6). Using this geometry, the black coating forms a meniscus in the very tip of the cone and hence increases the reflectance of the cavity. However, the reflectance corrections cancel out in the relative MITRA measurements and we are able to benefit from the inverted cavity geometry. The opening angle of the cone is designed such that radiation incident parallel to the optical axis, is reflected five times before leaving the cavity again. The absorbed solar power is dissipated only in the illuminated part of the cone and hence cavity differences create no asymmetric losses through the air.

The best way to reduce the losses through the air and hence minimizing the influence of the housing temperature, is to increase the distance between the detector and housing. The new cavity design allows to have larger clearances to neighboring parts (Figure 7.10).

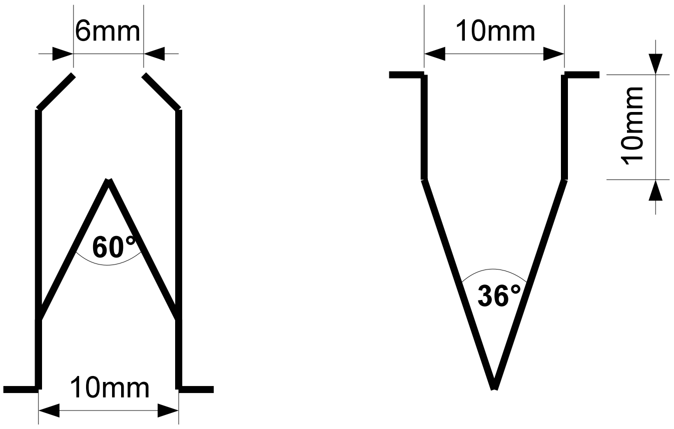

Figure 7.6: *Left, the classical PMO6-type cavity. The new MITRA silver cavity (right) is produced by electroforming and has a wall thickness of 0.1 mm. The outside is coated with a 0.005 mm gold layer whereas the inside is painted with the specular Aeroglaze Z302 black.*

Novel Thermal Resistor and Heat Sink Design

We analyzed the path passed by the heat flux from the cavity to the heat sink and found several obstructions in the classical PMO6-type detectors (Figure 7.7). Glueing the heater foil manually onto the cavity is not a reproducible technique and hence the resulting thermal contact resistances are not equal for any two cavities. The thermal resistor is connected to the cavity and the heat sink by using an automatic laser welding technique. However, we are not able to test the reproducibility and the quality of the obtained thermal contact and hence the introduced asymmetries remain uncertain.

The idea behind the new MITRA detectors is to reduce the number of thermal contacts. As the MITRA instrument operates passively, we can avoid the heater foil glued to the cone. Machining the thermal resistors and the heat sink from one piece of aluminum reduces the number of thermal contacts to one between the cavity and the thermal resistor. To merge the silver cavity and the aluminum thermal resistor, we used an ultrasonic welding technique. The advantage of this technique is the control and the gentleness of the process used to connect the two materials. It is a cold welding process where intensive friction first forces the oxide layer and the contaminations on the material surfaces to open. The simultaneously applied pressure activates the atomic cohesion in the fusion zone. As a result, we obtain the best reproducible thermal contact possibly achievable. TELSONIC is one of the world leading companies providing ultrasonic welding components and services. Together with the research division of TELSONIC we developed a process to connect the aluminum thermal resistor and the silver cavity (Figure 7.8).

The thermal resistance is realized by a thin maze structure leading the thermal heat flux from the cavity to the heat sink. Cutting out the maze structure by electrical discharge machining guarantees the high reproducibility of this work step. Moreover, the thermal resistance is dominated by the highly reproducible path length. A finite element analysis allowed us to dimension the maze according to our needs. We planned to achieve a cavity temperature rise of one Kelvin if 20 mW are dissipated in the cavity. Figure 7.9 shows the thermal simulation of the MITRA detector and its realization.

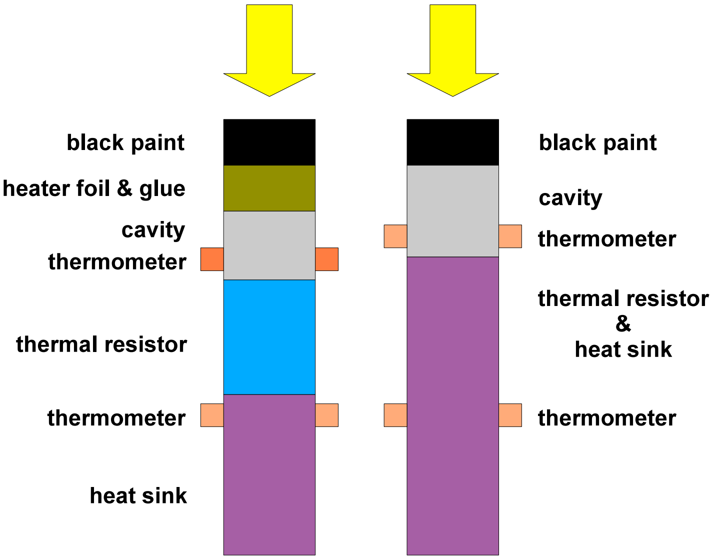

Figure 7.7: *The left figure schematically presents the path passed by the thermal energy in a PMO6-type cavity. Combining different components and materials creates thermal contact resistances. The novel MITRA detector design (right) uses a reduced number of components. Hence, we have less contacts and the thermal behavior of the entire detector can be reproduced with higher accuracy.*

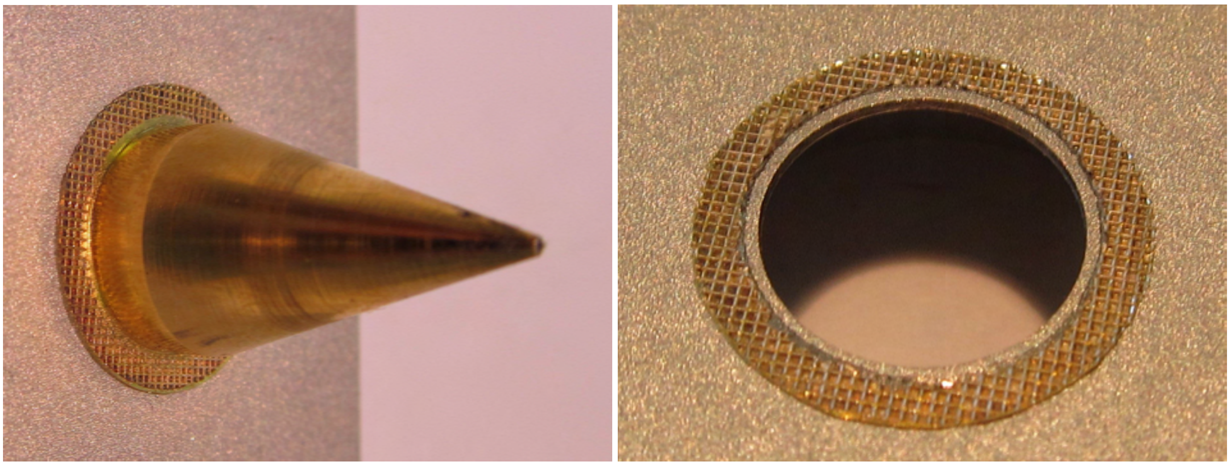

Figure 7.8: *A MITRA cavity that has been ultrasonically welded to an aluminum substrate (left). Applying stress to the silver-aluminum bonding resulted in a rupture of the cavity rather than a separation of the two materials (right). These tests prove the mechanical quality of the atomic bonding and hence the thermal contact is supposed to be excellent.*

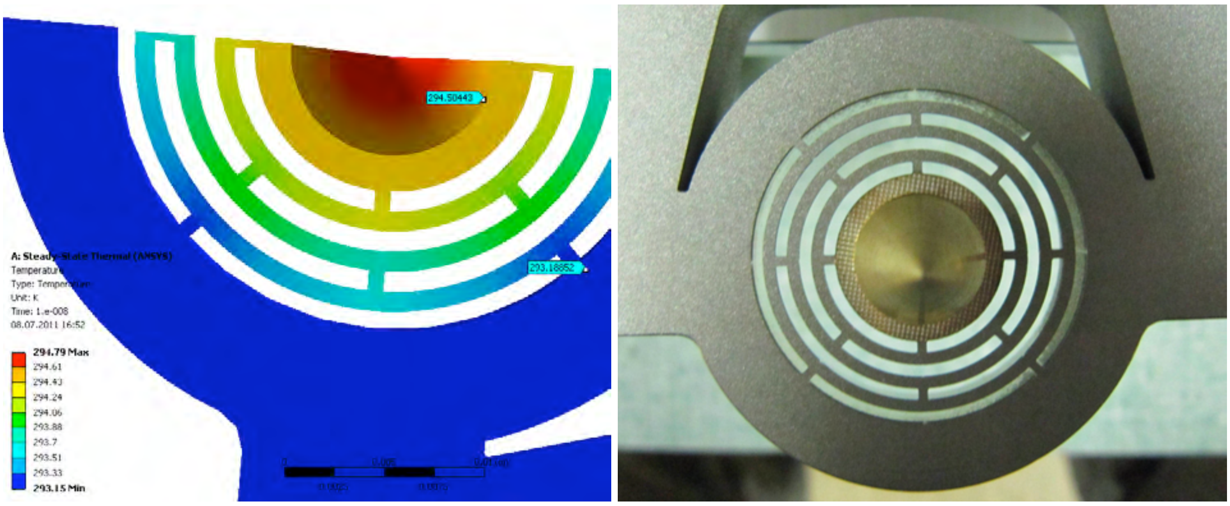

Figure 7.9: *ANSYS finite element thermal simulation of the MITRA detector (left). The model allowed to dimension the thermal resistor maze such that 20 mW dissipated in the cavity produce a temperature rise of 1 Kelvin. Right, the realization of the MITRA detector with the symmetric aluminum thermal resistor maze and the attached cavity.*

Design of the Complete Monitor

The complete design of MITRA is shown in Figure 7.10. The common heat sink is T-shaped with the foot point attached to the MITRA housing to guarantee symmetric responses of both detectors to ambient temperature changes (Figure 7.11). The distance from the cavities to the first shield is kept large to minimize the housing temperature influence on the cavities. Two additional shields protect the detectors from environmental influences like cooling breezes and two baffle apertures disturb the air flow if wind is blowing into the instrument. The view defining aperture geometry is kept similar to the one of the CSAR. The 5 mm diameter precision entrance apertures are from the same batch as the CSAR precision apertures. They have a volcano like shape with a 5 ° inclined front surface. Hence, the inter-reflections between the aperture front surface and the window are guided away from the aperture opening. During the commissioning, the apertures CSAR 02 and 04 were mounted on the MITRA. The larger view limiting aperture in the back of the instrument is mounted 5 mm away from the cavity and the thermal resistor in order to minimize the thermal heat exchange through the air. On the top of the instrument, a linear translation stage with two window inserts allows various operation modes. Under normal circumstances one window insert is left unoccupied to allow the calibration of the detector ratio but will be used to compare different windows. The front of the MITRA is covered by a shielding plate which minimizes the heating of the window and the dust aggregation on the window. All surfaces that may produce stray light were coated with a diffuse MAP black paint (Figure 7.12).

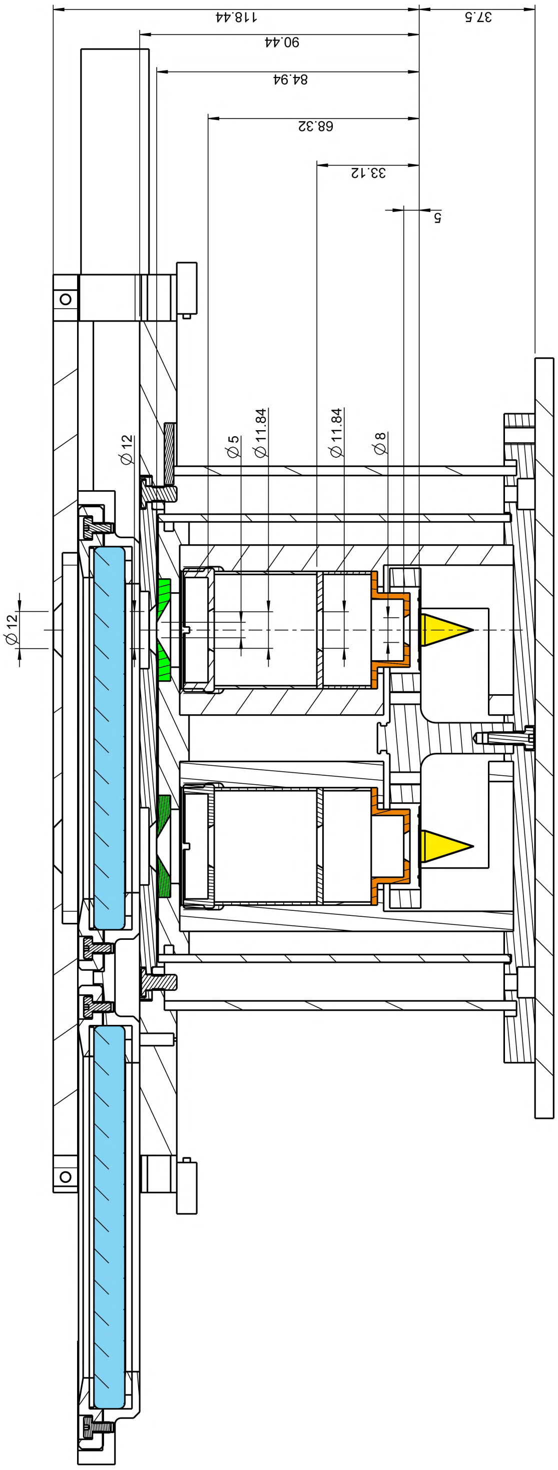

Figure 7.10: *Drawing of the final MITRA instrument. We have highlighted the main components: in blue, the windows; in green, the precision apertures; in orange, the view limiting apertures; in yellow, the cavities.*

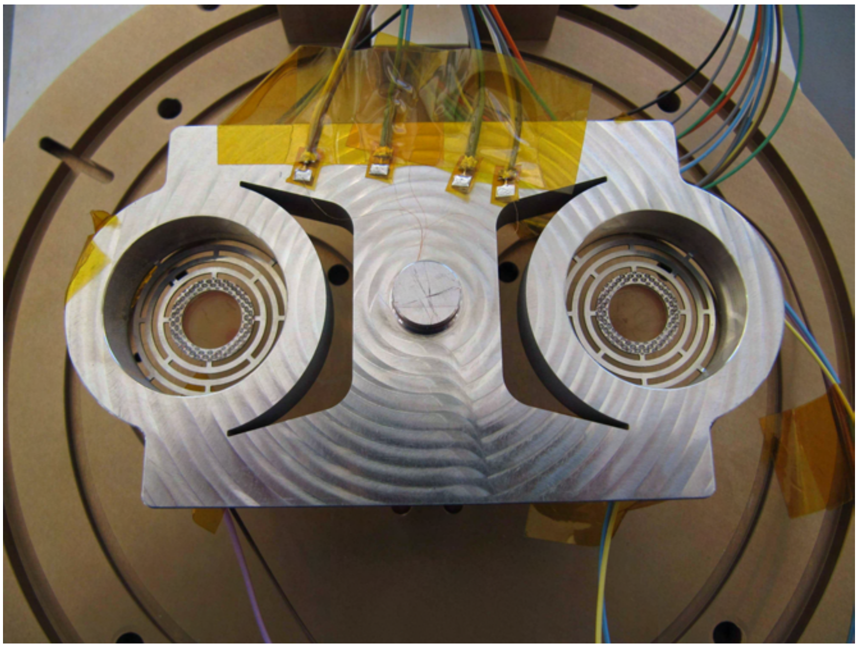

Figure 7.11: *The MITRA T-piece heat sink shape guarantees a symmetric heat flux between the heat sink and the cavities. The central knob holds the reference thermometer for both detectors.*

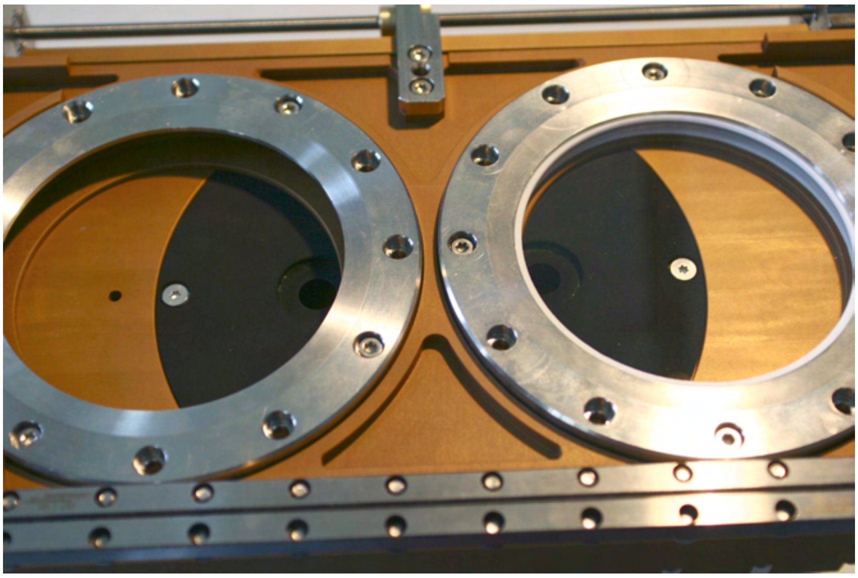

Figure 7.12: *The diffuse black MAP coating minimizes the amount of stray light. The geometry as well as the window retaining components are exactly the same as for the CSAR.*

7.3.2 Temperature Measurement

To use the operation modes discussed in section 7.1, we need to measure the temperature difference between the cavities and the heat sink. The symmetry of the heat sink allows to determine the reference heat sink temperature at a single central position for both cavities (Figure 7.11). We considered three different techniques to measure the temperatures of the heat sink and the cavities:

1. **SMD thermistors** have a large temperature coefficient of up to 0.6 % per Kelvin and if operated correctly, they produce a low amount of self-heating. Their drawbacks prevented us from using the thermistors on the MITRA. The flat contact surface can not reproducibly be attached to the curved surface of the cavities. Differences between any two thermistors would cause an asymmetry in the temperature measurement of the two cavities. And we are not able to guarantee a symmetric positioning on the cavities due to the small thermistor size.
2. **Thermocouples** have the advantage of being able to directly measure the temperature *difference* between two points. Commercially available products generate a small signal of maximally 60 μV per Kelvin making small temperature variation measurements difficult. Thermocouples are mostly point detectors which complicates the reproducible positioning on the cavities, the electrical insulation and the attachment in general. However, we have not yet completely abandoned this option for future versions of MITRA, given that the above stated problems can be resolved.
3. **Copper coils** are used as thermometers on the PMO6-type radiometer detectors. An insulated copper wire of 30 μm diameter is bifilarly wound around the cavity and the heat sink and we obtain a rotationally symmetric thermometer whose electrical resistance changes linearly with temperature. Because of the small copper temperature coefficient of $3.9 \cdot 10^{-3}$ per Kelvin, we have to use 4 m ($\approx 100\ \Omega$) long wires to achieve the desired resolution. The main disadvantage of the copper coil thermometer is the not well defined thermal contact with the cavity and the heat sink. Only the innermost layer of the copper coil is in direct contact with the cavity and the glue used to fix the thermometer, introduces small asymmetries in thermal capacity between two thermometers. As the coils are hand wound, we can not guarantee the exact equality of any tow thermometers.

We decided to use copper coil thermometers for the MITRA because of the long experience we have with this kind of thermometers and because we expect the least complications with this set up. Figure 7.13 shows the copper coil thermometer on a MITRA cavity. For the MITRA operating temperatures, we assume a linear behavior of the electrical thermometer resistance with temperature $R(T) = R_0(1 + \alpha(T - T_0))$ where $\alpha = 3.9 \cdot 10^{-3}$ K^{-1} is the temperature coefficient of copper. Even if the temperature dependence is not strictly linear, we can reduce any nonlinear material influence to the integral transmittance measurements by balancing the cavity thermometer resistances. The temperature rise of a cavity is calculated by

$$\Delta T = \frac{1}{\alpha} \cdot \left(\frac{R^{cavity}(T)}{R_0^{cavity}(T_0)} - \frac{R^{sink}(T)}{R_0^{sink}(T_0)} \right) , \tag{7.3}$$

where we assume an identical temperature coefficient α for all thermometers. T_0 is an arbitrary temperature at which we determined the electrical resistances R_0 after the MITRA reached a thermal equilibrium in a climate cabinet.

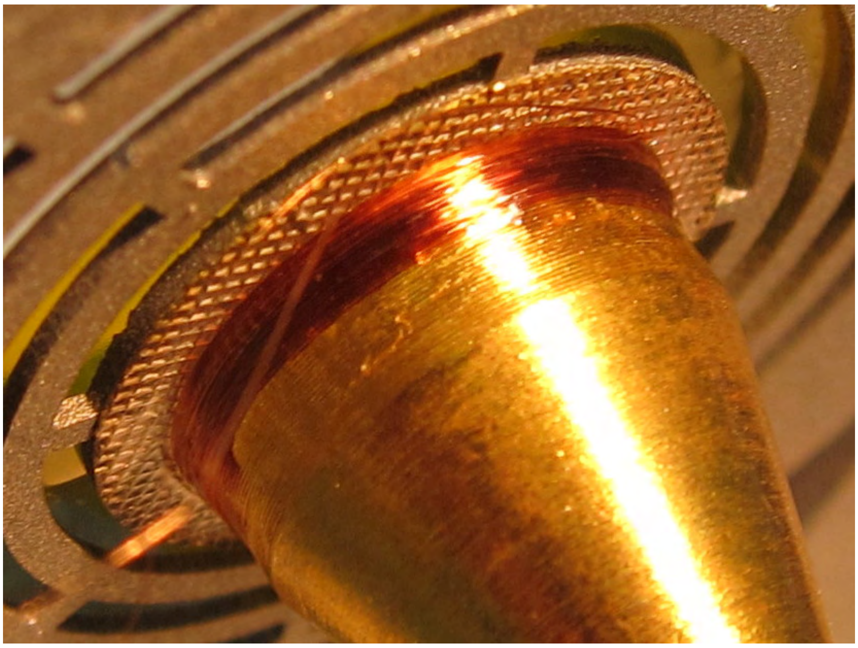

Figure 7.13: *A copper coil thermometer is manually wound around a MITRA cavity and fixed with glue.*

Self-Heating of the Thermometers

We determine the absolute electrical resistance of the thermometer using a four wire measurement. A Keithley 6220 precision current source alternately sends a small positive respectively negative current through the serially connected MITRA thermometers. After settling, a scanner subsequently closes the sensing circuit of the thermometers and an Agilent 34420A nanovoltmeter determines the voltage drop across each thermometer. Using negative and positive currents, we are able to apply a delta technique (Keithley, 2011) to accurately determine the electrical thermometer resistance. This technique eliminates errors introduced by thermocouples at different temperatures throughout the circuit.

A critical issue for the measurement of the electrical resistance is the self-heating of the thermometer. The power dissipated in a MITRA cavity is the sum of the absorbed solar power and the Joule losses from the thermometer $P_{cavity} = P_{sun} + P_{Joule}$. As the Joule losses change with the temperature of the thermometer, the ratio of the power measured by two different detectors will change with temperature. However, this ratio change decreases quadratically with the sensing current. Our calculations show that a sensing current of 100 µA, causes a detector ratio change of $<$ 5 ppm over a temperature range of -15 to 30 degrees Celsius. Hence this setting is the best trade-off between self-heating and achievable measurement resolution.

7.3.3 Thermal Relaxation Time Constant Tuning

We determined the thermal relaxation time constants of the MITRA detectors in the laboratory using a green intensity stabilized laser beam of 3 mm diameter. The applied power level of 20 mW changed the electrical cavity thermometer resistance by 0.39 %. This change represents a temperature rise of 1 Kelvin and perfectly confirms the finite element simulations. The difference in the thermal relaxation time constant between the two detectors initially was 0.12 seconds. We explain this difference by the distinct thermal capacities of the cavities which depend on the amount of glue used to attach the thermometers. Hence, we used the same glue to increase the thermal capacity of the faster detector and to balance the thermal relaxation time constants. The repeated determination of thermal relaxation time constants yielded mean values of 14.879 s and 14.829 s for the two MITRA detectors. The balancing is limited by the reproducibility of the thermal relaxation time constant measurements being of the order of 0.05 s. We repeated the simulation from subsection 7.2.1 for the novel MITRA aluminum design and found that the thermal relaxation time constant asymmetry of 0.35 % can produce an 0.2 % offset in the detector signal ratio (Figure 7.14).

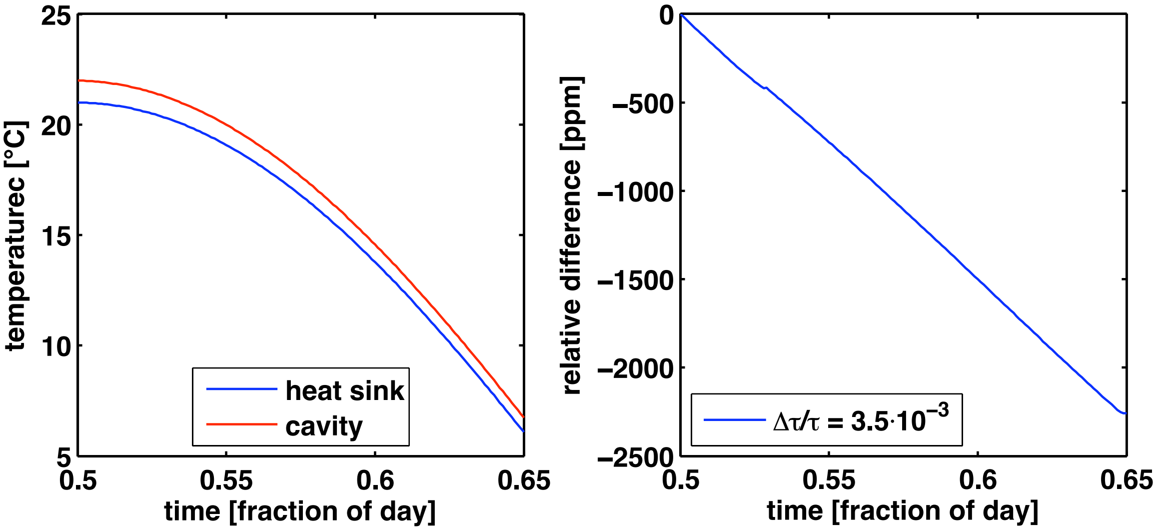

Figure 7.14: *The left figure shows the calculated cavity temperature for a given temperature profile of the heat sink. In the right graph, we introduce an asymmetry in the thermal relaxation time constant and present the determined ratio of the two cavity temperature rises. An asymmetry of 0.35 %, causes an offset of up to 2200 ppm.*

7.3.4 Thermal Stability Test

The temperature rise of the MITRA cavities above the heat sink temperature is 1 Kelvin and we have to reliably detect temperature changes of 0.1 mK to achieve the intended detector ratio uncertainty of 0.01 %. These small signals are sensitive to disturbances in the measurements of the electrical resistance. We performed thermal stability tests of the detector ratio where we measured the dark signals of the detectors with closed entrance apertures. But since we are interested in the variations expected for illuminated cavities , we introduced a virtual temperature rise of one Kelvin by adding 0.39 Ω to the cavity thermometer resistances.

The ambient temperature decreased by 12 Kelvin during the night we performed the experiment and we found a detector ratio change of 2400 ppm (Figure 7.15). This result is nearly the same as predicted by the simulation in the previous section and supports our assumption that the detector ratio drifts are caused by the thermal relaxation time constant asymmetry of the detectors. Removing the trend, we are able to determine the intrinsic scattering of the detector ratio with a standard deviation of 327 ppm.

The drift of the detector ratio can only be minimized, if we find a technique to further reduce the difference in the thermal relaxation time constants of the two detectors. The variation of the individual data points is caused by thermal fluctuations within the thermometers specifying the natural accuracy limits of the current system.

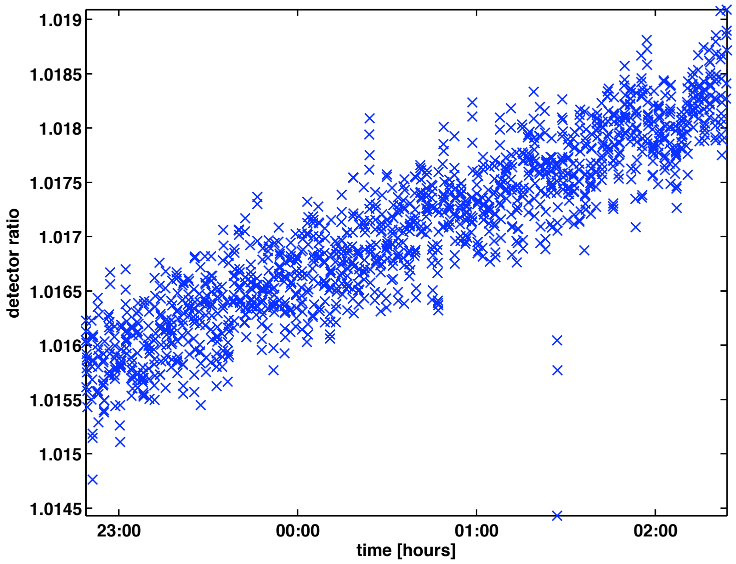

Figure 7.15: *The ratio of the two MITRA detector dark signals drifts as the temperature of the heat sink changes during the night. After removing the linear trend, the standard deviation of the detector ratio is 327 ppm.*

Using the two MITRA evaluation techniques, we successfully removed the trends of the detector ratio and obtained a stable integral transmittance of 100 % (Figure 7.16). The standard deviations of the two distributions are 395 ppm for the left-open evaluation and 376 ppm for the left-right technique.

We can also use the thermal stability test data to determine the variations in the integral transmittance calculation introduced by the fluctuations in the detector ratio measurements. To model the attenuation by a fused quartz window, we multiply parts of integral transmittance time series by a factor of 0.927. An offset function is then fitted to the data to determine the integral transmittance (Figure 7.17). The mean integral transmittance of the test period is 0.926962 which is close (-38 ppm) to the actually applied attenuation factor. The standard deviation of the result is

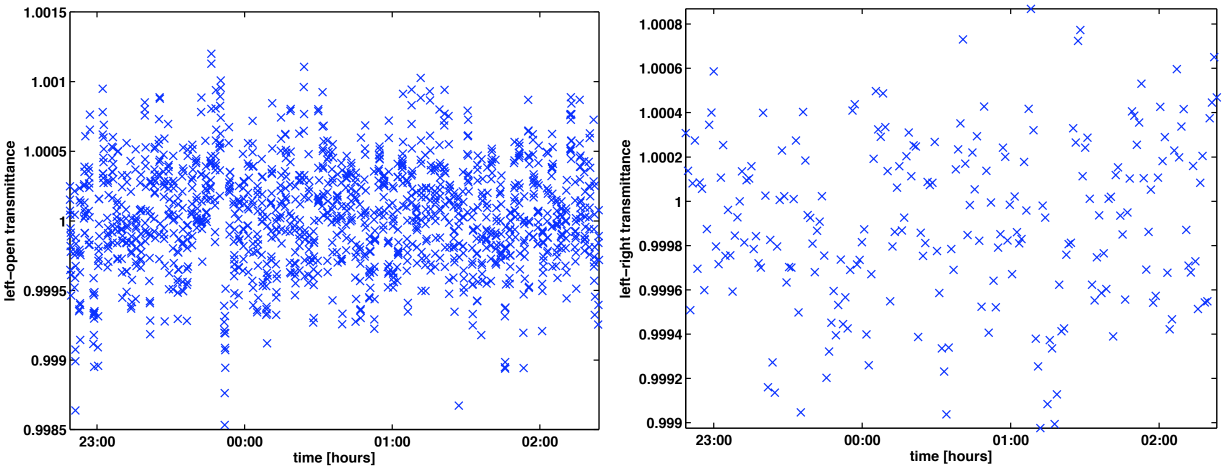

Figure 7.16: *The left-open (left) and the left-right (right) MITRA evaluation techniques successfully remove the detector drifts and yield a constant integral transmittance of 100 %. The left-right technique yields fewer data points because we show only the result from one cavity and because we average the data to obtain an accurate reference signal.*

0.000127. Hence, the fitting allows to reduce the variation of the integral transmittance values below the scattering of the detector ratio.

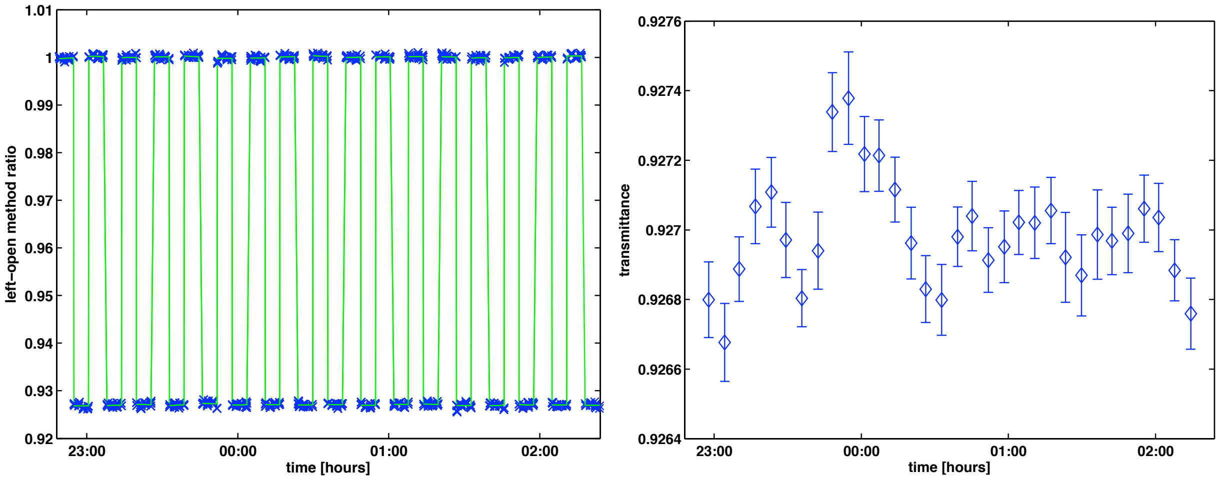

Figure 7.17: *We multiply sections of the thermal stability test data by 0.927 to simulate the attenuation by a fused quartz window (left). The offset fitting technique (green) described in section 4.1 is used to determine the integral transmittance of the simulated data. The mean integral transmittance of 0.926962 is close (-38 ppm) to the actually applied attenuation factor.*

7.3.5 Measurements in Front of the Sun

After the successful thermal stability tests, we performed the first measurements with the left-open method on the solar tracking platform in Davos (Figure 7.18). The determined integral transmittance values vary by 2 % during the first hour of the experiment which is much more than expected and in the course of the day, the scattering became even worse. Figure 7.19 illustrates the problem with the solar measurements. The detector ratio is stable as long as no window is introduced but with the window in place, the detector ratio starts to fluctuate. This scatter causes then variations in the determined integral transmittance which are larger than expected from the the theoretical calculations in section 6.4 and hence are not considered real changes due to the atmosphere. We are investigating plausible explanations for for this behavior like wind affecting the unattenuated detector despite the baffles and/or stray light effects.

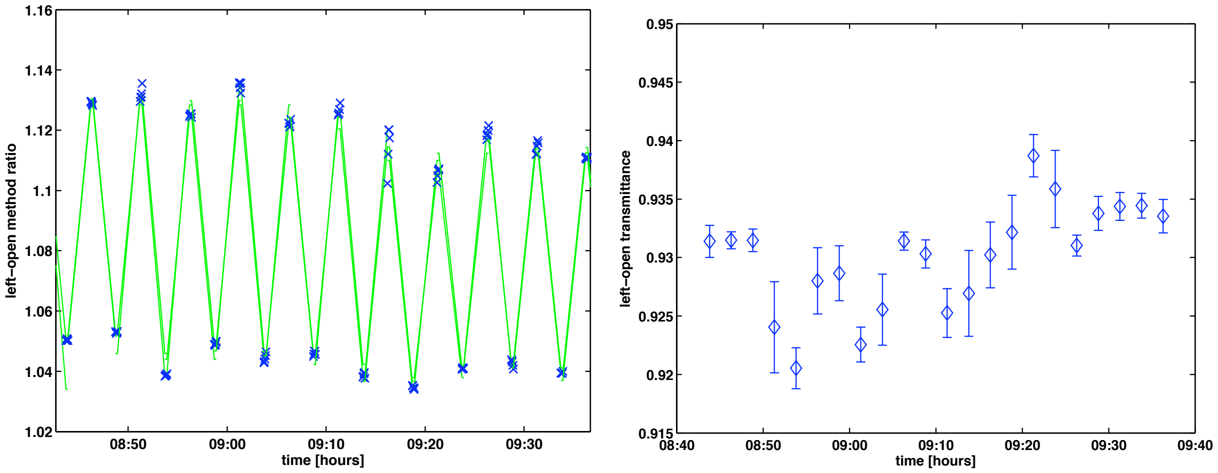

Figure 7.18: *Left-open MITRA integral transmittance measurements in front of the sun on the 14th October 2010. Left: Using the offset fitting technique (green) described in section 4.1, we find a integral transmittance peak to peak variation of 2 % (right). The error bars indicate the standard uncertainty (k=1) of the fitting procedure.*

7.4 Discussion

We have designed and built the first dual-cavity monitor capable of determining the integral transmittance of broadband windows with high accuracy. The centerpiece of the instrument is the novel detector that reduces the amount of thermal contacts and guarantees an unprecedented thermal symmetry of both detectors with respect to the heat sink and ambient temperature. Besides the MITRA, a three cavity absolute radiometer prototype called Davos Absolute RAdiometer (DARA) was built with our new detector design. And a solar absolute radiometer with the new detector design is part of the Sun Monitor (SuMo) package selected as core payload on the ESA PROBA3 space mission.

The selected copper coil thermometers are currently the best choice of measuring the cavity temperature rise above the heat sink temperature. However, we are investigating other solutions based on vapor depositing a thermometer layer on the cavity. Laser trimming would allow to balance the electrical resistances of the thermometers and hence to minimize drifts of the measured detector ratio. If we are able to embed the thermometer layer into the cavity walls, we could further reduce the environmental influences on the measured resistance. With these

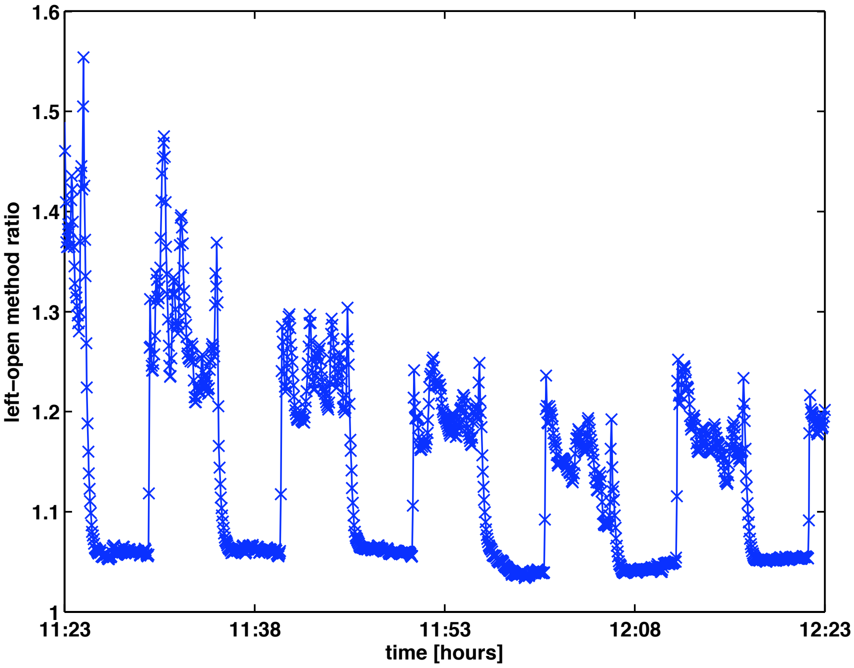

Figure 7.19: *This figure shows the problems with the MITRA measurements on the 14th October 2010. The detector ratio is stable when none of the detector signals is attenuated by a window. Once the window has been introduced in front of one detector, the detector ratio starts to scatter.*

new thermometers, we would avoid any manual labor on the detectors and could improve the symmetry of our instruments further.

Balancing the thermal relaxation time constants of the detectors is limited by the reproducibility of time constant determination. However, the detector ratio drift resulting from the remaining time constant imbalance, is removed in both of the two MITRA operation modes. Laser trimmable thermometers would allow an unprecedented accuracy of the balancing process.

The natural detector ratio variations observed in the thermal stability test limit the achievable uncertainty of the current system. The scanning device used to subsequently measure the voltage drops across the thermometers may contribute to the observed scattering. We invest in additional nano-voltmeters to allow a simultaneous sampling of all three thermometer resistances and hence will further reduce the variation of the detector ratio. However, the scattering induced by thermal fluctuations in the thermometers can only be reduced by averaging the measurements over one minute. The offset fitting function used to determine the integral transmittance allows to further reduce the uncertainty and to achieve the intended accuracy of 0.01 % in the laboratory.

The integral transmittance measurements on the sun tracking platform revealed a yet unsolved large scattering of the detector ratio whenever we introduce the window in front of one detector. Further testing is needed to eliminate the disturbances introduced by wind, stray light and/or other factors to exploit the full potential of the MITRA.

Chapter 8

The Cryogenic Solar Absolute Radiometer (CSAR)

The Cryogenic Solar Absolute Radiometer CSAR is the product of a collaboration between the PMOD/WRC, the NPL and METAS which started in 2007. The purpose of the joint effort was to adapt the advantages of cryogenic radiometers (Martin et al., 1985) to solar radiometry and to create a possible alternative to the World Radiometric Reference (WRR). Operating a radiometer at cryogenic temperatures allows the application of larger cavities with higher absorptance and ensures the equivalence of optical and electrical heating by minimizing the thermal gradients in the cavity material. To prove the concept of cryogenic solar radiometry and to introduce the instrument to the community, we participated with the CSAR in the IPC-XI.

The CSAR has also been designed with space flight in mind and the according TRUTHS mission has been proposed. Bringing a cryogenic radiometer on orbit would allow to calibrate radiometric detectors in space against an SI primary standard and hence to resolve observed offsets between current space radiometers. The CSAR incorporates 4 TSI cavities and 2 radiant power cavities operating at 20 Kelvin. The complete design and the data evaluation of the CSAR are presented in the associated thesis of Winkler (2011a). We present a short overview of the assembling and commissioning phase as well as the first preliminary measurement results. In the final design document the three parties agreed on the requirement specification given below (Winkler et al., 2007):

Operational Parameters

- **Ground**
  - TSI levels from 800 W/m^2 to 1100 W/m^2 can be measured.
  - The absolute accuracy of TSI measurements should be better than 0.01 % (k=1).
  - The resolution of the TSI measurement must be better than 0.001 %.
  - The thermal relaxation time constant of the TSI detector must be less than 10 s.
  - Radiant power levels of 1 mW must be measurable in order to perform direct comparisons to laboratory cryogenic radiometers.

- **Space**
    - TSI levels from 1300 W/m^2 to 1500 W/m^2 can be measured.
    - The absolute accuracy of TSI measurements should be better than 0.01 % (k=1).
    - The resolution of the TSI measurement must be better than 0.001 %.
    - The thermal relaxation time constant of the TSI detector must be less than 10 s.
    - The radiant power of monochromatic beams must be measured at levels of 1 to 100 µW.
    - The spectral range of 200 to 2500 nm must be covered for spectral radiant power measurements.
    - The absolute accuracy of radiant power measurements should be better than 0.1 % (k=1) for the wavelength intervals of 200 to 400 nm and 1000 to 12500 nm. In the range of 400 to 1000 nm the required absolute accuracy is 0.05 % (k=1).
    - The resolution of the radiant power measurements should be better than 0.1 % (k=1) for the wavelength intervals of 200 to 400 nm and 1000 to 12500 nm. In the range of 400 to 1000 nm the required absolute accuracy is 0.05 % (k=1).

Mechanical

- The mass of the complete system should not exceed 50 kg. Less than 31 kg are desirable.
- The volume of the complete system should be smaller than 500 mm x 300 mm 300 mm.
- Space qualified coatings, adhesives and materials can be used for the satellite instrument.
- Vibrations introduced by the cooler or environmental disturbances do not introduce a thermal noise larger than 0.001 µW (White and Meeson, 2002).
- The mechanical connections and the alignment have to survive the satellite launch.
- The heat transfer between the cold stages has to be adjustable to the available cooling power and the heat sink temperature.

Thermal

- The temperature stability of the reference block needs to be a few µK for TSI measurements and 0.1 µK for radiant power measurements.
- The resolution of the temperature sensors needs to be a few µK for TSI measurements and 0.1 µK for radiant power measurements.
- The thermal relaxation time constant of the temperature sensors must be 2 orders of magnitude lower than the time constant of the optical measurements (White and Meeson, 2002), i.e. 0.1 s for TSI and 0.01 s for radiant power.

- The temperature dependence of the thermal resistor is not relevant for radiant power measurements. For the TSI measurements a T^2 dependence is desirable.
- The thermal resistance of the leads going to the cavities should be as high as possible in order to minimize the difference between electrical and optical heating.

Electrical

- The resolution of the measured electrical power must be better than 10 nW for TSI and better than 50 pW for radiant power measurements.
- Pickup of external radio frequency signals and pickup of local signals from the measuring equipment must be minimized.
- The time constant of the control system has to be one order of magnitude lower than for the optical measurements (White and Meeson, 2002), i.e. 1 s for TSI and 0.1 s for radiant power measurements.
- For the design we assume that the actively controlled cavities perform at least as good as the open-loop system.
- The electrical resistance of the leads has to be as low as possible in order to minimize the difference between electrical and optical heating. Ideally we use superconducting wires.

Optical

- The aperture geometry must follow the WMO CIMO recommendation: 5° field of view and 1° slope angle.
- The absorptivity of the cavities should not change by more than 0.001 % over a lifetime of 10 years on the ground respectively 7 years in space. Otherwise the changes have to be trackable to that level of accuracy.
- Multiple cavities should guarantee redundancy.
- The diameter of the defining aperture depends on the available cooling power. Minimum 3 to 4 mm, maximum 5 to 10 mm.
- There should be no significant difference in the aperture diameter between the operating and room temperature. Changes must be known with an accuracy of below 0.01 %.
- The distance between the defining and the view limiting aperture needs to be chosen such that the diffraction correction is insensitive to the exact distance.
- An aperture changing mechanism should guarantee redundancy. In the event of a failure the mechanism must return to a defined default state.

8.1 Assembling Phase

The assembling phase began in March 2010 at the NPL after all parts and components had been delivered by the PMOD/WRC, the METAS and the NPL.

We started by attaching the gold plated shields to the Sumitomo Heavy Industries Cryocooler SRDK-305D-A31C (Figure 8.1). This mechanical Stirling cycle based cooling system provides a cooling power of 15 W at 40 Kelvin on the first stage and 0.4 W at 4.2 Kelvin on the second stage. We use a two stage system to cool an intermediate temperature heat shield between the detectors and the walls of the vacuum chamber. Nylon and steel heat links allow to control the temperature rise of shields above the temperature of the cold tips of the cooler. Flexible heat links are used to connect the shields with the 20 K and the 180 K reference block of the radiometer.

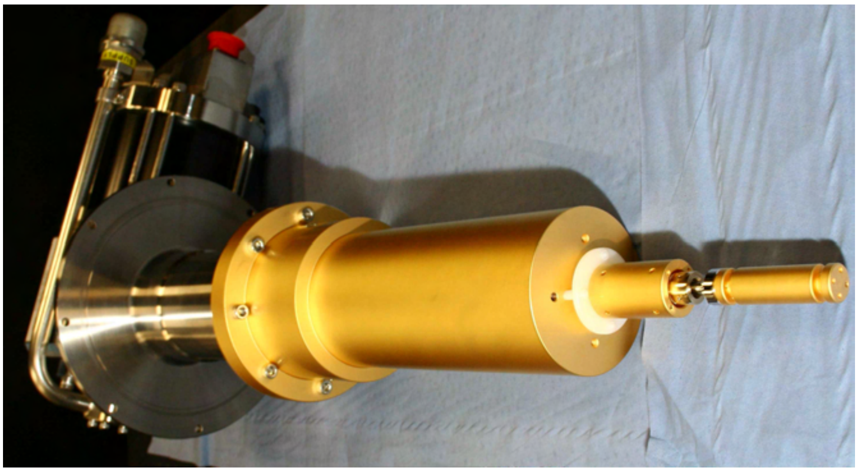

Figure 8.1: *The CSAR cooler with the attached gold plated heat shields. The very front tip is connected to the 4 K stage of the cooler via a steel heat link. A flexible heat link connects the tip to the 20 K radiometer reference block. The white nylon heat link connects the intermediate heat shield to the 40 K stage of the cooler. From the intermediate heat shield a flexible link connects to the 180 K radiometer reference block.*

The center piece of the CSAR is the reference block assembly (Figure 8.2). The 20 K copper reference block has six inserts for 2 radiant power cavities and 4 TSI cavities. Three TORLON links connect the 20 K reference block to the gold plated 180 K reference block. And the 180 K reference block is mounted on the ambient temperature reference block using three TORLON links. TORLON is a mechanically stable plastic with a low thermal conductivity. This properties guarantee a minimal heat exchange between the reference blocks and a mechanically robust set up which endures the satellite launch.

The TSI cavities (Figure 8.3) are 70 mm long cylinders of 20 mm diameter with a tilted back cover. The entrance aperture to the cavity has a diameter of 10 mm. The gold plated outside minimizes the radiative energy exchange with the surrounding heat shield. The cavity inside is coated with a diffuse Nextel black paint. Preliminary results from reflectivity measurements show that such a cavity absorbs 99.98 % of the incident radiation. This absorptance is lower than the specified requirement but could be improved with the better Nickel-Phosphorous black coating

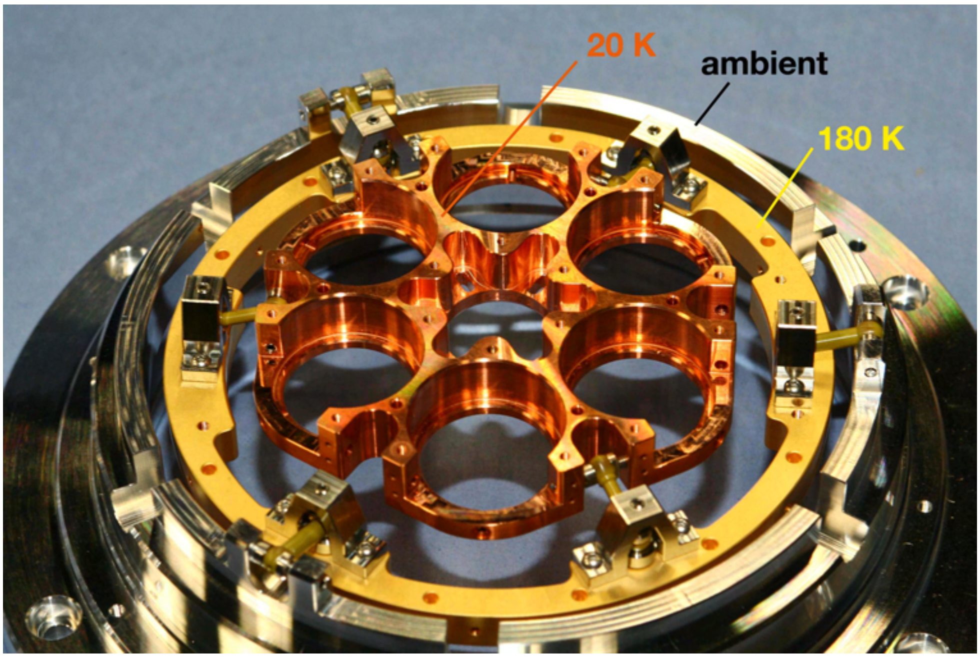

Figure 8.2: *The copper 20 K reference block has six cavity inserts. We use three TORLON links to connect the 20 K and the gold plated 180 K intermediate reference block. Another three TORLON links connect the 180 K reference block to the ambient temperature stage of the radiometer assembly.*

which was not available when needed. The cavities sit in a variable Nylon heat link sandwich in the reference block. Retaining rings and clamps press the cavities onto the reference block insert forming a tight thermal contact (Figure 8.7).

The main issue while assembling the CSAR was the attachment of the Rhodium-Iron resistance thermometers (Figure 8.4). We used the electrically insulating GE varnish to attach the thermometers at the desired positions to the radiometer. However, cooling down the radiometer to 20 K and reheating to ambient temperature caused the thermometers to detach. Inserting one layer of GE varnish soaked cigarette paper in between the thermometer and the substrate resolved this problem.

The testing and commissioning of the CSAR asked for a flexible data acquisition system. We decided to use Tinsley resistance bridges to measure the absolute resistance values of the thermometers. These bridges are capable of determining a resistance with an accuracy of 3 ppm using a sensing current of 0.1 mA. The small sensing current is needed to minimize the influence of the thermometer's self heating. We attached Vishay foil resistors to the cavities and the reference blocks to dissipate electrical power. Time Electronics precision sources deliver the current to drive the heaters. To determine the electrically dissipated power $P = U \cdot I$, we measure the voltage drop across the heater. The heater current I is determined by measuring the voltage drop across a calibrated reference resistor.

The data acquisition software was written in LabVIEW. Software implemented PID-controllers use the thermometer measurements and a heater to stabilize the 20 K reference block or a cavity temperature to the desired set-point.

Figure 8.3: *A fully assembled CSAR cavity covered with the 10 mm diameter view limiting aperture.*

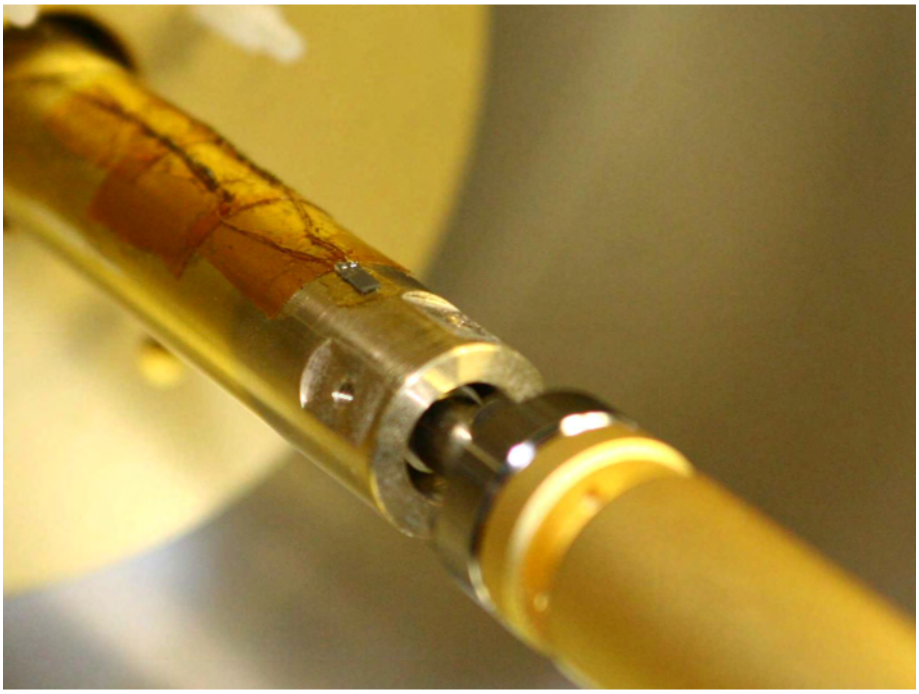

Figure 8.4: *The Rhodium-Iron resistance thermometers were attached to the radiometer using cigarette paper and GE varnish.*

8.2 Commissioning Phase

With the IPC-XI approaching, we moved the CSAR to Davos in July 2010 for the commissioning phase without prior optical measurements at the NPL.

Thermal stability tests showed that the original connection between the 4 K stage of the cooler and the 20 K reference block yields a too high reference block temperature. We manufactured a copper heat link having three flexible copper braid arms (Figure 8.5) that allows a cooling of the reference block down to 20 Kelvin. However, using this connection, the cooler tip temperature variations of ±0.15 K are transmitted without damping to the 20 K reference block. Our temperature control system was not able to balance these variations. We introduced a 500 gram lead cylinder between the 4 K stage of the cooler and the copper heat link. Lead has a large thermal mass at cryogenic temperatures and hence reduces the variations on the 20 K reference block to an acceptable level. Figure 8.6 shows the connection of the flexible heat links to the 20 K reference block and to the 40 K stage of the cooler.

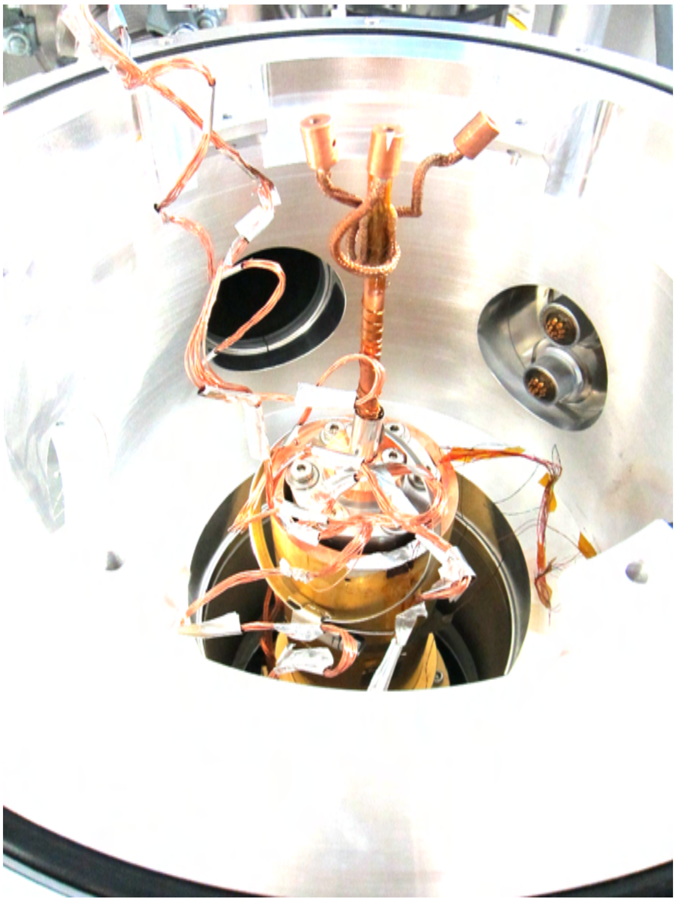

Figure 8.5: *The redesigned copper heat link between the cooler and the 20 K reference block has three flexible copper braid arms. The heat link is mounted on a lead cylinder that damps the temperature variations of the 4 K cooler stage.*

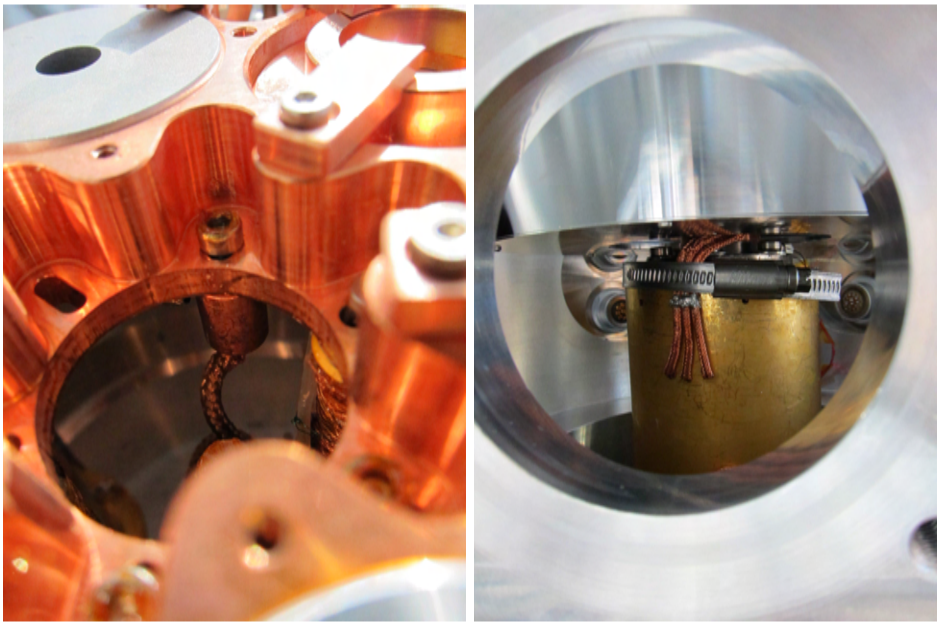

Figure 8.6: *The left picture shows the connection of the flexible heat links to the 20 K reference block. Apiezon high vacuum grease on the contact area enhances the thermal contact. On the right image, we see the jubilee clip fixation of the flexible heat links going from the intermediate 180 K reference block to the second stage of the cooler.*

The complete detector stage (Figure 8.7) has 4 TSI cavities using two different methods of retaining the cavities in place. Compensating aluminum targets are mounted in the radiant power cavity inserts allowing the accurate pointing of the instrument.

The specifications require redundancy of the space measurements. The CSAR design accounts for this demand by using an aperture and a shutter wheel. The aperture wheel allows to position every entrance aperture in front of any desired detector. The shutter wheel determines which of the six detectors is illuminated. However, the shutter and the aperture wheels could not be completed in time for the IPC-XI. As the redundancy is not crucial for the ground based measurements, we use a static aperture support (Figure 8.8) and a manual external shutter (Figure 8.10).

First tests investigating the heater power needed to obtain a stable cavity temperature with a closed shutter, revealed a drift of the closed heater power. This finding indicates an ambient temperature dependent heat exchange between the cavity and the environment. We applied Multi-Layer-Insulation (MLI) to the heat shields (Figure 8.9) and the vacuum chamber (Figure 8.10) to minimize the radiative heat exchange. But the closed heater power drifts persisted leaving an energy input through the wires to the cavity as the only explanation for the drift.

We were able to minimize the influence of ambient temperature changes by improving the heat sinking of the wires going to the cavity (Figure 8.11). While improving the heat sinking, we also modified the CSAR absorbing cavity by creating longer cavities and applying a specular Aerolgaze Z302 black coating. Hence, we achieve an improved cavity absorptance of 99.998 % and could obtain the first CSAR results.

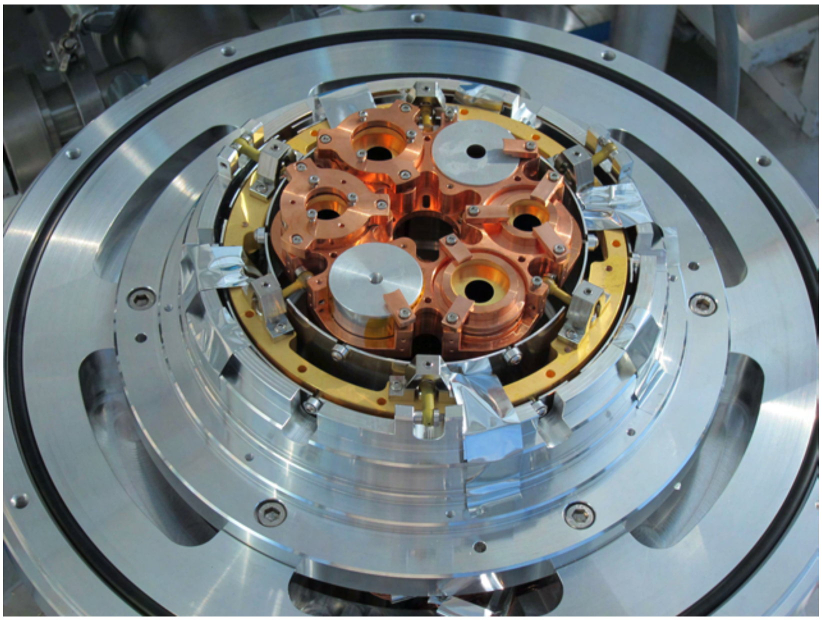

Figure 8.7: *The complete detector stage is mounted in the vacuum chamber. Two TSI cavities are fixed by clamps, the other two TSI cavities are retained in position by a ring. The ring fixation should guarantee a symmetric heat flux from the cavity to the heat sink. The radiant power cavities have not yet been produced. Compensating aluminum targets having the same thermal mass as the cavities, can be used to accurately point the radiometer.*

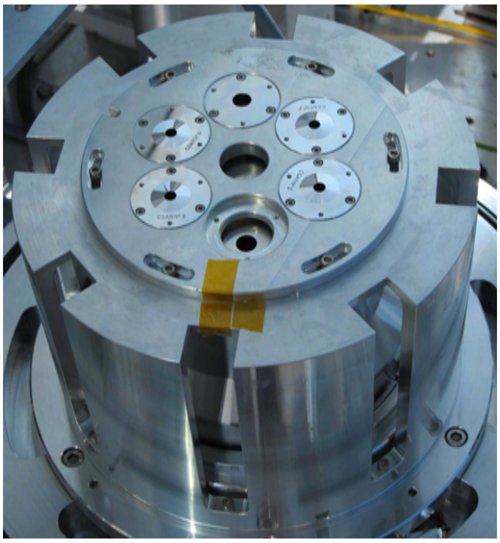

Figure 8.8: *A static aperture support holds the CSAR apertures in place.*

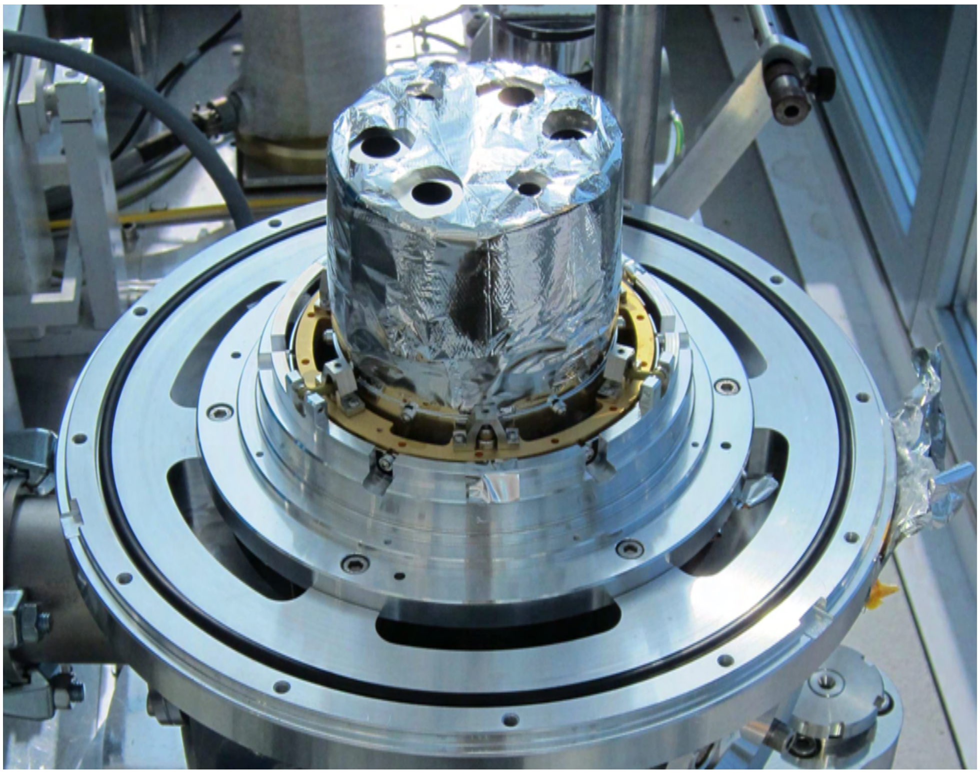

Figure 8.9: *Multi-Layer-Insulation covering the 20 K heat shield reduces the radiative energy exchange with intermediate heat shield.*

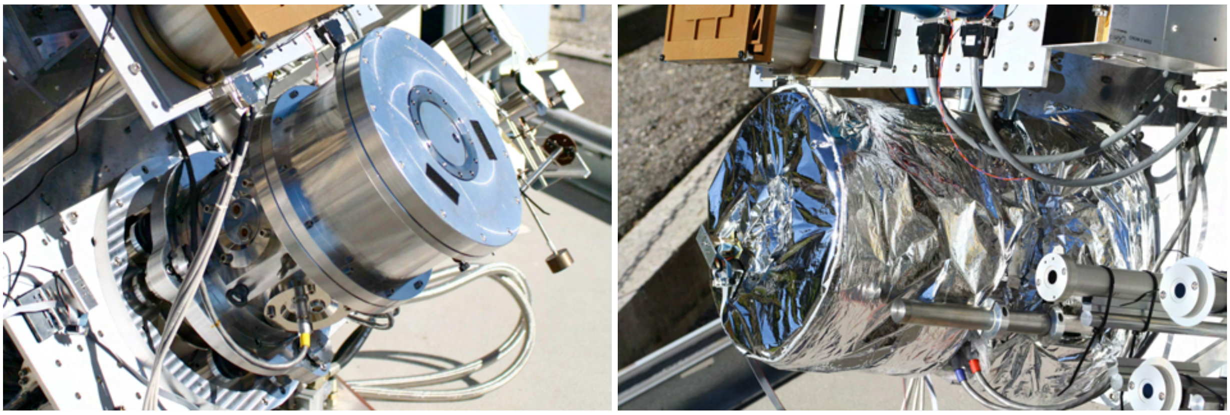

Figure 8.10: *Left, the CSAR on the sun tracking platform. Right, Multi-Layer-Insulation covering the vacuum chamber reduces the radiative energy exchange with the environment.*

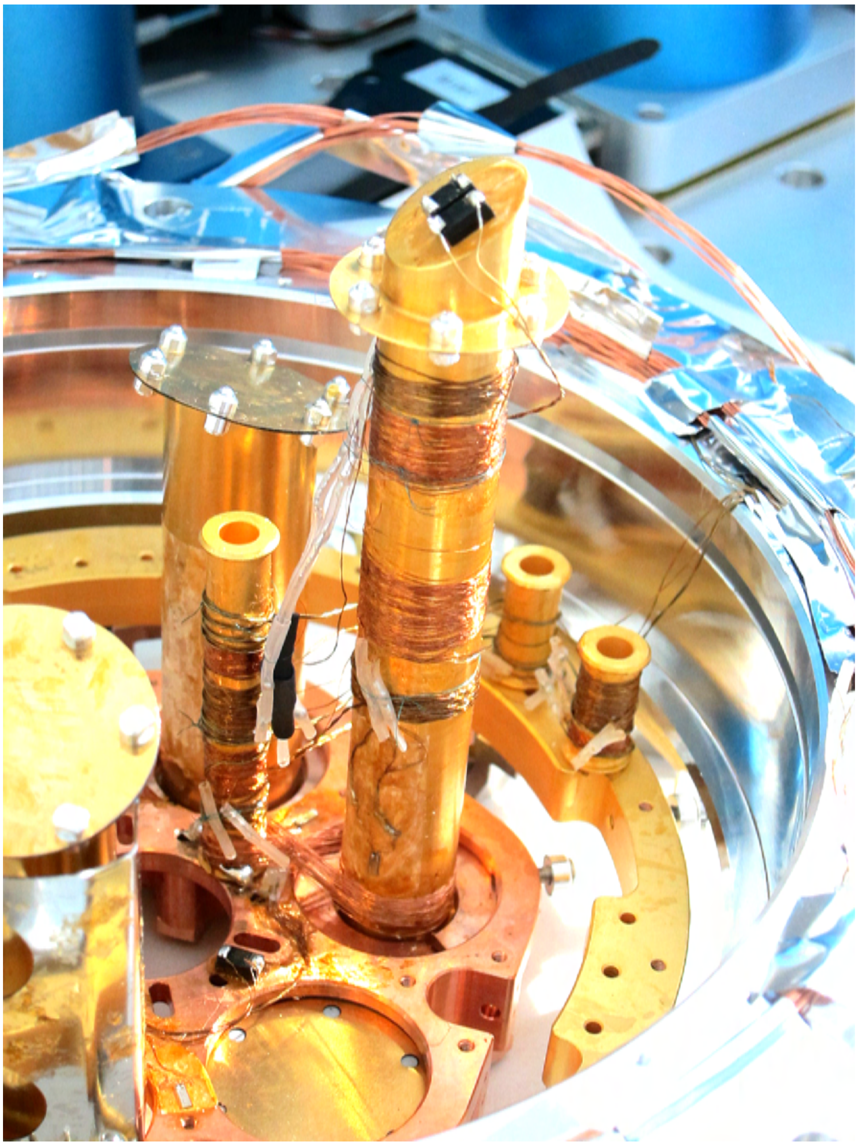

Figure 8.11: *This figure shows the backside of the CSAR detector stage with the extended cavity. The heat exchange between cavity and 20 K reference block is improved by a better heat sinking of the wires. Vishay foil resistors on the back plates of the cavities and on the reference block are used to electrically dissipate energy. The brittle superconducting Magnesium-Diboride current feeding wires are protected by shrinking tubes.*

8.3 Preliminary Results

The first results were obtained in passive mode, i.e. without thermal stabilization of the measuring CSAR cavity. To determined the total solar irradiance, we detected the cavity temperature rise above the stabilized reference block temperature induced by the optical heating and used closed measurements to electrically calibrate the temperature rise.

On the 27th January, 2nd and 7th February 2011 the CSAR measured the TSI though the Suprasil Ax window and on the 7th and 8th March 2011 the sapphire 1 window was installed. To correct the window transmission losses, we used the modified PMO6-0801 integral transmittance measurements presented in section 6.5. The preliminary data evaluation (Figure 8.13) shows a 0.3 % offset between the CSAR and the WRR with the CSAR measuring lower.

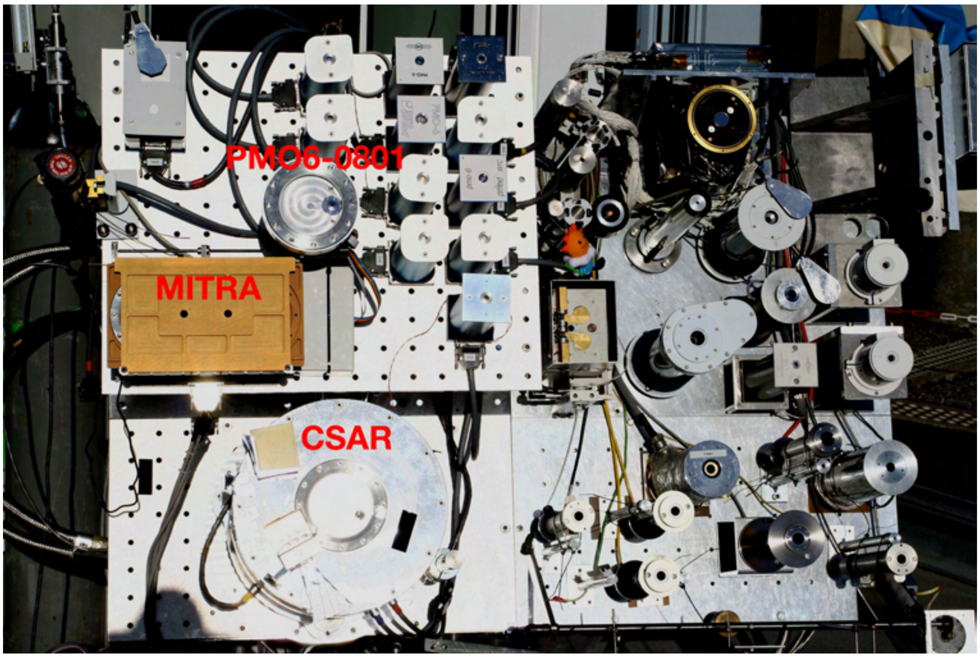

Figure 8.12: *This picture shows the sun tracking platform in Davos. The CSAR is mounted in the left lower corner, the MITRA and the modified PMO6-0801 are placed above the CSAR. On the right half of the platform the WSG is measuring the reference irradiance and the golden ring in the upper right corner is the TIM witness instrument participating in the IPC-XI.*

8.4 Discussion

The collaboration of the PMOD/WRC, the NPL and the METAS allowed to build a cryogenic radiometer for solar measurements. We were able to finish the assembling of the CSAR in time for the IPC-XI. However, the measurements suffered from a parasitic heat flow effect from the reference block to the cavities and hence the comparison to the World Radiometric Reference (WRR) is not reliable during that period.

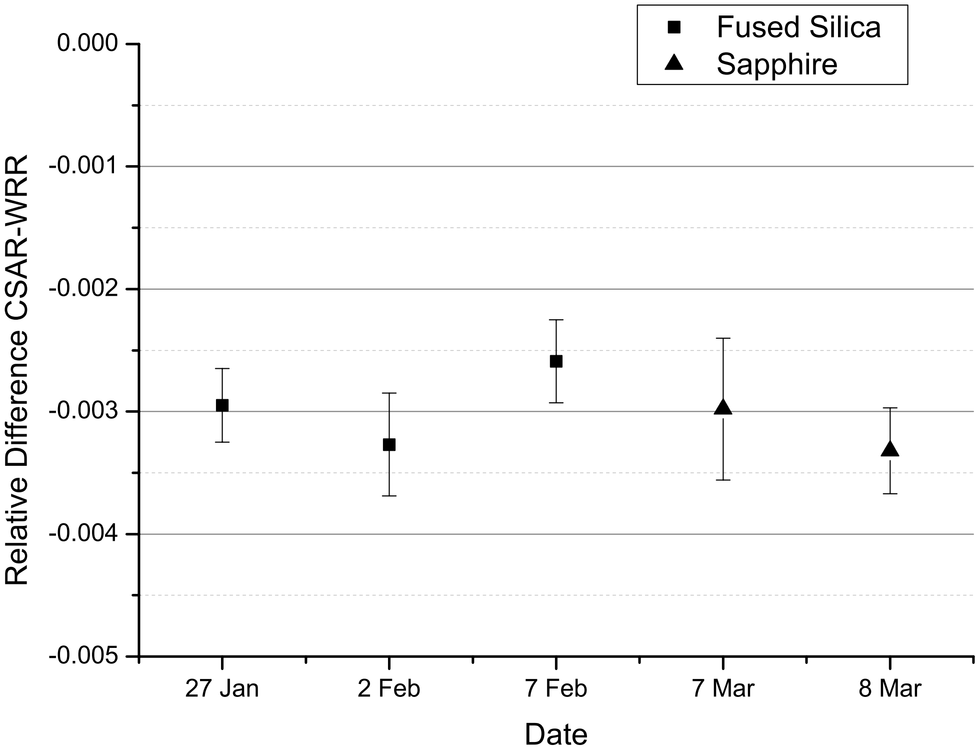

Figure 8.13: *The daily mean CSAR results using the integral window transmittance measurements of the modified PMO6 (section 6.5), are 0.3 % lower than the WRR represented by the PMO2 radiometer. The error bars indicate the expanded standard uncertainty (k=2). This figure courtesy of Winkler (2011a)*

After the IPC-XI, the CSAR was brought back to the NPL where the heat sinking of the wires leading to the cavities could be improved and hence the measurement sensitivity to ambient temperature changes is minimized. Comparisons to the SI radiant power scale confirmed the CSAR's ability to accurately detect optical power (Winkler, 2011a).

At the beginning of the year 2011, we moved the CSAR back to the sun tracking platform in Davos to perform comparisons to the WRR. We used suprasil and sapphire entrance windows to investigate the influence of the window material. To correct the window transmission losses, we used the modified PMO6-0801 integral transmittance measurements presented in section 6.5. The preliminary results show a constant offset by which the CSAR measures lower than the WRR. As the CSAR measurements agree with the SI radiant power scale, the offset found in Davos confirms the outcome of our WRR to SI comparison performed with the PREMOS radiometers (section 5.2). Hence, we have independent evidence that the SI radiant power scale is 0.3 % lower than the WRR.

To establish the CSAR, extended long term comparisons to the WRR are needed. Currently, we develop a dedicated electronics to transfer the CSAR operation from an experimental to a more user friendly set up. We are prepare tests of alternative window materials (CaF_2, KCl) having better transmittance properties and the CSAR/monitor window equivalence is enhanced by more precise spectral transmittance measurements of an increased number of windows.

The MITRA has proven its ability to determine the integral transmittance in the laboratory with high accuracy and we are working on the problems arising during solar measurements. Hence, the total uncertainty of the CSAR measurements is going to be further reduced and we are optimistic to achieve the intended accuracy.

Chapter 9

Circumsolar Radiation

Current absolute solar radiometers have a viewing aperture geometry defined by a large view limiting aperture at the entrance to the instrument, followed by a smaller precision aperture in front of the cavity (Figure 9.1). The field-of-view is define by two angles: 1) The slope angle Θ_{slope} defines the circular portion of the sky from which all the radiation falls directly into a radiometer cavity. 2) The limit angle Θ_{limit} represents the maximal angle from where light still can partly illuminate the radiometer cavity. Already Ångström and Rodhe (1965) realized the importance of the aperture geometry to the total solar irradiance measurements. They determined the contribution of the circumsolar radiation to the total solar irradiance measurements as a function of the opening angle of the instrument and the atmospheric turbidity. Their findings showed a difference of several percent between the radiometer measurements not sampling the identical portion of the sky around the sun. Hence, the Commission for Instruments and Methods of Observations (CIMO, 2008) recommends to use a half opening angle $\Theta_{fov} = 2.5°$ and a slope angle of $\Theta_{slope} = 1°$ for all new primary radiometers used to measure the direct total solar irradiance. Equation 9.1 presents the relation between the three angles defining the geometry of a radiometer.

$$\tan\Theta_{limit} = 2\tan\Theta_{fov} - \tan\Theta_{slope} \tag{9.1}$$

This relation is independent of the aperture radii and the aperture distance. However, if we choose either one of the aperture radii or the distance, the remaining radiometer geometry is defined.

The PREMOS stray light measurements (section 5.4) showed that it is better to invert the aperture geometry (Figure 9.1). Using this set up, we have to carefully interpret the CIMO opening angle recommendation. From a radiometric point of view, it is the slope and the limiting angle being of importance because they define the circumsolar radiation seen by the radiometer. To retain the recommended angles in the new geometry, we should define Θ_{fov} more precisely as half the opening angle under which the larger aperture is seen from the center of the smaller aperture.

In Table 9.1 we present the aperture geometries of absolute radiometers currently used to measure the TSI. Instruments like the DARA, the TIM, the SIAR and the modified PMO6 radiometer (section 6.5) have considerably larger limiting angles. Hence, they measure more of the

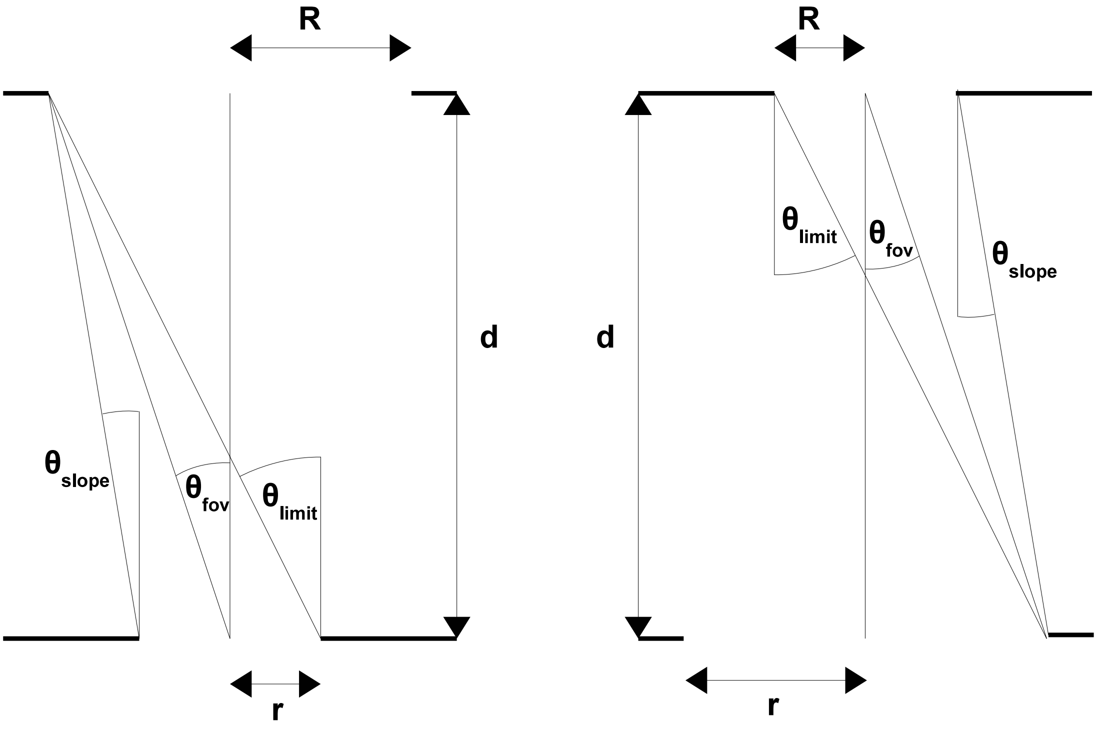

Figure 9.1: *Left, the classical aperture geometry used for absolute radiometers. Choosing two angles and one length completely defines the geometry. Right, the more precise definitions of the limiting and the slope angle for the inverted aperture geometry.*

circumsolar radiation resulting in an offset compared to the instruments that have the CIMO recommended geometry. As the scattered light in the atmosphere does change according to the amount and the properties of the aerosols, the difference between the radiometers changes as well.

The MITRA and the CSAR instrument also have slightly different aperture geometries and thus we have to characterize the difference caused by the circumsolar radiation. The difference between the CSAR and the PMO2 radiometer has to be known when we compare the CSAR to the WRR. We use the parameterized Simple Model of the Atmospheric Radiative Transfer of Sunshine (SMARTS; Gueymard, 2001, 2004) to simulate the direct and the circumsolar radiation measured by a radiometer with a certain aperture geometry. SMARTS uses a parameterization of the temperature profile, the water content, the gas concentration (O_3, CO_2, ...) and the aerosols to calculate the appropriate atmospheric extinction from the measurements of the input variables. Further, the model calculates the penumbra function (Figure 9.2) from the radiometer geometry. This function determines the fraction of the radiation originating from a certain direction that illuminates the detector. The integration over the penumbra weighted circumsolar radiance yields the circumsolar irradiance. The circumsolar radiation is dominated by the sun light scattered by the aerosols. Our theoretical calculation uses the implemented standard rural aerosol model determining the aerosol scattering and absorption from a measured Aerosol Optical Depth (AOD).

	front aperture [mm]	back aperture [mm]	aperture distance [mm]	slope angel [°]	half opening angle [°]	limit angle [°]
PMO2	3.60	2.50	75.00	0.84	2.75	4.65
PMO5	3.70	2.50	95.40	0.72	2.22	3.72
PMO6	4.20	2.50	98.50	0.99	2.44	3.89
PMO6-80022	4.10	2.50	94.00	0.98	2.50	4.02
modified PMO6	2.50	3.50	57.30	1.00	3.50	5.98
DARA	2.50	3.45	54.10	1.01	3.65	6.28
MITRA	2.50	3.87	79.94	1.08	2.86	4.65
CSAR	2.50	5.00	103.98	1.38	2.75	4.13
HF	5.81	3.99	134.70	0.77	2.47	4.16
CROM2L	6.29	5.00	144.05	0.51	2.50	4.48
TIM	3.99	7.62	101.60	2.05	4.29	6.52
SIAR	5.70	4.00	100.00	0.97	3.26	5.54
EPAC	8.32	5.64	190.50	0.81	2.50	4.19
MK	8.20	5.65	187.60	0.78	2.50	4.22
PAC3	8.18	5.64	190.50	0.76	2.46	4.15

Table 9.1: *Aperture geometry overview of absolute radiometers currently used to measure the total solar irradiance. Only the PMO6-type radiometers fulfill the CIMO geometry recommendation. Due to the differing limiting angles, some instruments collect more or less circumsolar radiation.*

The spectrum of the circumsolar radiation changes depending on the season, aerosol optical depth and solar zenith angle. The amount of circumsolar radiation above 2 µm contributes less than 0.8 % to the total circumsolar respectively less than 15 ppm to the total solar irradiance. Since our windows do not suffer from absorption losses below 2 µm, we can safely assume that the relevant fraction of the circumsolar radiation passes through the entrance windows. And The integral transmittance of the circumsolar radiation through the windows changes less than 0.15 % when the solar zenith angle increases from 0 to 80 degrees. Hence, the measured total solar irradiance behind a window will change by 5 ppm due to the increased circumsolar radiation.

MITRA sees 50 ppm more of the direct and circumsolar radiation compared to the CSAR (Figure 9.4). As the MITRA instrument monitors the integral transmittance and does not measure the total solar irradiance, this difference is only relevant for stray light considerations. The difference between CSAR and another reference instrument is more crucial. We chose the PMO6-79122 radiometer as reference because it best implements the CIMO aperture geometry recommendation. The calculations show that CSAR yields a total solar irradiance value which is between 0.015 and 0.05 % higher than the reference value (Figure 9.5).

We should as well consider the vertical displacement z in the beam geometry introduced by the window (Figure 9.3), to determine the circumsolar radiation correction. The limiting angle Θ_{limit} becomes apparently smaller by $(1 - \frac{x-z}{x})$. Similar calculations can be repeated for the slope and the half opening angle which become slightly wider. However, the differences are so small that we neglect them in our estimations.

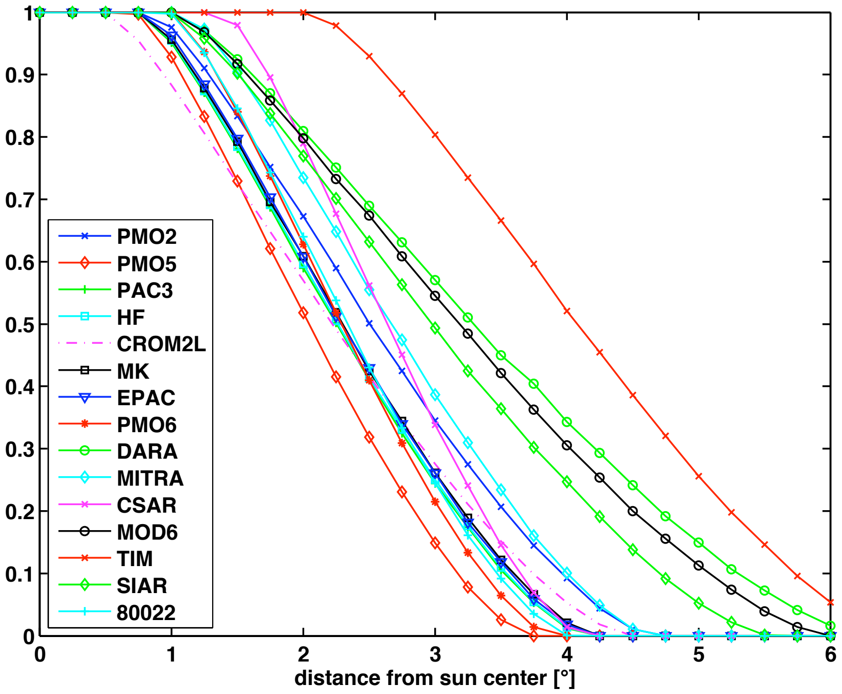

Figure 9.2: *The penumbra function determines the fraction of the radiation originating from a certain direction that illuminates the detector. This graph courtesy of M. Suter, PMOD/WRC.*

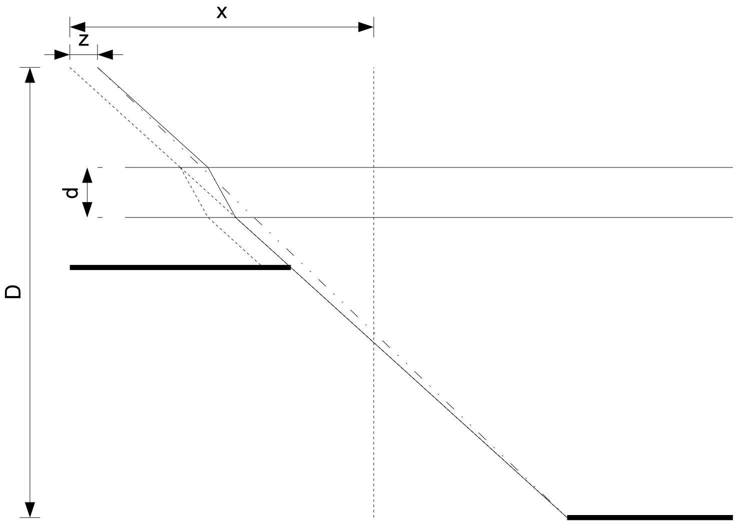

Figure 9.3: *The vertical displacement introduced by the entrance window results in a slightly narrower limiting angle (dashed-dotted line). However, using the large distance* x *covered by the radiometer and the small displacement* $z = 0.25\ mm$ *(refractive index* $n = 1.46$*), the difference becomes negligible.*

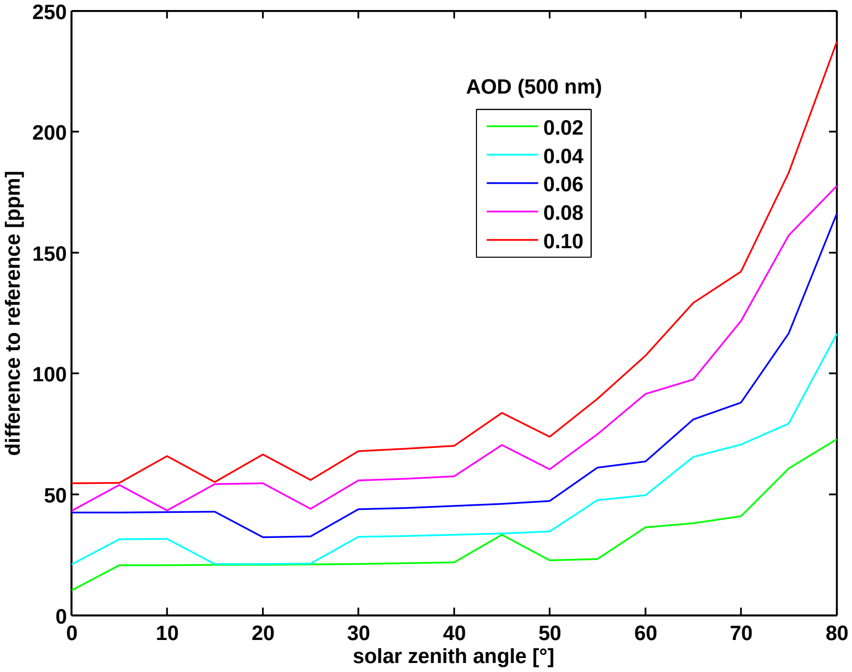

Figure 9.4: *The modeled difference between the CSAR and the MITRA measurements caused by the circumsolar radiation, lies below 50 ppm for the relevant solar zenith angles and the aerosol optical depths of 0.02 we expect in Davos for clear sky conditions.*

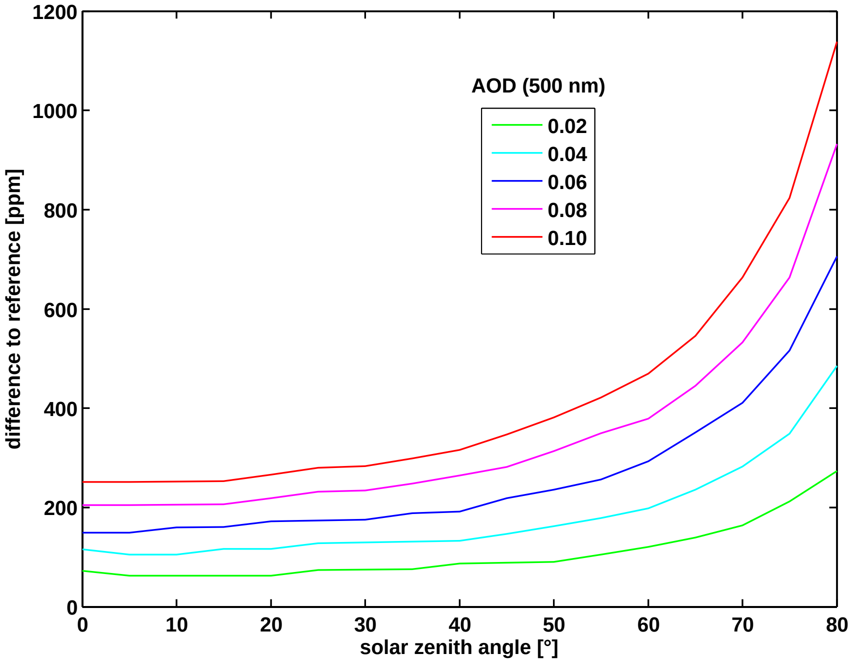

Figure 9.5: *The modeled difference between the CSAR and the PMO6-79122 measurements caused by the circumsolar radiation lies below 200 ppm for the relevant solar zenith angles and the aerosol optical depths of 0.02 we expect in Davos for clear sky conditions.*

9.1 Saharan Dust Event (SDE) during the IPC-XI

Differences in the measured circumsolar radiation was an issue in solar radiometry as a Saharan Dust Event (SDE) during the International Pyrheliometer Comparison XI (IPC) revealed. In Figure 9.7 we compare a number of radiometers to the PMO6-79122 instrument. From the 7^{th} to the 8^{th} of October 2010, the ratio changed by 0.1 to 0.3 %. Especially instruments like the TIM witness, the modified PM6-0801 or the SIAR which have a wider aperture geometry, show a prominent effect.

Investigating the AOD measurements during the IPC-XI, we found a changing aerosol extinction due to the SDE. Figure 9.8 presents the change of the aerosol and the atmosphere properties during IPC-XI used as input for a SMARTS simulation of the circumsolar irradiance. We used the modeled circumsolar irradiance to determine a correction factor yielding the direct solar irradiance without the contribution from the sky. For each instrument type we normalized the factor to the correction obtained for the PMO6-79122. Applying the correction to the instruments under investigation showed the intended effect of leveling out the measured ratios. However, the correction seemed too small by a factor of 3.5. The investigation of the SMARTS code revealed that manually entered aerosol properties cause the code to use a parameterization of the continental aerosol model of the IAMAP atmosphere (IAMAP, 1986). This aerosol model is not representative for the scattering processes in the atmosphere during a SDE in Davos. Gueymard (1998) showed that using a maritime aerosol model with larger particles instead of the continental model yields 2.5 times larger correction factors for the circumsolar radiation.

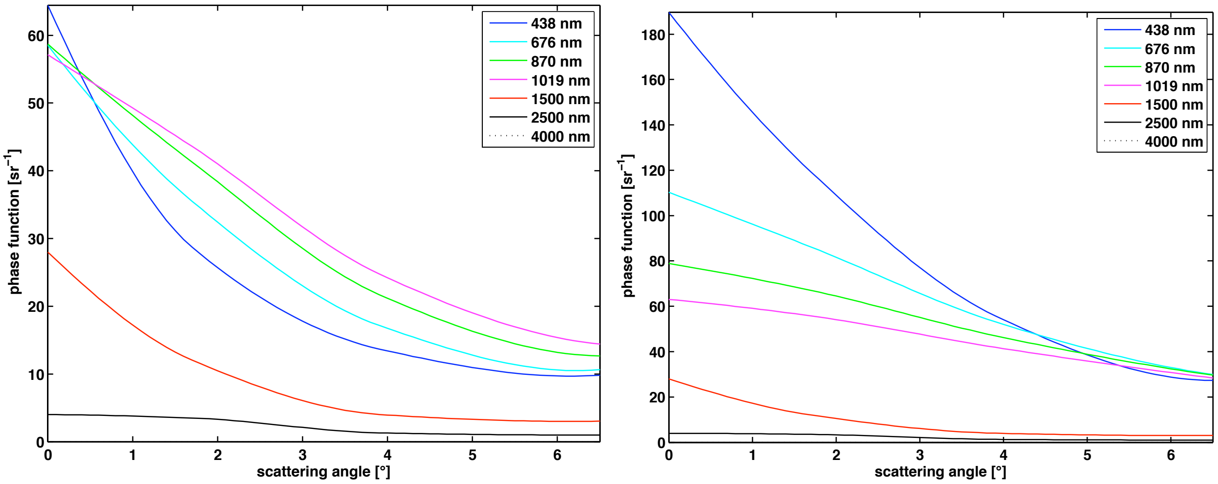

Figure 9.6: *The aerosol scattering phase function determined by the AERONET station located at the PMOD/WRC. Left, the result for the* 7^{th} *of October. Right, on the* 8^{th} *of October, the scattering phase function increased by a factor of three over night because of the Saharan dust arriving at our site.*

We identified the scattering phase function as the aerosol property causing the difference between the rural and the maritime model. Investigating the scattering phase function during the IPC provided as an inversion product by the AErosol RObotic NETwork (AERONET; Wehrli 2010), we can see that the desert particles scatter three times as much in the forward direction compared to normal aerosols (Figure 9.6). Hence ,we modified the SMARTS code to accept the measured scattering phase function. Applying the redetermined correction, we correct all instrument to the circumsolar radiation seen by a radiometer having the CIMO recommended aperture geometry (Figure 9.7). The correction factors displayed in Figure 9.9 show that on a clear day with no Saharan dust, the influence of the correction is small. For the World Standard Group, the corrections are below 50 ppm before and after the SDE and only the PMO2 and the PMO5 radiometers are affected in opposite sense by dust in the atmosphere (Figure 9.10). Hence the World Standard Group (WSG) yields a stable reference even in the rare case of a SDE. The instruments collecting more of the circumsolar radiation have larger corrections. Especially the TIM witness instrument has to be corrected by up to 500 ppm on a dust free day and by up to 4500 ppm with the Saharan dust in the atmosphere. The CSAR and MITRA instruments need a correction that lies below 100 ppm under normal circumstances. In chapter 8 we compared the CSAR measurements to those of the PMO2. The correction factors presented in Figure 9.9 show that the CSAR-PMO2 difference due to circumsolar radiation on a clear day is 50 ppm with the CSAR measuring higher.

9.2 Discussion

Our considerations have shown that radiation originating from the circumsolar portion of the sky cannot be neglected when measuring TSI at ground-level with differing radiometer viewing geometries. Even under clear sky conditions some instruments like the TIM radiometer have to be corrected by up to 500 ppm due to the extra circumsolar radiation. However, this instrument has been designed as a space experiment where circumsolar radiation is not an issue. For future ground based radiometers we strongly advise to follow the CIMO viewing geometry recommendations in order to guarantee the best possible comparability of instruments under all conditions.

The 11^{th} International Pyrheliometer Comparison (IPC) in September/October 2010 experienced a Saharan Dust Event (SDE). As a result the scattering phase function of the aerosols drastically changed and the influence of the circumsolar radiation increased yielding strong dependencies in the calibration factors of some radiometers. We were able to modify the SMARTS code to accept measured scattering phase functions as input. This model allowed us to determine a correction factor accounting for the changing circumsolar radiation which will be used in Finsterle (2011) to level out the calibration factors of the radiometers.

The circumsolar radiation contribution to the measurements of the radiometers forming the WSG is not strongly altered by the SDE. Only the PMO2 and the PMO5 radiometers are affected but in opposite directions. Hence, the WRR is a stable reference even in the case of a SDE.

The CSAR measurements need a circumsolar correction of 50 ppm if we compare them to the WRR represented by the PMO2 respectively a circumsolar correction of about 100 ppm if we compare them results obtained with a radiometer having the CIMO recommended viewing geometry. The MITRA uses a relative measurement principle and hence is not affected by the circumsolar radiation.

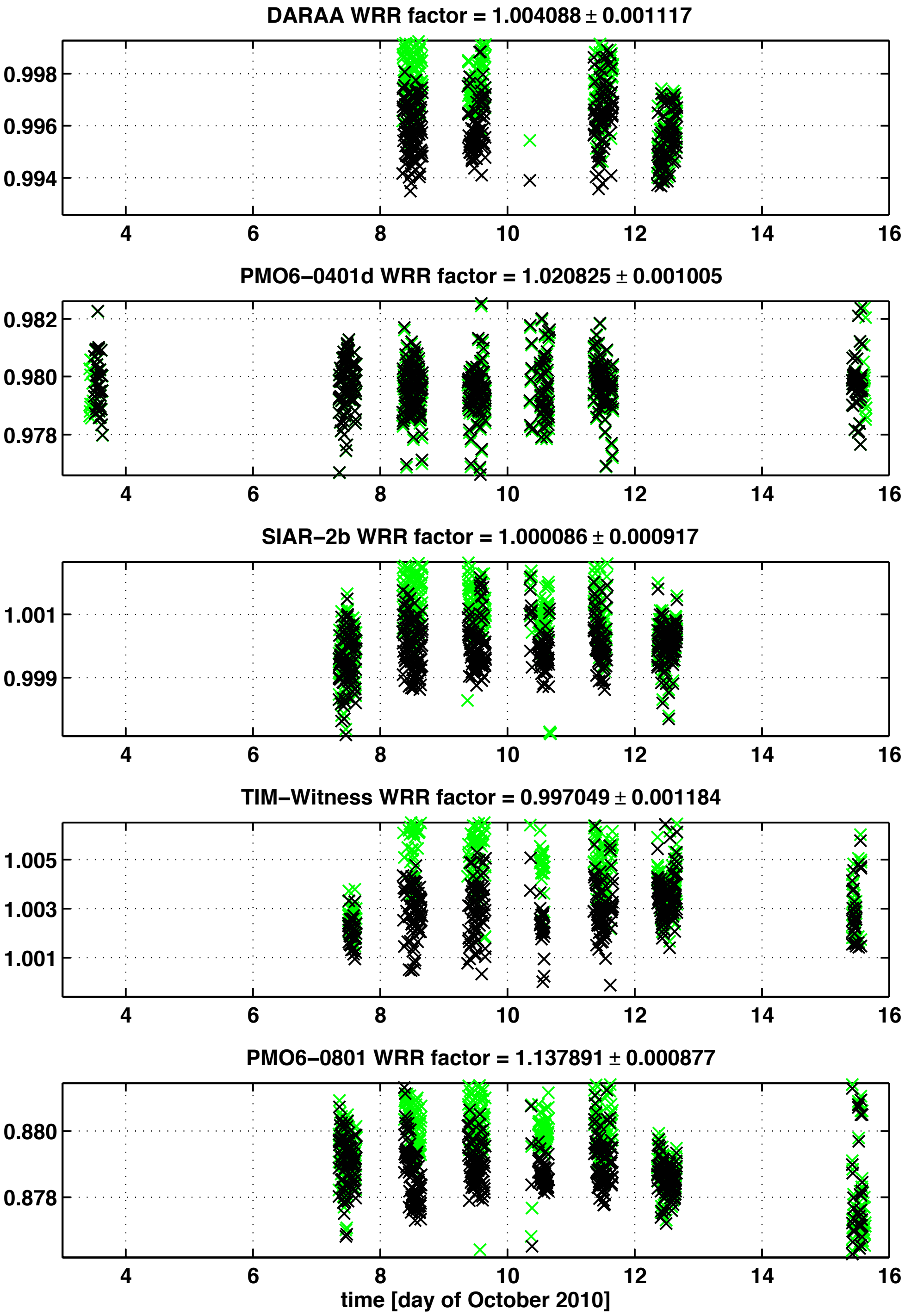

Figure 9.7: *Ratios to PMO6-79122 for selected radiometers during the SDE in October 2010. The green time series shows that some instrument ratios to the PMO6-79122 changed by 0.1 to 0.3 % from the 7th to the 8th of October 2010. Applying the circumsolar correction determined with SMARTS levels out the influence of the SDE over the entire observation period and disperses the daily variations in the morning and the evening (black).*

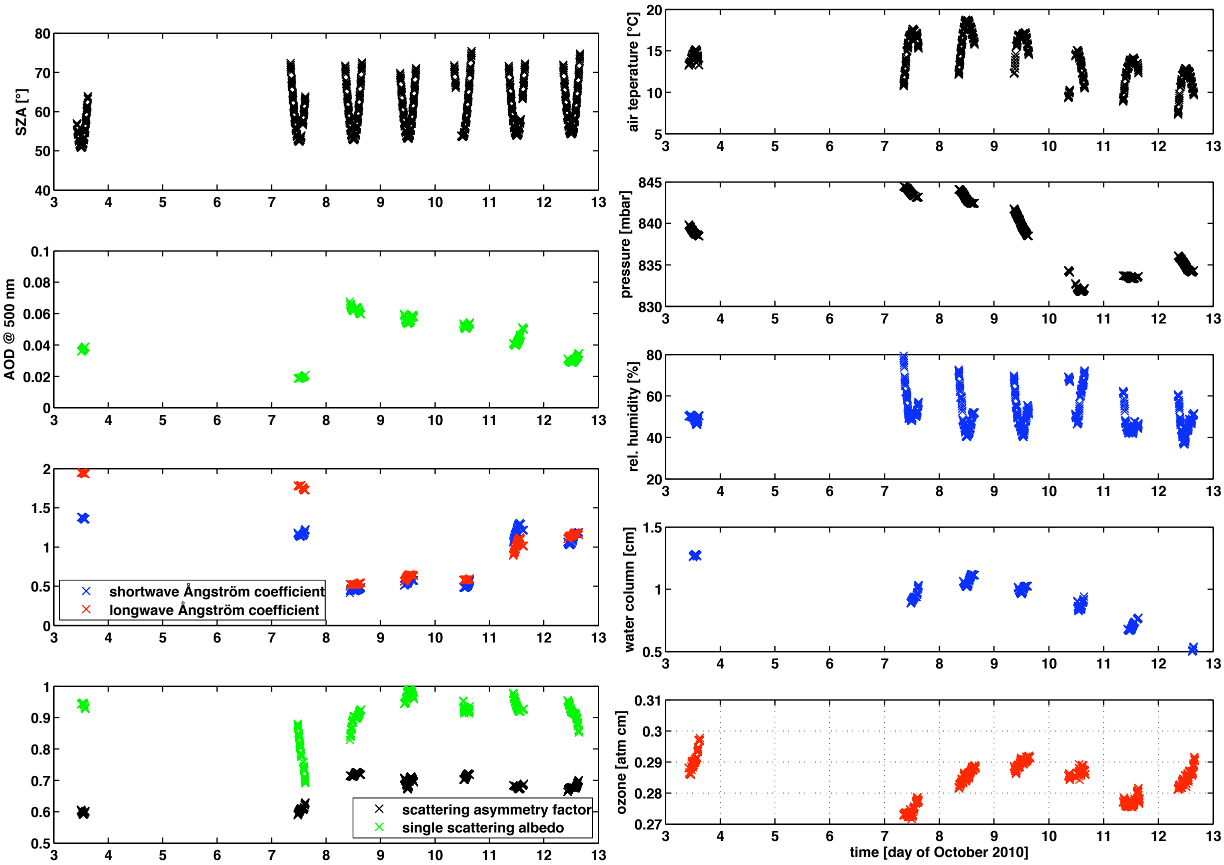

Figure 9.8: *The aerosol properties and the atmospheric conditions during IPC-XI were measured: AOD by PMOD/WRC precision filter radiometers; scattering asymmetry factor, single scattering albedo and water column by the AERONET (Wehrli, 2010) station located at the PMOD/WRCT; ozone by the PMOD/WRC Brewer #163; temperature, pressure and relative humidity by the METEO Swiss station located at the PMOD/WRC. The Ångström coefficients have been calculated from the AOD measurements. The Solar Zenith Angle (SZA) has been calculated using the solar position algorithm of Reda and Afshin (2003).*

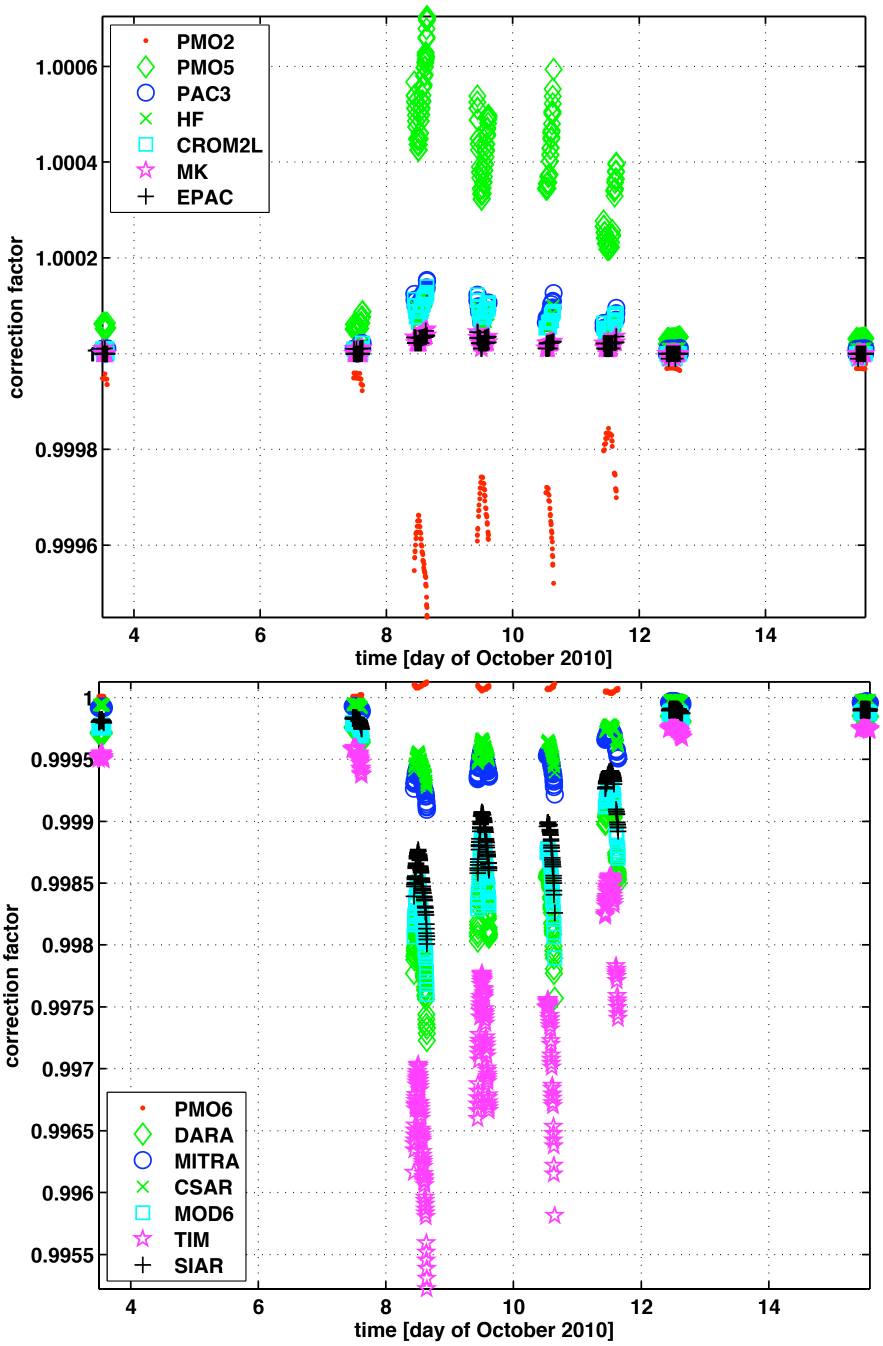

Figure 9.9: *Calculated correction factors for the SDE starting on the 8th of October and lasting for four days. Only the PMO2 and the PMO5 radiometer from the World Standard Group are strongly affected (upper panel). Other selected instruments (lower panel) like the TIM witness measure considerably more during a dust event and have to be corrected accordingly.*

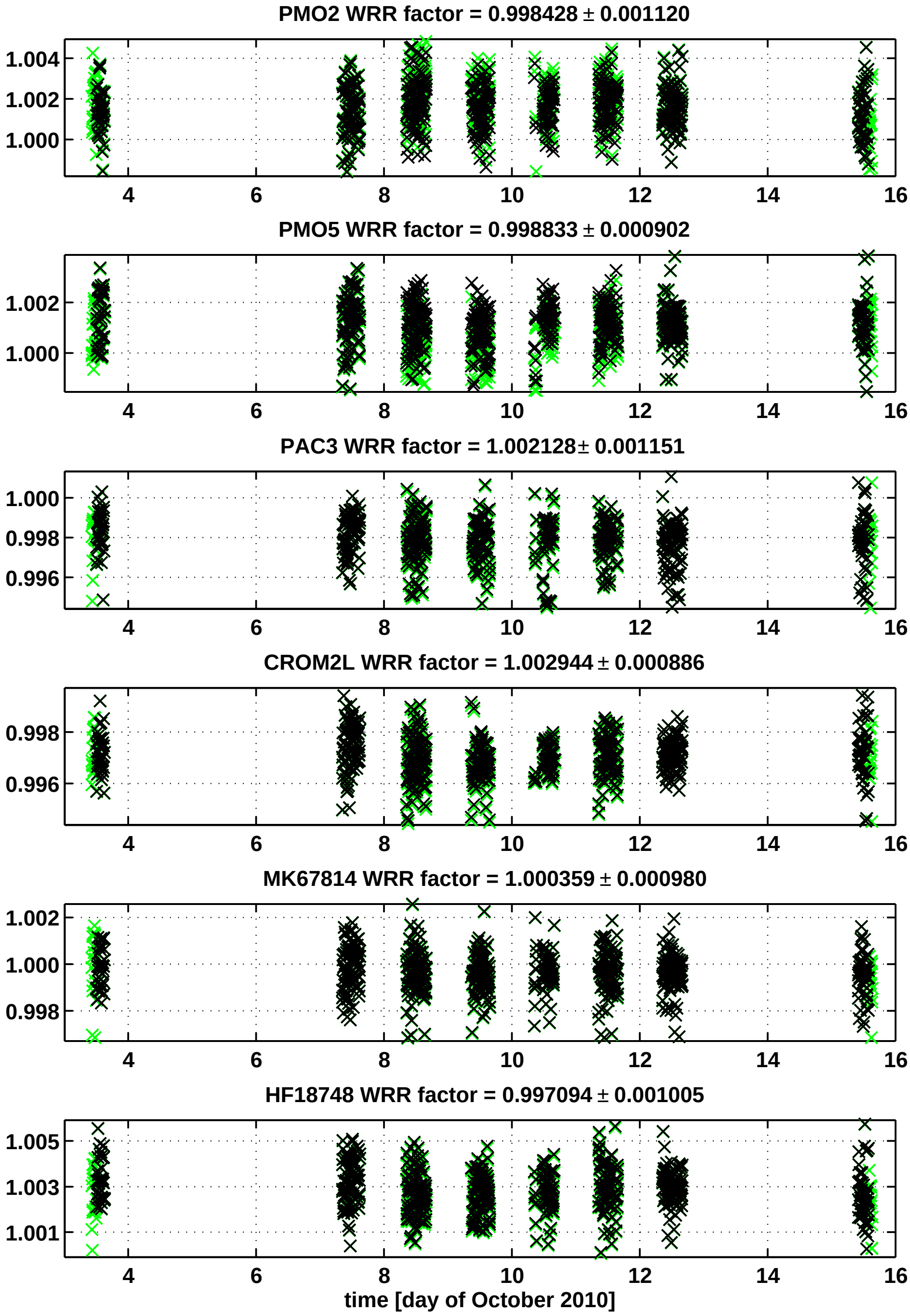

Figure 9.10: *Ratios to PMO6-79122 for selected radiometers during the SDE in October 2010. The green time series shows the uncorrected ratios of the WSG instruments to the PMO6-79122 radiometer. Applying the circumsolar correction determined with SMARTS does not noticeably affect the WRR calibration of the WSG instruments (black).*

Chapter 10

Conclusions and Perspectives

Our work focused on the problems and uncertainties involved in measuring the Total Solar Irradiance (TSI) on the ground and in space. We improved the calibration, characterization and traceability of existing absolute solar radiometers and developed a novel cryogenic radiometer for solar measurements.

The PREMOS/PICARD space mission allowed to investigate the characterization of PMO6-type radiometers. Our experiments and the SOVIM measurements revealed offsets in the irradiance measurements when the heat sink temperature of the instrument is drifting. We developed a model describing the temperature dependence and corrected the orbital variation of 1 W/m^2 in the SOVIM data. The model can also be used to correct the measurements of upcoming space experiments, the commercial PMO6-type radiometers and the VIRGO/SOHO results where the instrument shutter stays open for eight hours.

We encountered problems in determining the air-to-vacuum correction of the PREMOS radiometers and identified them as due to inter-reflections between the radiometric aperture and the entrance window to the vacuum tank, causing stray light. Inclining the entrance window by 2 degrees, we could resolve the inter reflection problem and improve the confidence in this PMO6-type radiometer correction.

A finite element model of PMO6-type detectors allowed to disentangle the individual thermal processes affecting the measurements. We were able to show that the heating of the precision apertures does not account for the entire early sensitivity increase of our radiometers on orbit. A burning in of the applied Aeroglaze Z302 cavity paint or a bleaching of the baffle coating which causes more stray light could explain the observed effect. Further testing of the paint properties and exposure experiments are needed to confirm this hypotheses.

The PREMOS radiometers were calibrated against the WRR like the PMO6-type radiometers (VIRGO/SOHO, SOVIM/ISS) in space. To obtain a second traceability chain, we calibrated the PREMOS instruments in vacuum against the SI radiant power scale realized by the NPL. Using the calibrations, we were able to perform the fourth WRR to SI radiant power scale calibration. Our results show a 1.001783 ± 0.001064 % (k=1) offset between the two scales with the WRR being higher. This scale difference accounts for half of the observed offset between PMO-6 type radiometer measurements and the TIM/SORCE (Kopp et al., 2005) in space.

The new TSI Radiometer Facility (TRF) at LASP in Boulder CO offered the opportunity to calibrate the PREMOS-3 flight instrument against a NIST SI radiant power scale in power and irradiance mode. Experiments using varying TRF beam diameters indicate that the standard characterization (Brusa and Fröhlich, 1986) underestimated the internal stray light produced in a PMO6-type radiometer. The radiation reflected by the precision aperture illuminates the baffle system creating stray light. Our experiments yield an additional stray light correction of 0.14 % for PREMOS-3. Using this correction, we performed a WRR to SI irradiance comparison and found an offset of 1.003148 ± 0.001112 % (k=1) between the two scales with the WRR being higher. The difference between the WRR to SI radiant power scale comparison respectively the WRR to SI irradiance comparison is explained by the additional stray light present only if the source over fills the precision aperture.

Applying the WRR respectively TRF calibration to the PREMOS on orbit values shows that the observed offset between PMO-6 type radiometer measurements and the TIM results can be explained by the two different scales. Taking into account these novel findings, we should reconsider the results of the previous space experiments measuring the TSI and the deduced TSI composite. However, we need the other instrument teams to confirm our results with radiometers of a different type, before we can discuss the absolute value of the TSI at the top of the atmosphere.

In collaboration with the NPL and the METAS the Cryogenic Solar Absolute Radiometer (CSAR) has been designed, built and tested within three and a half years. The transmittance of the solar radiation through the CSAR entrance window poses one of the major challenges of the project. Our MODTRAN simulations of the solar spectrum at ground-level and the spectral window transmittance measurements allowed to estimate the integral transmittance correction needed to obtain an absolute CSAR TSI value. However, the theoretical calculations cannot account for the day to day changes of the atmosphere and the according variations in the integral transmittance through the CSAR entrance window. Therefore we developed two types of integral transmittance monitors.

The modified PMO6-0801 radiometer shows a 0.1 % intrinsic scattering of the measured integral transmittance. Using daily mean values, we loose the information about the small integral transmittance variations caused by the solar elevation changes but we reduce the standard uncertainty of the measurement to 0.01 %. The total integral transmittance standard uncertainty (k=1) budget is dominated by the non-equivalence of the CSAR and the monitor window as well as the transmittance measurements. However, long term comparisons of the two windows will reduce this uncertainty contribution.

The novel dual-detector Monitor to measure the Integral Transmittance (MITRA) of windows uses relative measurements to avoid uncertainties caused by absolute measurements. Tests in the laboratory demonstrated MITRA's ability to determine relative irradiance variations at the 0.01 % accuracy level within 10 minutes. However, the MITRA measurements in front of the sun revealed a large variance due to wind, stray light and/or other factors if only one detector was covered by the monitor window. We are investigating this effect and are optimistic to resolve it allowing to use the full potential of MITRA.

The preliminary CSAR results using suprasil respectively sapphire windows and the measured modified PMO6-0801 integral transmittance values, show an 0.3 % offset between the

CSAR and the WRR measurements with the WRR being higher. This difference is independent of the window material and confirms the offset between WRR and SI irradiance found with the PREMOS radiometers. To establish the CSAR among the community and to prove its potential to replace current reference, we need extended long term comparisons to the WRR. Currently, we develop a dedicated electronics to simplify the CSAR operation and are preparing the radiant power detectors and we are discussing how to handle the difference between the reference scales.

We successfully accomplished the main objectives of the CSAR project. The explanation for the differing extraterrestrial TSI measurements brings the community one step closer to delivering a definitive absolute value of the solar energy input to the Earth's climate system. The CSAR proved its ability as a potential replacement for the WRR guaranteeing the continuity of a worldwide reference scale for solar irradiance measurements.

Appendix A

Suggestions to Improve the Absolute Characterization of Radiometers

A.1 Heating of the Leads

We suggest not to use a control electronics for the experiment. The heater current should be controlled manually with a precision source. A second source should provide the additional current through the feeding-sensing wire pair on one side of the heater. The reaction of the bridge signal to the additional current through the feeding-sensing wires can be calibrated. Since the thermal variations of the laboratory environment should be small over the short measurement period, the cavity temperature should not change and thus this set up would yield the correct lead heating effect.

A.2 Aperture Heating

To better understand the aperture heating influence on PMO6-type radiometer measurements we should investigate the absorptance properties of our precision apertures. Gordon (1960) has proposed a neat experiment to directly measure the solar absorptance to emissivity ratio of metals. The precision aperture of the SOVA 113R radiometer which has returned from space could deliver valuable information about the surface finish degradation on orbit.

A.3 Cavity and Muffler Reflectance

We think that the early sensitivity increase observed with VIRGO and PREMOS could be due to either a burning-in of the inorganic Aeroglaze Z302 cavity paint or a bleaching of the diffuse muffler coating. The burning in of the cavity coating would increase the absorptance of the cavity. Such a burning-in is observed with other instruments (DIARAD, Crommelynck 1981) increasing the absorptance in the early stage before the paint is bleaching out. The bleaching of the muffler coating would probably increase the stray light detected by the radiometer.

We should repeat and improve the reflectance measurements for our cavities and perform degradation experiments with the Aeroglaze Z302 paint. Further, we should investigate the muffler coating and its outgassing behavior in vacuum and the bleaching properties when exposed to hard UV radiation.

Acronyms

ACRIM	Active Cavity Radiometer Irradiance Monitor, 5
AERONET	AErosol RObotic NETwork, 154
ANSYS	ANalysis SYStem, 15
AOD	Aerosol Optical Depth, 150
BIPM	Bureau International des Poids et Mesures, 4
CIMO	Commission for Instruments and Methods of Observations, 149
CIPM	International Committee for Weights and Measures, 4
CSAR	Cryogenic Solar Absolute Radiometer, 7
CVD	Chemical Vapor Deposition, 82
DARA	Davos Absolute RAdiometer, 132
DIARAD	Dual Irradiance Absolute RADiometer, 165
DLC	Diamond Like Carbon, 84
EO	Earth Observation, 7
EURECA	EURopean REtrievable CArrier, 13
GUM	Guide to the Expression of Uncertainty in Measurement, 38
IPC	International Pyrheliometer Comparison, 3
IPPC	Intergovernmental Panel on Climate Change, 1
IPS	International Pyrheliometric Scale, 3
IRC	International Radiation Commission, 3
ISS	International Space Station, 14
LabVIEW	Laboratory Virtual Instrumentation Engineering Workbench, 58
LASP	Laboratory for Atmospheric and Space Physics, 9

METAS	Bundesamt für Metrologie - Federal Office of Metrology, 4
MITRA	Monitor to measure the Integral TRAnsmittance of windows, 7
MLI	Multi-Layer-Insulation, 142
MODTRAN	MODerate resolution atmospheric TRANsmission, 76
MRA	Mutual Recognition Arrangement, 4
NIST	National Institute of Standards and Technology, 41
NMI	National Metrology Institute, 4
NPL	National Physical Laboratory, 4
PMOD	Physikalisch Meteorologisches Observatorium Davos, 3
PREMOS	PREcision MOnitoring Sensor, 9
SARR	Space Absolute Radiometric Reference, 5
SDE	Saharan Dust Event, 154
SI	International System of Units, 4
SMARTS	Simple Model of the Atmospheric Radiative Transfer of Sunshine, 150
SMD	Surface Mounted Device, 127
SODISM	SOlar Diameter Imager and Surface Mapper, 72
SOHO	SOlar and Heliospheric Observatory, 18
SORCE	SOlar Radiation and Climate Experiment, 161
SOVA	SOlar VAriability, 13
SOVIM	SOlar Variable and Irradiance Monitor, 14
SSI	Spectral Solar Irradiance, 5
SuMo	Sun Monitor, 132
SZA	Solar Zenith Angle, 157
TIM	Total Irradiance Monitor, 5
TOA	Top Of Atmosphere, 1
TRF	Total solar irradiance Radiometer Facility, 5
TRUTHS	Traceable Radiometry Underpinning Terrestrial- and Helio- Studies, 7
TSI	Total Solar Irradiance, 1

VIRGO	Variability of Solar Irradiance and Gravity Oscillations, 41
WMO	World Meteorological Organization, 1
WRC	World Radiation Center, 4
WRR	World Radiometric Reference, 3
WSG	World Standard Group, 4

Bibliography

Abbot, C. G., Aldrich, L. B., and Hoover, W. H. (1942). Chapter 6. Discussion of Solar-Constant Values. *Annals of the Astrophysical Observatory of the Smithsonian Institution*, 6:163–197. 5

Abbot, C. G. and Fowle, F. E. (1908). Silverdisk Pyrheliometer. *Ann. Astrophys. Obs.*, 2:39–47. 3

Anderson, G. P., Chetwynd, J. H., Theriault, J. M., Acharya, P. K., Berk, A., Robertson, D. C., Kneizys, F. X., Hoke, M. L., Abreu, L. W., and Shettle, E. P. (1993). MODTRAN2: suitability for remote sensing. In Kohnle, A. and Miller, W. B., editors, *Atmospheric Propagation and Remote Sensing II*, volume 1968, pages 514–525. SPIE. 76

Ångström, A. and Rodhe, B. (1965). Pyrheliometric measurements with special regard to the circumsolar sky radiation. *Tellus*, XVIII(1). 149

Ångström, K. (1893). A electrical substitution principle to measure radiant heat. *Nova Acta Reg. Soc. Sc. Upsal.*, 3:1–8. 3

Berk, A., Anderson, G., Acharya, P., and Shettle, E. (2008). *MODTRAN 5.2.0.0 USER'S MANUAL*. 76

Berk, A., Anderson, G. P., Acharya, P. K., Bernstein, L. S., Muratov, L., Lee, J., Fox, M., Adler-Golden, S. M., Chetwynd, J. H., Hoke, M. L., Lockwood, R. B., Gardner, J. A., Cooley, T. W., Borel, C. C., and Lewis, P. E. (2005). MODTRAN 5: A Reformulated Atmospheric Band Model with Auxiliary Species and Practical Multiple Scattering Options: Update. In Shen, S. S. and Lewis, P. E., editors, *Algorithms and Technologies for Multispectral, Hyperspectral, and Ultraspectral Imagery XI*, volume 5806, pages 662–667. SPIE. 76

BIPM (2008). *Guide to the expression of uncertainty in measurement, Supported by BIPM, IEC, IFCC, ISO IUPAC, IUPAP and OIML*. International Organization for Standardization, Geneva. 38, 52

Boivin, L. P. (1993). Automated Absolute and Relative Spectral Linearity Measurements on Photovoltaic Detectors. *Metrologia*, 30(4):355. 33

Bolle, H. (2008). International Radiation Commissions 1896 to 2008: Research into Atmospheric Radiation from IMO to IAMAS. (No. 1). 4

Born, M. and Wolf, E. (1999). *Principles of Optics: Electromagnetic Theory of Propagation, Interference and Diffraction of Light (7th Edition)*. Cambridge University Press, 7th edition. 24

Brusa, R. W. and Fröhlich, C. (1986). Absolute radiometers (PMO6) and their experimental characterization. *Appl. Opt.*, 25(22):4173–4180. 9, 12, 13, 24, 25, 48, 49, 64, 71, 162

Butler, J. J., Barnes, R., c. Johnson, Rice, J. P., and Shirley, E. L. (2008). Sources of Differences in On-Orbit Total Solar Irradiance Measurements. *Journal of Research*, 113(4):187–203. 5, 25, 61

CIMO (2008). *Guide to Meteorological Instruments and Methods of Observation*. World Meteorological Organization. 149

Crommelynck, D. (1981). Fundamentals of absolute pyrheliometry and objectie charachterisatio. *Earth Radiation Science Seminars, NASA Conference Publication*. 165

Crommelynck, D., Domingo, V., Fichot, A., Fröhlich, C., Penelle, B., Romero, J., and Wehrli, C. (1993). Preliminary Results from the SOVA Experiment on Board the European Retrievable Carrier (EURECA). *Metrologia*, 30(4):375–379. 13

Crommelynck, D., Fichot, A., Lee, R. B., and Romero, J. (1995). First realisation of the Space Absolute Radiometric Reference (SARR) during the ATLAS 2 flight period. *Advances in Space Research*, 16(8):17 – 23. 5

Dewitte, S., Crommelynck, D., Mekaoui, S., and Joukoff, A. (2004). Measurement and Uncertainty of the Long-Term Total Solar Irradiance Trend. *Solar Physics*, 224:209–216. 10.1007/s11207-005-5698-7. 5

Ediss, G. A. (2006). Effect of Vacuum Pressure on the Thermal Loading of the ALMA Cryostat. Technical report, National Radio Astronomy Observatory. 60

Finsterle, W. (2011). International Pyrheliometer Comparison IPC-XI - Final Report. Technical report, WMO IOM Report No. 108. 155

Finsterle, W., Blattner, P., Moebus, S., Ruedi, I., Wehrli, C., White, M., and Schmutz, W. (2008). Third comparison of the World Radiometric Reference and the SI radiometric scale. *Metrologia*, 45(4):377–381. 4, 31, 34

Fischer, J. and Fu, L. (1993). Photodiode nonlinearity measurement with an intensity stabilized laser as a radiation source. *Appl. Opt.*, 32(22):4187–4190. 33

Fox, N., Aiken, J., Barnett, J. J., Briottet, X., Carvell, R., Fröhlich, C., Groom, S. B., Hagolle, O., Haigh, J. D., Kieffer, H. H., Lean, J., Pollock, D. B., Quinn, T., Sandford, M. C. W., Schaepman, M., Shine, K. P., Schmutz, W. K., Teillet, P. M., Thome, K. J., Verstraete, M. M., and Zalewski, E. (2003). Traceable radiometry underpinning terrestrial- and helio-studies (TRUTHS). *Advances in Space Research*, 32(11):2253 – 2261. Calibration, Characterization of Satellite Sensors, Physical Parameters Derived from Satellite Data. 7

Fox, N. P. (1991). Trap Detectors and their Properties. *Metrologia*, 28(3):197. 31, 33

Fröhlich, C. (1978). World Radiometric Reference. Technical Report WMO 490, World Meteorological Organization, Commission for Instruments and Methods of Observation. Final Report. 3

Fröhlich, C. (1991). History of Solar Radiometry and the World Radiometric Reference. *Metrologia*, 28(3):111. 4

Fröhlich, C. (2006). Solar Irradiance Variability Since 1978. *Space Science Reviews*, 125:53–65. 10.1007/s11214-006-9046-5. 5, 6, 25, 28, 62

Fröhlich, C. (2008). personal communication. PMOD/WRC. 76

Fröhlich, C., Andersen, B. N., Appourchaux, T., Berthomieu, G., Crommelynck, D. A., Domingo, V., Fichot, A., Finsterle, W., Gomez, M. F., Gough, D., Jimenez, A., Leifsen, T., Lombaerts, M., Pap, J. M., Provost, J., Cortes, T. R., Romero, J., Roth, H., Sekii, T., Telljohann, U., Toutain, T., and Wehrli, C. (1997). First results from VIRGO, the experiment for helioseismology and solar irradiance monitoring on SOHO. *Solar Physics*, 170:1–25. 10.1023/A:1004969622753. 5

Fröhlich, C., Romero, J., Roth, H., Wehrli, C., Andersen, B. N., Appourchaux, T., Domingo, V., Telljohann, U., Berthomieu, G., Delache, P., Provost, J., Toutain, T., Crommelynck, D. A., Chevalier, A., Fichot, A., Däppen, W., Gough, D., Hoeksema, T., Jimenez, A., Gomez, M. F., Herreros, J. M., Cortes, T. R., Jones, A. R., Pap, J. M., and Willson, R. C. (1995). VIRGO: Experiment for helioseismology and solar irradiance monitoring. *Solar Physics*, 162:101–128. 10.1007/BF00733428. 5

Goebel, R., Stock, M., and Köhler, R. (2000). Report on the International Comparison of Cryogenic Radiometers Based on Transfer Detectors. *BIPM Report*, (2000/9). 4

Gordon, G. D. (1960). Measurement of Ratio of Absorptivity of Sunlight to Thermal Emissivity. *Review of Scientific Instruments*, 31(11):1204–1208. 27, 165

Gueymard, C. A. (1998). Turbidity Determination from Broadband Irradiance Measurements: A Detailed Multicoefficient Approach. *Journal of Applied Meteorology*, 37(4):414–435. 154

Gueymard, C. A. (2001). Parameterized transmittance model for direct beam and circumsolar spectral irradiance. *Solar Energy*, 71(5):325 – 346. 150

Gueymard, C. A. (2004). The sun's total and spectral irradiance for solar energy applications and solar radiation models. *Solar Energy*, 76(4):423 – 453. 150

http://www.pmodwrc.ch/pmod.php?topic=tsi/composite/SolarConstant (2011). PMOD/WRC TSI composite. 6

IAMAP (1986). A preliminary cloudless standard atmosphere for radiation computation. Technical Report WMO/TD-No. 24, World Meteorological Organization. 154

IPPC (2007). *Climate Change 2007: The Physical Science Basis. Contribution of Working Group I to the Fourth Assessment Report of the Intergovernmental Panel on Climate Change.* Cambridge University Press, Cambridge, United Kingdom and New York, NY, USA. 2

Karlsson, B. and Ribbing, C. G. (1982). Optical constants and spectral selectivity of stainless steel and its oxides. *Journal of Applied Physics*, 53(9):6340–6346. 22, 25, 28

Keithley (2011). Achieving Accurate and Reliable Resistance Measurements in Low Power and Low Voltage Applications. Technical report, Keithley Instruments Inc. 128

Kendall, J. M. S., Haley, F., and Plamondon, J. (1965). Cavity Type Absolute Total Radiation Radiometer. Los Angeles, Calif. 3, 9

Kopp, G. (2010). TSI Radiometer Facility (TRF) Measures Irradiance. SORCE science meeting TSI workshop. 74

Kopp, G., Heuerman, K., Harber, D., and Drake, G. (2007). The TSI Radiometer Facility: absolute calibrations for total solar irradiance instruments. *Earth Observing Systems XII*, 6677(1):667709. 5, 9, 41, 42, 43, 53

Kopp, G., Lawrence, G., and Rottman, G. (2005). The Total Irradiance Monitor (TIM): Science Results. *Solar Physics*, 230:129–139. 10.1007/s11207-005-7433-9. 161

Kurucz, R. L. (1997). The Solar Irradiance by Computation. http://kurucz.harvard.edu/sun/irradiance/. 76

Lawrence, G. M., Rottman, G., Harder, J., and Woods, T. (2000). Solar Total Irradiance Monitor (TIM). *Metrologia*, 37(5):407. 5

Lommel, E. (1885). Die Beugungserscheinungen einer kreisrunden Öffnung und eines kreisrunden Schirmchens theoretisch und experimentell Bearbeitet. *Abh. Bayer. Akad.*, 15:233–328. 24

Lu, F., Yang, B., Cheng, D., Ye, R., Yu, W., and Sun, J. (1992). Low hydrogen content diamond-like carbon coatings of KCl optics for high power industrial CO2 lasers. *Thin Solid Films*, 212(1-2):220 – 225. Special Issue: Diamond Films and Related Materials. 84

Martin, J. E., Fox, N. P., and Key, P. J. (1985). A Cryogenic Radiometer for Absolute Radiometric Measurements. *Metrologia*, 21(3):147. 4, 135

Moebus, S. (2005). Experimenteller Vergleich von Primärstandards für optische Strahlungsmessung. Master's thesis, Fachhochschule Ravensburg-Weingarten. 34, 60

Nelson, P. G. (2007). An Analysis of Scattered Light in Reflecting and Refracting Primary Objectives for Coronagraphs. Technical Note 4, High Altitude Observatory. 108, 109

Pouillet, C. S. M. (1838). Mémoire sur la chaleur solaire, sur les pouvoirs rayonnants et absorbants de l'air atmosphérique, et sur la témperature de l'espace. *Compt. rend.*, 7:24–28. 3

Reda, I. and Afshin, A. (2003). Solar Position Algorithm for Solar Radiation Applications. Technical Report TP-560-34302, NREL, Golden, Colorado. Revised 2008. 157

Rohsenow, W. M., Harnett, J. P., and ChoYoung, I., editors (1998). *Handbook of Heat Transfer (3rd Edition)*. McGraw-Hill. 28

Romero, J., Fox, N. P., and Fröhlich, C. (1991). First Comparison of the Solar and an SI Radiometric Scale. *Metrologia*, 28(3):125–128. 4, 31, 34

Romero, J., Fox, N. P., and Fröhlich, C. (1995). Improved comparison of the World Radiometric Reference and the SI radiometric scale. *Metrologia*, 32(6):523–524. 4, 31

Schmutz, W., Fehlmann, A., Hulsen, G., Meindl, P., Winkler, R., Thuillier, G., Blattner, P., Buisson, F., Egorova, T., Finsterle, W., Fox, N. P., Grobner, J., Hochedez, J., Koller, S., Meftah, M., Meisonnier, M., Nyeki, S., Pfiffner, D., Roth, H., Rozanov, E., Spescha, M., Wehrli, C., Werner, L., and Wyss, J. U. (2009). The PREMOS/PICARD instrument calibration. *Metrologia*, 46(4):S202–S206. 38, 39

Shelton, D. P. (1992). Lens induced by stress in optical windows for high-pressure cells. *Rev. Sci. Instrum.*, 63(8):3978–3982. 110

Shirley, E. L. (1998). Revised Formulas for Diffraction Effects with Point and Extended Sources. *Appl. Opt.*, 37(28):6581–6590. 24

Shirley, E. L. (2004a). Diffraction corrections in radiometry: spectral and total power and asymptotic properties. *J. Opt. Soc. Am. A*, 21(10):1895–1906. 24

Shirley, E. L. (2004b). Diffraction Effects on Broadband Radiation: Formulation for Computing Total Irradiance. *Appl. Opt.*, 43(13):2609–2620. 24

Sterne, T. E. and Dieter, N. (1958). The Constancy of the Solar Constant. *Smithsonian Contributions to Astrophysics*, 3:9–+. 5

Suter, M. (2007). Experimentelle Charakterisierung des Einflusses der Blendenerwärmung auf das Messresultat von PMO6 Absolutradiometern. Bachelor's thesis, University of Zürich. 25, 26, 27

Thuillier, G., Dewitte, S., and Schmutz, W. (2006). Simultaneous measurement of the total solar irradiance and solar diameter by the PICARD mission. *Advances in Space Research*, 38(8):1792 – 1806. Magnetospheric dynamics and the international living with a star program. 9

Thuillier, G., Fröhlich, C., and Schmidtke, G. (1999). Spectral and Total Solar Irradiance Measurements on Board the International Space Station. In *Utilisation of the International Space Station 2*, volume 433 of *ESA Special Publication*, pages 605–+. 14

Trenberth, K. E., Fasullo, J. T., and Kiehl, J. (2009). Earth's Global Energy Budget. *Bulletin of the American Meteorological Society*, 90(3):311–323. 2

Wehrli, C. (2010). AERONET. http://aeronet.gsfc.nasa.gov/. 154, 157

White, G. K. and Meeson, P. J. (2002). *Experimental techniques in Low-Temperature Physics*. Oxford University Press, New York. 136, 137

Willson, R. C. (1979). Active cavity radiometer type IV. *Appl. Opt.*, 18(2):179–188. 5

Willson, R. C. and Mordvinov, A. V. (2003). Secular total solar irradiance trend during solar cycles 21-23. *Geophys. Res. Lett.*, 30(5):1199–. 5

Winkler, R. (2011a). *Cryogenic Solar Absolute Radiometer - a potential replacement for the World Radiometric Reference*. PhD thesis, University College London. 7, 109, 110, 135, 147

Winkler, R. (2011b). personal communication. January. 38, 39

Winkler, R., Fehlmann, A., and Usadi, E. (2007). Functional Requirement Specification for the Cryogenic Solar Absolute Radiometer. 135

WMO (1979). Technical Regulation. (WMO 49). 4

FEHLMANN André

Geburtsdatum: 22. Januar 1981 Heimatort: Staffelbach AG

AUSBILDUNG

- ◇ **Höheres Lehramt**, an der ETH Zürich, November 2010.
- ◇ **Promotionsstudium**, Doktorand am PMOD/WRC in Davos seit 1. April 2007; Betreuung an der Universität Zürich durch Prof. Dr. U. Straumann. Eingeschrieben an der Universität Zürich seit dem Herbstsemester 2007/2008.
- ◇ **Praktikum**, Physik Gymnasiallehrer, Alte Kantonsschule Aarau (Oktober – Dezember 2006).
- ◇ **Eidgenössische Technische Hochschule**, Zürich (2001- 2006)
  Diplom [M.Sc.] in Physik, mit Schwerpunkt in Astrophysik, Oktober 2006. Titel der Diplomarbeit: *Polarization of the Flash Spectrum of the 29 March 2006 Solar Eclipse.*
- ◇ **Maturität**, Typ C, Alte Kantonsschule Aarau, 2001.

PRÄSENTATIONEN

- ◇ **Teilchenphysik Doktorandenseminar der Universität Zürich und der ETH Zürich**, 2007, Vortrag.
- ◇ **Teilchenphysik Doktorandenseminar der Universität Zürich und der ETH Zürich**, 2008, Vortrag.
- ◇ **Interdisziplinäre Konferenz - Graubünden Forscht**, Young Scientists in Contest 2008, Vortrag.
- ◇ **NCCR Summer School**, 2008, Poster.
- ◇ **NEWRAD Conference**, 2008, 2 Poster.
- ◇ **Teilchenphysik Doktorandenseminar der Universität Zürich und der ETH Zürich**, 2010, Vortrag.
- ◇ **Interdisziplinäre Konferenz - Graubünden Forscht**, Young Scientists in Contest 2010, Vortrag.
- ◇ **SORCE Workshop**, 2010, Vortrag und Poster.
- ◇ **International Pyrheliometer Comparison - Seminar**, 2010, Vortrag.
- ◇ **NEWRAD Conference**, 2011, Vortrag und Poster.

PUBLIKATIONEN

- ◇ **S**chmutz, W., Fehlmann, A., Hulsen, G., Meindl, P., Winkler, R., Thuillier, G., Blattner, P., Buisson, F., Egorova, T., Finsterle, W., Fox, N. P., Grobner, J., Hochedez, J., Koller, S., Meftah, M., Meisonnier, M., Nyeki, S., Pfiffner, D., Roth, H., Rozanov, E., Spescha, M., Wehrli, C., Werner, L., and Wyss, J. U. (2009). The PREMOS/PICARD instrument calibration. Metrologia, 46(4):S202-S206.
- ◇ **F**ehlmann, A., Kopp, G., Schmutz, W., Winkler, R., Finsterle, W., Fox, N. P. (2011). Fourth World Radiometric Reference to SI radiometric scale comparison and implications to on-orbit measurements of the total solar irradiance. Submitted to Metrologia.
- ◇ **K**opp, G., Fehlmann, A., Finsterle, W., Harber, D., and Heuermann, K. (2011). Total Solar Irradiance Data Record Accuracy and Consistency Improvements. Submitted to Metrologia.